STRESS CORROSION CRACK INITIATION OF COLD-WORKED ALLOY 600 AND ALLOY 690 IN PWR PRIMARY WATER

Technical Milestone Report: M2LW-14OR0404023
PNNL-23712 September 2014

S. M. Bruemmer, M. J. Olszta, D. K. Schreiber and M. B. Toloczko
Pacific Northwest National Laboratory

Research Project:
Stress Corrosion Crack Initiation of Nickel-Base Alloys in LWR Environments
Project Manager: S. M. Bruemmer
Pacific Northwest National Laboratory

Conducted for:
Office of Nuclear Energy, U.S. Department of Energy
Light Water Reactor Sustainability Program
Materials Aging and Degradation Pathway
Pathway Manager: J. T. Busby
Oak Ridge National Laboratory

Table of Contents

Project Background **4**

Objective *4*

Approach *4*

Focus of Current Report *4*

Experimental Details **5**

SCC Initiation Test Systems *6*

DCPD Measurement *7*

Load Train *13*

Testing Methodology *14*

Overview of Characterization Approaches *15*

SCC Initiation Tests on Alloy 600 Materials **19**

Alloy 600 Materials Information and Specimens *20*

Microstructural and Microchemical Characterizations on Alloy 600 Heats *21*

SCC Initiation Test Results on Cold-Worked Alloy 600 ..... *33*

SCC Crack Initiation of 18% Tensile Strained CRDM Heat (Specimens IN002 & IN003) *33*

SCC Crack Initiation of 19% Cold-Rolled Plate Heat (Specimens IN016, IN017 and IN018) *46*

SCC Crack Initiation Tests on 20% Tensile Strained CRDM Heat M3935 from PWR Service (IN022) and 5% Tensile Strained CRDM Heat 93510 (IN023) *54*

SCC Crack Initiation of 8% Tensile Strained (TS) Plate Heat (Specimen IN052) *62*

SCC Initiation Testing of As-Received Alloy 600 ..... *64*

As-Received Plate Heat NX6106XK-11 Specimens (IN013, IN014, and IN015) *65*

As-Received CRDM Heat 93510 Specimens (IN045, IN046 and IN047) *66*

Service CRDM Heat M3935 Specimens (IN048, IN049 and IN050) *66*

Discussion of Alloy 600 SCC Initiation Results *70*

Processes Controlling SCC Initiation in Alloy 600 ..... *72*

Effect of Surface Conditions on SCC Initiation *74*

Comments on Criteria for Selecting an Initiation Time *74*

Summary Comments for Alloy 600 ..... *75*

SCC Initiation Tests on Alloy 690 Materials **75**

Alloy 690 Materials Information and Specimens *75*
Overview of Alloy 690 Corrosion Test Results *78*
General Approach for SCC Initiation Testing for Alloy 690 ..... *81*
SCC Initiation Test Results on SCC Susceptible Alloy 690 (IN006, IN007) *84*
TEM of Cracks in IN007 ..... *112*
SCC Initiation Test Results on Tensile Strained Alloy 690 (IN009-IN012) *117*
Blunt Notch SCC Initiation Tests on Cold-Worked CRDM Specimens *125*
Critical Stress Intensity for SCC Growth on Cold Worked Alloy 690 ..... *140*
Constant Load Tensile Tests on 31% Cold Forged Alloy 690 (IN024 – IN032) and 21% Cold Forged Alloy 690 (IN033 - IN044) *143*
Discussion of Alloy 690 SCC Initiation Results *145*
Summary and Conclusions **148**
Acknowledgments **148**
References **149**

Project Background

Objective

This research project addresses one of the least understood aspects of stress corrosion cracking (SCC) for light-water reactor (LWR) pressure boundary components - crack initiation. The focus of the work is to investigate important material (composition, processing, microstructure) and environmental (water chemistry, temperature, electrochemical potential, stress) effects on the SCC susceptibility of corrosion-resistant, nickel-base alloys. The primary objectives are to identify mechanisms controlling crack nucleation, investigate the transition to long crack growth in these alloys under realistic LWR conditions and help establish the framework to effectively model and mitigate SCC initiation processes.

Approach

Alloy 600 materials were selected for the first phase of SCC initiation experimentation followed by testing on the more resistant alloy 690 materials. For both alloys, material variants known to influence SCC response are being examined including cold work (forged, rolled and tensile strained), banded/inhomogeneous microstructures (plate versus extruded pipe), grain boundary precipitation (heat-to-heat variations and changes due to thermal treatments) and surface grinding (various depths of damage). Materials and material conditions have been identified and obtained from ongoing research projects where stress-corrosion crack growth has been characterized, thus creating an important link between SCC initiation and propagation behavior. Detailed examinations have been performed using optical and electron microscopy to establish key bulk and surface microstructural features that may act as initiation precursors. Dedicated test systems with continuous in-situ detection of crack formation were designed and constructed enabling SCC initiation experimentation of a range of alloy 600 and 690 materials. After SCC testing in high temperature autoclave systems, surface and near-surface characterizations were conducted to document nano-to-microscale initiation precursors leading to macroscopic stress corrosion cracks. The fundamental understanding of how the near-surface microstructure is degraded during high-temperature water exposure is essential to an improved predictive methodology for SCC initiation.

Focus of Current Report

This report reviews recent SCC initiation testing on alloy 600 and alloy 690 materials in high-temperature, simulated PWR primary water. It follows earlier milestone reports that described our first SCC initiation tests and corrosion-structure characterizations on alloy 600 [1] and alloy 690 [2] materials. Current results have established baseline responses for cold-worked alloy 600 with constant load, SCC initiation tests performed on three material heats. Cold-work levels from 7% to 20% have been assessed along with ongoing tests on specimens in the as-received, mill-annealed condition. SCC initiation tests have also been performed on three heats of alloy 690 in the highly cold-worked condition. Due to its much higher resistance to SCC, tensile and blunt-

notch initiation tests have included minor applications of dynamic strain to promote crack nucleation. Scanning electron microscopy (SEM) is used extensively for the characterization of material, corrosion and crack microstructures. Observations of nanoscale precursor corrosion and crack structures are linked to macroscopic SCC initiation. Critical assessments have been performed to determine the fidelity of in-situ direct current potential drop (DCPD) detection capability and provide insights into mechanisms controlling crack nucleation.

Experimental Details

A key goal for this program is to be able to correlate the SCC initiation time to various aspects of materials processing including bulk microstructure, near surface microstructure, surface texture, existence of surface defects and applied stress level. Prior experience with alloys 600 and 690 has shown that their SCC crack growth resistance is extremely sensitive to the degree of plastic deformation, and therefore being able to accurately characterize it in the test specimen was an important factor in the selection of specimen type. Several different specimen types were considered for the crack initiation testing including U-bend, bent beam, tensile, and blunt-notch compact tension (CT) geometries.

Ultimately, a tensile specimen geometry was the most attractive because it has none of the shortcomings associated with U-bend, bent beam and blunt-notch specimens. This design produces a uniaxial stress state, the gauge length is easily accessible allowing control over the surface microstructure, various types of defects can be easily generated, and there are several ways to produce specimens with well-known amounts of uniform plastic strain. In addition, prior work at KAPL [3] has shown that DCPD can be effectively used to detect crack initiation. This capability was confirmed by our measurements in a previous report [1], and results are expanded within the current document.

Several factors played into the specific design of the tensile specimens employed for SCC initiation testing, however the most important of which was maximizing the ability of DCPD to detect crack initiation. One practical issue was the desire to have an initiation specimen size that fit within the dimensions of a 0.5T CT specimen such that any material prepared for SCC crack growth studies could also be used for SCC crack initiation studies. The final tensile design was refined to the point that a crack initiation specimen could be cut from an SCC-tested 0.5T CT specimen as long the crack length to width ratio (a/W) in the CT specimen did not exceed 0.7. This a/W is below the range of typical crack lengths in SCC studies conducted by PNNL allowing routine extraction of crack initiation specimens as desired. Other factors that went into the design were a need to electrically isolate the specimen and eliminate any significant stress risers. A photograph of the final design is shown in Figure 1.

Application of surface damage is achieved by applying various grinding tools to the gauge section while rotating the specimens in a lathe. A controlled load is applied while systematically

moving the tool across the gauge section. Grinding tools that have been used include wood-backed sandpaper of various grits and a rotary tool with different roughness grinding disks.

As part of this research, complimentary surface oxidation studies were performed on small rectangular coupons (30 mm x 20 mm) that were mechanically polished to a colloidal silica finish (~100 nm diameter particles). The amount of surface damage remaining was evaluated in cross-section using low kV, SEM backscatter electron (BSE) imaging and determined to be negligible, as the bulk grain contrast was observed to within ~5 nm of the surface. These samples have been tested both concurrently with the initiation samples as well as in dedicated exposure autoclaves to better understand the effect of surface finish and lack of stress on the oxidation behavior of these materials.

Figure 1. PNNL 1.2" tall SCC tensile initiation specimen.

SCC Initiation Test Systems

Test systems have been built to allow in-situ monitoring of crack initiation in an environment that provides a high degree of control over load (stress), water temperature and water chemistry including B/Li content, dissolved gas content and impurity content. These test systems are very similar in design to systems built at PNNL to measure SCC crack growth of LWR pressure boundary component materials [4,5].

The key components of these test systems are: (1) a servo-electric load control system capable of maintaining a stable constant load for very long periods of time and capable of providing a wide range of cyclic loading conditions, (2) a recirculating water system that that is used to control water chemistry, (3) an autoclave for specimen exposure at high temperatures and pressures, (4) a DCPD system for in-situ monitoring of crack initiation, and (5) a continuous data acquisition system. Careful consideration went into design and equipment selection to optimize control of all system variables. Some of the most important optimizations were to: (1) use wetted components that release no contamination into the water, (2) have a sufficiently high water flow rate through the autoclave to maintain the target chemistry, (3) maintain uniform temperature and pressure at the specimens, (4) obtain highly accurate measurements of the test environment (temperature, conductivity, pH, load, dissolved gas content), and (5) create a sensitive DCPD-based crack initiation detection system. Each of the subsystems will be discussed in further detail below.

The water flow system is comprised of low- and high-pressure loops as shown in Figure 2. The purpose of the low-pressure loop is to control dissolved gas content and impurity level by flowing water through a column where selected gases and ionic impurities are dissolved or injected into the water. A side stream of this mixing loop feeds the high-pressure loop. The large pressure pulses and flow surges created by the piston pump are dampened with pulsation dampers at the inlet and outlet of the pump. The high-pressure water flows into a regenerative heat exchanger where hot water leaving the autoclave preheats the incoming water. Just prior to entering the autoclave, the incoming partially heated water is brought up to test temperature using a preheater. After the water flows through the heated autoclave, it travels back through the regenerative heat exchanger and then through a water cooler that brings the water back down to room temperature. The cooled water then passes through a back-pressure regulator and emerges at ~0.07 MPa (10 psi) of pressure. The water runs through a flow meter, a conductivity sensor, a mixed resin bed demineralizer, and is dumped back into the low-pressure mixing loop.

Boron (B) and lithium (Li) levels for PWR primary water testing are controlled by pre-saturating the mixed resin bed demineralizer with boric acid and lithium hydroxide to specific levels that will result in tailored near-constant B and Li content. Some drift in the Li level in the water is expected because it is singly ionized and is easily displaced from the demineralizer by more highly positively ionized species (e.g., chromate) coming off the autoclave. To account for this, displaced Li is removed by periodic partial replacement of water in the mixing loop with water having little or no Li (and some B). Boron and Li levels in the mixing loop are determined from measurements of water conductivity, pH and temperature. Water flow through the autoclave is maintained at ~125 cc/min to provide a consistent chemistry environment.

DCPD Measurement

PNNL uses a reversing DCPD system developed by Peter Andresen of General Electric. As with all DCPD measurement systems, a constant current is run though the sample. However, by using a solid-state polarity-reversing switch built into the current path, potential drop is measured in both a forward and reverse current flow condition. By measuring the average of the voltage in the forward and reverse current conditions, contact voltages are eliminated from the measurement. Finite element modeling was used to visualize the voltage distribution in the interior of the specimen and on the surface. Wire attachment positions were selected in regions where voltage was relatively uniform on the surface, thus making it relatively easy to remove and reinsert specimens for testing as needed without significantly changing the DCPD response. Platinum wire is used for current and voltage feeds into the autoclave and are spot welded onto the sample. For PWR water testing, segmented transformation toughened zirconia (TTZ) tubing is used to help prevent shorting of the Pt wires against other wires or any metal surfaces in the autoclave. Some crosstalk in the voltage wires occurs and is minimized by keeping the wires separated as far as reasonably possible from each other. In addition, the current wires are kept away from the voltage measurement wires. Specimens are electrically insulated from the load train using ceramic spacers.

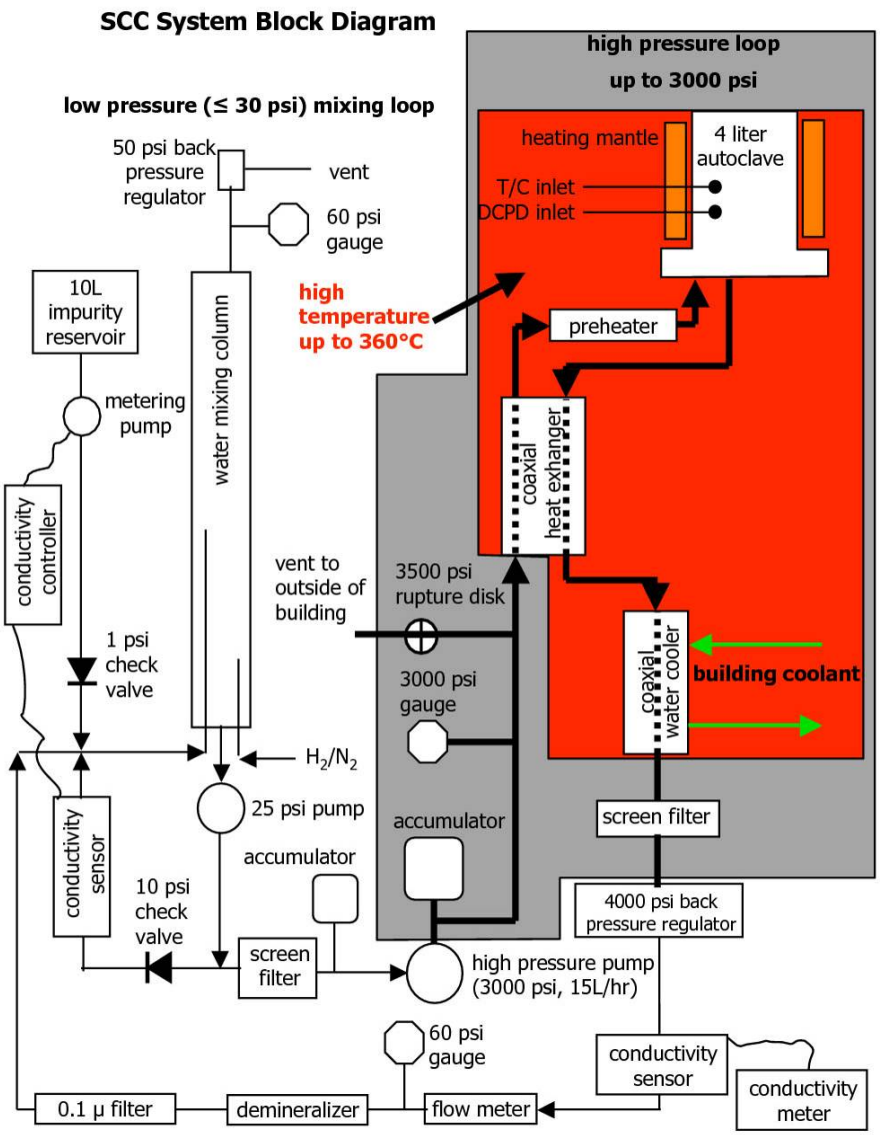

Figure 2. General water flow diagram for PNNL SCC crack-growth and initiation test systems.

A sketch of the tensile geometry and how DCPD is applied is shown in Figure 3. The voltage across the gauge section (V_{gauge}), is sensitive not only to a change in the cross-sectional area of the gauge region due to crack formation, but also to changes in gauge length and diameter caused by tensile deformation. Although crack initiation is the phenomenon of interest, a crack initiation test is actually a creep test up until the point of crack initiation. Because specimens are typically tested at their yield stress, measurable creep strains occur despite a relatively low test temperature of 360°C. Thus, the DCPD data are plotted in terms of strain with the understanding that crack initiation will produce a significant deviation from the creep strain trajectory. The relationship between gauge voltage and volume-conservative true tensile strain is given by:

$$\varepsilon = \frac{1}{2}\ln\left(\frac{V_{DCPD}}{V_{DCPD_o}}\right) \tag{1}$$

DCPD voltage is sensitive not only to crack formation and creep strain, but also to changes in the resistivity of the material. Both alloys 600 and 690 are known to exhibit a change in resistivity when exposed to LWR-relevant temperatures, and while this must be due to changes in the alloy microstructure, these microstructural features have yet to be identified. In order to remove this resistivity-based DCPD change and ensure the highest possible degree of sensitivity in detecting crack initiation, the specimen was designed to have a region where the inherent resistivity of the specimen would be monitored and subtracted from the resistivity change of the gauge section. This is accomplished by having a region of the specimen with larger diameter where the stress is ~15% of the gauge stress. The formula for the reference-corrected strain is:

$$\varepsilon_{referenced} = \frac{1}{2}\left[\ln\left(\frac{V_{gauge}}{V_{gauge_o}}\right) - \ln\left(\frac{V_{ref}}{V_{ref_o}}\right)\right] \tag{2}$$

In this formula, V is a DCPD-measured voltage. Note that the reference DCPD voltage will be sensitive not only resistivity-driven changes, but it will also be sensitive to creep strains that occur in the reference region that is at ~15% of the gauge stress. Thus, a small amount of creep strain may also be subtracted, although the value is expected to be negligibly small. It will also be sensitive to elastic strains that occur in the reference region. This basic formula has been found to work quite well at estimating the strain when the reference region has the same bulk microstructure as the gauge region. However, when the microstructures are different, such as when a specimen is cold worked by tensile straining, the different dislocation densities between the gauge and the reference region cause different material resistivity evolution with time. For this reason, the preferred cold working processes (e.g., cold rolling or forging) are those that can be applied uniformly to the specimen or source material entirely.

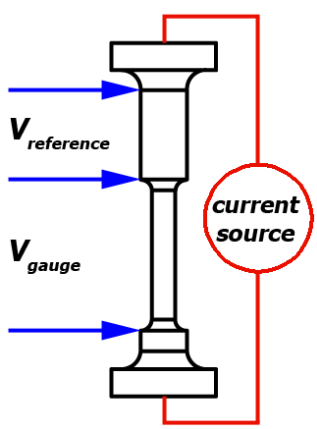

Figure 3. Schematic of the ideal DCPD measurement points on the tensile geometry.

Equations 1 and 2 are based on idealized measurement locations where the voltage leads are attached at each end of the gauge section. However, these are impractical locations for a number of reasons, perhaps the most important being that a stress riser affecting initiation response would form around the spot weld on the gauge section. The simplest solution would have been to move the spot weld locations to the just beyond the fillet, but this was determined to be impractical due to the small specimen size in combination with the thickness of the fixturing that would have been necessary to adequately support the specimens. The selected locations are shown in Figure 4. To better understand how these measurement locations would cause deviation from the idealized values given by Equations 1 and 2, finite element modeling was performed. An axisymmetric model utilizing elements that calculate stress, strain, and resistivity were used for the simulations. Voltage at the actual attachment points and directly across the gauge was calculated as part of the simulation. It was found that the relationship between strain and the voltage directly across the gauge was well represented by Equation 1. The correlation between strain and V/Vo (the actual DCPD measurement points) was found to continue to be adequately represented by a simple natural log function, but with a scaling coefficient larger than 1/2. In the case of the standard 3 mm diameter gauge, the scaling coefficient was found to 0.9417 as shown in Figure 5(a). Through additional simulations, the scaling coefficient was determined as a function of gauge diameter for the range of diameters used for this research as shown in Figure 5(b).

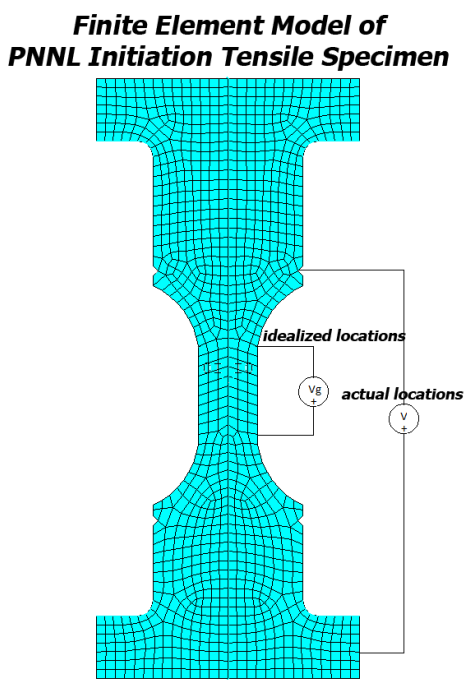

Figure 4. 2D representation of the axisymmetric finite element model. Actual gauge spot-weld locations versus idealized gauge spot weld locations are shown.

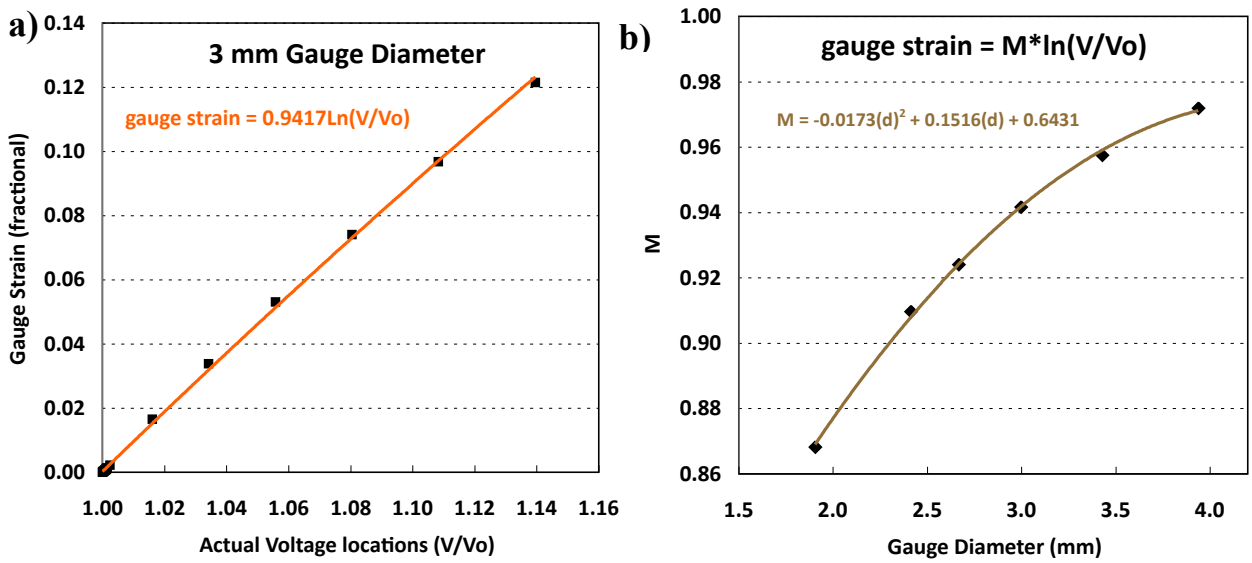

Figure 5. Results of finite element simulations to determine the relationship between strain and voltage measured from the actual locations on the specimen as shown in Figure 4.

Since contributions to the voltage change across the gauge region from strain and resistivity cannot be separated, this scaling factor is applied to both. Thus when using a reference correction to remove the effect of resistivity change, the same scaling factor must be applied to the reference measurement:

$$\varepsilon_{referenced} = M\left[\ln\left(\frac{V_{gauge}}{V_{gauge_o}}\right) - \ln\left(\frac{V_{ref}}{V_{ref_o}}\right)\right] \tag{3}$$

Finite element analysis has not yet been used to estimate the effect of crack growth on the DCPD signal; however, consideration has been given to the relationship between stress intensity and crack depth. The stress intensity for a thumbnail type crack growing through a rod under tension is covered in several stress intensity factor compilations and has been the subject of numerous journal articles [6-10]. Since analytic solutions for this geometry are not possible, stress intensities were determined using finite element modeling. Straight, elliptical and circular cracks (Figure 6) are all typically assessed with the latter two being most representative of what have been observed in our initiation tests. The finite element analysis results in the literature are presented as a dimensionless stress intensity factor, F_I, given by:

$$F_I = \frac{K}{\sigma\sqrt{\pi a}} \tag{4}$$

F_I is typically plotted or tabulated against a/D as defined in Figure 6. One of the more concise results provided by Shin [9] in Figure 7 reveals that F_I is ~0.8 for likely crack shapes having a depth of ~150 µm (a/D = 0.05).

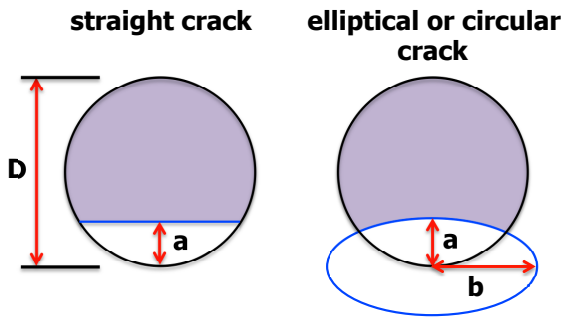

Figure 6. Types of cracks considered for stress intensity calculations.

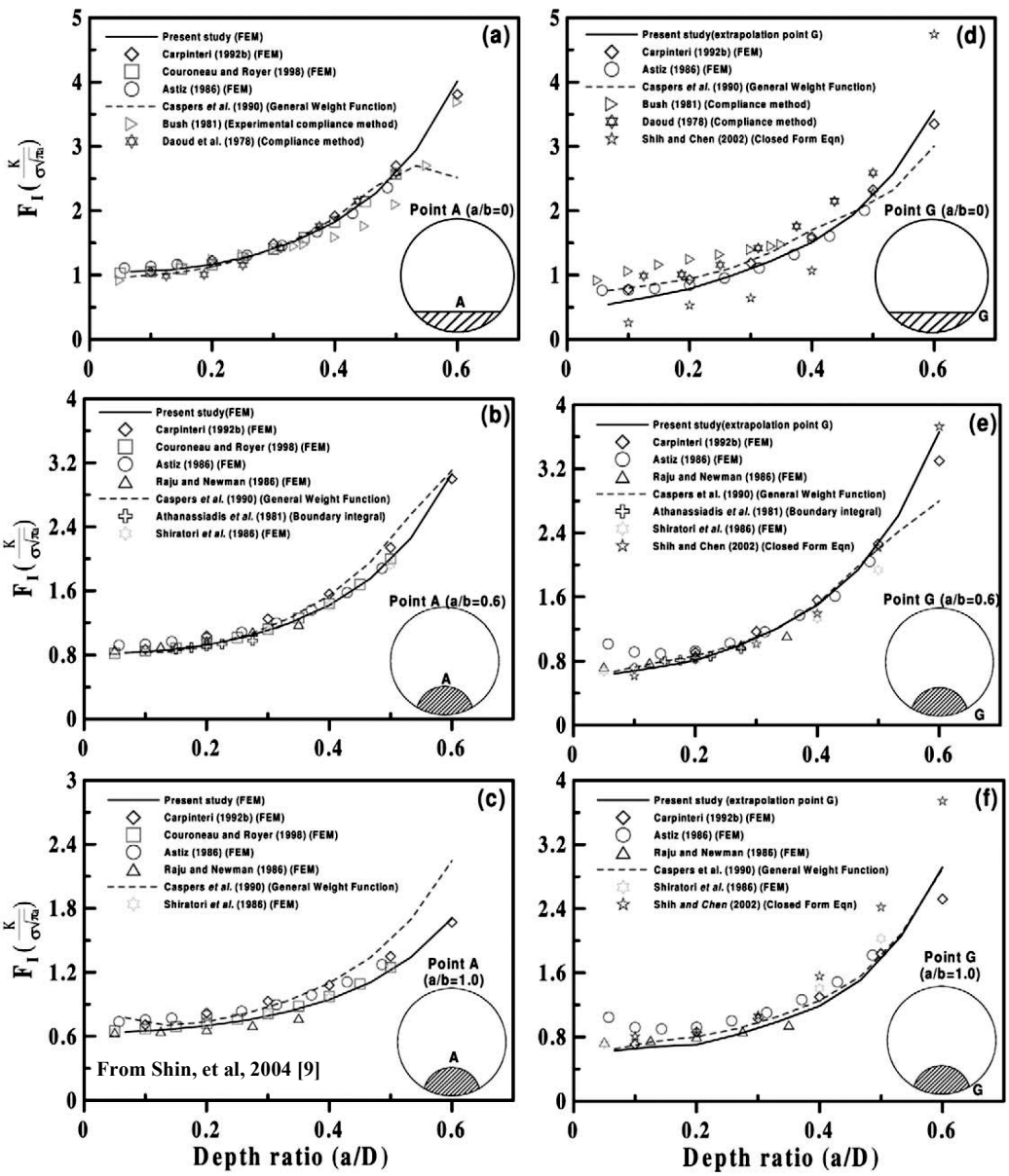

Figure 7. Dimensionless stress intensity factor at either the center or edge of the crack plotted against a/D for three different crack shapes as given by Shin [9].

For 20-30% cold-worked materials that have a yield strength of ~600-650 MPa, this results in a stress intensity of ~10-11 MPa√m. For a crack depth of ~300 μm, the stress intensity increases up to ~15-16 MPa√m, and becomes >20 MPa√m as crack depth reaches ~500 μm. SCC crack growth is thought to have a strong dependence on stress intensity within this range [11], and it is believed that one of the key contributors to conversion from a nascent crack to an actively growing SCC crack is this increase in stress intensity [12].

Another important factor in the mechanical response of the specimen is the rise in stress as the cross sectional area is decreased during crack growth. Since testing is routinely performed at the yield strength, any reduction in area drives up the stress beyond the original yield stress. For as-received or lightly cold-worked material where substantial work hardening can occur, the specimen can strain harden to continue carrying the load. However for highly cold-worked materials where there is very little remaining strain hardening capacity, the specimen can only accommodate a small decrease in load bearing area before runaway strain, and possibly crack growth, will occur.

Load Train

Load is applied using a servo-electric motor that can hold a steady load for indefinite periods of time while also providing the ability to perform cyclic loading in either position or load control up to about 3 Hz. Load from the servo-electric motor is transmitted into the autoclave with a pullrod guided through the base of the autoclave. Specimens are braced from above by a top plate and multi-bar linkage that transmits load from the top plate to the base of the autoclave. Two types of specimen loading systems were developed, one for testing 1-3 specimens, and a second that was developed for testing up to 36 specimens using a single servo motor and autoclave, both of which are shown in Figure 8. These system designs rely on series loading to allow multiple specimens to be tested with a single servo motor. All specimens in the 1-3 specimen load train can be simultaneously monitored with DCPD, whereas due to the cost and physical constraints associated with running a large number of Pt wires for DCPD, the 36 specimen system is currently limited to monitoring up to 20 specimens. Series loading, with all specimens supported in a single string, is utilized in the 1-3 specimen load train. The 36-specimen load train has three strings of 12 specimens. All three strings are firmly bolted to the upper support plate while the bottom of the strings are attached to a plate that is allowed to pivot around the load rod and the ends of each string using ball joints. This equilateral triangle arrangement forces all three strings to carry 1/3 of the load generated by the servo motor. Since all specimens cannot be monitored simultaneously, each string is designed so that if an individual specimen cracks to the point of failure, the string will pick up the load allowing the test to continue.

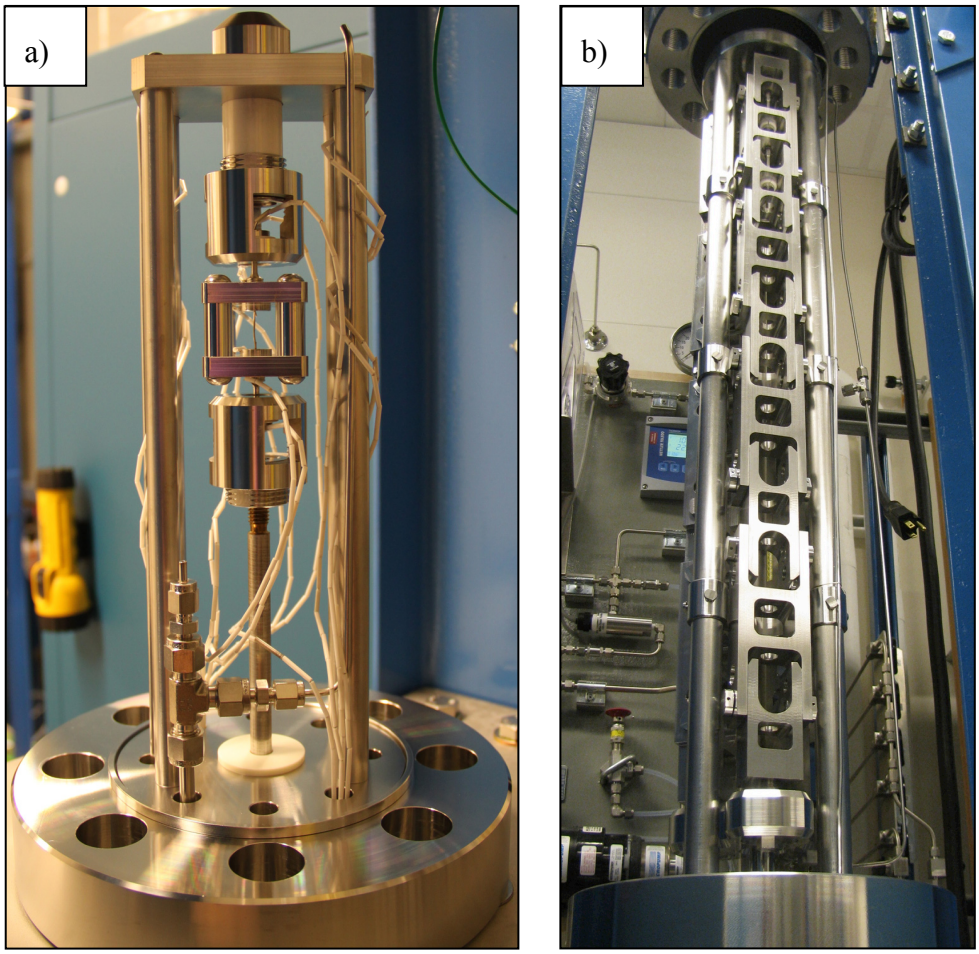

Figure 8. Crack initiation test system load trains at PNNL for (a) 1-3 specimens and (b) up to 36 specimens.

Testing Methodology

All testing is performed with specimens loaded to their yield stress. For these multi-specimen load trains, where all specimens are at the same load but may vary in strength, it requires determination of the necessary gauge diameter for each specimen to be at its yield stress. In order to accomplish this, 360°C air tensile tests are performed on all materials prior to machining the initiation specimens. Gauge diameters are then machined based on this information and the desired system load, which is typically 455 kg (1000 lbs).

At the onset of an initiation test, specimens are brought up to their yield stress by constant extension rate, usually over a period of ~1 hour. DCPD is used to monitor the stress versus strain, thus providing direct evidence that the specimens have reached their yield stress. As shown in Figure 9, a typical stress versus strain trace is obtained, and some variability in the yield load among the different materials typically occurs. It is desired to have direct evidence that all specimens have reached their yield stress, hence all specimens are given a small amount of plastic strain, some having slightly more than others.

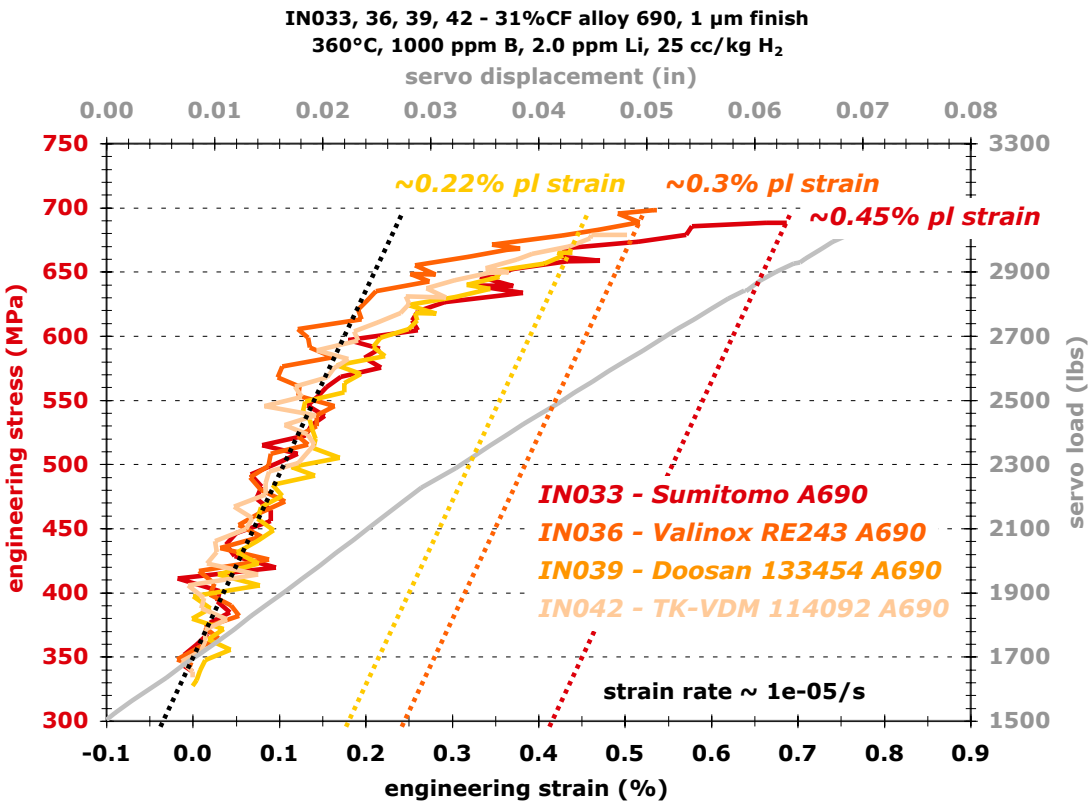

Figure 9. Typical stress versus strain response when loading up multiple specimens for the start of an SCC initiation test. The loading process is typically arranged to take ~1 hour.

Materials, such as cold-worked alloy 600, that are expected to undergo SCC initiation in a reasonable amount of time are held at constant load at the yield stress for the duration of the test. Initiation resistant materials, such as alloy 690, may be subjected to other loading scenarios. In some cases, the stress may be periodically increased over a period of ~1 hour or over much longer periods. In all cases, test data are plotted at least daily to observe for signs of SCC initiation.

Overview of Characterization Approaches

The traditional assessment of SCC in CT samples in our previous research has revolved around ex-situ examinations of SCC crack growth surfaces as well as cross-sections of the SCC crack using a suite of techniques including scanning electron microscopy (SEM), transmission electron microscopy (TEM), and atom probe tomography (APT). Similar approaches are used for the crack initiation specimens. Examination of a specimen starts with optical and SEM observations of the gauge region at a variety of magnifications. To facilitate mapping out the location of cracks or other interesting surface features, four fiducial marks are made on the button ends of the tensile specimens to serve as reference points. Utilization of the montaging feature in the Oxford Aztec software allows for rapid collection of spatially correlated data. Because this program has a key interest in understanding precursors to crack initiation, specimens are

sometimes removed from a test system prior to DCPD-observed crack initiation so that precursor surface microstructures can be documented. By this methodology, cracks observed at any given exposure time can be tracked for the remainder of a continuing test. One such example is shown in Figure 10 where a progression in cracking is between 1870 h and 2750 h can be seen.

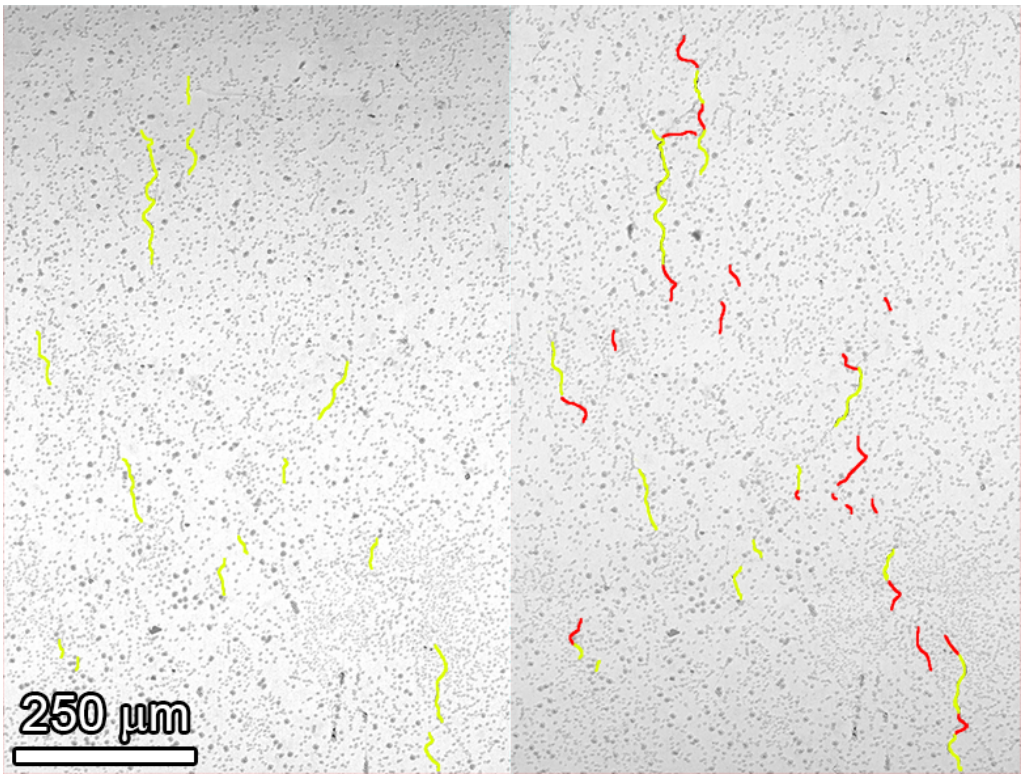

Figure 10. SEM (BSE) micrographs of the surface of an alloy 600 tensile specimen between two exposures (left 1870 hours and right 2750 hours). The presence of cracks at 1870 hours is highlighted in yellow and new cracks and crack extensions at 2750 hours are highlighted in red.

The size and shape of the PNNL miniature tensile specimen also conveniently allows for examination and manipulation in a focused ion beam (FIB) microscope. Specific cracks identified in the SEM at a given fiducial orientation can be located in the FIB, and a number of procedures can be performed. Using the gallium ion beam, trenches can be cut in the middle of cracks to determine crack depths. Serial trenching can also be performed starting ahead of a crack and subsequently moving into the crack to determine the morphology along the length of the crack (Figure 11).

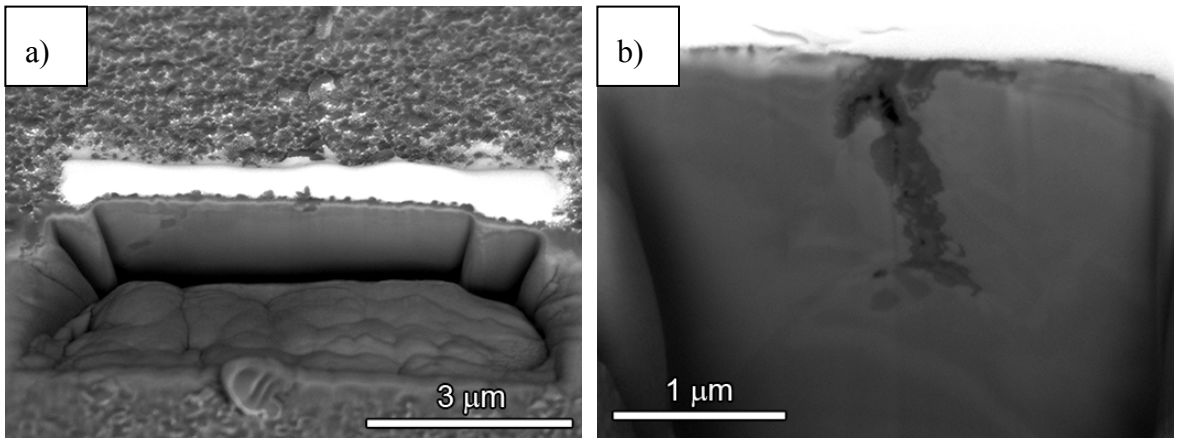

Figure 11. SEM (BSE) micrographs of FIB trenches cut across a) a grain boundary and b) a crack in an alloy 690 sample. The size of the trench is significantly wider than any observed cracking.

FIB can also be used to extract site-specific TEM samples using traditional lift-out techniques. The first step to achieve this is to sputter coat the tensile specimen surface with a thin layer (~50 nm) of Pt. A sample ~10-15 μm wide x 5 μm deep x ~200 nm thick is removed from the surface and thinned to electron transparency. Prior to performing TEM, low-kV SEM backscatter electron (BSE) imaging provides high-resolution imaging from the top ~10-200 nm depending upon accelerating voltage. Rapid morphological investigation of the penetrative oxidation layer is achieved, and the shallow interaction volume assists in discriminating projection issues in subsequent TEM and APT investigations. Scanning TEM (STEM) in conjunction with energy dispersive spectroscopy (EDS) elemental mapping can be performed on site-specific grain boundary FIB lift-outs. APT analysis can also be performed on site-specific grain boundary and surface locations in order to help elucidate the chemistry and microstructure of oxides along with compositional changes in the metal ahead of the oxidation front.

As the trenches imparted by the FIB milling procedures (for both examination and TEM sample preparation) were considerably larger than the cracks themselves, one potential concern was that they would act as stress concentrators, thus introducing crack initiation artifacts within subsequently exposures. Figure 12 illustrates trenches that had been milled in initiation specimens and subsequently re-loaded as testing continued. It was determined that this additional exposure did not promote additional cracking emanating from the trench. In many instances, surface spinels were observed to form in the trenches.

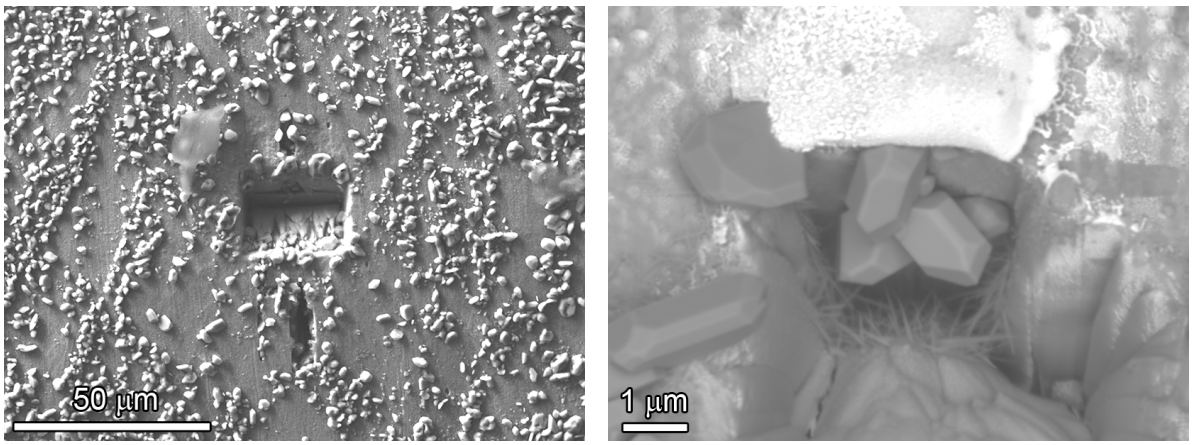

Figure 12. SEM (SE and BSE) images of an alloy 690 initiation sample that had been FIB milled and then subsequently exposed. No apparent enhanced cracking emanated from these trenches (which could be on the order of tens of micrometers). In certain cases, surface spinels nucleated in the trench.

After an SCC initiation test was completed on a specimen, microstructural damage, surface roughness and crack morphology were documented not only by the surface examination methods just described, but also by cross-section examinations. Areas of interest were first identified in the SEM, and then the specimen was sectioned to capture these features in cross section. Cross-section samples were polished to a colloidal silica finish to allow detailed examination of crack morphology by optical and SEM methods. Figure 13 illustrates low and high magnification cross-section micrographs of surfaces ground with a rotary tool and the edge of a silicon carbide blade attachment. The level of roughness and metal fold over is apparent at the surface (ranging from 5-10 µm), and a recrystallized zone ~5 µm near the surface is also observed.

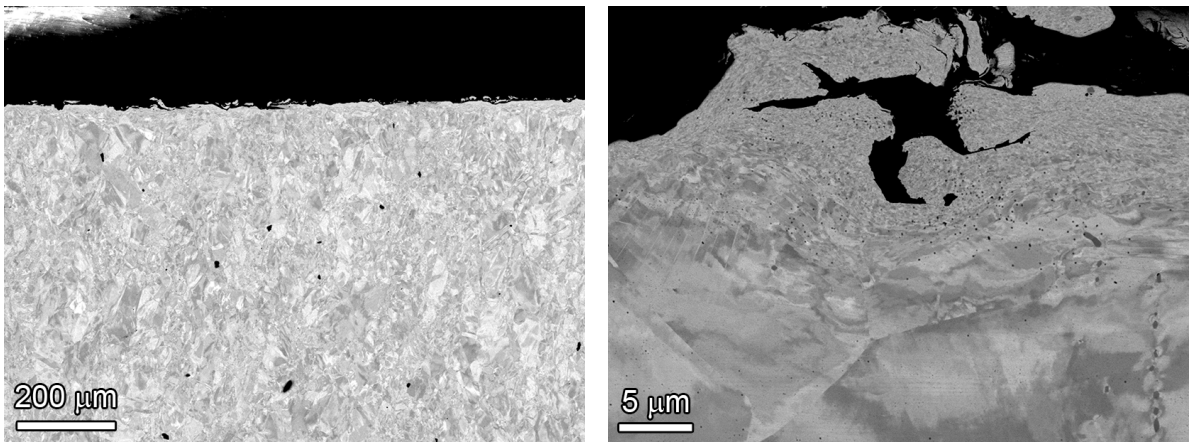

Figure 13. SEM (BSE) micrographs of the cross-section of an alloy 600 miniature tensile specimen ground using a rotary tool (left) and the edge of a SiC blade attachment (right).

SCC Initiation Tests on Alloy 600 Materials

Early efforts associated with SCC initiation experimentation focused on the design of the test systems, tensile specimens and the specimen load trains. Three test systems were constructed along with two different load trains. A detailed description of these activities was provided in earlier milestone reports in 2013 [1,2] along with the first proof of concept SCC initiation tests. Constant load, SCC initiation tests on as-received and cold-worked alloy 600 materials are summarized in this section (Table 1). These tests represent the first step to building a database for alloy 600 initiation response, evaluating the influence of surface condition, degree of cold work and applied stress on SCC initiation times for three different mill annealed (MA) alloy 600 heats. The in-situ DCPD measurements are illustrated for each test followed by SEM characterizations to document crack nucleation sites and morphologies.

Table 1. Alloy 600 Constant Load SCC Initiation Tests

Specimen	Material	Material Condition	Surface Condition	Applied Stress, MPa
IN002	CRDM 93510	MA + 18%TS	1 µm Polish	740
IN003	CRDM 93510	MA + 18%TS	60 grit Ground	740
IN013	Plate NX6106XK-11	MA	1 µm Polish	310
IN014	Plate NX6106XK-11	MA	60 grit Ground	310
IN015	Plate NX6106XK-11	MA	60 grit Ground	310
IN016	Plate NX6106XK-11	MA + 19%CR	1 µm Polish	610
IN017	Plate NX6106XK-11	MA + 19%CR	60 grit Ground	610
IN018	Plate NX6106XK-11	MA + 19%CR	60 grit Ground	610
IN022	Service CRDM M3935	MA + 20%TS	1 µm Polish	420
IN023	CRDM 93510	MA + 7%TS	1 µm Polish	425
IN045	Plate NX6106XK-11	MA	1 µm Polish	285
IN046	Plate NX6106XK-11	MA	1 µm Polish	290
IN047	Plate NX6106XK-11	MA	60 grit Ground	290
IN048	Service CRDM M3935	MA	1 µm Polish	255
IN049	Service CRDM M3935	MA	1 µm Polish	255
IN050	Service CRDM M3935	MA	60 grit Ground	255
IN052	Plate NX6106XK-11	MA + 8%TS	1 µm Polish	435

Alloy 600 Materials Information and Specimens

Three alloy 600 materials have been examined as part of this project and the reported bulk compositions for these materials are listed in Table 2. All materials were evaluated were in the mill-annealed condition. A section of CRDM nozzle #1 from the original Davis Besse RPV head (in storage at PNNL) was decontaminated and sectioned by Babcock & Wilcox Technical Services. . This alloy 600 heat (M3935) exhibited high SCC susceptibility in PWR primary water service and during crack-growth tests [13,14] at PNNL and Argonne National Laboratory. It is important to note that a very high B concentration was measured by glow discharge mass spectroscopy (GDMS) for the Davis Besse heat. This heat was in a mill-annealed (MA) condition and was reported to have a final MA temperature of 871 to 927°C and a yield strength of 334 MPa. Blanks for CT and tensile specimens were obtained as shown in Figure 14.

The additional CRDM heat (93510) was obtained from GE, and its bulk composition is listed below from the mill specs. The yield and tensile strengths for this material were reported as 269 and 678 MPa with an elongation to failure of 48%. Ladle analysis did indicate some level of B in this heat, but GDMS measurements were not conducted to corroborate this measurement. The final alloy 600 heat (NX6106XK-11) was purchased as 2" thick plate. Mill specs indicated that the yield and tensile strengths were 259 and 667 MPa with an elongation to failure of 43%. GDMS measurements were not conducted on this heat to quantify trace levels of B.

Table 2. Alloy 600 composition (wt% unless noted)

Product	Heat	Ni	Cr	Fe	Mn	C	Si	Cu	P	S	B, appm
Service CRDM	M3935	77.9	15.6	6.3	0.27	0.028	0.37	0.01	0.004	0.002	69
CRDM Tube	93510	74.4	15.4	8.9	0.23	0.047	0.30	0.01	0.005	0.002	NM
Plate	NX6106XK-11	74.0	16.4	8.5	0.23	0.060	0.22	0.01	0.004	0.001	NM

*NM = not measured.

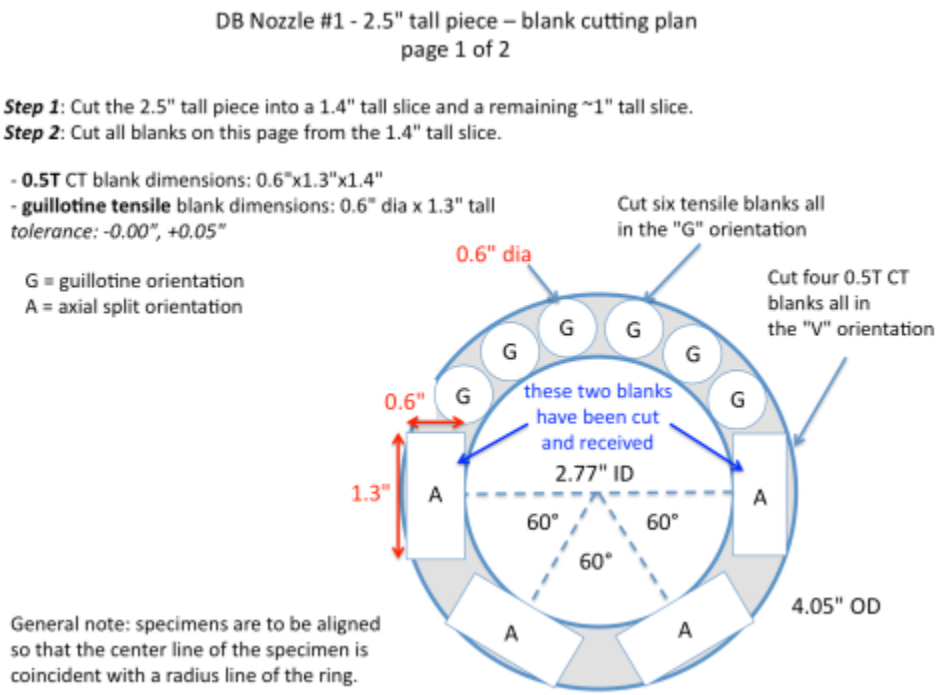

Figure 14. Sectioning plan for 0.5T CT specimens and tensile specimen blanks for a 1.4 inch tall slice of nozzle #1 of the original Davis Besse RPV head.

Microstructural and Microchemical Characterizations on Alloy 600 Heats

Detailed examinations have been performed on the Davis Besse service material as part of an NRC project at PNNL where SCC growth rate tests were performed. General microstructures for this mill-annealed material are illustrated in Figures 15 and 16. A very large grain size was found, ranging from ~150-400 µm in diameter. Carbides in M3935 are nearly all IG and spaced ~500 nm apart. The extremely large grain size indicates that it was mill annealed at a temperature sufficient to dissolve most, if not all, of the carbides and promote significant grain growth. Grain boundaries exhibited a semi-continuous distribution of carbides consistent with a slower cooling rate from the annealing temperature enabling precipitation to occur. At higher magnification using a 3 kV accelerating voltage (Figure 16), BSE imaging illustrated a population of elongated white particles was observed on many grain boundaries. These particles were determined to be Ni borides by atom probe tomography (APT) and are probably $Ni_{23}B_6$ forming adjacent to the Cr_7C_3 carbides. Lastly, sporadic particles with dark contrast were determined to be TiN (Figure 16).

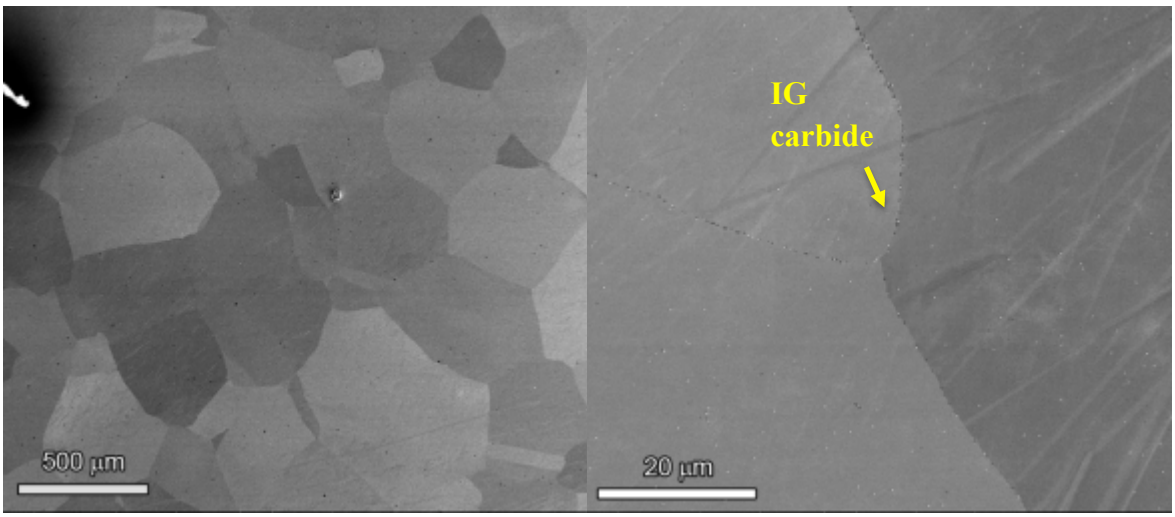

Figure 15. SEM (BSE) images illustrating the general microstructure and large grain size in the mill-annealed alloy 600 CRDM heat M3935 material.

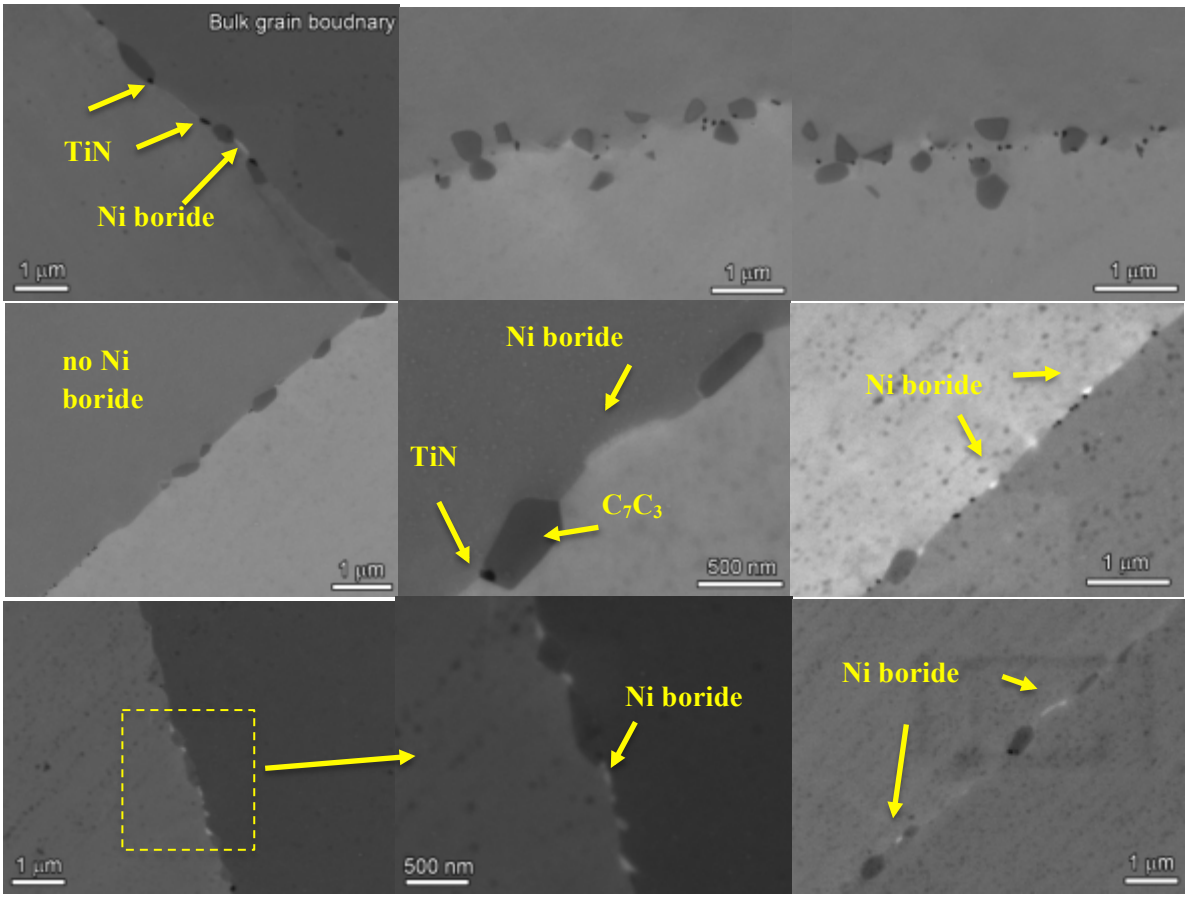

Figure 16. SEM (BSE) images illustrating the general microstructures in the mill-annealed alloy 600 CRDM heat M3935 material at higher magnification illustrating the distribution of Cr_7C_3, TiN and Ni borides on the grain boundaries.

Additional characterizations were performed on the Davis Besse heat using electron backscatter diffraction (EBSD) and hardness measurements. The overall general microstructure for heat M3935 is represented by EBSD in Figure 17 revealing the extremely large grain size and a very low density of twins. Consistent with the lack of deformation twins, the misorientation density map of this area reveals low strains. A Vickers hardness map of a representative region from the side-surface cross-section sample is presented in Figure 18. With the exception of a single indentation that produced a hardness of ~180 kg/mm^2, this region exhibited a consistent hardness of 160.2 kg/mm^2 with a standard deviation of 6.5 kg/mm^2.

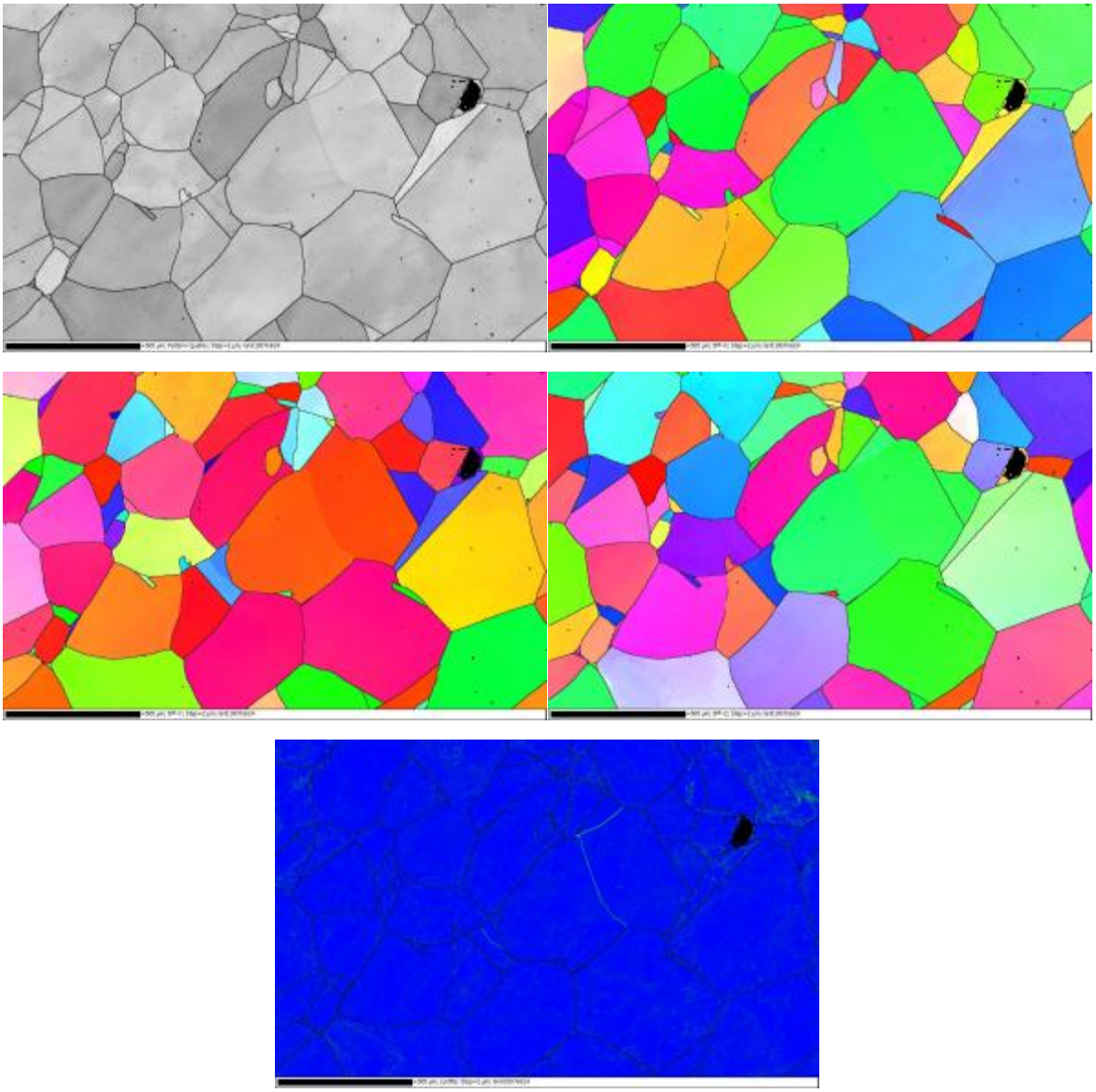

Figure 17. EBSD pattern quality map is shown in upper left image, inverse pole figure maps in upper right (X orientation), middle left (Y orientation) and middle right (Z orientation) images along with misorientation density map in bottom center for Davis Besse heat M3935.

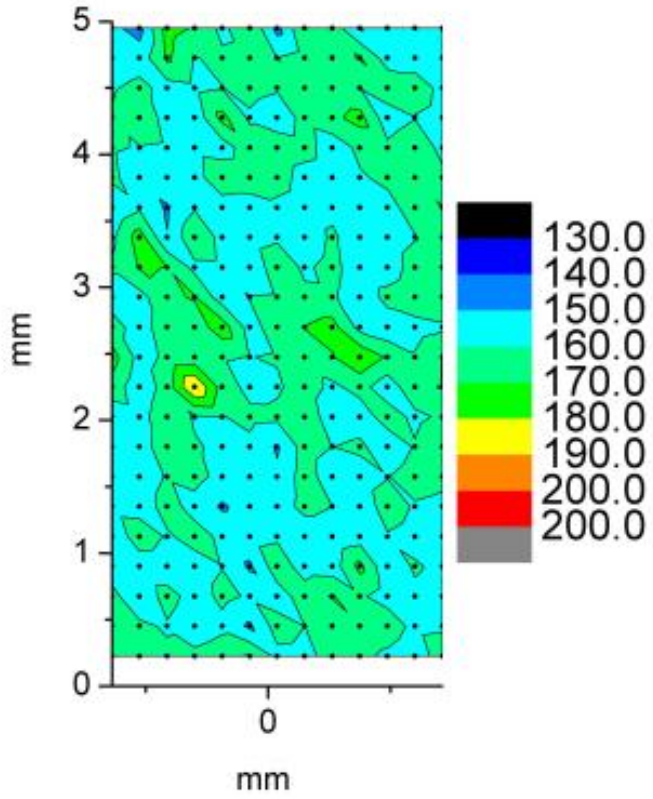

Figure 18. Vickers hardness map for Davis Besse heat M3935. The average measured hardness was 160.2 kg/mm^2 with a standard deviation of 6.5 kg/mm^2.

Limited TEM examinations were performed on high-angle grain boundaries from the Davis Besse heat to investigate grain boundary precipitate distributions and local compositions. A SEM (BSE) image of a FIB-machined TEM sample from heat M3935 is shown in Figure 19. A high density of Cr carbides and sporadic TiN are observed along the grain boundary. Unlike the majority of BSE images of this material in Figure 16, there are no apparent bright IG phases (Ni borides) in this section of grain boundary. The Cr rich carbides were determined to be primarily Cr_7C_3 by diffraction and darkfield imaging. Significant Cr depletion was identified to levels below ~10 wt% in EDS line scans of grain boundary regions between carbides. More detailed analyses of grain boundary composition were made using APT and is described in the following section. Both the TEM and APT characterizations were conducted under funding from a Department of Energy, Office of Basic Energy Sciences project at PNNL.

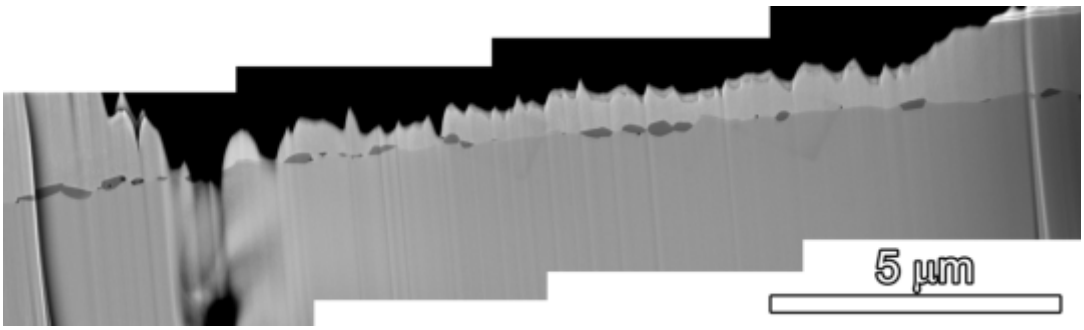

Figure 19. SEM (BSE) montage of FIB machined TEM plate sample containing a grain boundary from alloy 600 M3935. In this region, there does not appear to be any Ni boride particles.

Much attention has been given to the role of microstructure on the SCC susceptibility of alloy 600 materials in PWR primary water. These studies, typically leveraging optical, SEM and TEM microanalyses, have identified some microstructural features as being either advantageous or detrimental to SCC resistance. The most frequent observation seems to be the beneficial effect of a high density of IG Cr carbides. Conversely, a low density of IG Cr carbides and a high density of TG carbides have been suggested to be detrimental to SCC resistance. Despite these generalizations, some heats of alloy 600 exhibit unexpectedly high SCC susceptibility despite typical or supposedly SCC-resistant microstructures. One possible explanation for this variability in SCC response may be unexpected and previously unobserved segregation of difficult-to-detect species on the grain boundary.

APT is one technique that is capable of analyzing grain boundary segregation of nearly all species independent of atomic number. This is particularly advantageous to describing the segregation of light elements (e.g., B, P and C) in small concentrations that are difficult to describe by ATEM. Early applications of APT were plagued by small datasets and thus poor counting statistics that were inherent to the technique at that time. Since these early studies, relatively little attention has been given to alloy 600 grain boundary segregation using modern APT instrumentation that can provide dramatically improved counting statistics and thus quantitative accuracy. To put the difference in perspective, the matrix compositions reported in one of these previous studies were based on datasets containing between 3,000 and 18,000 detected ions. With modern instrumentation, a “small” dataset consists of >2,000,000 ions and more typically contains on the order of 10,000,000 ions. The improved counting statistics negate the effect of counting error on the resulting quantitative measurements. Such an improvement in data size results in the error of compositional measurements being dominated not by counting statistics but instead being a measure of variability from specimen to specimen or grain boundary to grain boundary. Therefore, it is very beneficial that grain boundary composition be revisited as a potential contributor to SCC susceptibility utilizing modern APT instrumentation.

APT analyses have now been performed on general, high-angle grain boundaries for seven alloy 600 materials including 3 CRDM nozzle, 3 steam generator tube and a steam generator divider plate heats. Results for the Davis Besse CRDM nozzle materials are shown here.

Two APT specimens from heat M3935 were collected intersecting IG precipitates. The first specimen was found to contain a Ti carbo-nitride covering the grain boundary across the entire width of the APT needle. The corresponding APT reconstruction is presented in Figure 20. The carbo-nitride precipitate is strongly enriched in Ti, C and N and strongly depleted of Ni, Fe, Al and Mn. Interfacial segregation is apparent for B and P. Note that peak overlap between $^{28}Si^{2+}$ and $^{14}N^{1+}$ prevents the analysis of any potential Si segregation in this specimen.

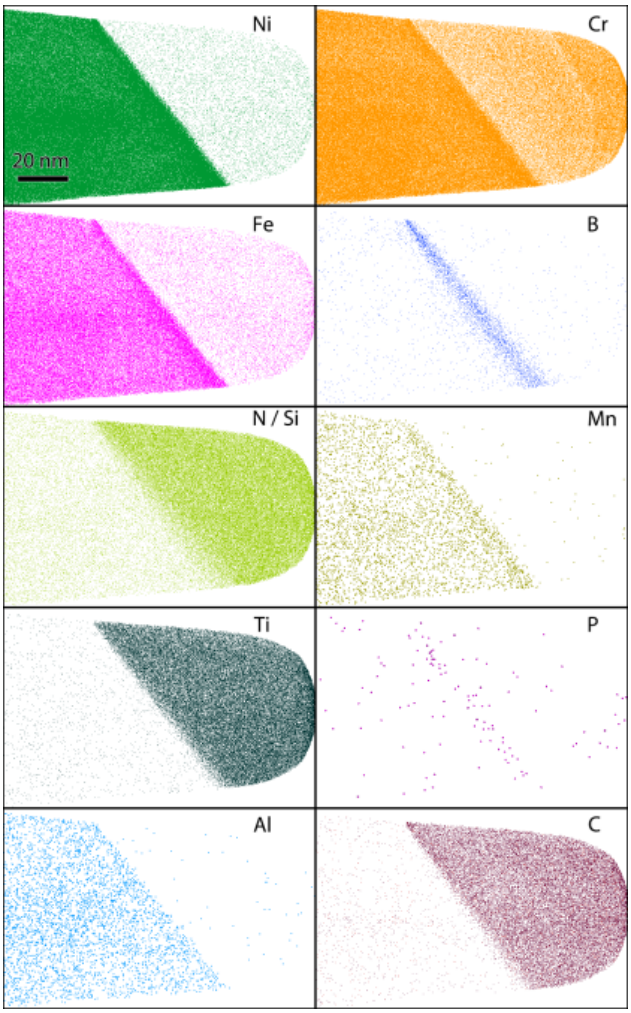

Figure 20. Atom map (10 nm image depth) of an IG Ti carbo-nitride in Davis Besse CRDM heat M3935. Strong interfacial segregation is apparent for B and weak segregation for P. Note that Si and N peaks are convoluted with one another and impossible to differentiate.

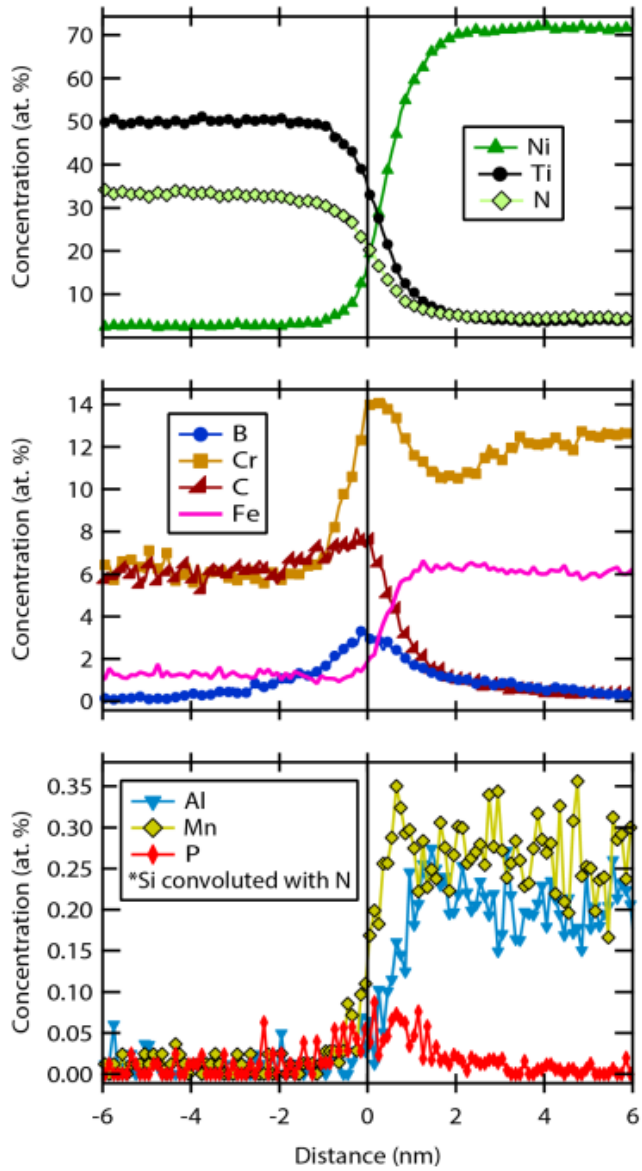

Figure 21. Proximity histogram across the Ti carbo-nitride/metal matrix interface in M3935. The precipitate contains a moderate concentration of Cr that is also strong segregated to the interface. B is strongly segregated (~3.3 at%) along with a small enrichment of P (~0.06 at%).

A proximity histogram was produced at the carbo-nitride/metal interface to quantify both the precipitate composition and the interfacial segregation (Figure 21). The precipitate consists of ~50 at% Ti, 33 at% N, 6 at% C and 6 at% Cr. Interfacial segregation is very significant. Pronounced enrichment is apparent for B (to ~2.5 at%) and P (to 0.08 at%). Chromium exhibits a more complicated behavior in which some enrichment is apparent at the metal/precipitate interface, while Cr depletion also exists just outside this enriched interface, down to ~11 at%. Interfacial segregation to ~8 at% is also indicated for C.

A second APT dataset on M3935 was collected on a needle containing an IG Cr carbide precipitate. Representative atom maps from this dataset are presented in Figure 22. A Cr carbide precipitate is apparent at the specimen apex and is surrounded by very strong B segregation and Cr depletion. A small region of metal/metal grain boundary is also apparent, extending past the bottom-right corner of the carbide particle to the edge of the APT needle reconstruction. Very strong, pockets of Cr and Fe depletion along the carbide periphery (arrowed) correspond to localized enrichment of B, which could suggest that the carbide/metal interface is decorated by nanoscopic Ni boride precipitates.

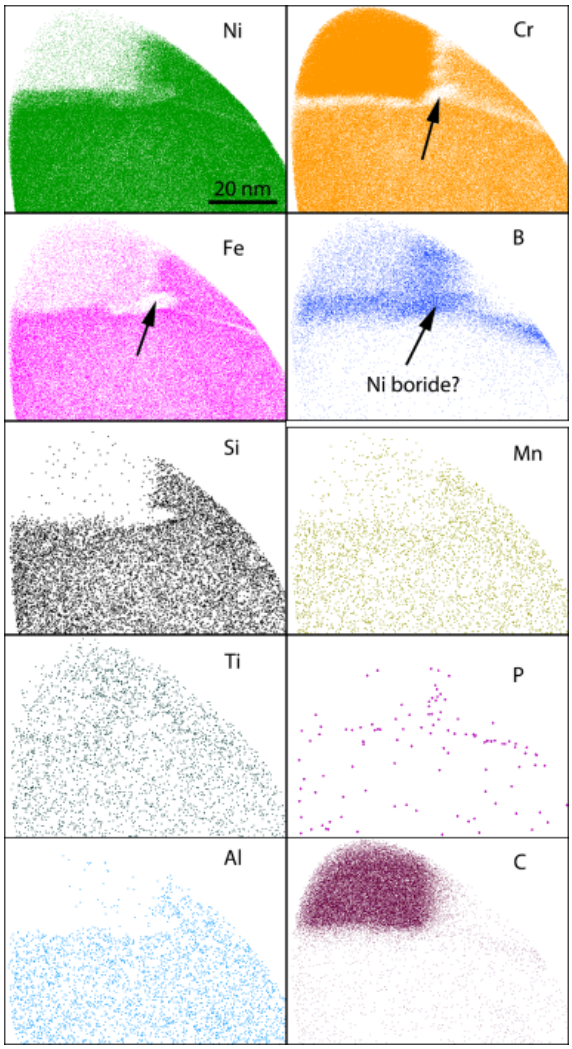

Figure 22. Atom maps from an IG Cr carbide and surrounding grain boundary in Davis Besse CRDM heat M3935. Very strong Cr depletion and B enrichment are apparent along the grain boundary and metal/carbide matrix. Particularly strong localized B enrichment and Cr depletion is suggestive of possible Ni boride precipitations (arrowed).

Concentration profiles were produced across the metal/metal grain boundary adjacent to the IG carbide and also from the carbide/metal interface in Figure 23. Each profile quantifies extraordinarily high levels of interfacial B segregation up to 5 at% B and 11 at% B at the metal/metal and carbide/metal interfaces, respectively. These represent the highest levels of B segregation among alloy 600 examined by PNNL. Similar to another CRDM heat (M7929), the grain boundary does not exhibit any detectable segregation of Si. Slight segregation is apparent for C, P, Mn and Ti at the grain boundary. IG Cr depletion, expected to be severe in such close proximity to an IG Cr carbide, was only moderate, with a minimum value of ~8 at% Cr. In general, the carbide/metal interface was very similar to the metal/metal grain boundary. Cr was depleted to ~7 at%, while slight segregation was seen for P and Ti with no Si enrichment.

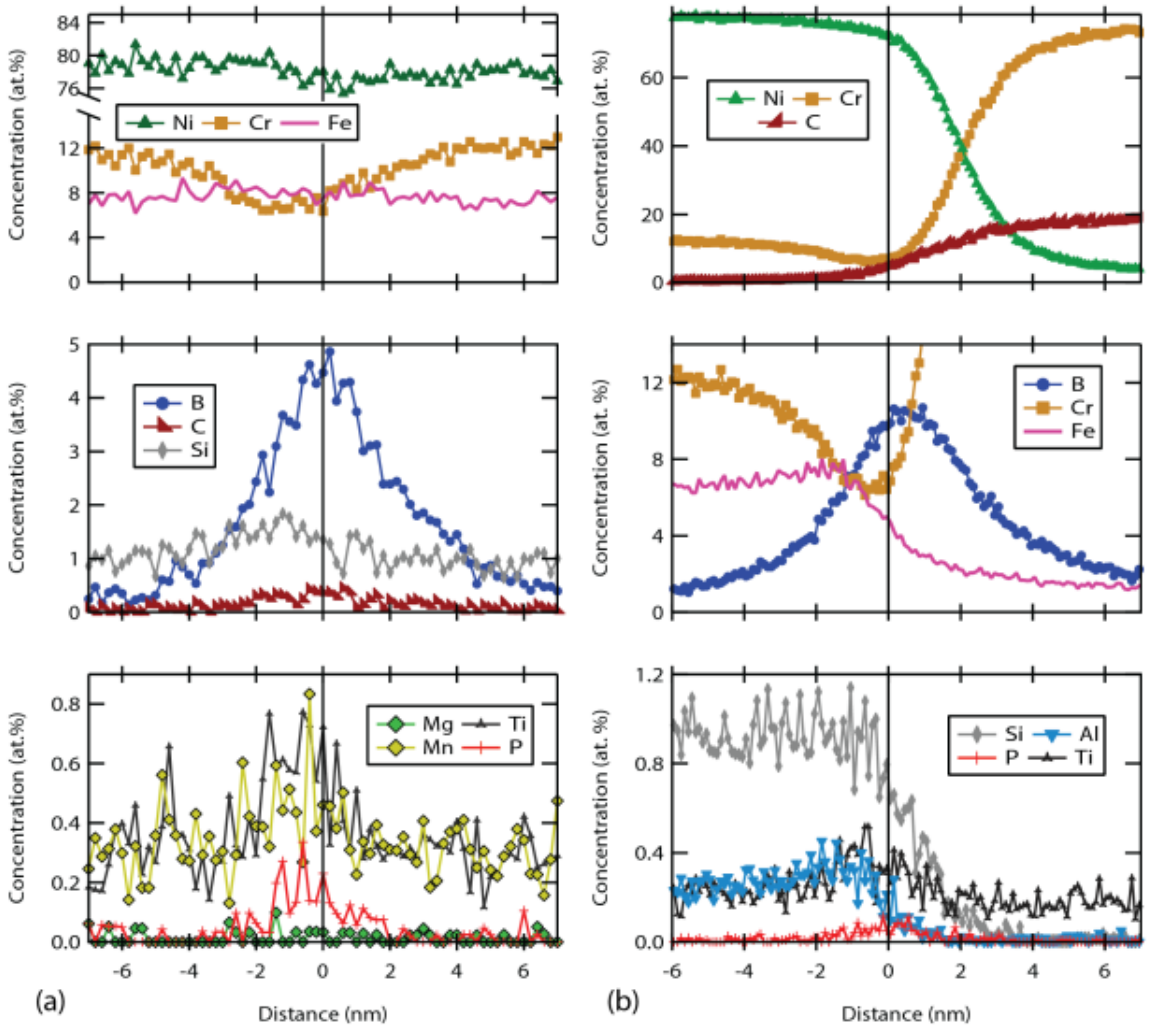

Figure 23. Concentration profiles across (a) the metal/metal grain boundary and (b) across the IG Cr carbide / metal interface in Davis Besse CRDM heat M3935. Both types of interfaces exhibit particularly strong B segregation (5 at% and 11 at%, respectively) and Cr depletion (<8 at% each). Relatively strong P segregation is apparent at each interface (~0.2 at%) and no significant Si segregation is observed.

As mentioned when discussing the atom maps of this dataset, the extraordinarily high levels of B and localized Cr depletion at the carbide/metal interface suggest the possibility of Ni boride precipitation at the carbide/metal interface. To better visualize this possibility, a full three-dimensional reconstruction (rather than a thin two-dimensional slice of data) is presented in Figure 24. The three-dimensional morphology of the carbide is defined using a 5 at% C isoconcentration surface (maroon). Localized regions of particularly high B concentrations are defined along the carbide/metal interface with 13 at% B isoconcentration surfaces (blue).

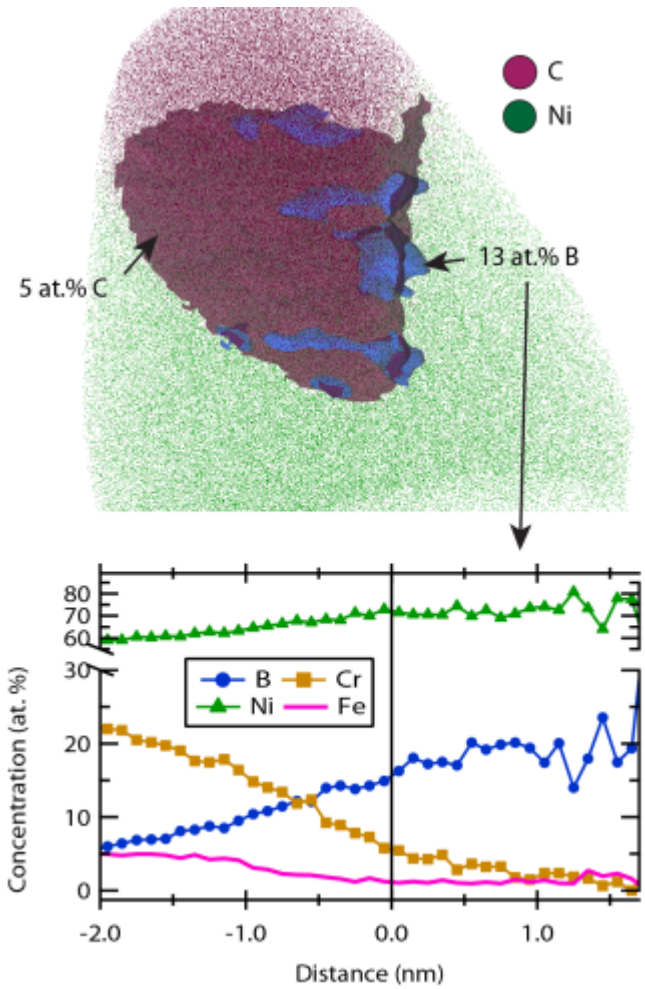

Figure 24. APT reconstruction of the IG carbide in the Davis Besse CRDM heat M3935. Iso-concentration surfaces at 5 at% C (maroon) and 13 at% B (blue) outline the Cr carbide and possible Ni boride, respectively. A proximity histogram (bottom) from around the 13 at% B iso-concentration surface confirms the coincident enrichment of Ni and B (up to 20 at%) that is suggestive of an interfacial Ni boride phase.

Numerous small islands of B enrichment decorate the interface especially near the lower-right corner where the carbide meets the metal/metal grain boundary. A proximity histogram is plotted below the three-dimensional reconstruction. The center of the B enrichment peaks at ~20 at% B and coincides with very strong Cr depletion to less than 2 at% Cr. Considering that APT typically underestimates B concentrations, it is plausible that these B-rich particles could be $Ni_{23}B_6$. Careful examination of similar IG carbides by TEM was unable to reveal similar nanoscopic boride precipitates. It is unclear right now whether this is because of an absence of a stable Ni-boride phase at other carbide/metal interfaces or whether the boride particles were too small or crystallographically too similar to the carbide to be detected by TEM.

Characterization of the two other alloy 600 heats (CRDM tube heat 93510 and plate material heat NX6106XK-11) was limited to SEM examinations to document grain size and precipitate distributions. Both of these heats were also in the MA condition and showed a much smaller grain size (heat 93510 having a grain size of ~20-25 µm and NX6106XK-11 being ~65 µm) as illustrated in Figures 25 and 26, respectively. The CRDM tube heat 93510 showed transgranular (TG) carbides on ghost grain boundaries, while the plate heat NX6106XK-11 also exhibited TG carbides on ghost grain boundaries as well as grain boundaries with random IG carbides and a low density of grain boundaries with intergranular carbides that were spaced ~0.5-1.5 µm apart on average. These aspects are summarized in Table 3.

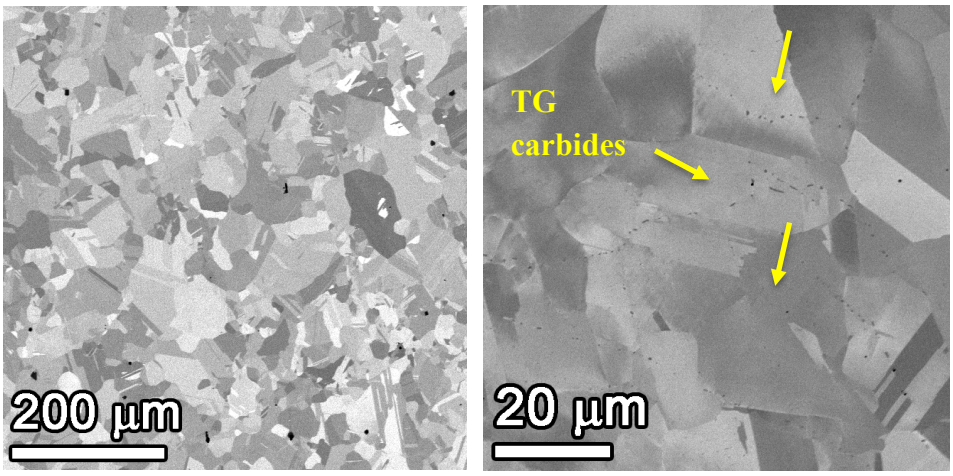

Figure 25. SEM (BSE) micrographs illustrating the microstructure of CRDM tube heat 93510 and the transgranular nature of the carbides.

Table 3. Microstructural characterization of alloy 600 materials.

Component	Heat or ID #	Grain Size (µm)	Strain Contrast	Primary Carbide Location	IG Carbide Density
CRDM Nozzle	M3935	~300	Low	IG	500 nm spacing
CRDM Tube	93510	~20-25	Low	TG	N/A
Plate	NX6106XK-11	~65	Low	TG on ghost grain boundaries + low density of IG on non-migrated boundaries	0.5-1.5 µm spacing on IG boundaries

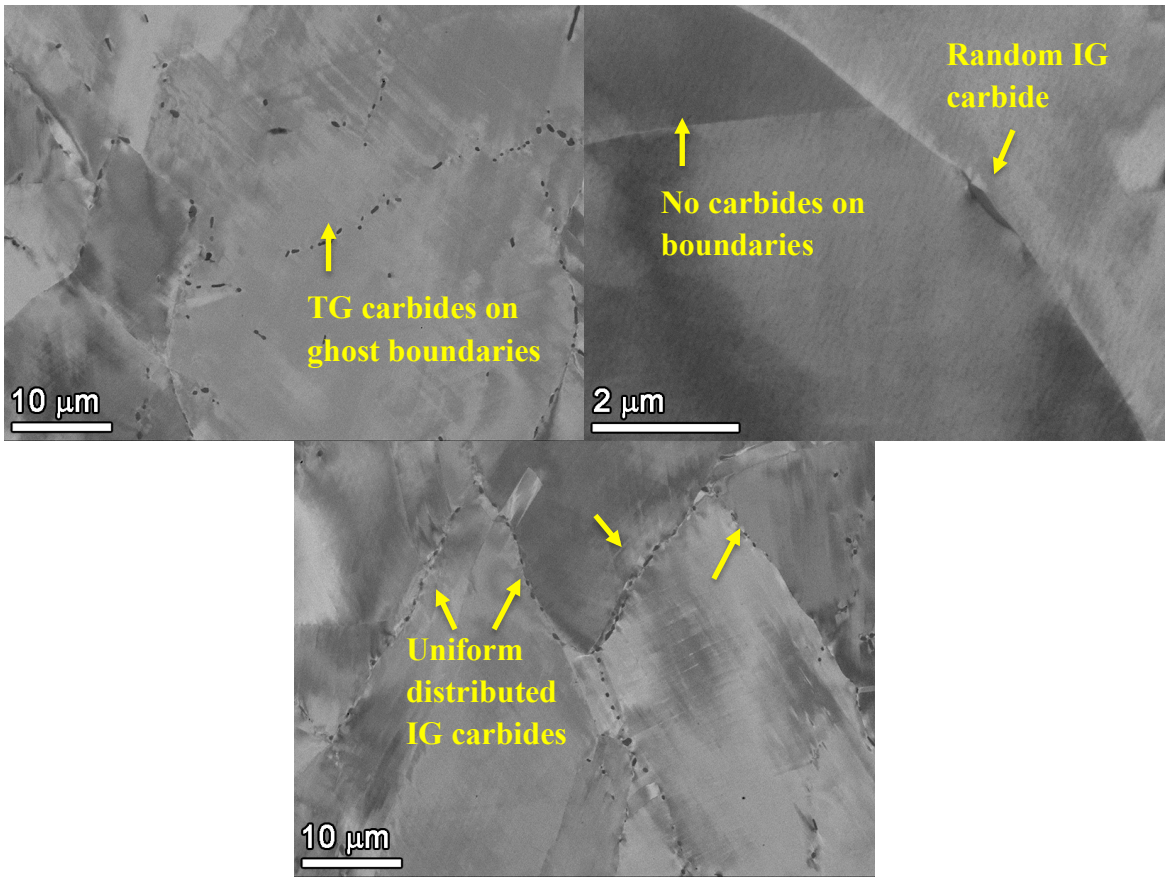

Figure 26. SEM (BSE) micrographs illustrating the microstructure of plate material NX6106XK-11and the intergranular nature of the carbides.

SCC Initiation Test Results on Cold-Worked Alloy 600

SCC Crack Initiation of 18% Tensile Strained CRDM Heat (Specimens IN002 & IN003)

This first test was performed on a pair of specimens cut from the CRDM alloy 600 heat 93510 received from General Electric. The goals of this test were to assess the ability to perform series loading of specimens and to make a first attempt at looking at the effect of surface condition on crack initiation. These specimens were prestrained to 18% plastic strain at room temperature. After prestraining, IN002 was ground to a 1200-grit surface finish in the gauge region, while IN003 was polished to a 1-µm finish. The gauge diameter was documented using an optical comparator, and then the specimens were inserted into the load train. Because the gauge region was tensile strained but not the reference region, these two regions underwent different resistivity evolution as explained in the Experimental Details section, and the reference DCPD values could not be used to effectively normalize the gauge DCPD values. Thus the indicated "strains" include not only contributions from a real change in gauge length due to creep but also due to material resistivity evolution.

Testing began at 630 MPa (~85% of the 360°C yield stress), and the load was increased (at a constant displacement rate) at 650 hours until yielding was observed to occur. No two specimens will yield at exactly the same load, and in this case, the specimen with the 1 µm finish yielded first resulting in a small amount of plastic strain (~0.05%) before switching back to constant load at 740 MPa. The increase in stress caused no obvious change in the trajectory of the DCPD data. As shown in Figure 27, evidence for crack nucleation was first observed in the IN003 specimen with the 1 µm surface condition. A sharp change in the slope of the non-referenced strain occurred at 1775 h and was detected ~10 h later. The applied load on specimens was then dropped to a low value, the system was shut down and the IN003 specimen was removed for characterization. The test was restarted on the IN002 specimen (1200-grit surface finish) at the same conditions. No indication of additional plastic strain was seen in the DCPD response during slow reloading 740 MPa. The prior trajectory of the non-referenced strain with time reproduced until 2025 h when a sharp increase was detected (Figure 27). This time the event was discovered within 20 h, and loading was decreased at ~2045 h followed by test system shutdown for specimen removal and examination.

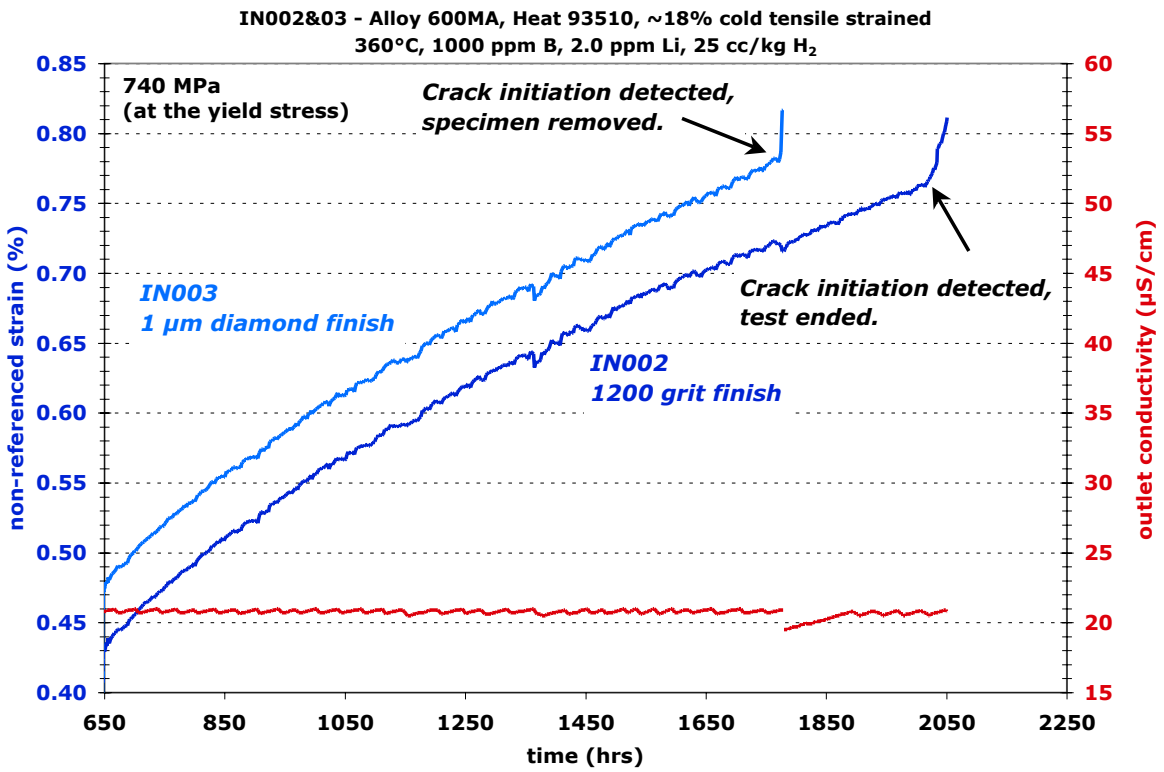

Figure 27. SCC crack initiation tests on 18% tensile prestrained alloy 600 CRDM Heat 93510.

Specimen gauge sections were first examined optically and by SEM to document cracks. The specimens were then cut into four 1/4 pie-shaped pieces and each cross-section was polished to reveal near-surface microstructural features. Low-to-high resolution SEM was used to document surface oxide films, local and general damage, grain boundary morphologies, corrosion structures and cracks.

In-situ DCPD detected cracking first (1775 h) on IN003 with the 1 µm surface finish. Figures 28 and 29 are low magnification SEM-BSE montages showing the gauge region at two rotations separated by 120°. In both figures, the montages are repeated side by side with the observable cracks highlighted in red for Figures 28(b) and 29(b). Although there appeared to be a limited number of cracks, more detailed examination at higher magnification revealed many smaller cracks. The tensile specimens used for this test were an early design that was found to be prone to cracking in the fillet due overly aggressive fillet radius. Hence, the majority of cracking was observed in this region. The specimen design was later reworked to the design shown in the Experimental Details section to eliminate the stress riser.

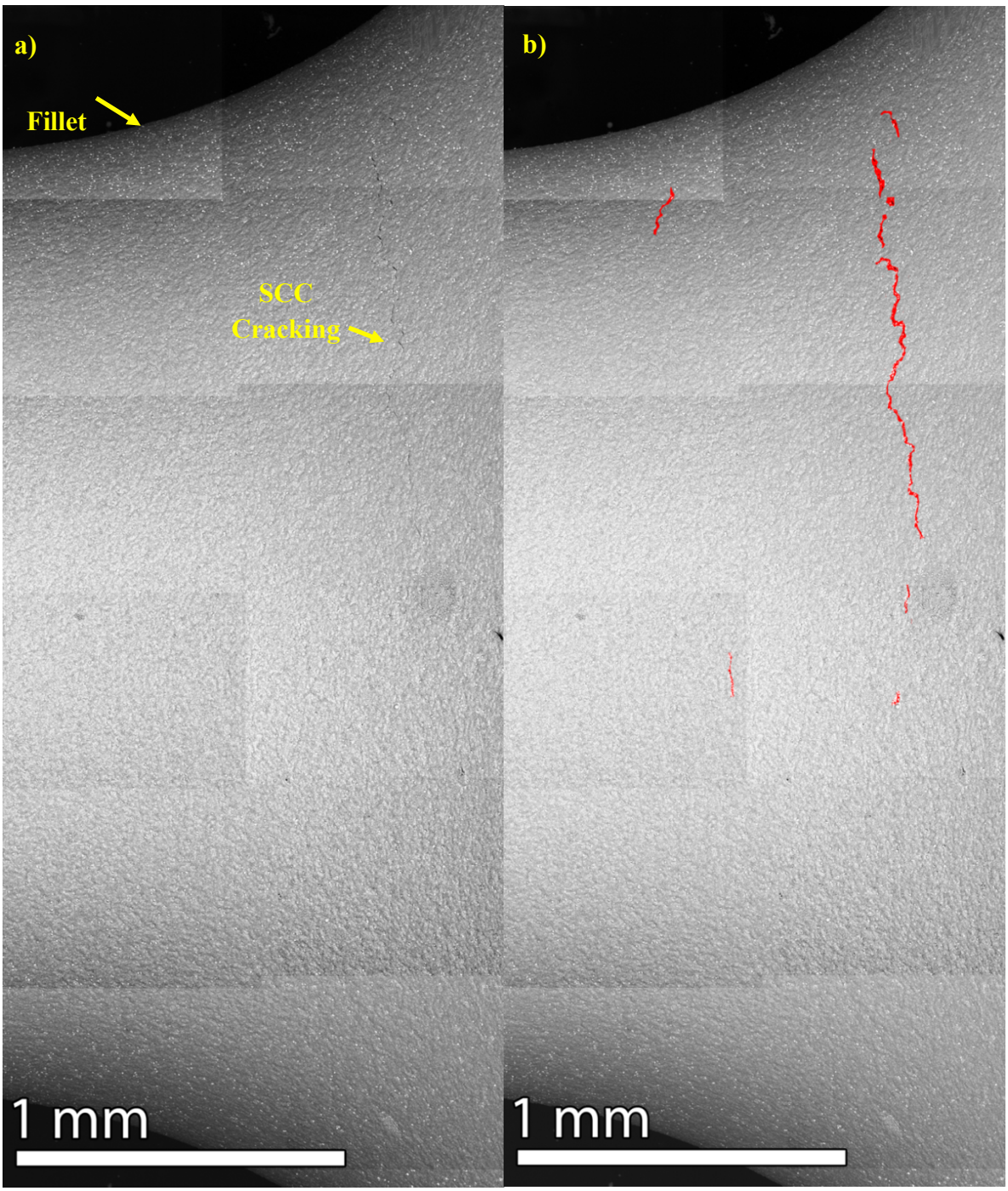

Figure 28. SEM (BSE) images of the alloy 600 tensile initiation specimen IN003 surface that exhibited cracking near the fillet. Image (b) is identical image to (a), but cracks have been colored red as guide to the eye. The longest crack observed in this region was nearly 1 mm in length.

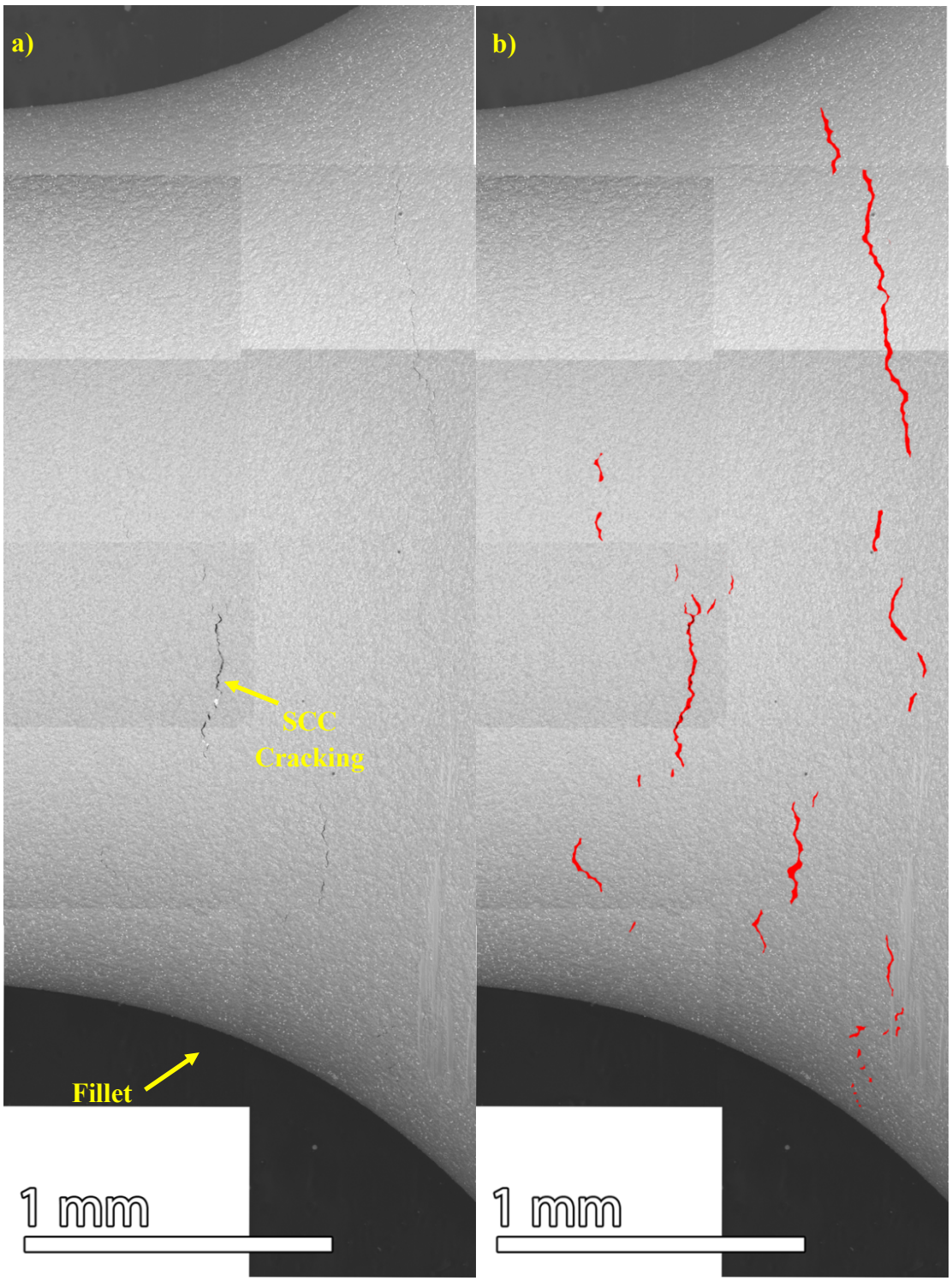

Figure 29. SEM (BSE) image of the alloy 600 tensile initiation specimen IN003 (rotated 120° from Figure 28) that exhibits cracking near the fillet. Image (b) is the identical image but cracks have been colored red as guide to the eye. SCC cracks were observed with a circumferential length as long as ~1 mm.

Representative SCC surface crack microstructures are shown in Figure 30. As this specimen was in test for ~1775 h in 360°C simulated PWR primary water, an appreciable amount of spinel crystals and fibrous oxide formed on the surface of the specimen (Figure 30d). While the large grain spinel crystals do not inhibit the view of the grain microstructure, the highly dense, fibrous oxide (which is on the order of 10s of nanometers) obstructs any view the underlying grain boundary microstructure and as well any cracks that have an opening of less than ~1 μm. Formation of the Ni/Fe-rich spinel particles on the surface are commonly seen after exposure of alloy 600 to high-temperature water, while the fibrous oxide is often observed after exposure in simulated PWR primary water with dissolved hydrogen concentration at or above the Ni/NiO stability line.

SEM examinations of the specimen cross-sections provide more insights into the crack distributions and morphologies. The low magnification image in Figure 31 documents the location of cracks in the fillet region, and the BSE contrast reveals the alloy 600 grain microstructure. Differences can be seen moving from the highly deformed gauge section into the fillet region that experienced lower deformation during prestraining. A distribution of crack depths is present in the fillet regions as illustrated in Figure 32. All cracks are IG with openings tending to scale with crack depth. The deepest cracks (~200 μm) have openings approaching 5 μm. Characterization of the gauge section showed IG attack of nearly all grain boundaries intersecting the surface. General surface corrosion and oxide formation was typically ~200 nm thick (Figure 33a), and the grain boundaries were routinely attacked to depths of ~1 μm with the widths <20 nm. The IG attack structure was continuous up to their tips in most of the gauge section. Small cracks were seen as areas closer to the fillet were analyzed. An interesting aspect of the IG attack microstructure was the observation of grain boundary migration ahead of the oxidation front (Figure 33b). Penetrative IG oxidation in this example ended immediately before a triple point, but the contrast at the triple point indicates that grain boundary migration and composition change has occurred on the order of 20-50 nm. Grain boundary migration during IG attack has been observed in other alloy 600 samples as well as Ni-Cr binary alloys. The contrast mechanism is typically the result of Cr depletion and Ni enrichment, where the Cr depletes in the alloy 600 case from 16 to ~5 wt% which provides enough Z (atomic weight) contrast in low-angle backscatter imaging to see a change in grain boundary position. Another key indicator is that the contrast is highest at the triple point and then tapers back to the original grain boundary position about ~1 μm past the triple point. This tapering can be seen on both grain boundaries beyond the triple point.

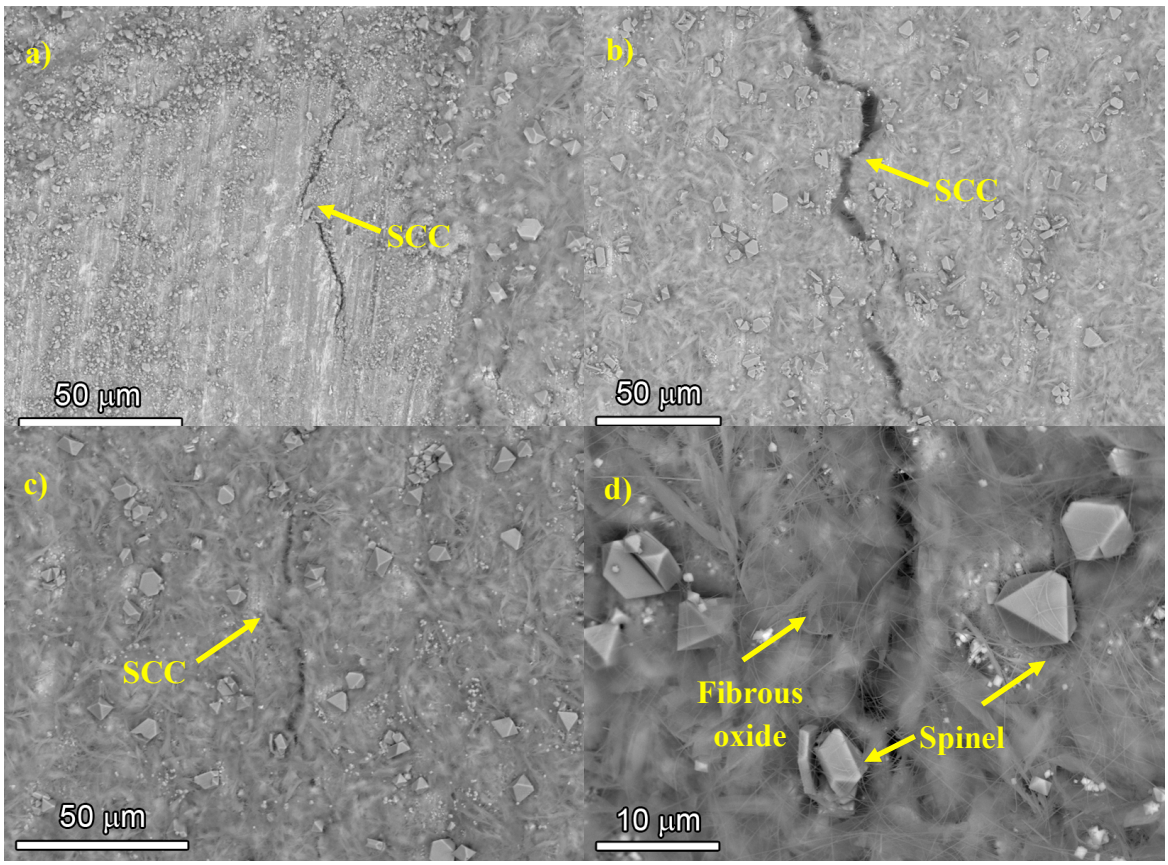

Figure 30. Low magnification SEM (BSE) images of the surface of the IN003 alloy 600 tensile initiation specimen illustrating various SCC cracks and surface oxides.

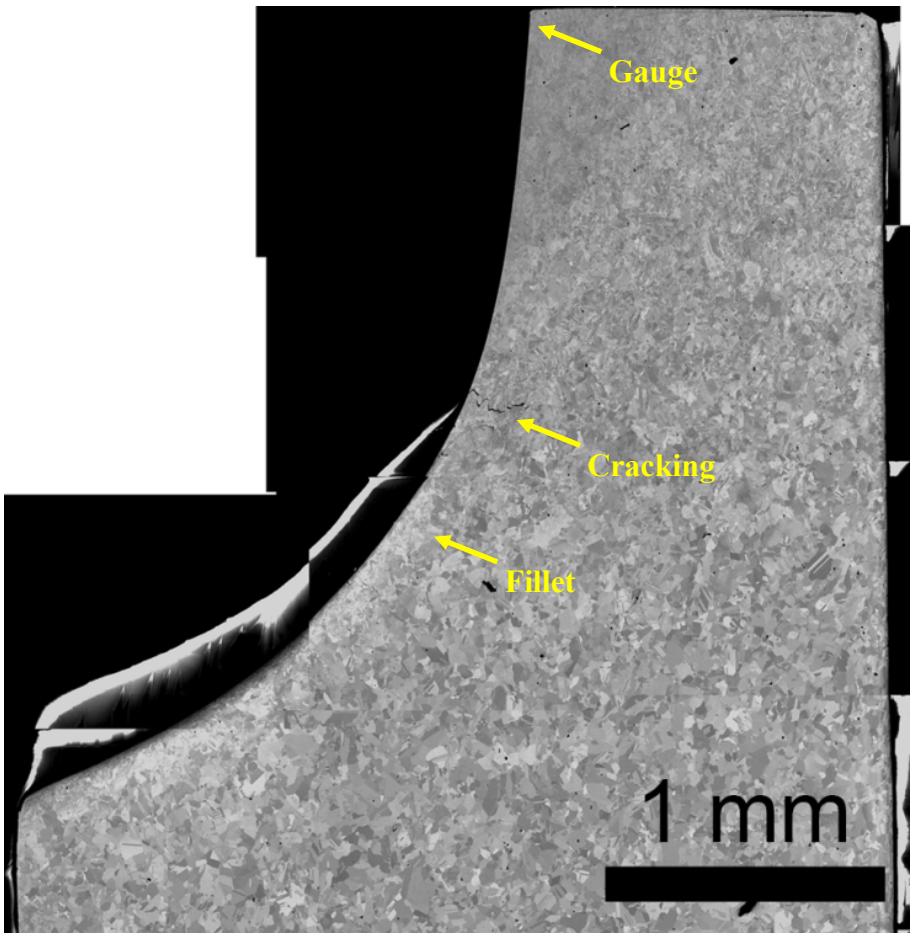

Figure 31. SEM (BSE) images of a cross-section from the alloy 600 tensile initiation specimen IN003 that exhibited cracking near the fillet. Note that strain contrast in the gauge section obscures the grain morphology.

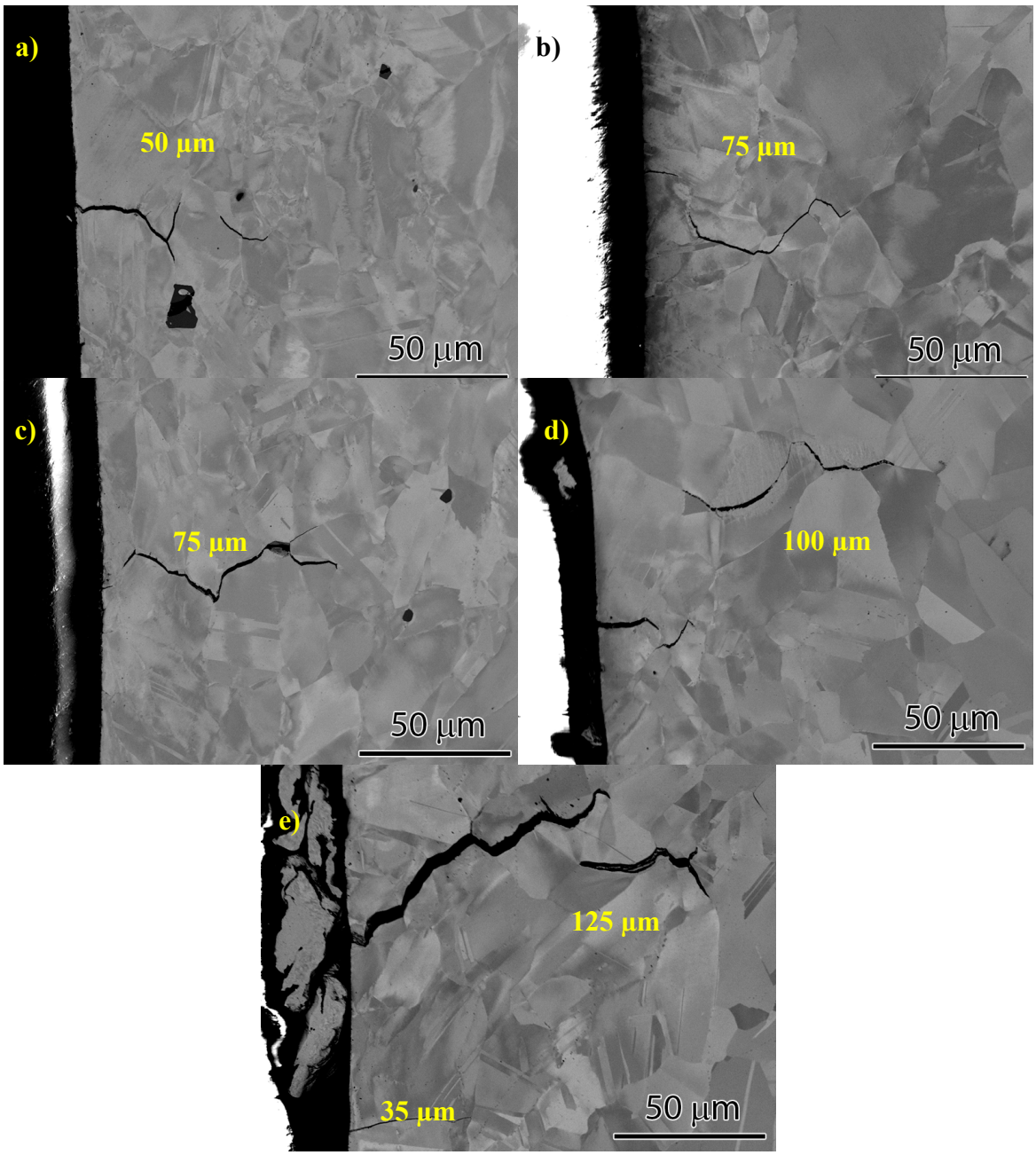

Figure 32. SEM-BSE images of a cross-section for the alloy 600 tensile initiation specimen IN003 showing deep SCC cracks initiating from the surface. Apparent crack depths are listed for each figure.

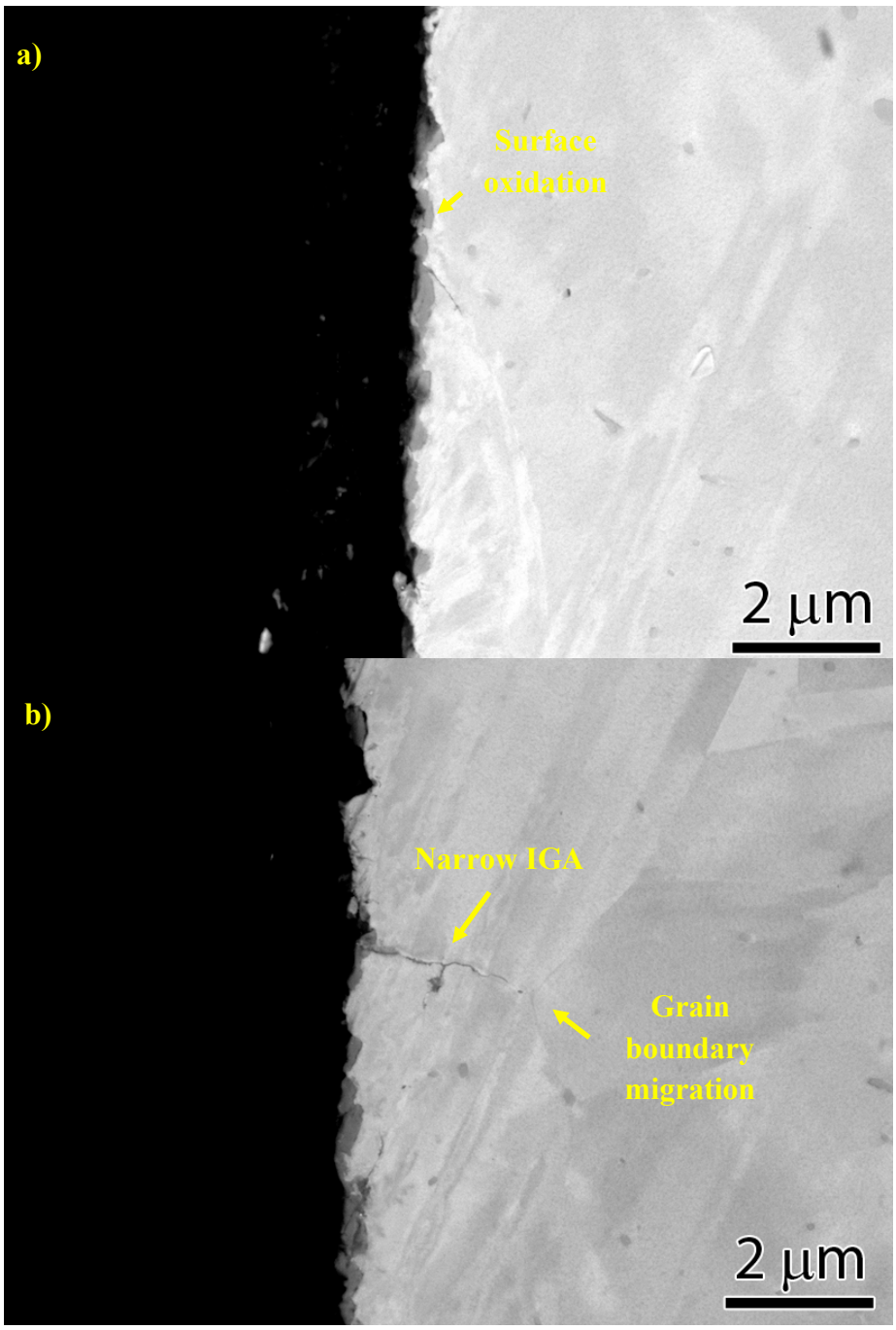

Figure 33. SEM-BSE images of a cross-section for the alloy 600 tensile initiation specimen IN003 illustrating representative TG (surface oxidation) and IG corrosion in the gauge section.

The observation of IG attack throughout the gauge section that transitioned to cracked IG attack near the fillet region suggests that SCC initiation begins with IG attack that eventually cracks and becomes a propagating IGSCC crack (Figure 34). Shallow (<3 μm) IG penetrations with a very prominent example of grain boundary migration are shown in Figures 34(a) and (b). The grain boundary has migrated at least 80 nm for ~2 μm ahead of the IG oxidation front. Figure 34(c) and (d) provide examples of IG attack regions that have cracked. These types of cracked IG attack structures were observed to be ~10 μm long and usually observed between the fillet and gauge regions. One of the indicators that this was most likely IG attack that had eventually cracked open due to stress is shown in Figure 34(d) where the leading crack tip has strong bright contrast just ahead of the leading tip. This contrast when observed in backscatter SEM and then in a subsequent TEM examination of the same region showed Cr depletion/Ni enrichment. An example of a long SCC crack is illustrated in Figure 34(e) located in the high stress fillet region. At this point, the crack openings even to the leading tip are large without any indication of IG oxidation or composition changes ahead of the open crack tip.

Gauge surface and cross-section examinations were also performed on the companion specimen, IN002 that was ground a 1200 grit SiC sandpaper. It showed very similar SCC initiation response (crack nucleation in 2025 hours versus 1775 hours for the 1 μm specimen). Although not shown in detail here, the overall distribution and depth of cracks in IN002 was roughly the same as for the IN003 specimen. The outer surface of each specimen is shown in Figure 35. The only observable difference between the two samples is that sanding grooves can be observed in the ground sample. It is only when the cross-section of the exposed surfaces was analyzed did the microstructural differences between the polished and ground surfaces become evident. For the 1 μm finish specimen (IN003), IG attack was observed to occur immediately from the surface on high-energy grain boundaries (Figure 36a). A different near-surface microstructure and corrosion was seen for the 1200-grit finish specimen (IN002). The SEM-BSE contrast in Figure 36b highlights a nanocrystalline grain microstructure that varies in thickness across the surface reaching a maximum value of ~1 μm. This damage of the surface was apparently not sufficient to promote a measureable difference in SCC initiation response, however, the near-surface corrosion behavior was modified. Numerous instances of corrosion and IG attack were observed through the nanocrystalline region and continued into bulk grain boundaries.

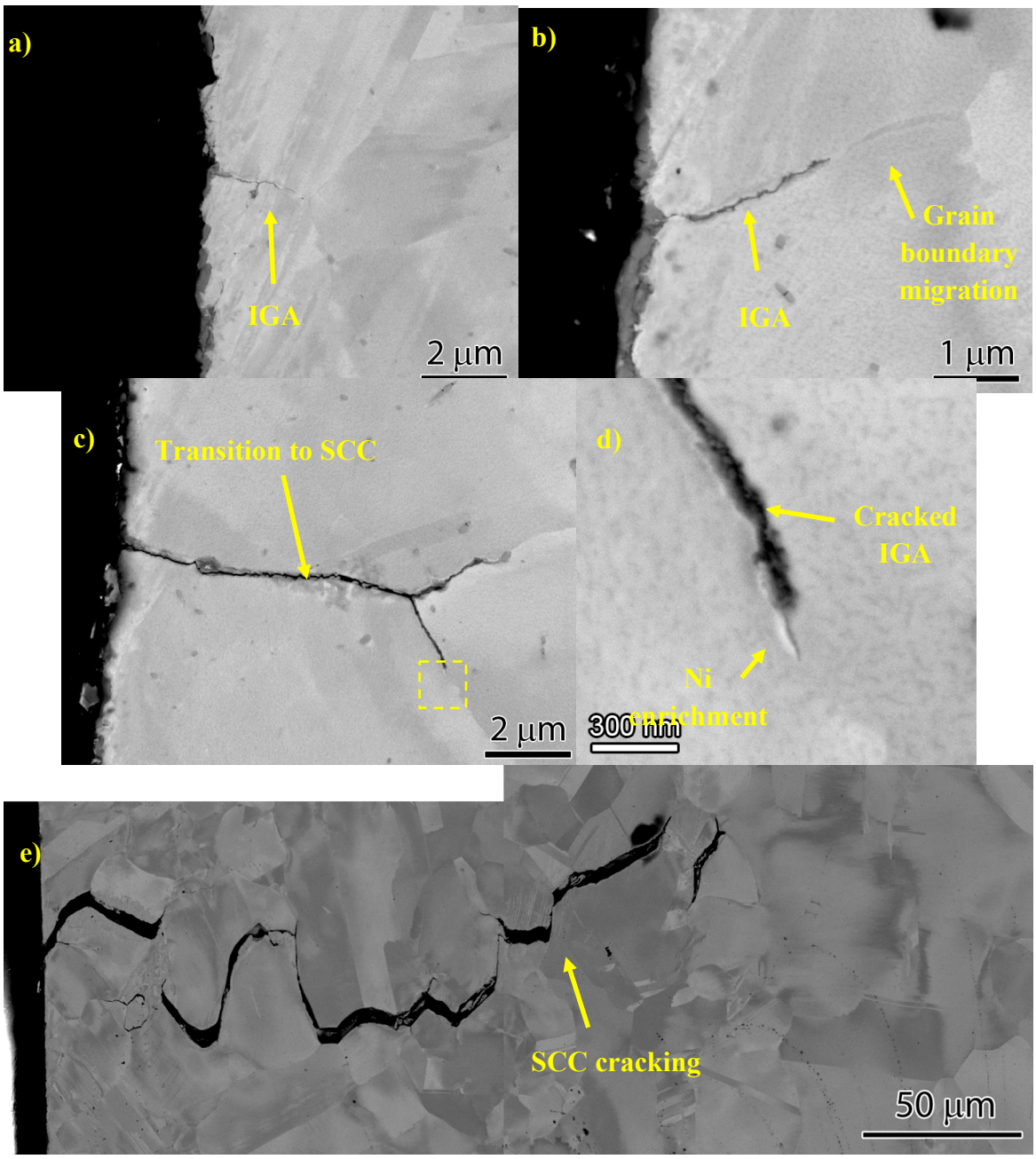

Figure 34. SEM-BSE images of the cross-section for the alloy 600 initiation specimen IN003 highlighting various stages of SCC cracking: (a,b) IG attack in gauge section without cracks, (c,d) IG attack transitioning to an IGSCC crack and e) a long IGSCC crack in the fillet region.

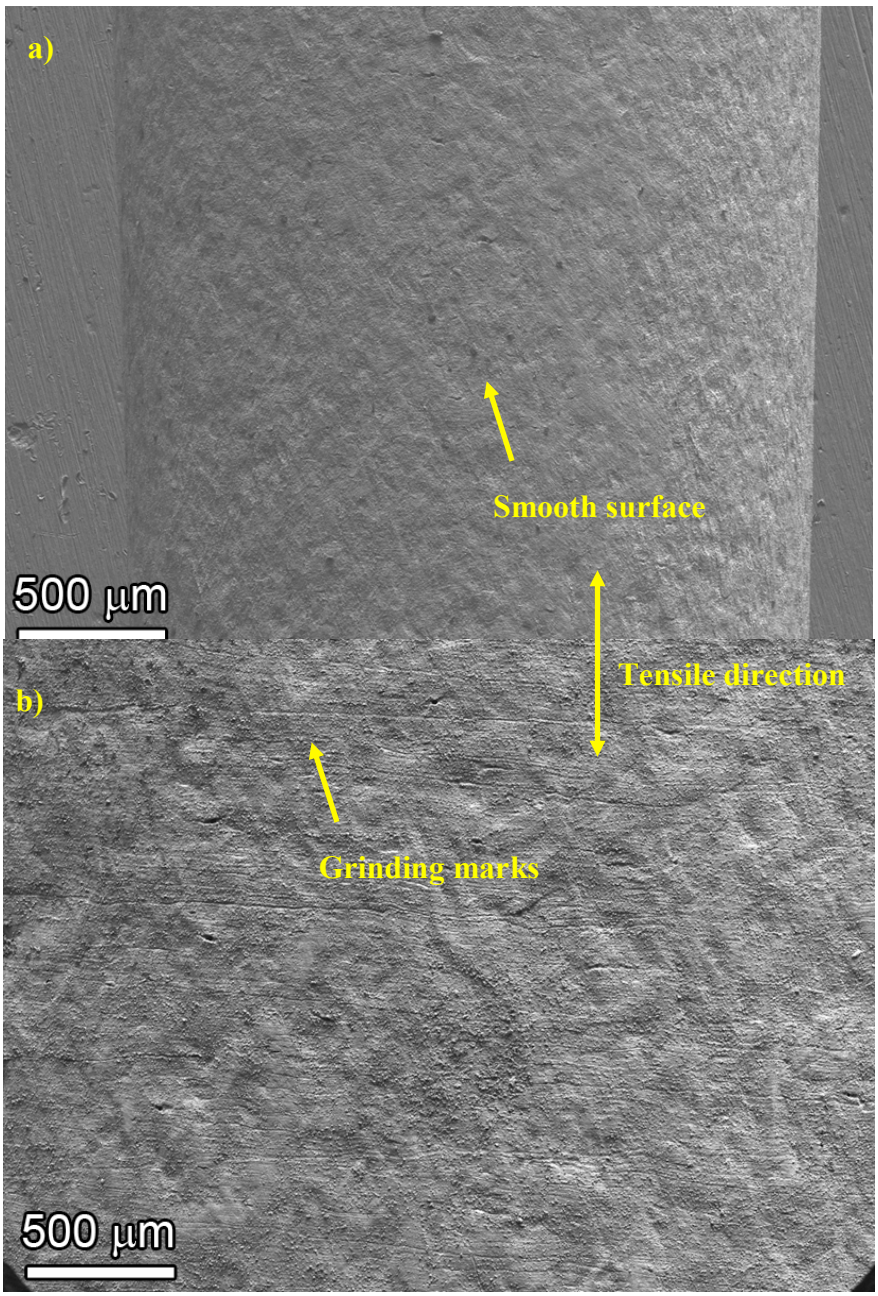

Figure 35. SEM-SE images of exposed surfaces for the alloy 600 initiation specimens that had a) highly polished gage section surface (IN003) or b) surfaces polished to 1 µm and then ground with 1200 grit SiC ground gage section surface (IN002).

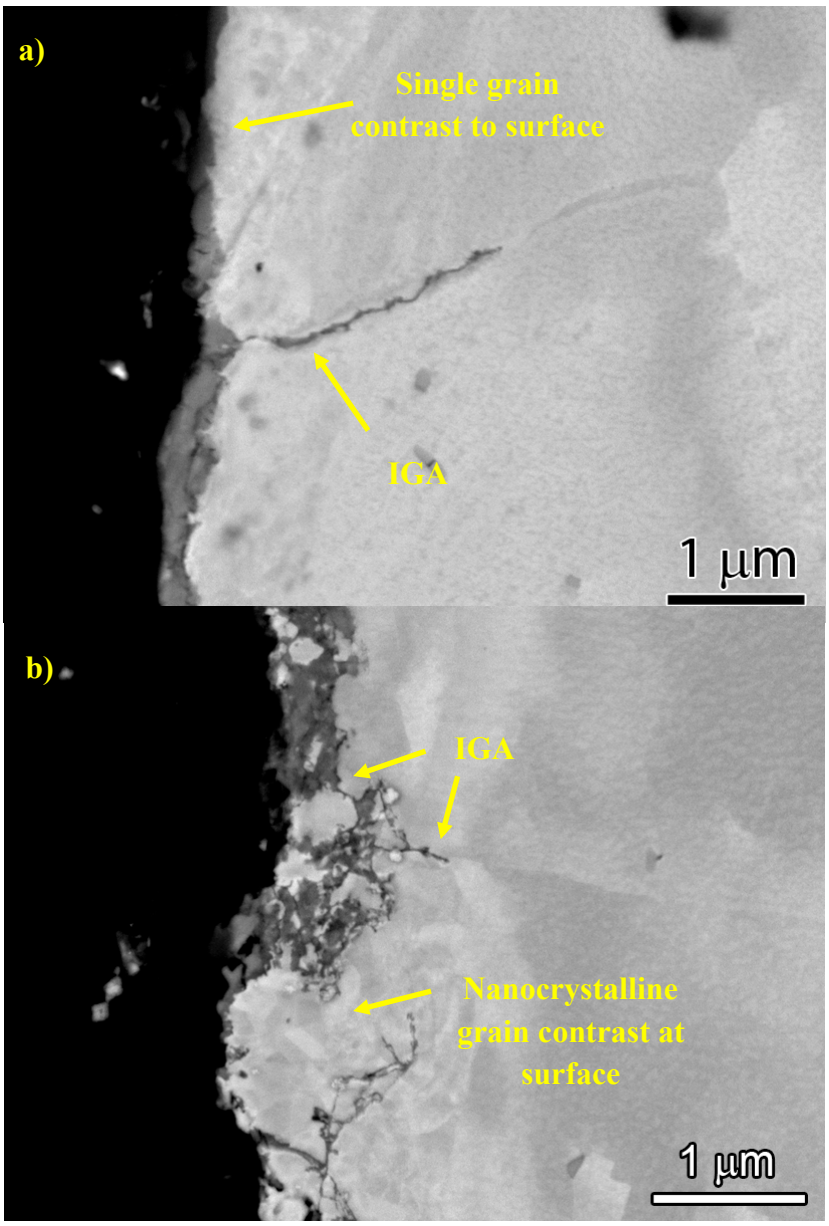

Figure 36. SEM-BSE images of cross-sections from the alloy 600 initiation specimens with surfaces of 1um diamond (IN003) and 1200 grit SiC (IN002) after exposure to PWR primary water.

SCC Crack Initiation of 19% Cold-Rolled Plate Heat (Specimens IN016, IN017 and IN018)

These specimens were made from an alloy 600 plate heat (NX6106XK-11) that was cold rolled at PNNL to a measured reduction of 19% in two passes. All three specimens were first polished to 1 µm surface finish in the gauge region, and then IN016 and IN017 were ground to a 60-grit surface finish. Specimens were inserted in LWRS system #1 along with three other MA alloy 600 specimens during its demonstration test. Pictures illustrating the set up for the demonstration test are presented in Figure 37 showing the load train and instrumented specimens.

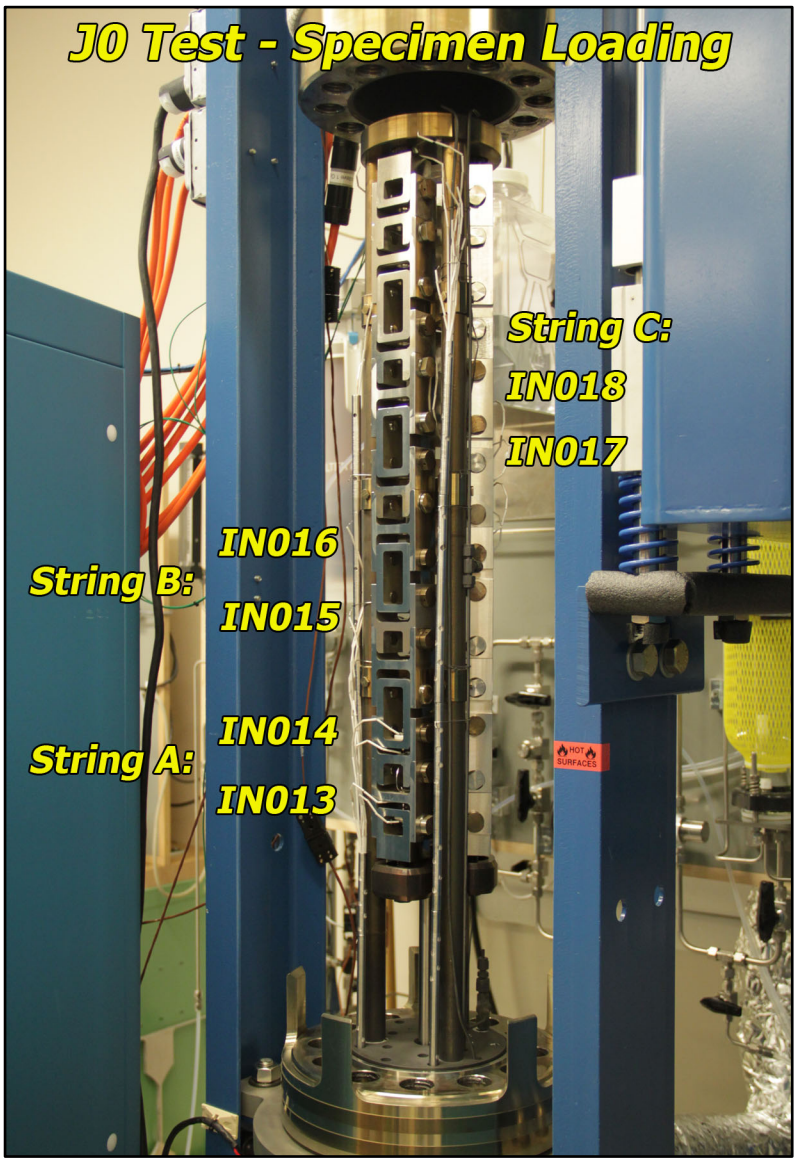

Figure 37. Load train for the LWRS system #1 crack initiation test system set up for the demonstration test.

The specimens were loaded to 610 MPa in 360°C PWR primary water, extremely close to their 620 MPa yield strength (predetermined by an air tensile test). Typical DCPD response for the specimens is shown in Figure 38(a). All three specimens reveal an increasing non-referenced strain with the rate of increase decreasing with test time. As discussed in the Experimental Details section, the majority of the non-referenced strain is predominantly due to resistivity evolution of the material. At ~1520 h, the IN016 (1 µm surface finish) strain trajectory exhibited a change from a decreasing slope to a rapidly increasing slope signifying crack initiation and rapid crack growth as documented in Figure 38(b). Because this was a demonstration test, the system load was maintained to observe the response of all three specimens during this rapid growth period and eventual failure. Upon completion of the test, the fracture surface for the IN016 specimen was characterized in the SEM as illustrated in Figure 39. The cracking morphology was IG across the crack growth surface. The gauge surfaces of IN017 and IN018 were also examined in the SEM, but it was found that the 60 grit finish was too rough to allow detection of any small cracks that may have been present.

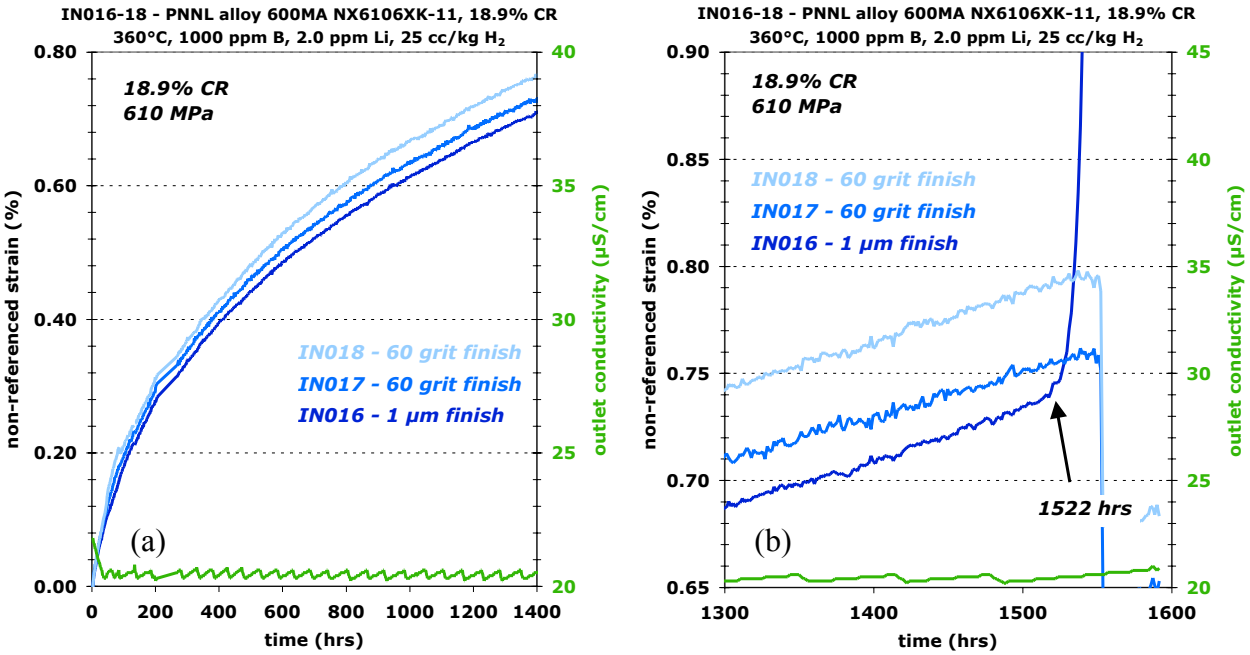

Figure 38. SCC initiation test plots for 19%CR alloy 600 specimens IN016, IN017 and IN018 during testing in 360°C PWR primary water: (a) early DCPD response and (b) observation of crack initiation and growth for the IN016 specimen.

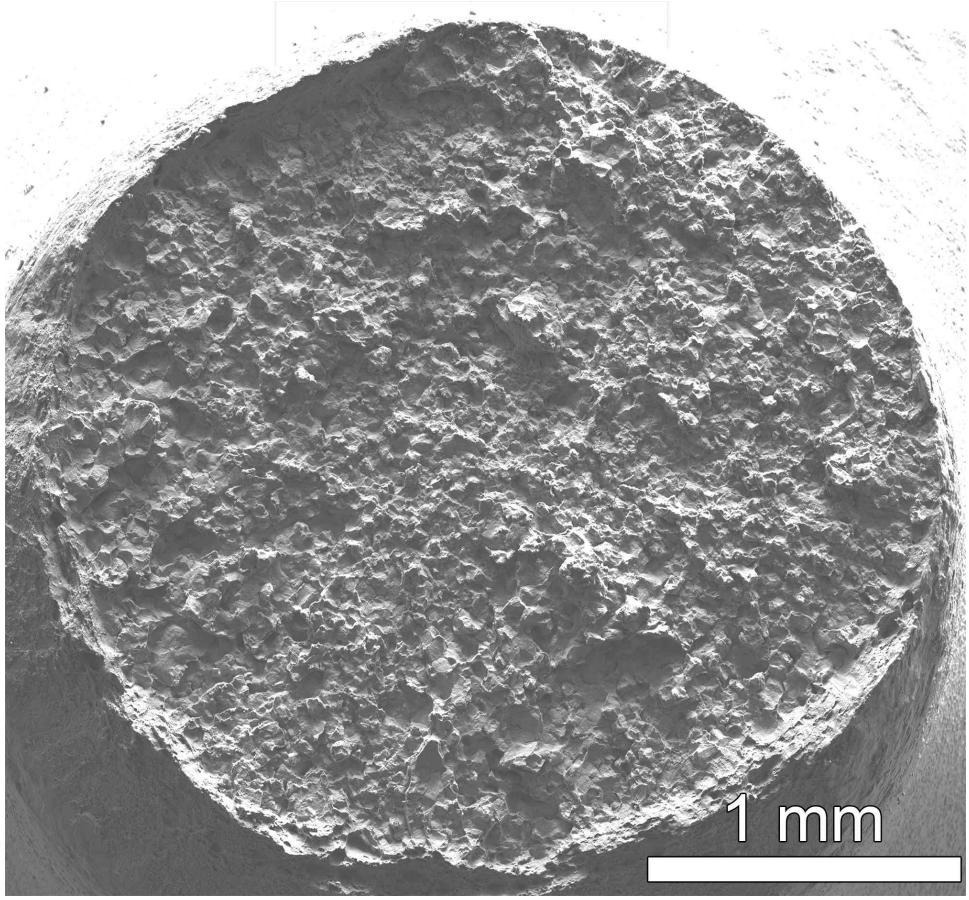

Figure 39. SEM-SE image showing IG fracture surface for 19%CR alloy 600 specimen IN016 after testing in PWR primary water.

SCC initiation testing continued on the two remaining 19%CR specimens (IN017 and IN018) in LWRS system #2. The specimens were reloaded to their yield stress (634 MPa) and held at constant load as shown in Figure 40. DCPD response exhibited a decreasing slope for the non-referenced strain over the first ~120 hours. A clear indication of an increasing slope characteristic of initiation to rapid crack growth was observed at ~160 hours for IN018. Because of this sharp upturn, the decision was made to end the test at 178 hours and a total exposure time of ~1770 hours for these two specimens. IN017 was put back into test where SCC initiation was observed to occur 20 hours after being reloaded (Figure 41). Optical (Figure 42) and SEM (Figure 43) examinations of the IN018 gauge surface were performed, however the surface damage from the 60-grit grinding made identification of small cracks extremely difficult. Plan views both normal and parallel to the gauge section shown in Figure 43 illustrate the roughness imparted by the grinding. Gouges on the order of 10 μm are observed and are corroborated by a SEM-BSE images on the cross-section specimens. To illustrate why crack initiation is difficult to observe in ground specimens using intermittent surface analysis via SEM, a cross-section image of IN018 is shown at high magnification in Figure 43(c). Attempts to image the cracks

normal to the gauge through this recrystallized zone into grain boundaries in the bulk material was impossible.

More detailed cross-sectional analysis of the IN018 sample (Figures 44 and 45) provide an indication of how this highly roughened surface corroded. Once exposed to water, the grain boundaries of the nanocrystalline grains in the recrystallized zone are attacked. Existing cracks within the recrystallized zone were observed, but may have been created during surface grinding and not during the initiation testing. Small cracks were also observed to emanate from TiN particles found near the surface. If the oxidation does extend through the recrystallized zone to reach a bulk grain boundary (Figure 45), IGA is observed. Typical Cr depletion ahead of the attack was observed. As can be seen in Figure 44, for the length of this test, the oxidation of the recrystallized zone on the majority of the surface has only penetrated a third of the way through and had not reached the bulk grain boundaries.

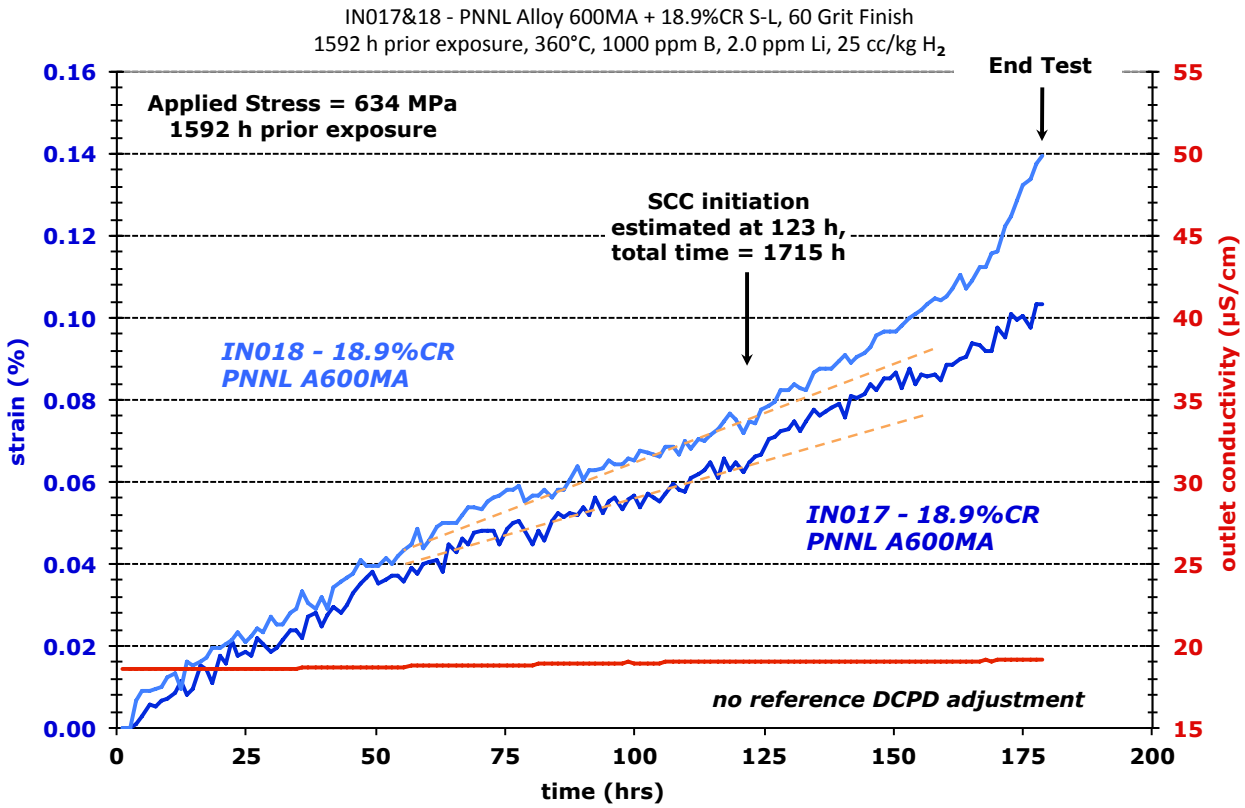

Figure 40. SCC initiation test plot for the continuing test on 19%CR alloy 600 specimens IN017 and IN018 in 360°C PWR primary water.

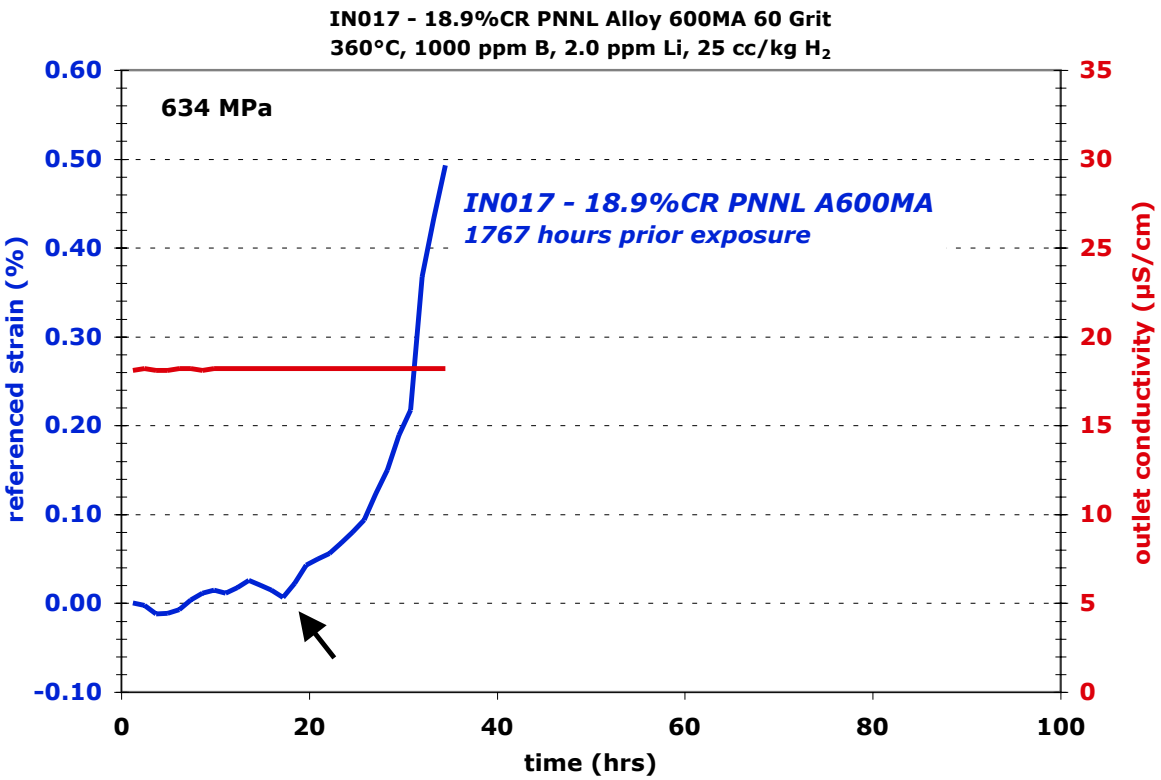

Figure 41. SCC initiation plot for 19%CR alloy 600 specimen IN017 that had a 60 grit finish.

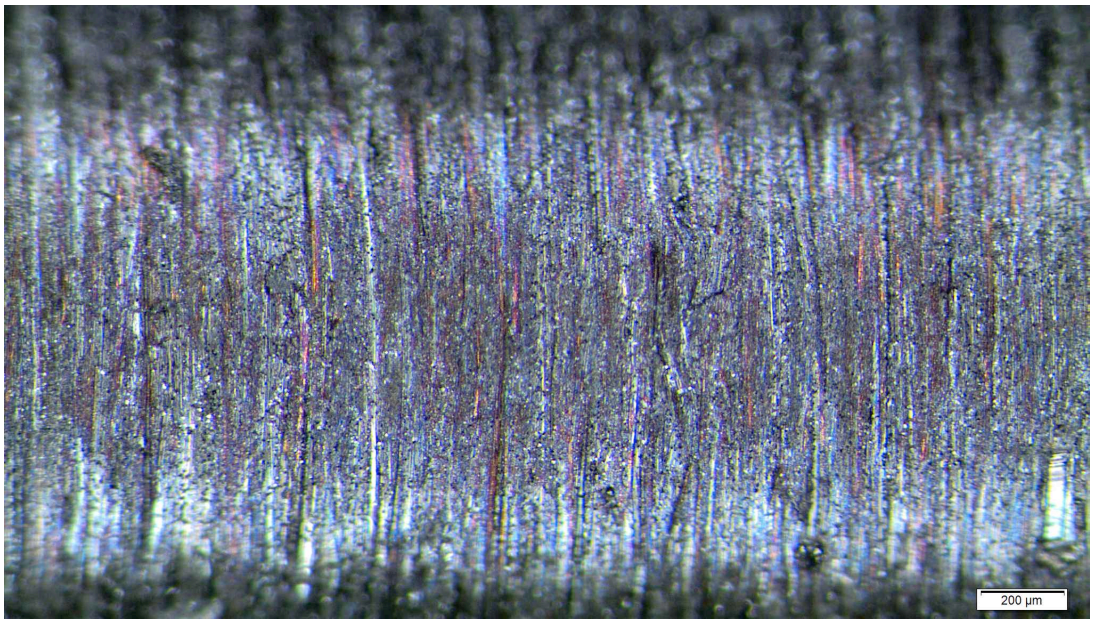

Figure 42. Optical image of the heavily ground IN018 gauge section after SCC initiation test.

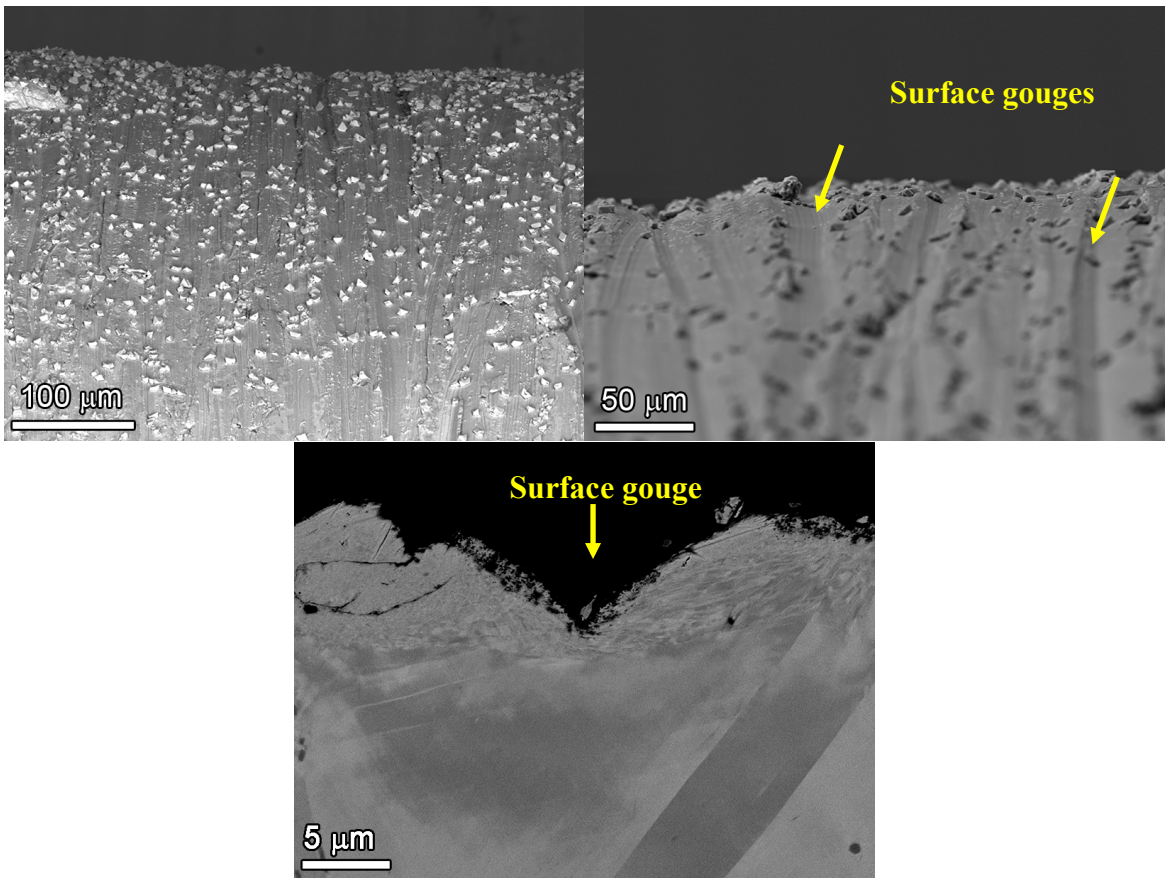

Figure 43. SEM-BSE images of IN018 gauge section in both plan view at two different angles as well as a cross-sectional example. The depth and microstructure of the gouges observed in the plan view can clearly be observed in the cross-section image to be on the order of tens of micrometers.

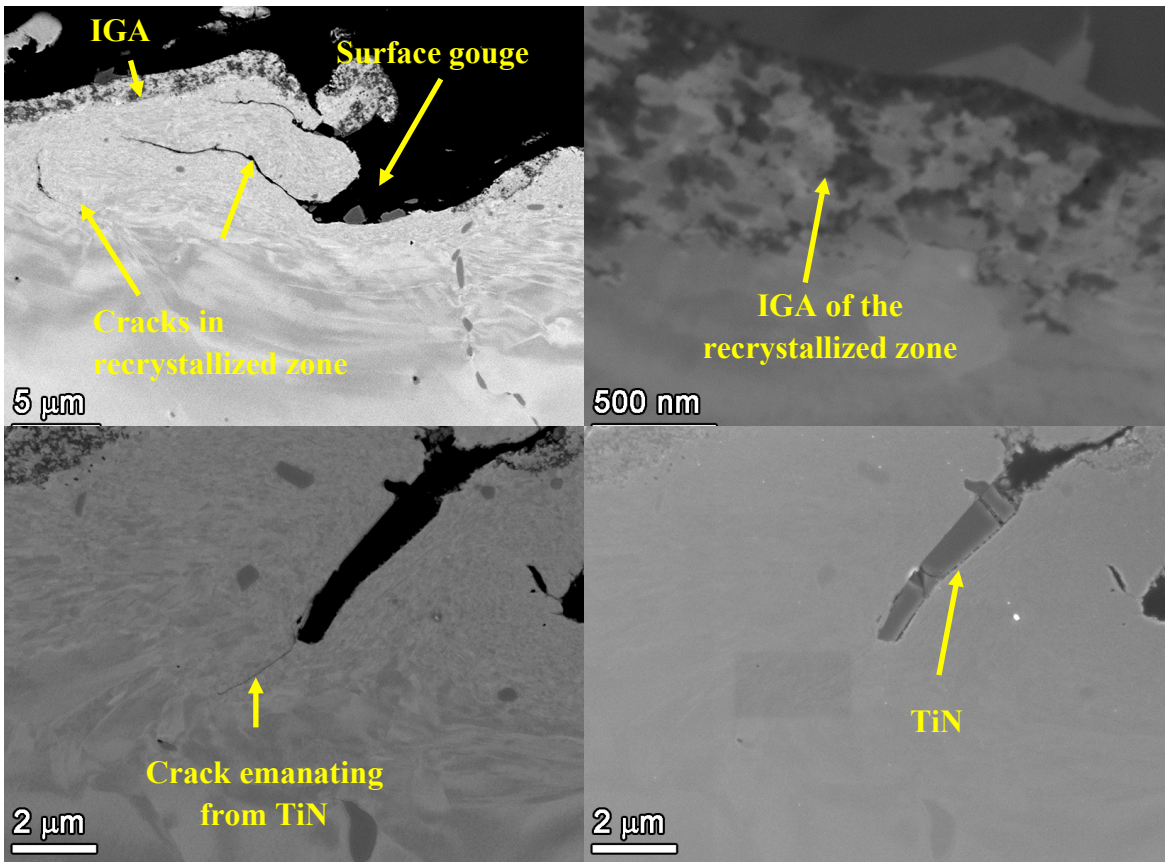

Figure 44. SEM-BSE image of the IN018 cross-section showing that the surface is comprised of a recrystallized zone of nanocrystalline grains. Once exposed, this surface slowly corrodes. Random cracking within the nanocrystalline zone was observed and was most likely imparted during grinding. Lastly, cracks were observed to emanate from TiN particles near the surface.

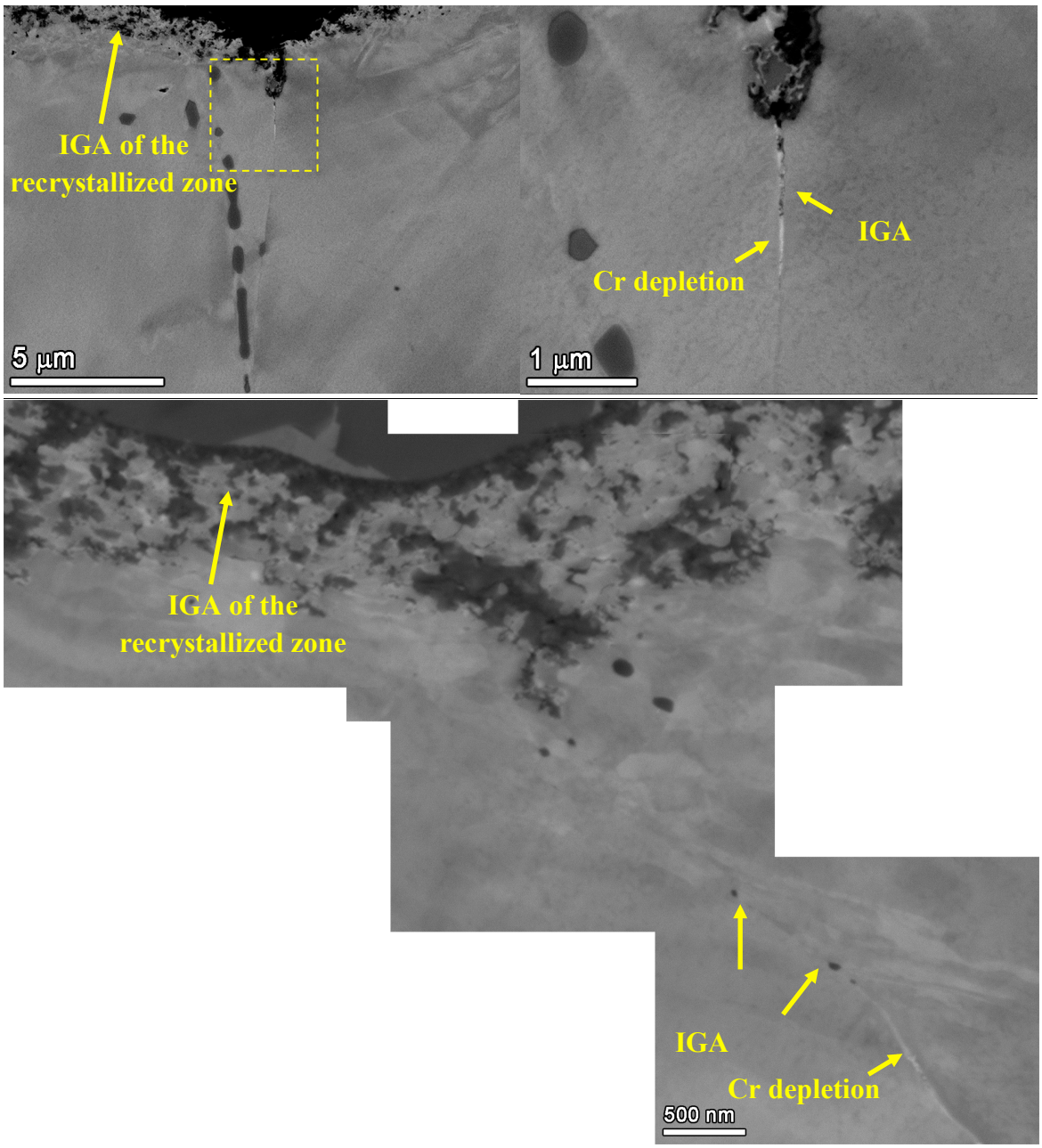

Figure 45. SEM-BSE micrographs of IN018 showing IG attack of boundaries that intersect the surface as well as a boundary below the recrystallized layer.

SCC Crack Initiation Tests on 20% Tensile Strained CRDM Heat M3935 from PWR Service (IN022) and 5% Tensile Strained CRDM Heat 93510 (IN023)

This test was performed on a pair of specimens. IN022 was cut from the original Davis Besse alloy 600 RPV head, CRDM nozzle #1 that exhibited SCC in PWR service and then was 20% tensile strained. In the mill-annealed, condition this material was found to be very susceptible to PWSCC during prior crack growth tests [13,14]. IN023 was cut from a CRDM alloy 600 tube received from General Electric and then tensile strained until reaching the same load that was needed to obtain 20% TS for IN022, which resulted in ~5% tensile strain. The gauge section of both specimens was polished to a 1-µm finish prior to testing. Upon starting the test at the yield strength of the materials, a distinct difference in the reference DCPD response was observed for the Davis Besse service material (IN022) as presented in Figure 46. The reference voltage exhibited a flat DCPD response with time indicating that the previous plant exposure to high temperatures had fully evolved the resistivity change that occurs in this material. Recall that the response for alloy 600 with no prior PWR-relevant temperature exposure is an increasing reference DCPD voltage as illustrated for IN023. The rate of change of resistivity (slope of the trend line) decays with time at temperature and approaches a steady value after many months (or years). No evidence for crack initiation was seen for IN023, however as shown in Figure 47, a steady strain rate (rather than a decreasing rate or no growth) was seen for IN022 suggesting that cracks had initiated very early in the test and were growing. As a result, the test was ended at ~380 hours and the gauge sections of both specimens were characterized.

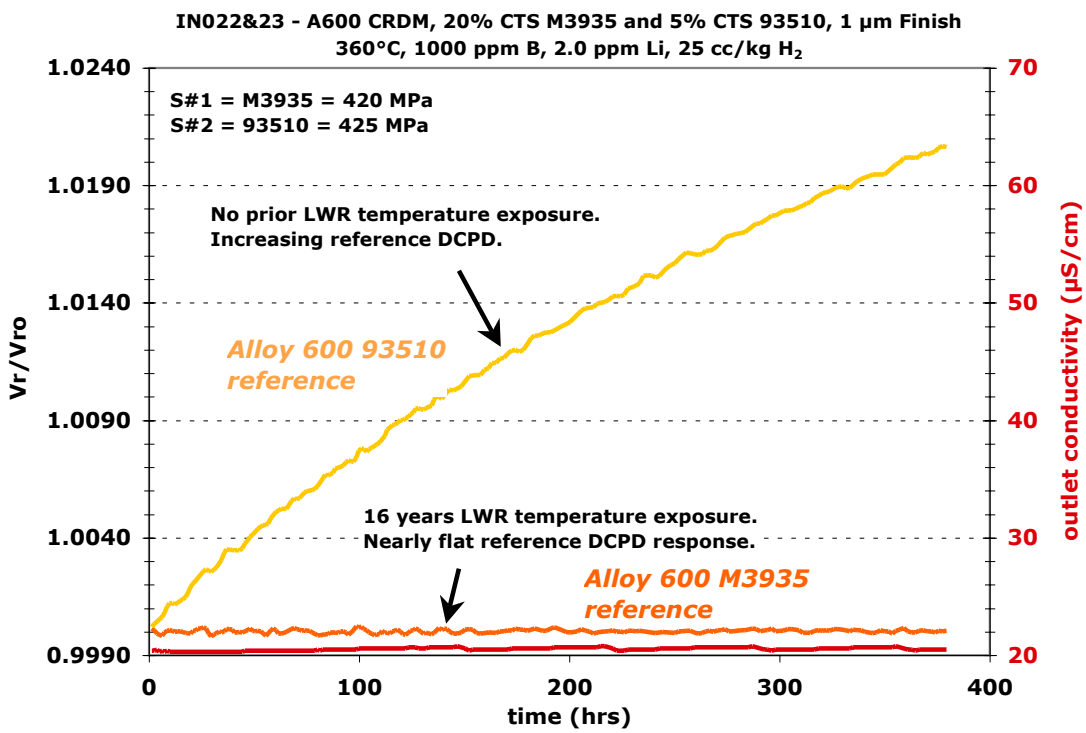

Figure 46. DCPD response for the reference locations in specimens IN022 and IN023.

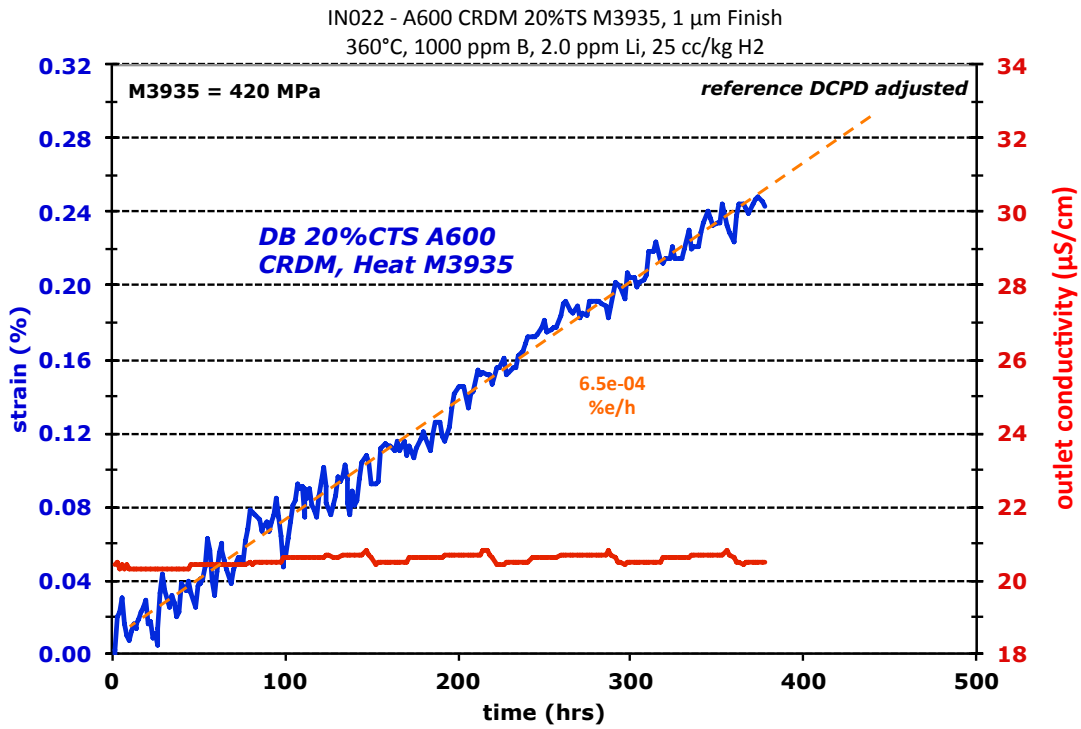

Figure 47. Strain versus time plot for specimen IN022 showing a steadily increasing strain during test in 360°C PWR primary water.

Optical and SEM examinations of the IN022 gauge surface revealed several large IGSCC cracks (100-200 µm in length) and a significant distribution of small IG cracks (<20 µm). Examples of the largest cracks are presented in Figure 48. These were found to be adjacent to a region of surface damage (minor indentation) on the tensile specimen. It is possible that this surface damage promoted higher local stresses and helped facilitate early crack nucleation. The presence of many small IG cracks in other locations suggests that SCC initiation would have occurred in other locations on this 20%TS material. The gauge is currently being sectioned into quarters and the distribution of crack depths will be obtained from polished cross-sections particularly associated with the larger IG cracks found on the surface.

Reference-adjusted DCPD response for IN023 in Figure 49 shows an apparent creep transient followed by little or no strain. No evidence for SCC cracks was identified on the IN023 surface consistent with the DCPD response. Testing continued on the IN023 specimen in LWRS system #2, this time paired with an 8% tensile strained plate specimen IN052 (reported in the next section). Somewhat surprisingly, crack initiation was detected for the IN052 specimen after an exposure time of ~1250 hours while DCPD response for the IN023 specimen gave no indication of crack nucleation (total test time of ~1870 hours) as documented in Figure 50. However, numerous small surface cracks were identified by SEM examinations (Figure 51). Three different rotations were evaluated and crack distributions were documented for each area. Examples of typical cracks are presented in Figure 51 for the area in rotation #1. All cracks were

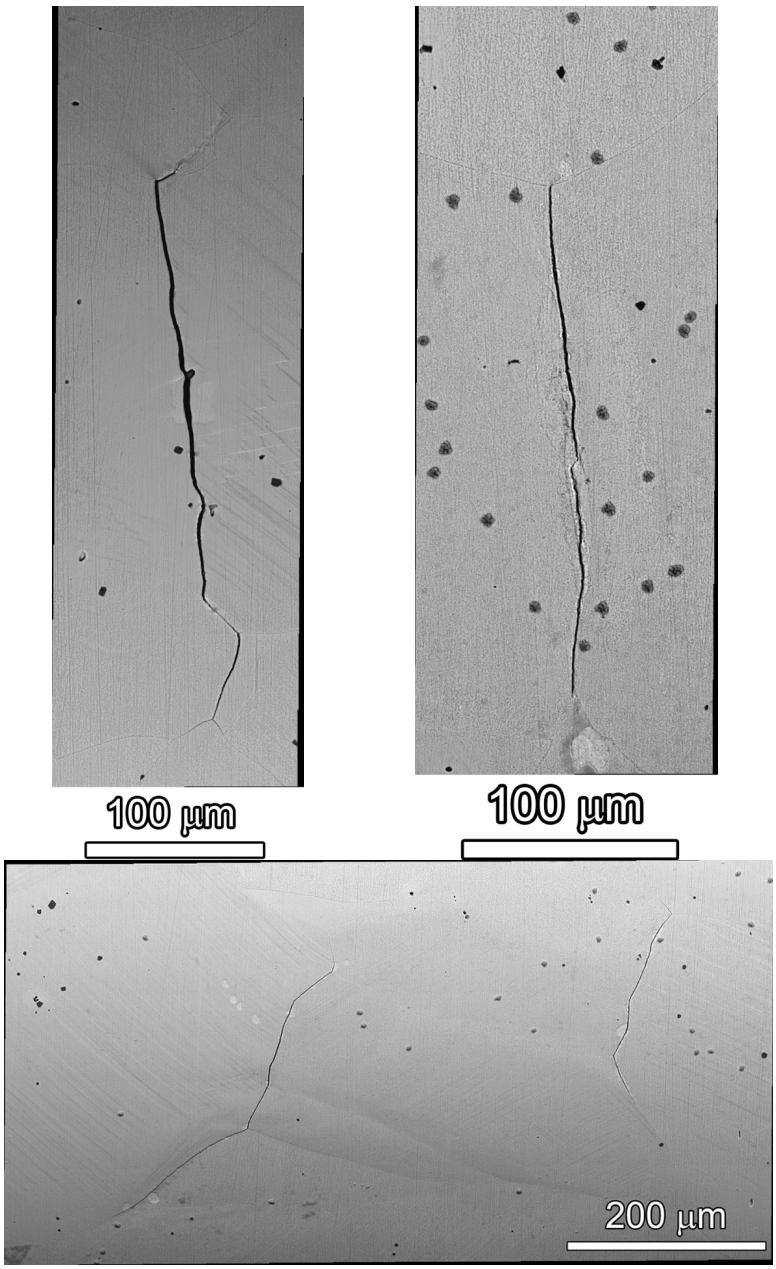

Figure 48. SEM-BSE images illustrating morphology of several large IGSCC cracks on the gauge surface of the IN022 specimen.

extremely tight with most exhibiting an apparent length on the surface of <50 µm. The maximum crack length for isolated cracks (observed in rotation #3) may have reached ~150 µm. It is difficult from the surface evaluations to determine whether adjoining cracks were connected. In order to estimate the approximate depth of these cracks, a focused-ion beam (FIB) system was used to trench below the surface and reveal the crack in profile. This cursory examination is shown in Figure 52 and indicated that the crack depth was ~15 µm for a surface crack length of ~100 µm.

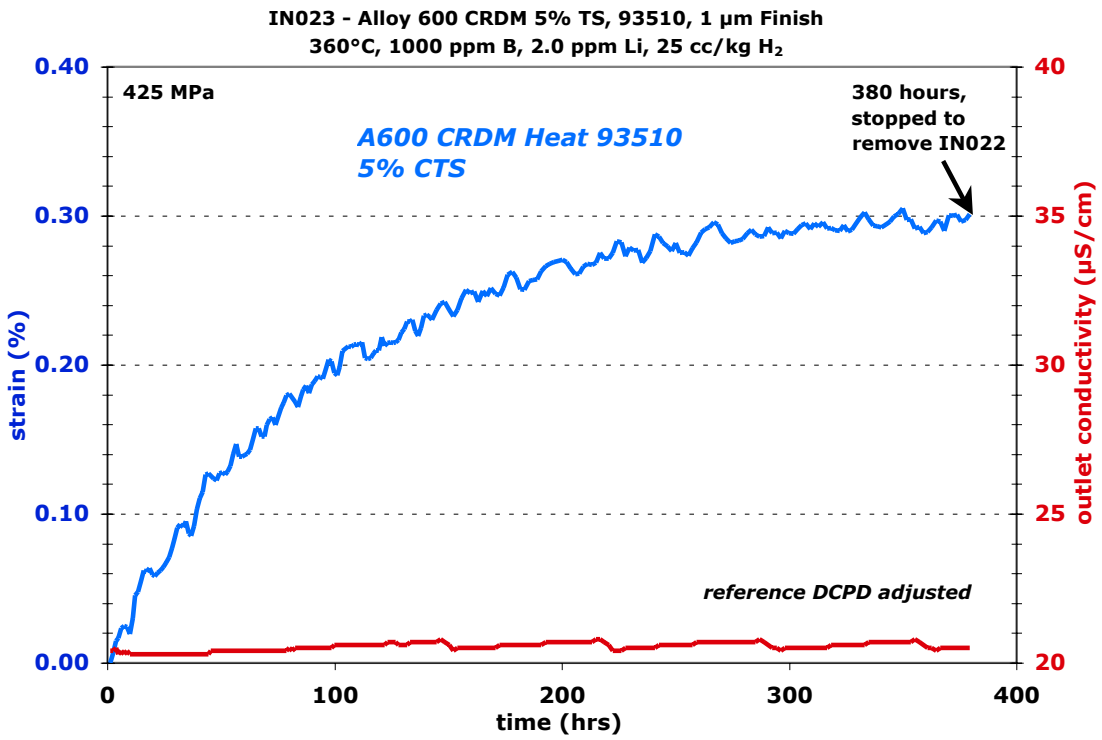

Figure 49. Strain versus time plot for specimen IN023 showing reference DCPD adjusted strains during testing in 360°C PWR primary water.

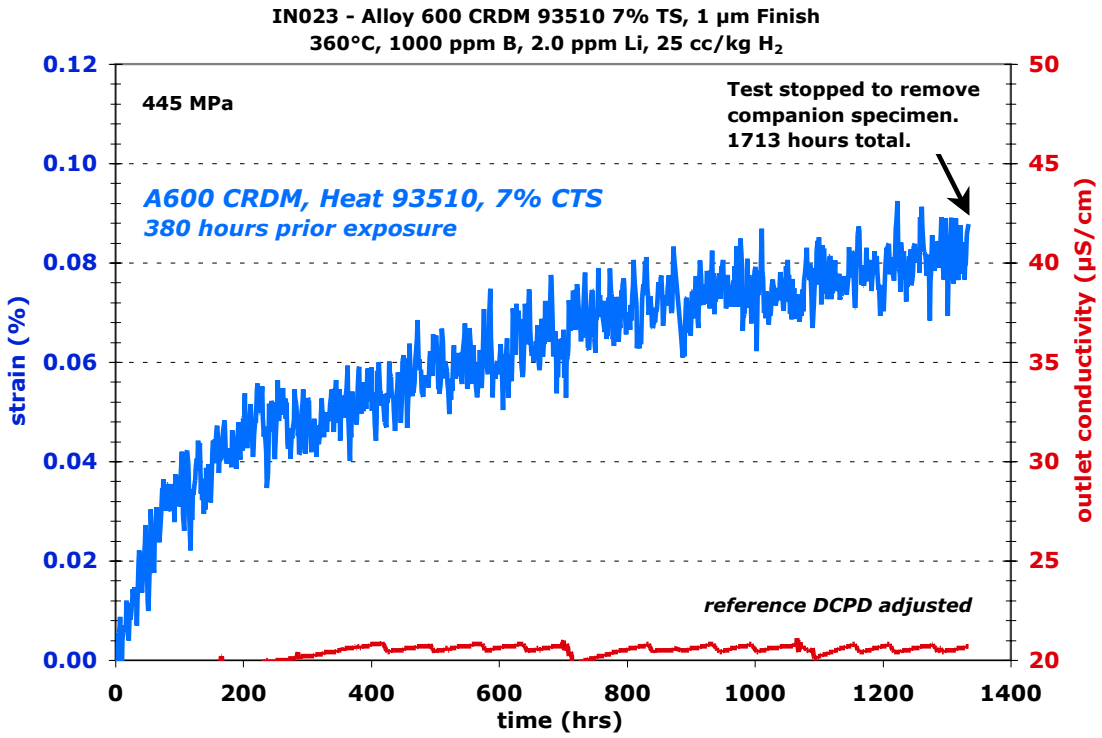

Figure 50. Strain versus time plot for specimen IN023 after restart showing DCPD adjusted strains during testing in 360°C PWR primary water with 1713 hours total exposure at this point.

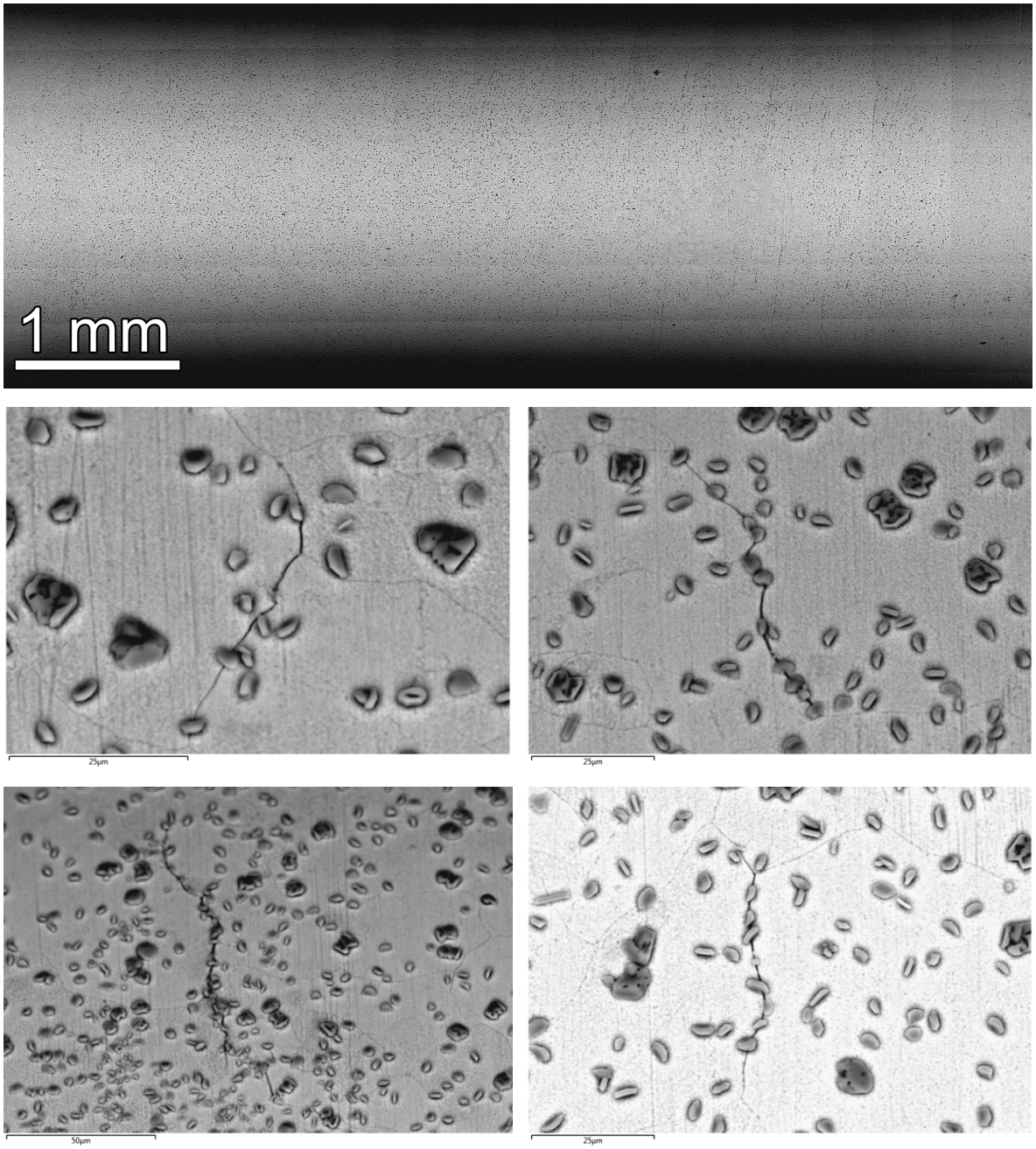

Figure 51. SEM-BSE examples of small surface cracks on the IN023 specimen gauge after a combined test time of ~1870 hours. The top image shows rotation 1 at low magnification illustrating that no obvious SCC cracks are present. The bottom four images provide examples of typical small cracks that were extremely tight and reached lengths approaching ~100 µm in isolated locations.

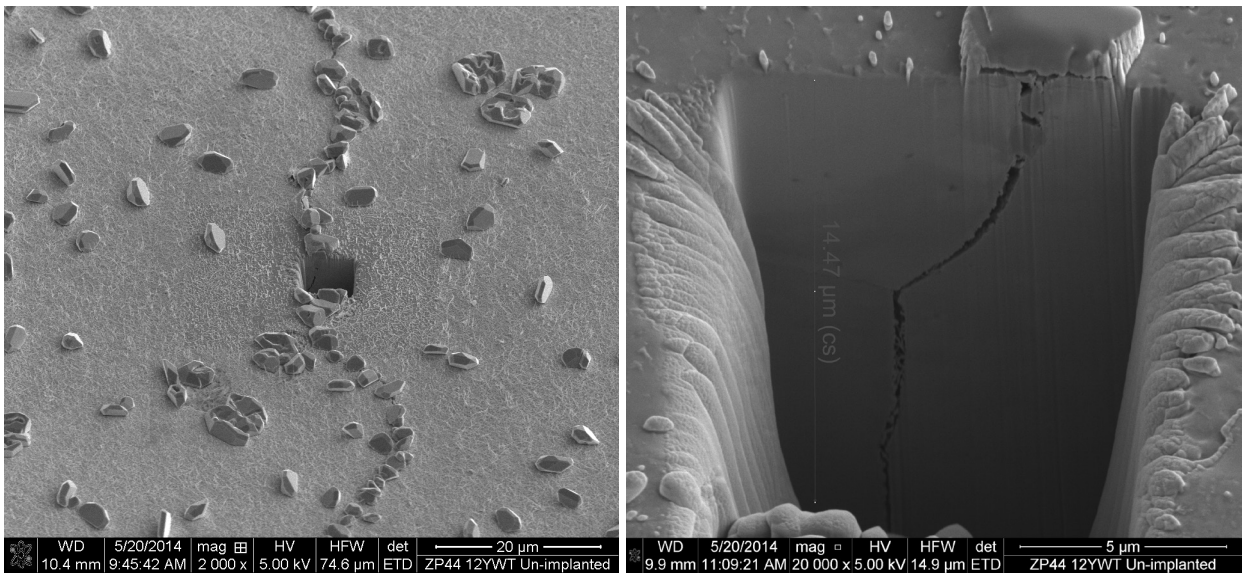

Figure 52. SEM-SE image of a FIB trench into IN023 surface to examine crack depth from the specimen surface.

Results during the final constant load exposure of IN023 are shown in Figure 53 and indicate a distinct change in DCPD response after ~470 hours of additional exposure on top of the prior 1713 hours of exposure. This change in response corresponds to a total time to initiation of ~2183 hours. The test was continued for another ~400 hours to confirm the in-situ detection of cracking and then ended after a total test time of ~2591 hours. The slow evolution in transition from a decreasing strain rate to an increasing strain rate indicative of SCC initiation is much different than that of most of the more highly cold-worked alloy 600 specimens where the transition rapidly took place within hours rather than days. This suggests that cold working increases the SCC initiation susceptibility, however since all specimens were tested at their yield strength, the more highly cold worked specimens were tested at higher stress. As discussed in the Experimental Details section, the crack tip stress intensity is directly proportional to the applied stress, and thus, lower strength materials see a lower crack-tip stress intensity. For this material that was tested at 445 MPa, the stress intensity is ~65% of the more highly cold-worked materials that were discussed prior to this.

SEM characterization of the IN023 gauge surface was again performed after the full exposure time of 2591 hours. Three different rotations were examined and a direct comparison between observed crack distributions is illustrated in Figures 54-56. The density of small IG cracks has clearly increased along with the length of the longest cracks. These results provide insights into the in-situ detection limits and show that some evolution of the crack distribution is required for DCPD to identify SCC nucleation. Based on these observations and those from other alloy 600 tests, it appears that multiple cracks with a length ~150 µm on the surface are necessary for consistent in-situ detection by DCPD. The gauge is being sectioned and the distribution of crack depths will be obtained to help determine a critical crack depth for DCPD detection.

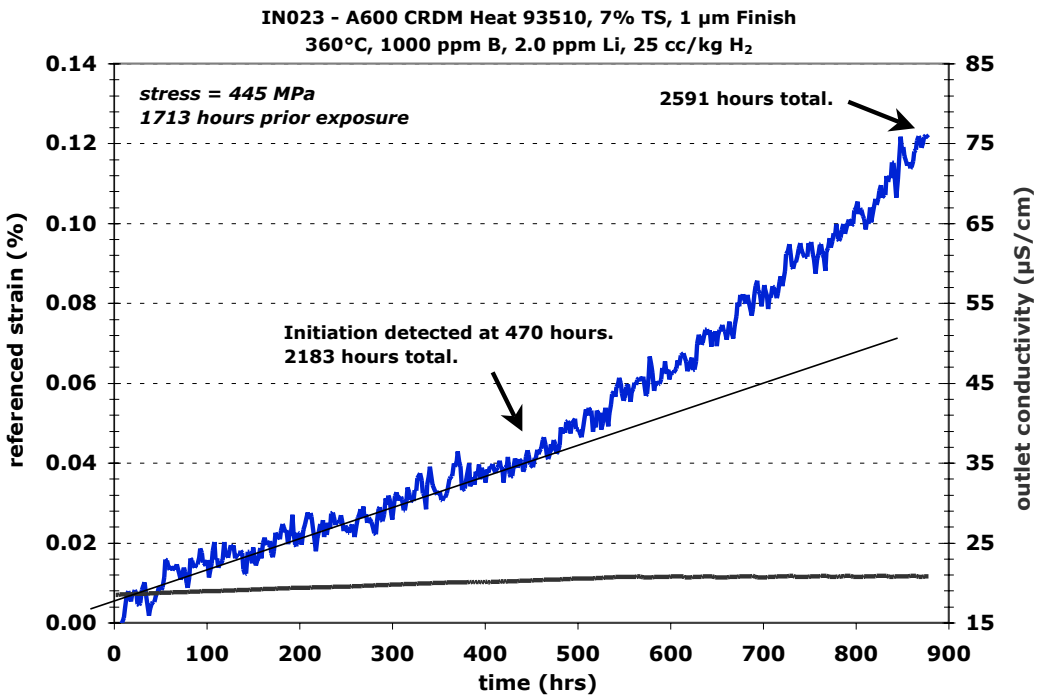

Figure 53. SCC initiation plot for specimen IN023 showing reference DCPD adjusted equivalent strains during the third exposure in 360°C PWR primary water. Initiation detected after 2183 hours total.

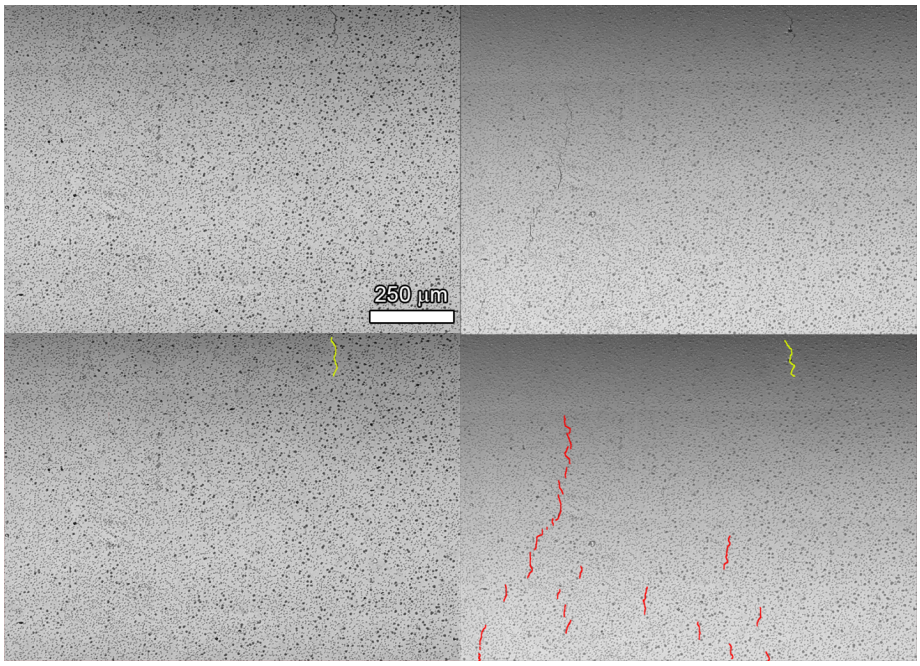

Figure 54. SEM-BSE images of IN023 Rotation #1 illustrating the extent of surface crack formation at 1713 hours (left) and 2591 hours (right). Upper and lower images are identical. In the lower images, present cracks that were present after 1713 hours are yellow while those found after 2591 hours are red.

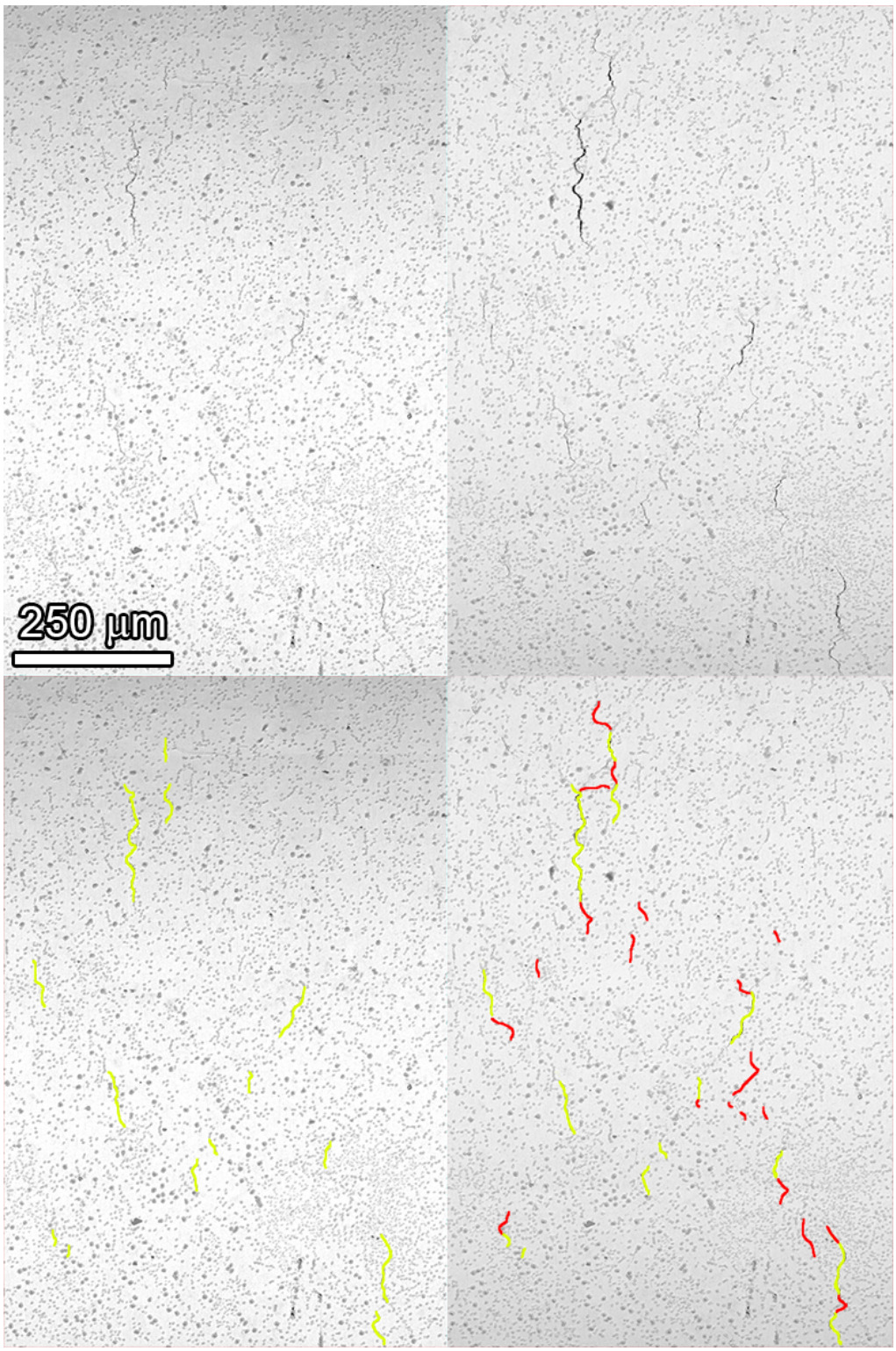

Figure 55. SEM-BSE images of IN023 Rotation #2 illustrating the sample at 1713 hours (left columns) and 2591 hours (right columns). The bottom two figures highlight the cracks in yellow present at 1713 hours and new cracks in red present at 2591 hours (red).

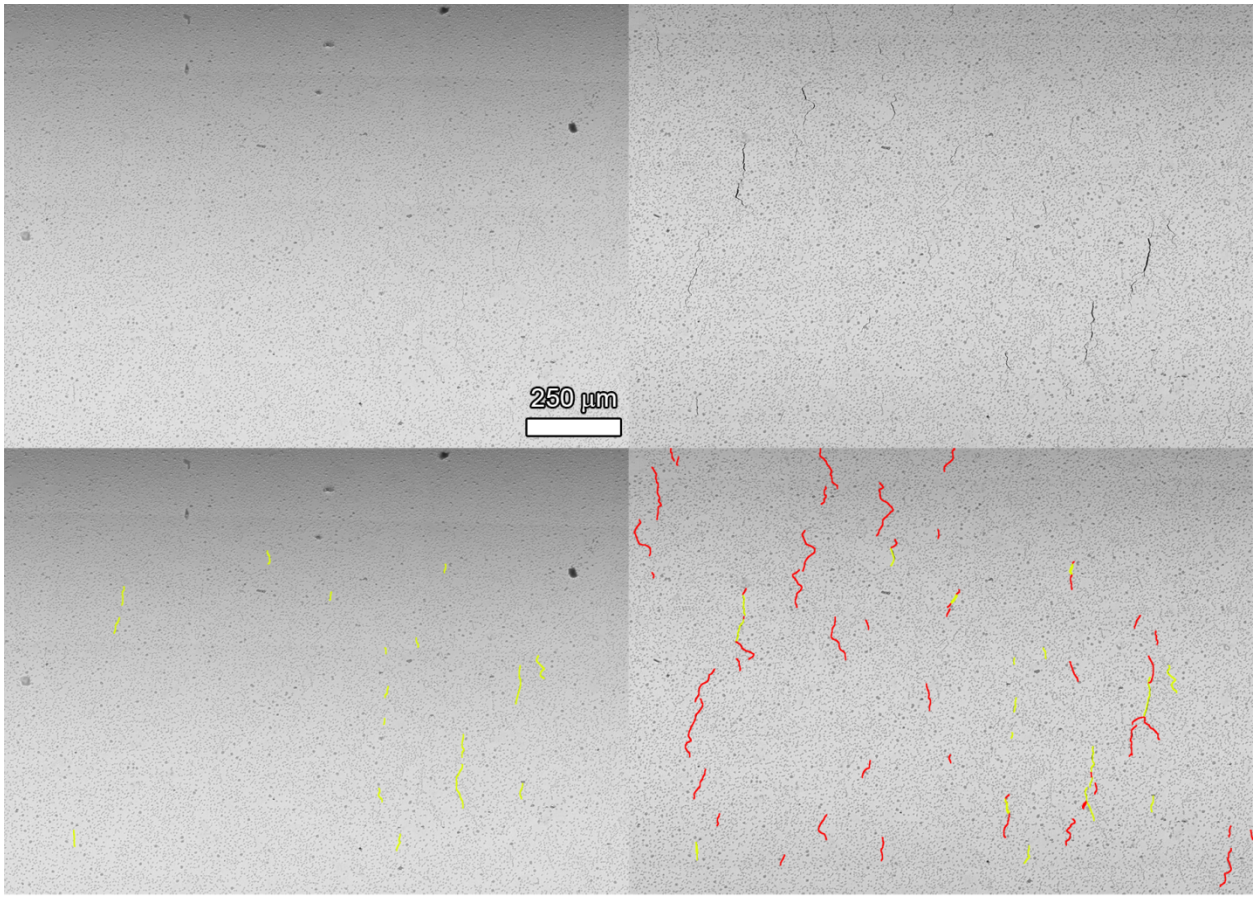

Figure 56. SEM-BSE images of IN023 Rotation 3 illustrating the sample at 1713 hours (left columns) and 2591 hours (right columns). The bottom two figures highlight the cracks in yellow present at 1713 hours and new cracks in red present at 2591 hours (red).

SCC Crack Initiation of 8% Tensile Strained (TS) Plate Heat (Specimen IN052)

This specimen was cut from the mill-annealed alloy 600 plate (heat NX6106XK) and tensile strained to 8% in air followed by polishing the gauge section to 1 µm finish prior to SCC initiation testing. Steadily increasing DCPD response was observed over the first ~1250 hours in 360°C PWR primary water at constant load equivalent to its yield stress of 435 MPa. This behavior is presented in Figure 57. A very distinct break in the response was observed at this point in the test. Once the new response was confirmed, the test was shut down at 1334 hours and the specimen was removed for characterization. Many small IG cracks were discovered along with two larger primary IGSCC cracks (150-300 µm in length) as shown in Figure 58. This specimen will also be sectioned to determine the depth of the two primary IG cracks identified on the surface.

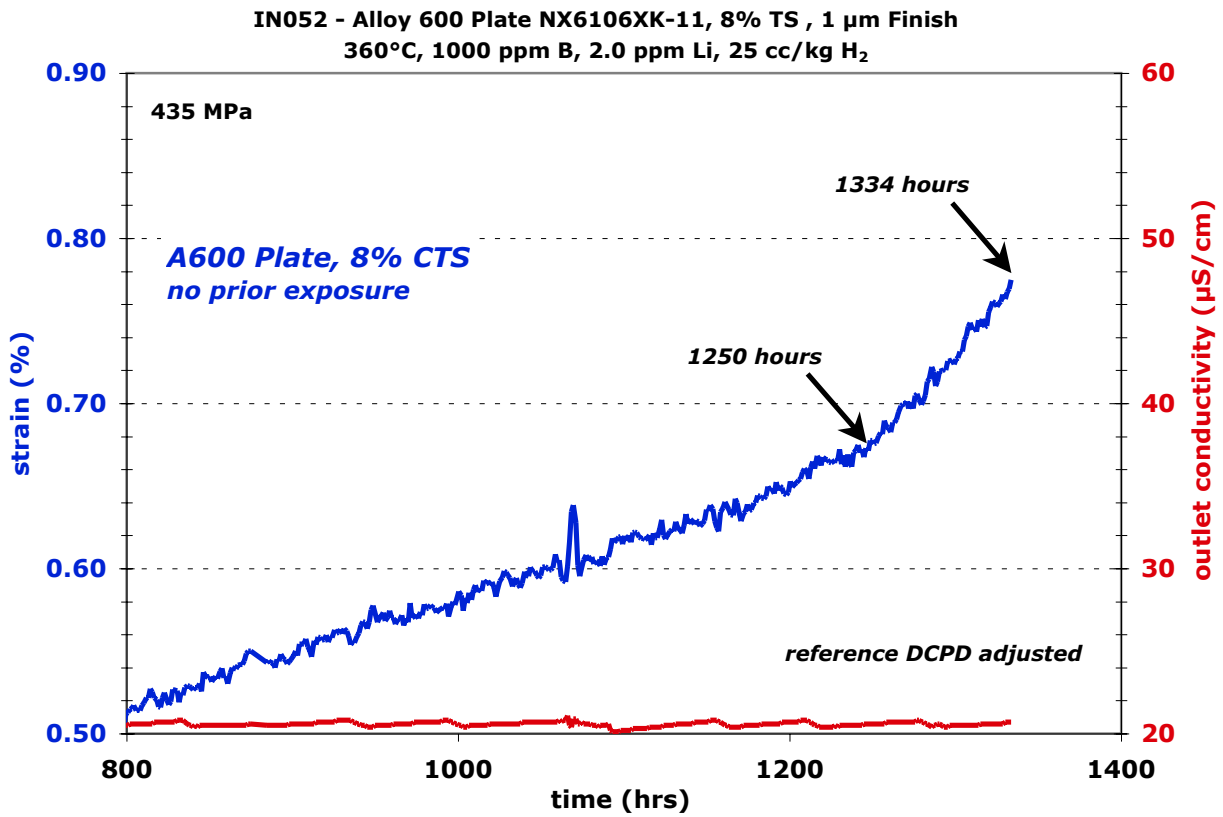

Figure 57. SCC initiation plot for the 8%TS alloy 600 specimen IN052 revealing evidence for crack nucleation at ~1250 hours.

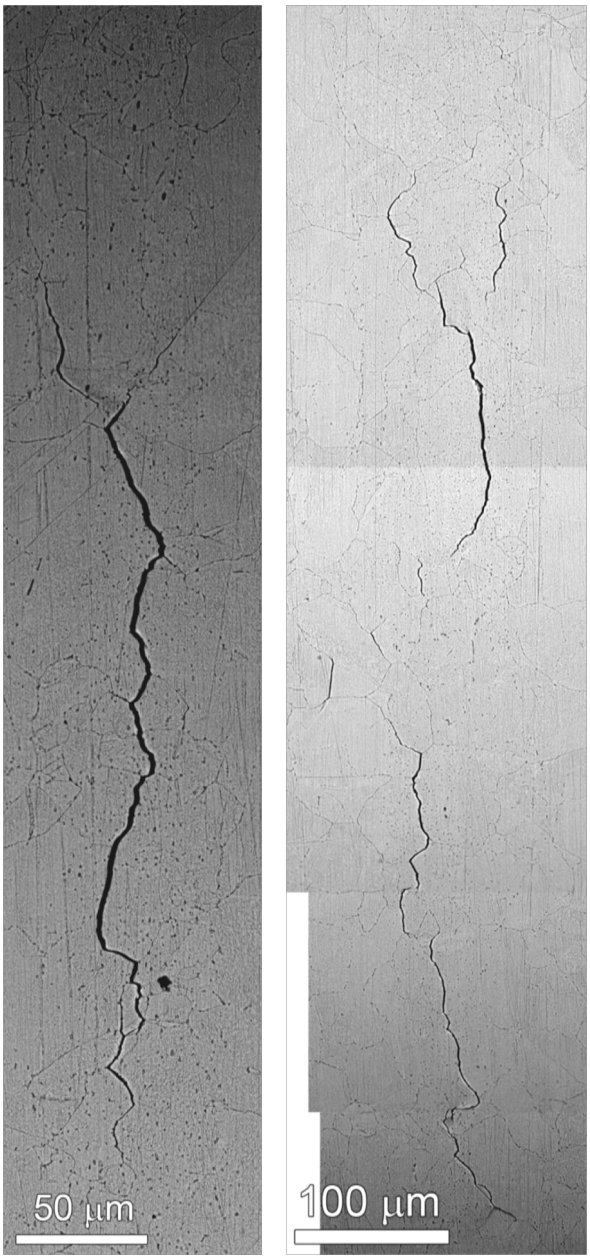

Figure 58. SEM-BSE images of the two primary IGSCC cracks identified on the IN052 gauge.

SCC Initiation Testing of As-Received Alloy 600

Testing is underway on nine as-received alloy 600 specimens representing three different heats of material. As of this time, none of the specimens have shown a positive indication of initiation with six of the nine specimens having surpassed 3400 hours of exposure. However, mid-test surface examinations have revealed that cracks are present in many of the specimens.

As-Received Plate Heat NX6106XK-11 Specimens (IN013, IN014 and IN015)

These three specimens were cut from mill-annealed alloy 600 plate (heat NX6106XK-11) with all three polished to a 1 µm finish and then a 60 grit SiC sandpaper finish subsequently applied to IN014 and IN015. This material when tested in a 5% or 18% CW condition (at its yield stress) underwent initiation in no more than ~2000 hours. Their first round of exposure was in the LWRS1 demonstration test for 1552 hours at their yield stress of ~310 MPa. For this exposure, only IN013 and IN014 were instrumented, and as shown in Figure 59, the non-referenced strain exhibited typical decreasing slope due to resistivity evolution of the alloy. No examinations were performed on these specimens after removal. The specimens were then transferred to the first full-scale test in LWRS1 where they received another 1840 hours of exposure at their yield stress. For this exposure, only one specimen, IN013 was instrumented, and it again exhibited a decreasing slope without any sign of SCC initiation as shown in Figure 60. Examinations of the gauge surface on the polished IN013 specimen revealed a few locations where small surface cracks ≤20 µm surface length were identified as illustrated in Figure 61. IN014 and IN015 could not effectively be examined because of their 60 grit surface finish that obscures any cracks. These three specimens will continue to be exposed in future tests.

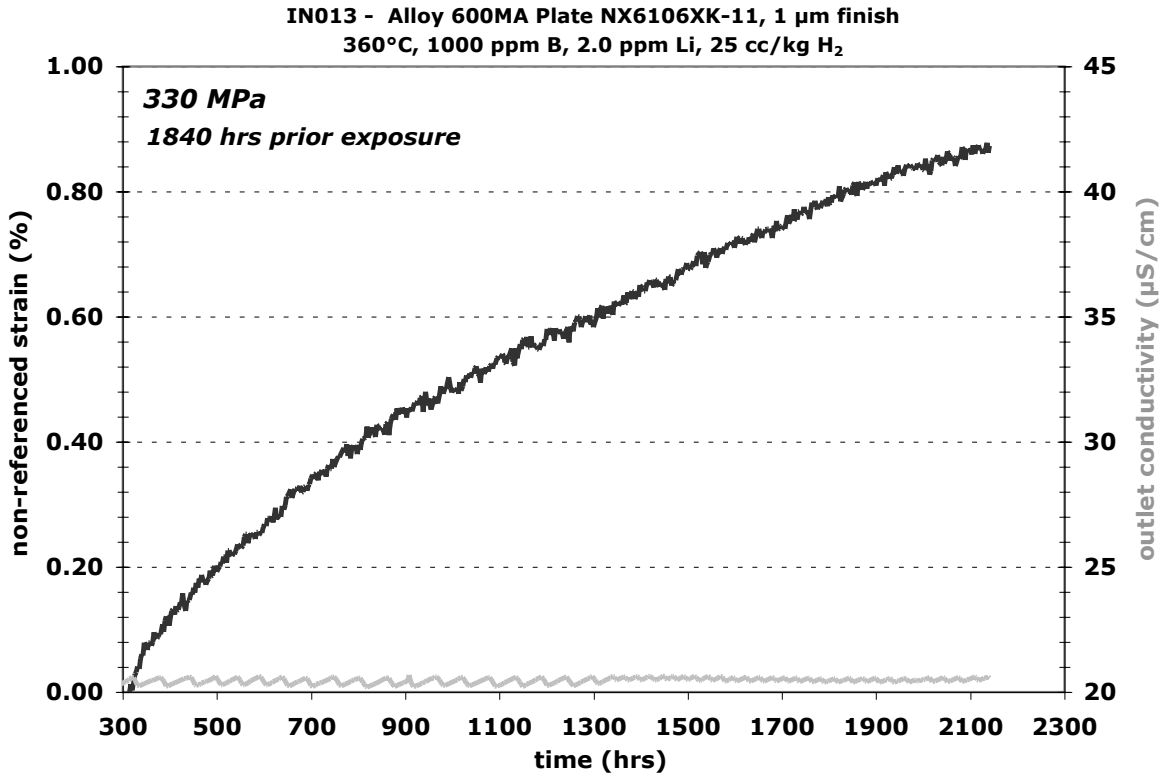

Figure 60. DCPD response for as-received alloy 600 plate specimen IN013 during its second exposure that lasted for 1840 hours giving a total exposure of 3392 hours. Neither IN014 nor IN015 were instrumented for DCPD measurement during this exposure.

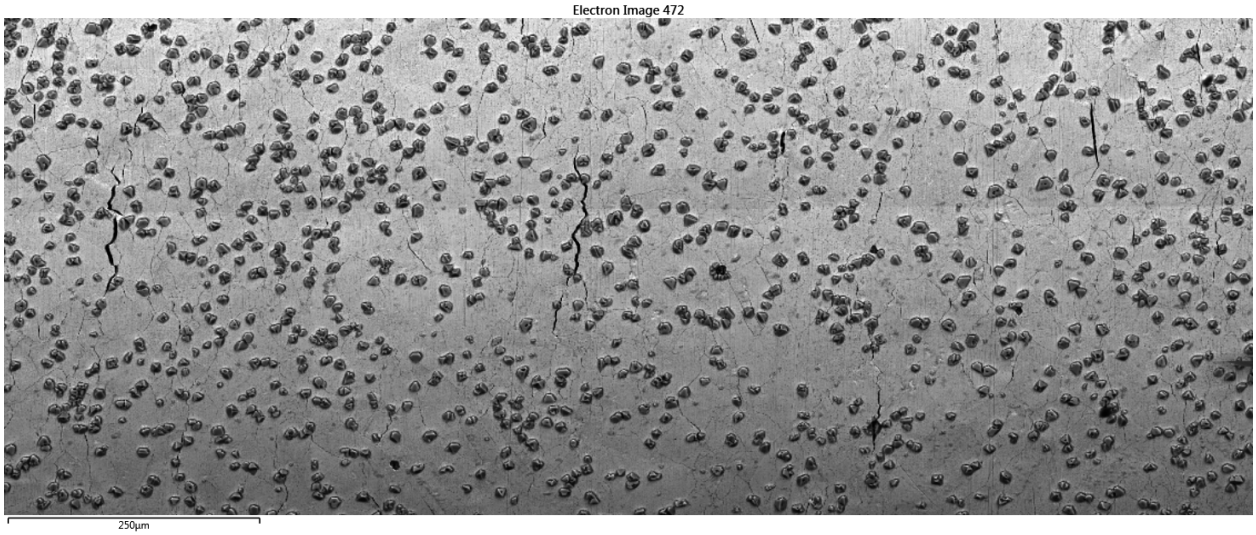

Figure 61. SEM-BES image showing examples of small surface cracks in the as-received alloy 600 plate IN013 specimen after testing in 360°C PWR primary water for a total of 3392 hours.

As-Received CRDM Heat 93510 Specimens (IN045, IN046 and IN047)

Specimens were cut from the mill-annealed alloy 600 CRDM tube (heat 93510) with IN045 and IN046 having a 1 µm surface finish and IN047 having ground finish that was applied by running a Dremel cutoff wheel back and forth across the gauge section as the specimen was spun in a lathe. This surface condition is called a "C" finish. They were loaded into LWRS1 at their yield stress of ~290 MPa for their first only exposure thus far. Two of the three specimens, IN045 and IN046, were instrumented with DCPD across their gauge section. Both specimens exhibited the expected asymptotically increasing non-referenced strain as a function of time as shown in Figure 62. All three were removed after 1840 hours of exposure, and examinations of the gauge surface on the polished IN045 specimen did not reveal any indication of cracking, nor were there obvious regions of IG attack. These specimens will be further exposed in a future test.

Service CRDM Heat M3935 Specimens (IN048, IN049 and IN050)

The last three as-received materials undergoing testing were cut from Davis Besse CRDM Nozzle #1 from the original reactor RPV head (heat M3935). The gauge section for specimen IN048 was prepared to a final 1 µm finish, while the gauge section of the IN049 and IN050 were prepared to a "C" finish as previously described. The yield strength for this large grained material was very low at 240 MPa. Two of the three specimens were instrumented for DCPD across their gauge when they were loaded into LWRS1. These specimens exhibited a different non-referenced strain response than the other non-cold worked alloy 600 specimens. Rather than exhibiting an asymptotically increasing strain, both instrumented specimens exhibited an approximately steadily increasing strain with test time as shown in Figure 63.

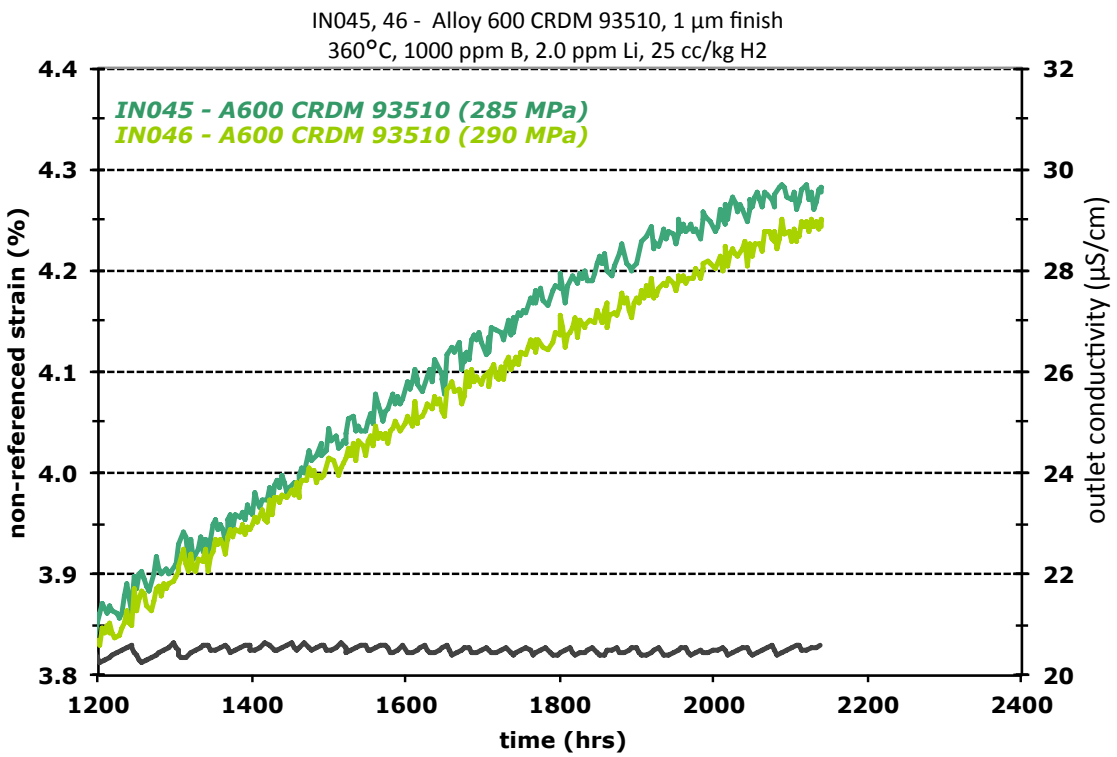

Figure 62. DCPD response for as-received alloy 600 CRDM specimens IN045 and IN046 during their first exposure in 360°C PWR primary water. IN047 was not instrumented in this exposure.

This unique response was thought to be due, in part, to the long PWR exposure causing significant evolution of the resistivity change that occurs in these materials. However, a fully evolved resistivity change would suggest that the specimens should exhibit little or no non-referenced strain, but instead, they underwent rather significant strains of ~0.3-0.6%. Assuming that there was little or no resistivity evolution, these observed strains should be due to creep. A unique aspect of this material is an extremely large grain size ranging from ~150 µm to 400 µm. This may be a factor in the apparent creep strains. Another possibility is that IG cracking began from almost the moment when the test was started (similar to when this material was tested in the 20%TS condition) and this response represents crack nucleation and short crack growth.

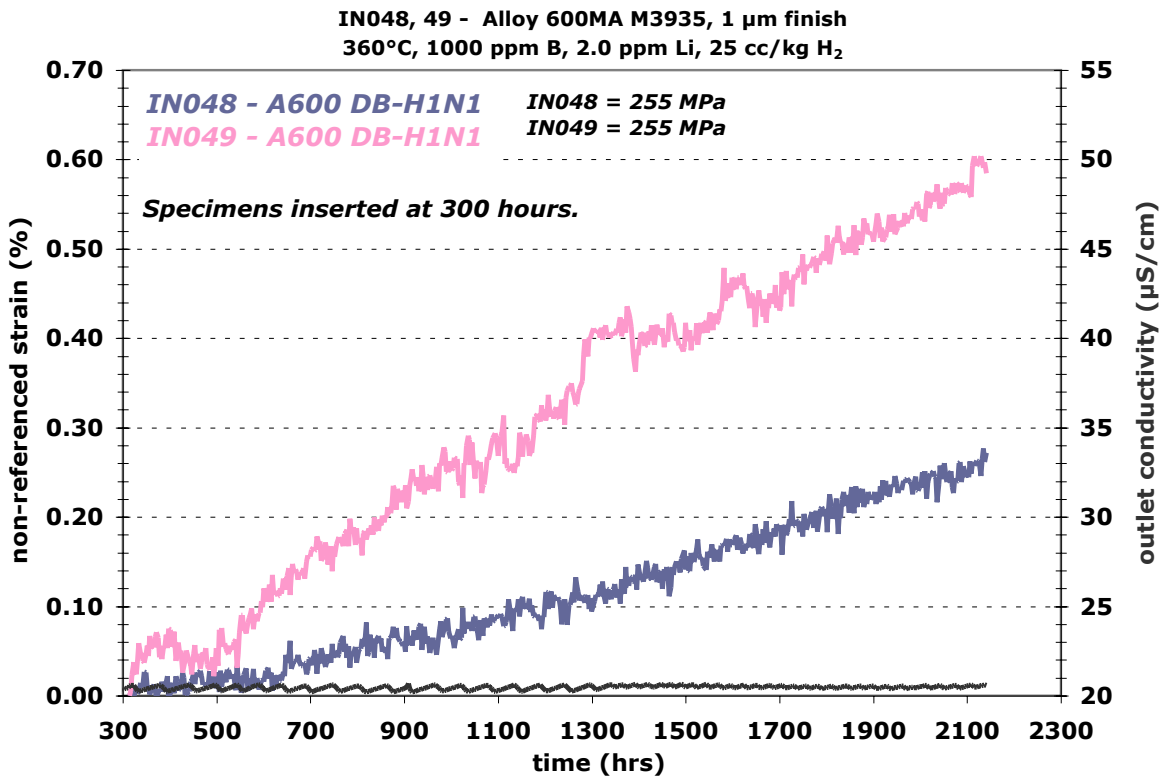

Figure 63. DCPD response for the two instrumented alloy 600 CRDM specimens from PWR service (IN048 and IN049) during their first exposure in 360°C PWR primary water for 1840 hours.

SEM examinations of the polished IN049 gauge surface after this exposure to a total of 1840 hours at load revealed several IG cracks up having an observable length of ~100-200 µm. Examples of these cracks are presented in Figure 64 and were detected in all three rotations of the specimen. These observations were somewhat surprising due to the low stress and the material being in the least susceptible (non cold worked) condition. Depths of these IG cracks were not determined, and it was decided to continue testing in one of the smaller SCC initiation test systems.

The IN048, IN049 and IN050 specimens were reloaded in series under identical 360°C PWR primary water conditions and yielding was identified in one of the three specimens at a load corresponding to an applied stress of 240 MPa. This was slightly below the previous load corresponding to an applied stress of 255 MPa, but this may be due to a slight difference in autoclave pressure that affects the pullrod tare load (in the range of 5-10 lbs). This second exposure is ongoing with the current response shown in Figure 65. Reference adjusted DCPD-indicated strain can be seen to increase with time for all three specimens, however the rate of increase has decreased slightly and does not provide evidence for growing SCC cracks in the tensile specimens. Current plans are to remove these specimens for additional SEM characterizations after ~4000 hours if initiation is not identified by in-situ DCPD.

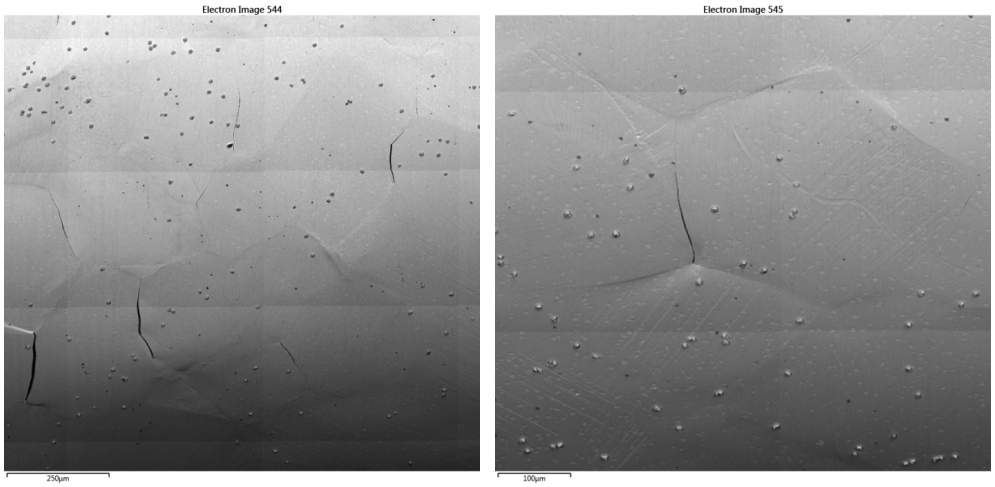

Figure 64. Examples of apparent SCC cracks in the IN049 specimen after the demonstration test exposure for 1840 hours under constant load at the yield stress in 360°C PWR primary water.

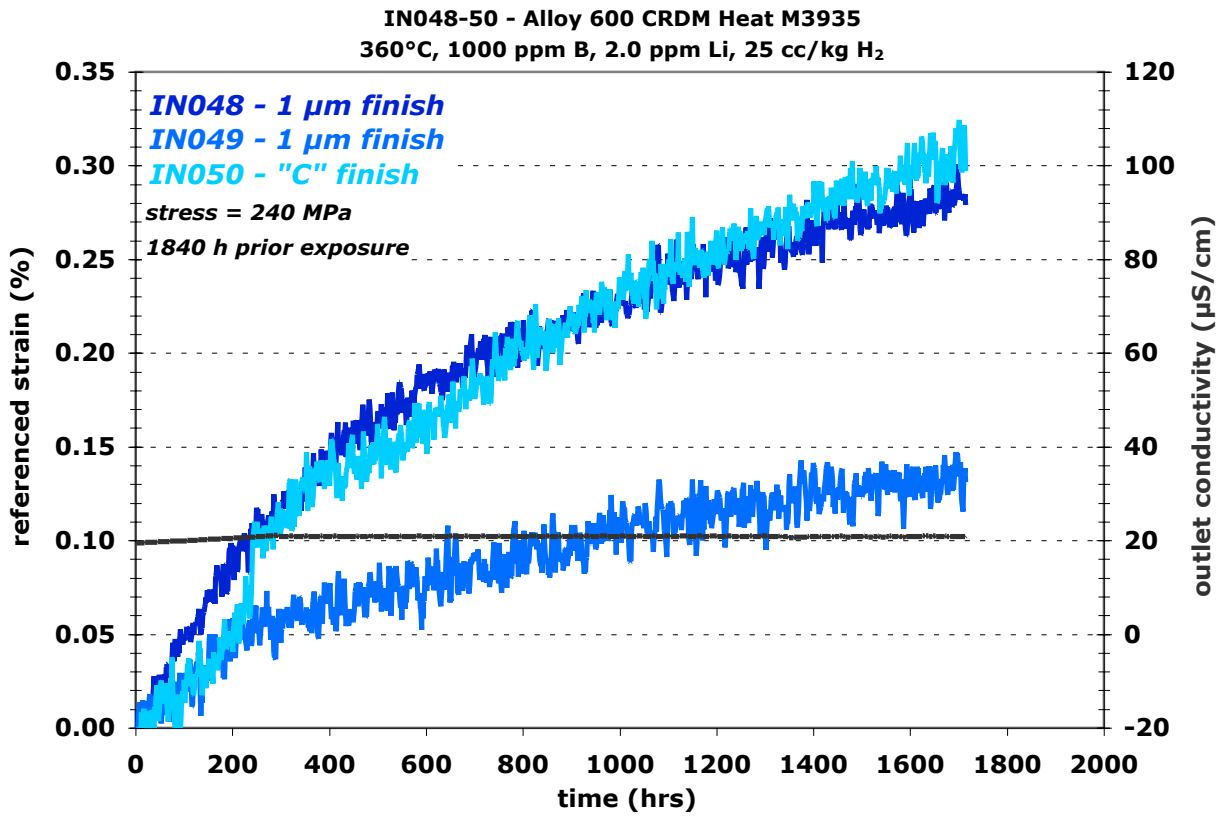

Figure 65. DCPD response for the alloy 600 CRDM specimens from PWR service (IN048, IN049 and IN050) during the ongoing second exposure in 360°C PWR primary water.

Discussion of Alloy 600 SCC Initiation Results

Tests on cold-worked alloy 600 materials have established the capability to measure SCC initiation in 360°C simulated PWR primary water. Preliminary tests have begun to build a baseline response for alloy 600 and determine critical DCPD detection limits. A summary of the alloy 600 test specimens and results are presented in Table 4. SCC initiation has been detected and characterized for 8 constant load, SCC initiation tests on 3 cold-worked alloy 600 heats in 360°C simulated PWR primary water. Nine additional tests are ongoing for long times on as-received, non cold-worked materials. While this test matrix is not sufficient to fully establish alloy 600 behavior or gain a solid understanding of SCC nucleation processes, key basic information has been obtained. The relationship between SCC initiation time and applied stress is shown in Figure 66(a) and to the level of cold work in Figure 66(b). It is notable that all alloy 600 materials with cold work (loaded to their yield stress) have initiated in less than 2200 hours, while no initiation has yet been observed in non-cold worked materials, some of which are have reached exposure times >3600 hours. However, small microscopic surface cracks have been observed in the non-CW materials that have not yet transitioned to macroscopic, growing SCC cracks, even in the service heat (M3935) that exhibited very high PWSCC CGRs at 325°C [13,14]. The initiation time data trend versus stress and plastic strain is in excellent agreement with results on tensile specimens reported by KAPL [3]. In addition, the critical applied stress intensity for alloy SCC initiation is consistent with CGR vs K trend line in MRP-55 [11].

Table 4. Summary of alloy 600 SCC tests and measured initiation times.

Spec. ID	Material Type	Heat Number	CW level	Finish	Applied Stress (MPa)	Initiation Time (h)
IN002	MA Plate	NX6106XK-11	18% TS	1200 grit	740	2025
IN003	MA Plate	NX6106XK-11	18% TS	1 µm	740	1775
IN016	MA Plate	NX6106XK-11	19% CR	1 µm	610	1522
IN017	MA Plate	NX6106XK-11	19% CR	60 grit	610-634	1787
IN018	MA Plate	NX6106XK-11	19% CR	60 grit	610-634	1715
IN022	MA CRDM	M3935	20% TS	1 µm	420	385
IN052	MA Plate	NX6106XK-11	8% TS	1 µm	435	1250
IN023	CRDM	93510	5-7% TS	1 µm	425-445	2183
IN048	MA CRDM	M3935	AR†	1 µm	240-255	NI* (3600)
IN049	MA CRDM	M3935	AR	1 µm	240-255	NI (3600)
IN050	MA CRDM	M3935	AR	"C"	240-255	NI (3600)
IN013	MA Plate	NX6106XK-11	AR	1 µm	330	NI (3392)
IN014	MA Plate	NX6106XK-11	AR	60 grit	330	NI (3392)
IN015	MA Plate	NX6106XK-11	AR	60 grit	330	NI (3392)
IN045	CRDM	93510	AR	1 µm	290	NI (2140)
IN046	CRDM	93510	AR	1 µm	290	NI (2140)
IN047	CRDM	93510	AR	"C"	290	NI (2140)

† AR = as-received condition, no cold work.
* NI = no initiation, ongoing test. Time in parenthesis is the total accumulated time.

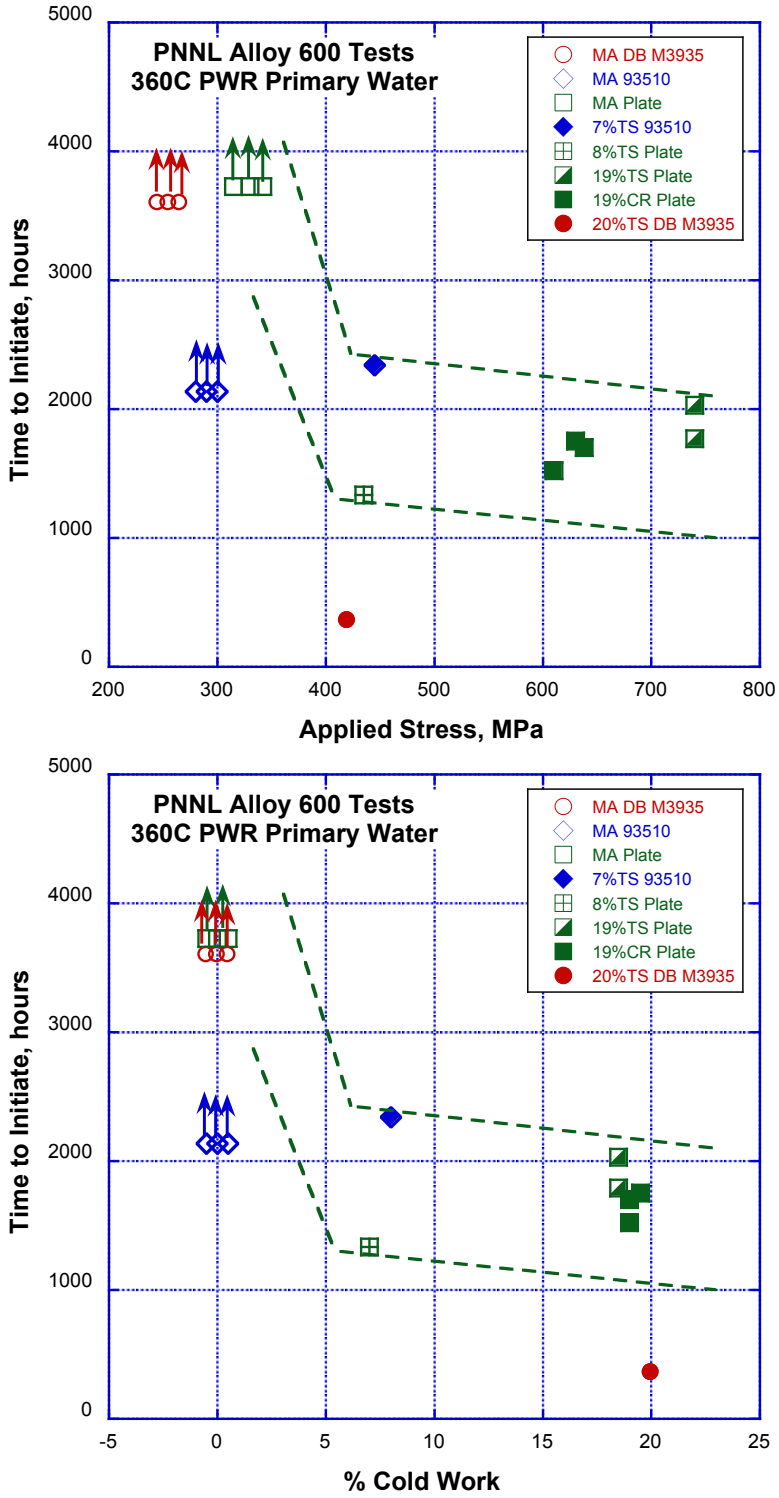

Figure 66. Summary of PNNL SCC initiation test results for alloy 600 heats showing no failures for as-received materials at applied stresses below ~400 MPa. All specimens were tested at their yield strength.

Processes Controlling SCC Initiation in Alloy 600

Extensive IG attack on grain boundaries intersecting the surface was found on most alloy 600 specimens and acts as a precursor to detectable IGSCC initiation. More research is required to obtain evidence of what is happening during this evolution to detectable crack depths, but definite stress-assisted IGA occurs in these alloy 600 heats and can lead to shallow crack formation. Post-test examinations after DCPD initiation detection have revealed that crack lengths *on the surface* are typically up to ~200 µm. However, a typical *crack depth into the specimen* has yet to be established. The one extensive observation revealed a maximum crack length of ~150 µm, but is believed to be <50 µm in other specimens. A key ongoing activity is more examinations to better determine this critical detection depth.

In order for DCPD to detect initiation, the cracking component of the DCPD signal must be discernable above the component of the DCPD signal due to creep and resistivity evolution. This can be accomplished in two ways. The first is that the increase in DCPD voltage due to a unit change in crack length would have to be very large. A slow growing crack with this attribute would be readily detected above the creep and resistivity evolution components. If the increase in DCPD voltage due to a unit change in crack length is small, then crack growth would have be rapid enough to cause a sufficient increase in the DCPD signal to be detectable above creep and resistivity evolution components. It is thought that this latter scenario best describes what is taking place when SCC initiation is detected by DCPD.

Evidence for this behavior can be seen in the rate of change of the DCPD signal as crack initiation becomes detectable. In the more highly cold-worked materials such as the 20%TS CRDM tube (Figure 27) or the 19%CR plate (Figures 38, 40 and 41), the initiation response is very dramatic with progression to potential failure taking place within a few days. The lower cold-worked materials, such as the 7%TS strained CRDM (Figure 53) or the 8%TS plate (Figure 57), exhibit a progression from initiation to potential failure that takes place over a period of weeks. This varied response results from differences in the material SCC growth rates under the given test conditions. A number of factors may play a role, but two factors are believed to be the most relevant: (1) the highly cold-worked materials are tested at a higher applied stress (equivalent to its yield stress) and (2) SCC growth rates increase with the degree of cold work. As a result, the transition from a nucleated surface crack to short/long crack growth is much easier for the highly cold-worked materials under a higher applied load. Secondary factors may have an influence including crack-tip blunting that may be more pronounced in the lower strength materials. Blunting would tend to reduce the crack-tip stress intensity and delay the transition to SCC growth.

Experiments have not been performed to try to determine the relative role of these possible contributions, but the observation of SCC initiation correlating to surface cracks ~200 µm in length and up to ~150 µm in depth (for IN003) agrees well with the estimated build up in stress intensity to values of ≥10 MPa√m from finite element modeling. Thus, the current hypothesis is

that stress-assisted IGA drives the formation of shallow precursor cracks, and their conversion to a fully initiated SCC crack takes place when the stress intensity reaches a sufficiently high value to drive stable SCC growth. This more readily occurs in higher strength materials for the reasons just described and is pictorially represented in Figure 67. These aspects are consistent with that given by LeHong [15] for a combination of constant load and constant extension rate tests on alloy 600.

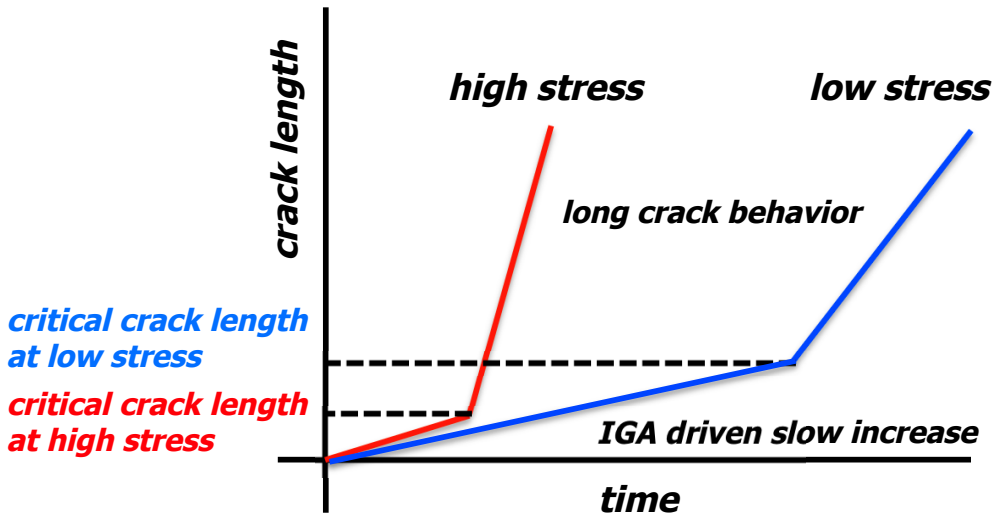

Figure 67. Qualitative representation of possible differences in initiation response between a material in a low cold work and a high cold-work condition that are tested at their yield stress.

Several experiments could be performed to help better understand the relative roles. Perhaps the most important is to determine the critical stress intensity for SCC initiation. For susceptible alloy 600 and alloy 182, IG attack occurs without external stress and can be accelerated with applied stress. Therefore, it is essential to understand the transition from the grain boundary degradation rate at low stress to stable IGSCC rates that increases with stress intensity. This can be done for any specific heat by performing SCC crack-growth-rate tests at low stress intensities. Because of the expected low CGRs, such testing would require extreme patience to obtain representative response. Previous research suggests that SCC-susceptible alloy 600 will exhibit propagation rates of ~$5x10^{-9}$ mm/s at stress intensities of 10-15 MPa√m [11,13]. The exact behavior at even lower stress intensities is not known, but the SCC growth rate will continue to decrease and should approach the rate of stress-assisted IG attack that is probably on the order of $1x10^{-9}$ mm/s [15,16]. Quantifying this behavior can provide the basic controlling information to understand IGSCC initiation response in alloy 600. With this information established for a specific alloy 600 heat, tensile initiation tests can be performed on cold-worked materials as a

function of cold work (yield stress) and applied stress (fraction of its yield stress) enabling the influence of applied stress to be isolated from the influence of the cold-worked microstructure.

A fundamental need to understand precursor damage development in alloy 600 (and alloy 182) requires a better understanding of its susceptibility to IG attack and the influence of applied stress on the grain boundary degradation kinetics. Time dependent IG attack can be determined as a function of applied stress and establish baseline response at low stress intensities. In addition to this baseline behavior at one temperature and one dissolved hydrogen concentration (ECP), it will be important to establish IG attack and SCC growth response as a function of these key variables in order to quantify an effective model for SCC initiation.

Effect of Surface Conditions on SCC Initiation

The available data indicate a consistent trend for the ground specimens to initiate slightly after the polished specimens. The few post-test microstructural observations have been performed suggest that additional time is required for corrosion to proceed through the ground region. Several possible reasons for this exist. For less aggressive grinding (e.g., 1200 grit), a thin layer of recrystallized nanocrystalline grains are created at the surface and may accelerate Cr diffusion to the surface producing a less porous, more protective oxide. More aggressive grinding produces more complex, near-surface damage microstructures (Figure 43 and 44) that promote corrosion throughout the ground layer and delay water access to bulk grain boundaries. In comparison, a highly polished surface ensures that all grain boundaries reaching the surface are exposed to water. As a result, high-energy grain boundaries have direct access to corrosion environment and IG attack begins immediately on exposure. Morris, et al [17] examined the effect of surface condition on IG attack for alloy 600 in some detail and reached similar conclusions. From a testing perspective, a polished surface eliminates the complicating factors produced by the less-controlled ground surfaces and enables a better assessment of IG attack and SCC initiation as a function of the material, environment and test conditions. The polished surface also allows small surface defects and cracks to be readily detected by SEM for a detailed examination of precursor damage evolution leading SCC nucleation.

Comments on Criteria for Selecting an Initiation Time

The SCC test results on cold-worked alloy 600 materials described here consistently show a unique point in the tests where the in-situ DCPD response clearly changes from a nascent condition to a condition of accelerated crack growth. This transition appears to be related to the change from shallow surface precursor damage to well-developed SCC cracks at a stage consistent with long crack growth. The time between DCPD-observed initiation and failure is short for highly cold worked alloy 600 due to higher applied stresses and SCC growth rates, while lower cold-worked alloy 600 materials exhibit DCPD-observed crack initiation followed by slow growth due to lower applied stresses and SCC growth rates. In comparison to U-bend tests where initiation might be defined as the time for the formation of observable cracks that can happen well before conversion to long crack growth or the time for specimen failure that can

happen well after initiation, the ability of DCPD to uniquely identify the onset of conversion to long crack growth response allows a more accurate determination of actual initiation times. This point in a test is, in our opinion, the best representation of when crack nucleation has occurred as it represents the transition from SCC initiation to SCC growth and can serve the basis for modeling of SCC behavior.

Summary Comments for Alloy 600

Considerable information has been generated from these SCC initiation tests on alloy 600. The details of initiation processes and what factors play a role in SCC crack formation remain a critical focus of the ongoing and future research in this project. More extensive destructive examinations are needed to better quantify the length, depth, and distributions of IGA and initiated SCC cracks in the alloy 600 specimens. Targeted tests will be performed to help clarify the roles of applied stress and material strength on SCC initiation, the influence of applied stress on IG attack and the transition from IG attack to SCC growth at low stress intensities. Although these experiments will be on alloy 600 materials, they will provide critical information to understand factors that promote SCC initiation in alloy 690.

SCC Initiation Tests on Alloy 690 Materials

Alloy 690 Materials Information and Specimens

Six commercial alloy 690 heats were chosen for characterization and crack initiation testing: three CRDM heats from Valinox, Sumitomo and TK-VDM (Doosan) along with three plate heats from ATI Wah Chang (ANL), ATI Allvac B25K (GE) and TK-VDM. Heat designations, bulk compositions, material conditions and microstructural information on these materials are summarized in Tables 5 and 6. A more detailed explanation of the first three commercial alloys can be found elsewhere [5] along with a summary of their SCC response. Grain structure and carbide morphology images for the second set of three commercial alloy 690 materials (i.e., Sumitomo, Doosan and TK-VDM) are shown in Figures 68 and 69.

Table 5. Alloy 690 Materials

Material and Heat Number	Description	Composition, wt%	Heat Treatments
Valinox Alloy 690TT RE243	CRDM Tube 2360 1.4" wall	Ni-28.9Cr-10.4Fe-0.02C-0.3Mn-0.35Si-0.14Al-0.23Ti-0.024N-0.008P-0.0005S	1122°C/~1 min, WQ + 716-725°C/10.5 h, air cool
ANL Alloy 690MA NX3297HK12	ATI Wah Chang 2.125" Plate	Ni-30.8Cr-8.5Fe-0.04C-0.33Mn-0.02Si-0.18Al-0.27Ti-0.037N-0.0006S-0.006P	1038°C/2 h, air cool (MIL-DTL-24802)
GE Alloy 690MA B25K	ATI Allvac 3.25" Plate	Ni-29.3Cr-9.2Fe-0.034C-0.22Mn-0.06Si-0.26Al-0.37Ti-0.026N-0.006P-<0.0003S	996°C/0.33 h, air cool
Sumitomo Alloy 690TT E67074C	CRDM Tube 1.31" wall	Ni-29.8Cr-9.8Fe-0.020C-0.29Mn-0.23Si-0.0002S	725°C/10 h/AC
TK-VDM (Doosan) Alloy 690TT 133454	CRDM Round Bar 6.0" OD	Ni-29.1Cr-8.9Fe-0.020C-0.26Mn-0.29Si-0.26Al-0.32Ti-0.02N-0.005P-<0.002S	1045°C/3.9 h/WQ + 720°C/10 h/AC
TK-VDM Alloy 690TT 114092	Plate	Ni-29.2Cr-9.5Fe-0.020C-0.25Mn-0.26Si-0.32Al-0.36Ti-<0.002S-0.003P	1030°C/1.08 h/WQ + 715°C/10 h/AC

Table 6. Microstructure for Alloy 690 Materials

Sample	Microstructure
Valinox CRDM Tube Alloy 690TT RE243	Semi-continuous (discrete + cellular) IG carbides, few IG and matrix TiN; slightly elongated grains; grain boundary Cr depletion to ~21 wt%
GEG Bar Alloy 690MA B25K	Well-spaced IG carbides, higher density in banded areas, IG and matrix TiN, slightly elongated grains; no grain boundary Cr depletion
ANL Plate Alloy 690MA NX3297HK12	Semi-continuous IG carbides, IG and matrix TiN, no banding in SCC plane, slightly elongated grains; grain boundary Cr depletion to ~22 wt%
Sumitomo CRDM Tube Alloy 690TT	Semi-continuous (discrete + occasional cellular) IG carbides; Matrix TiN.
TK-VDM (Doosan) CRDM Bar 21-31%CF Alloy 690TT	Semi-continuous IG carbides; Matrix TiN
TK-VDM Plate Alloy 690 TT	Semi-continuous IG carbides, Matrix TiN

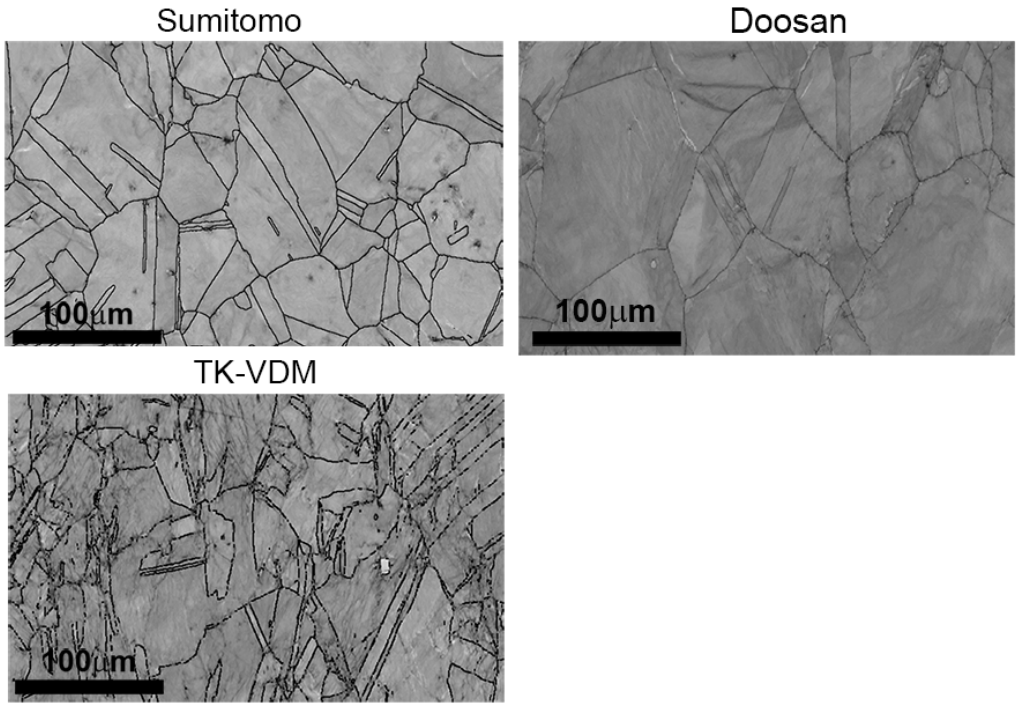

Figure 68. EBSD pattern quality images showing the grain size and microstructure of the Sumitomo, Doosan and TK-VDM materials.

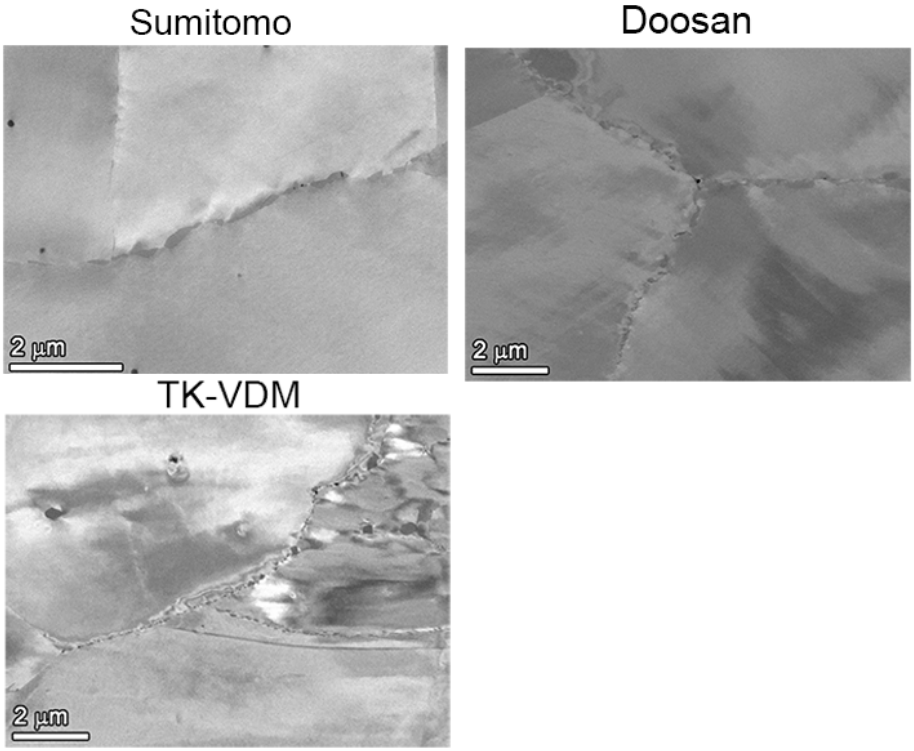

Figure 69. SEM-BSE micrographs showing carbide microstructure of the Sumitomo, Doosan and TK-VDM materials.

Overview of Alloy 690 Corrosion Test Results

Alloy 690 has been found to be highly resistant to SCC initiation and propagation in PWR primary water environments both from service experience and laboratory testing. This enhanced corrosion resistance is typically accepted as being the result of a protective Cr-rich oxide that forms over the surface. Surface science experiments (e.g., x-ray photoelectron spectroscopy, secondary ion mass spectroscopy, etc.) have illustrated the existence of this behavior in both PWR primary water conditions and supercritical water, however these analyses focus on overall bulk surface oxidation [18-20]. In order to better understand the microstructure of these films, electron microscopy analysis has been performed to achieve the vertical spatial relationships of the oxides formed to the exposed bulk surface [18,21-25]. From these experiments, the corrosion has been described as having a bi-layer structure, consisting of external and internal oxide layers. The external layer, typically depending on dominant reactor or laboratory autoclave pressure boundary material, is comprised of faceted Ni/Fe rich spinels that have a cube/cube orientation relationship with the internal layer. The internal layer has been described as a mixed iron and nickel chromite ($Ni_{(1-x)}Fe_xCr_2O_4$) which has a cube/cube orientation to the matrix below. Selected research has identified small islands of chromia (on the order of 5-10 nm) in between the internal layer and the matrix. Lastly, there have been conflicting reports of a Cr depletion layer below the internal oxide layer [21,26-27].

Through the combination of high-resolution SEM-BSE imaging, TEM/EDS analysis and APT alloy 690 coupons exposed to simulated PWR primary water conditions, corrosion-induced surface oxidation structures are clearly shown to be different at grain boundary/surface intersections than over bulk matrix grains. In previous research, the internal layer at crack walls and polished surfaces was found to be much more complex than a single layer of oxide [23]. While the matrix surface layer most likely begins as a uniform Cr-rich mixed oxide, penetrative oxidation proceeds into the bulk grains demonstrating that a protective stable oxide does not form at these highly polished surfaces exposing grain interiors. More recent research at PNNL [28] revealed that a continuous, protective chromia film does form at the surface over high-energy grain boundaries. The overall surface oxide film characteristics for alloy 690 materials exposed to PWR primary water are pictorally illustrated in Figure 70 with a continuous Cr_2O_3 film above grain boundaries and a mixed oxide film above the matrix regions with isolated pockets of Cr_2O_3 along with filamentary oxidation into the metal.

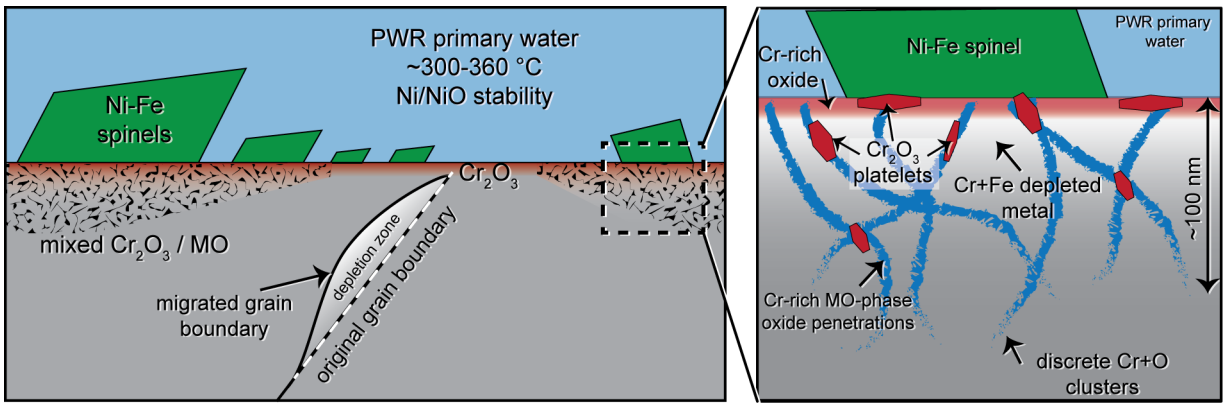

Figure 70. Enhanced Cr diffusion from grain boundaries allows protective Cr_2O_3 film (~0.5-1 µm wide) to form over grain boundary. Non-protective thin film of Cr_2O_3 and Cr rich MO forms over bulk grains due to slower Cr bulk diffusion. Oxygen diffusion through non-protective film allows penetrative oxidation to occur in bulk grains. Additionally, increased Cr diffusion continues along grain boundary to edge of protective film and forms continuous Cr_2O_3 layer between bulk and penetrative oxidation.

From these distinct microstructural features, several insights have been determined as to how grain boundaries behave when exposed to high-temperature PWR primary water conditions. There is a zone above high-energy grain boundaries where a continuous protective chromia film forms blocking IG and TG penetrative oxidation. This has been consistently observed on cross-sections of as-received and cold-worked alloy 690 materials with highly polished surfaces. It is believed that during initial exposure, Cr diffuses rapidly along the grain boundaries to the surface and forms a protective Cr_2O_3 layer that spans ~200 nm on either side of the grain boundary. Past this near-boundary region, the amount of Cr diffusing from the bulk matrix grains is not sufficient to immediately form a protective layer, and instead, a mixed oxide surface layer forms that enables local TG penetrative oxidation into the metal matrix.

In these 1000-h exposures, characterizations indicate that there are isolated islands of Cr_2O_3 and possibly of metal islands within the inner oxide above the bulk grains. If the closest metal islands were to be used as a fiducial mark in the corroded materials, the inner Cr-rich surface oxide would be somewhere between 10 to 50 nm in thickness with thicker films for the highly cold-worked materials and thinner for the as-received materials. TEM data indicate that the matrix mixed oxide inner layer is primarily an MO-structure oxide, but APT analysis has shown that chemically it relates closer to the M_3O_4 spinel. Regardless, the fact that it is not comprised of continuous Cr_2O_3 allows for O ingress and penetrative oxidation possibly along preexisting dislocation structures. This formation of Cr_2O_3 islands has been suggested previously to exist in between the internal spinel layer and the alloy 690 matrix. Exposures of surfaces at high O_2 potentials have shown similar chromia islands surrounded by a MO microstructure [29]. A critical difference between current and prior surface oxidation studies has been the initial surface condition. It is clear that deformed/disturbed surfaces promote more rapid Cr diffusion to the surface and alter formation of the Cr-rich inner layer film. It is believed that this rapid Cr

diffusion in the altered surfaces could be an explanation for reported Cr depletion layer below the inner oxide layer [25]. Experiments are underway evaluating corrosion structures in alloy 690 materials as a function of surface grinding conditions that produce a highly deformed metallic subsurface with near-surface nanocrystalline grains.

This research illustrates unique observations of the formation of surface oxide (both above grain boundaries and bulk grains) on highly polished coupons when exposed to simulated PWR water conditions at high temperatures. Understanding the resultant thin film oxide microstructures as well as Cr depletion along grain boundaries intersecting the surface provides a good basis for identifying crack initiation precursors in SCC testing. In order for IGSCC initiation to occur, the protective chromia film formed over the grain boundaries must be cracked or thinned such that water can access the Cr depleted grain boundary below. The subsurface grain boundary, which is typically depleted to 5-10 wt% Cr, should be much more susceptible to corrosion and crack nucleation. An iterative process can be envisioned where IG crack advance can proceed through the depleted grain boundary until sufficient Cr is available to reform the protective Cr_2O_3 film at the tip. The formation and growth of the chromia film would again produce a Cr depleted grain boundary ahead of the oxidation front and create a situation where the process can be repeated. A critical issue for this precursor microstructure to promote IGSCC is the applied stress and dynamic strain required to breach the protective film. Based on service experience and laboratory test results for alloy 690, it appears that local grain boundary Cr depletion near the surface is not a sufficient condition to promote a high susceptibility to SCC initiation in PWR primary water.

Experiments are underway to investigate static and dynamic loading effects on IGSCC initiation processes in alloy 690. Preliminary SCC initiation testing is described and discussed in the following section focused on cold-worked alloy 690 material conditions shown to be susceptible to SCC crack growth.

General Approach for SCC Initiation Testing for Alloy 690

Development of the DCPD tensile initiation test system and test method began with alloy 600 tests. As described in the previous section, crack initiation of cold worked alloy 600 was successfully detected in less than 2500 hours for several constant load tests where the specimens were held at the yield stress. Because cold worked alloy 690 can exhibit crack growth rates comparable to cold worked alloy 600, the initial approach for alloy 690 crack initiation testing was similar to that for alloy 600 in terms of material condition (highly cold worked), specimen surface preparation, and general test approach.

Experimentation was started on two highly cold-rolled (CR) alloy 690 materials that exhibited high SCC propagation rates (~$1x10^{-7}$ mm/s) during crack growth rate testing in simulated PWR primary water at 360°C [5]. Materials selected were the 26%CR ANL plate and the 31%CR CRDM RE243 tubing. Composition and basic microstructural information on these two heats (NX3297HK12 and RE243) was summarized in Tables 4 and 5. These two materials are unique in that SCC behavior has been evaluated at multiple laboratories and their cold-worked microstructures have been extensive characterized. Examples of the damage induced by cold rolling are illustrated in Figures 71 and 72 for the Valinox CRDM and ANL plate, respectively. The ANL material exhibited extensive permanent damage due to cold rolling including void formation at grain boundary carbide interfaces, cracked grain boundary carbides and cracked TG nitrides. Even though these voids and cracked precipitates were not directly responsible for the high IGSCC growth rates [29], this damage could make IG crack initiation more likely.

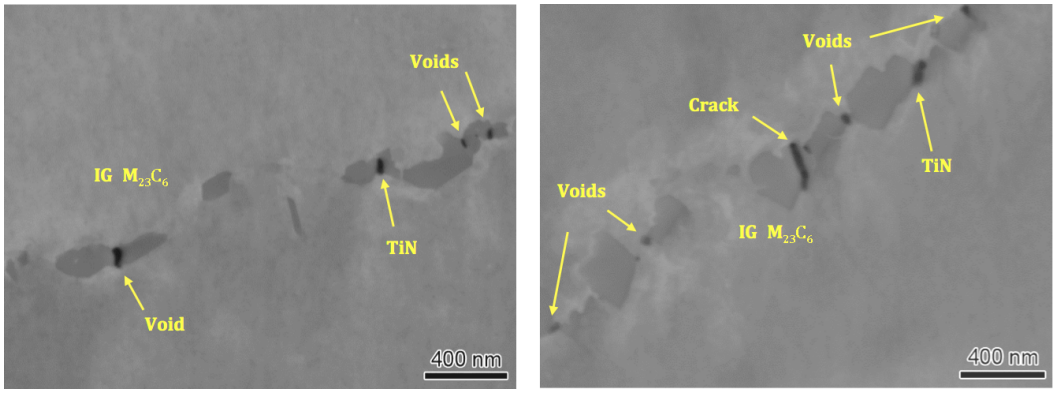

Figure 71. SEM-BSE images of the Valinox 31%CR alloy 690TT CRDM material showing voids and cracked carbides on grain boundaries in this material.

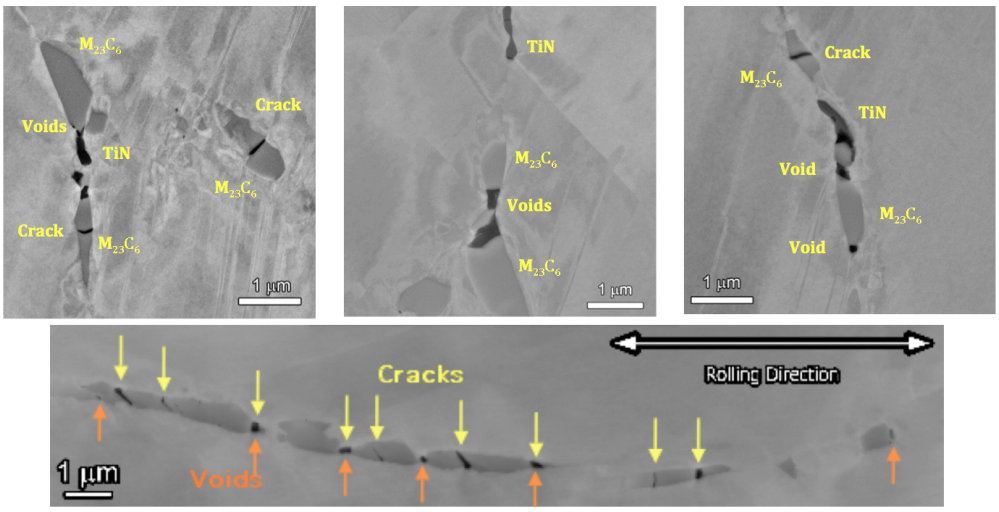

Figure 72. SEM-BSE images of the ANL 26%CR alloy 690MA plate material showing voids and cracked carbides on grain boundaries in this material.

The intent for the first tests was to start with materials highly susceptible to SCC, and run them at the highest possible stress (at the yield stress) to produce a baseline minimum crack initiation time for alloy 690. After long-term (~3600 hours) exposures had not produced crack initiation, alternate testing conditions were considered. Because unstressed samples were observed to form a protective Cr_2O_3 film formed at grain boundaries intersecting the surface, it was decided to evaluate dynamic straining as a means to accelerate the crack initiation testing process. For the CR alloy 690 specimens, it was decided to begin periodically inducing very small amounts of plastic tensile extension. Other methods (load cycling within the elastic strain region and slow, continuous plastic straining) were also explored on the tensile strained alloy 690 specimens and will be discussed below. A summary of all alloy 690 initiation tests on tensile specimens is given in Table 7 along with a description of the test approach, i.e., constant load (CL) or CL combined with occasional slow-strain-rate (SSR) deformation.

Another aspect of the crack initiation testing approach on alloy 690 has been periodic inspections of the specimens to look for initiation precursor microstructures, in particular, to look for small cracks that might not yet have been detected by DCPD. Examinations were initially limited to documenting the surface of the gauge section using SEM, however after small cracks had nucleated from corroded TiN particles, it was decided to employ FIB milling to create shallow trenches to probe the structure of these cracks in cross section. The trenches were quite small, typically ~5-10 µm wide in both directions on the surface and ~5 µm deep, and present minimal if any stress riser on the specimen or the crack. This technique enables surface and near-surface SCC precursor damage to be investigated without destructive sectioning that would render continued testing impossible.

Table 7. Alloy 690 SCC Initiation Tests on Tensile Specimens

Specimen	Material	Material Condition	Surface Condition	Applied Stress, MPa
IN006 (CL+SSR)	ANL Plate	MA + 26%CR	1 µm Polish	500-860
IN007 (CL+SSR)	Valinox CRDM	TT + 31%CR	1 µm Polish	500-905
IN009 (CL+SSR)	GE Plate B25K	MA + 18-22%TS	1 µm Polish	500
IN010 (CL+SSR)	ANL Plate	MA + 18-31%TS	1 µm Polish	500-800
IN011 (CL+SSR)	Valinox CRDM	TT + 41%TS	1 µm Polish	510
IN012 (CL+SSR)	Valinox CRDM	TT + 24%TS	1 µm Polish	510
IN024 (CL)	Sumitomo CRDM	TT + 21%CF	1 µm Polish	575
IN025 (CL)	Sumitomo CRDM	TT + 21%CF	60 grit Ground	575
IN026 (CL)	Sumitomo CRDM	TT + 21%CF	60 grit Ground	575
IN027 (CL)	Valinox CRDM	TT + 21%CF	1 µm Polish	510
IN028 (CL)	Valinox CRDM	TT + 21%CF	60 grit Ground	510
IN029 (CL)	Valinox CRDM	TT + 21%CF	60 grit Ground	510
IN030 (CL)	Doosan CRDM	TT + 21.6%CF	1 µm Polish	540
IN031 (CL)	Doosan CRDM	TT + 21.6%CF	60 grit Ground	540
IN032 (CL)	Doosan CRDM	TT + 21.6%CF	60 grit Ground	540
IN033 (CL)	Sumitomo CRDM	TT + 31%CF	1 µm Polish	690
IN034 (CL)	Sumitomo CRDM	TT + 31%CF	60 grit Ground	690
IN035 (CL)	Sumitomo CRDM	TT + 31%CF	60 grit Ground	690
IN036 (CL)	Valinox CRDM	TT + 31%CF	1 µm Polish	700
IN037 (CL)	Valinox CRDM	TT + 31%CF	60 grit Ground	700
IN038 (CL)	Valinox CRDM	TT + 31%CF	60 grit Ground	700
IN039 (CL)	Doosan CRDM	TT + 31%CF	1 µm Polish	665
IN040 (CL)	Doosan CRDM	TT + 31%CF	60 grit Ground	665
IN041 (CL)	Doosan CRDM	TT + 31%CF	60 grit Ground	665
IN042 (CL)	TK-VDM Plate	TT + 31.9%CF	1 µm Polish	680
IN043 (CL)	TK-VDM Plate	TT + 31.9%CF	60 grit Ground	680
IN044 (CL)	TK-VDM Plate	TT + 31.9%CF	60 grit Ground	680

CL = constant load; SSR = slow strain rate deformation applied during test

SCC Initiation Test Results on SCC Susceptible Alloy 690 (IN006, IN007)

As part of ongoing research for other programs, the SCC crack growth resistance of alloy 690 is being assessed [4,5]. Through this testing it has been found that the SCC susceptibility of alloy 690 greatly increases when it is cold rolled or cold forged and then crack growth tested in the pancake plane (S-L orientation for cold-rolled material). Two cold-rolled (CR) heats that exhibited high crack growth rates of ~$1x10^{-7}$ mm/s were selected for the first alloy 690 crack initiation tests. Specimen IN006 was cut from the 26%CR ANL alloy 690MA plate and IN007 was cut from 31%CR CRDM alloy 690TT tubing. Specimens were machined into the 1.2" tensile geometry so that the normal to the rolling plane was parallel to the axis of the tensile specimens, and then the gauge sections were finished with 1 µm diamond polish. The polishing process leaves minimal surface damage and SEM-BSE imaging was able to reveal the grain boundary carbide structure as shown in Figure 73. TiN particles were also observed and often had a stringer shape perpendicular to the specimen axis in the alloy 690 plate specimen, while they were typically block shaped in the alloy 690 CRDM. As will be shown later, the TiN stringers in the plate material were found to act as microcrack initiation sites during in-situ plastic straining.

The specimens were loaded in series as illustrated earlier in this report (Figure 4a). Each specimen experiences the same loads in this configuration, but stress is determined by its gauge diameter. Therefore, each specimen deforms according to where it lies on its stress versus strain curve. This test ran entirely in 360°C simulated PWR primary water with 2000 ppm of boron, 2 ppm of lithium, and a dissolved hydrogen content of 25 cc/kg (corresponding to the Ni/NiO stability line).

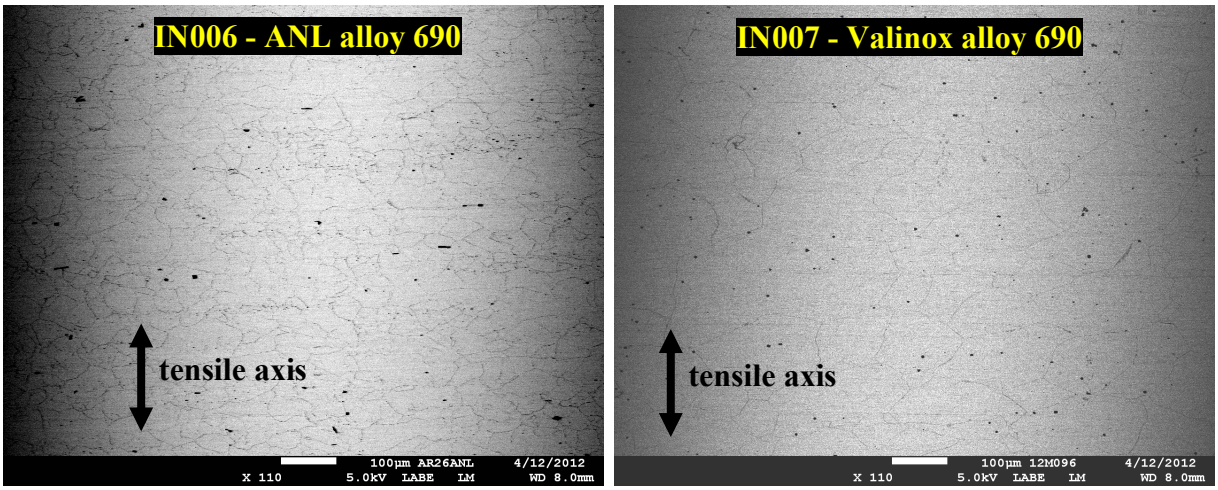

Figure 73. SEM-BSE images of a portion of the polished gauge section of IN006 and IN007 prior to testing revealing grain boundary carbides and TiN particles intersecting the specimen surface.

An overview of the entire test is summarized in Figure 74. The specimen response is plotted as strain versus time using the referenced strain value as discussed in the Experimental Details section. The stress level on the specimens is listed and "R&E" indicates that the specimens were removed and examined. The reference DCPD measurement primarily removes any phantom strains due to resistivity drift of the material, but it also partially removes elastic and creep strains as well. Increases in stress were accomplished by constant displacement rate straining at $5x10^{-4}$ s^{-1} for all but the final application of strain that was applied exclusively to IN007 (CRDM material). That final application of strain was applied at a much lower rate of ~$1x10^{-8}$ s^{-1}. The test was started at 500 MPa (~70% of the initial 360°C yield strength for the specimens) and the detailed DCPD-based strain response during the first 1000 hours is presented in Figure 75. The peak-to-peak variability in the measurements is ~0.05% strain, and trends in the strain response can be identified to approximately that same value. After 1000 hours, the specimens were removed for an initial examination. SEM backscatter images in Figure 76 show that the TiN particles in both materials had started to corrode. Neither specimen showed surface damage or cracks beyond that present in the CR materials prior to testing.

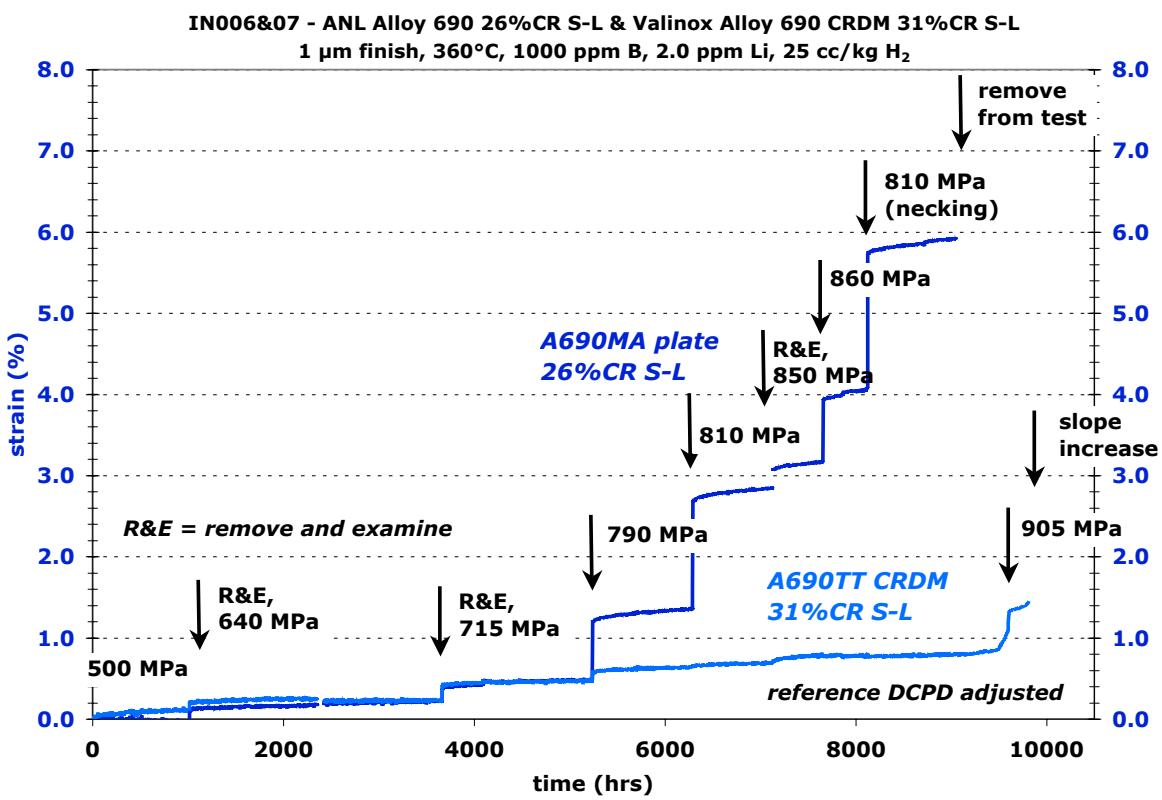

Figure 74. Overview of the test on the two cold-rolled and SCC susceptible alloy 690 specimens, IN006 and IN007. Changes in stress on the specimens are listed.

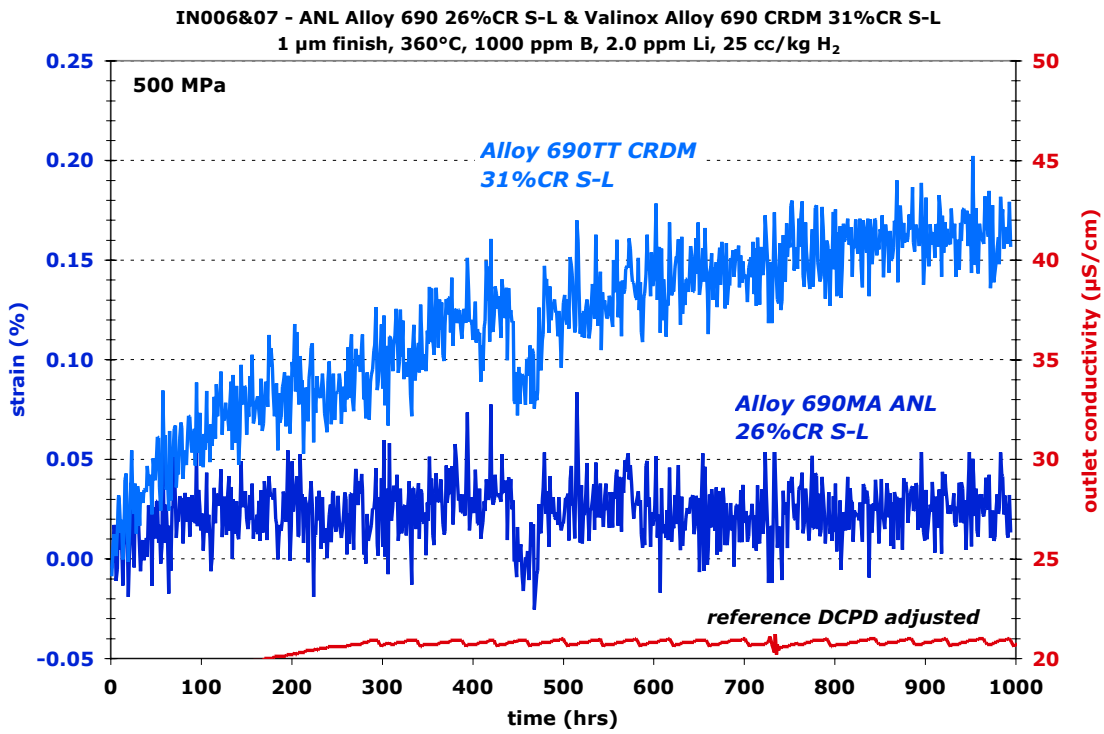

Figure 75. DCPD-based strain response for specimens IN006 and IN007 during the first 1000 hours of testing.

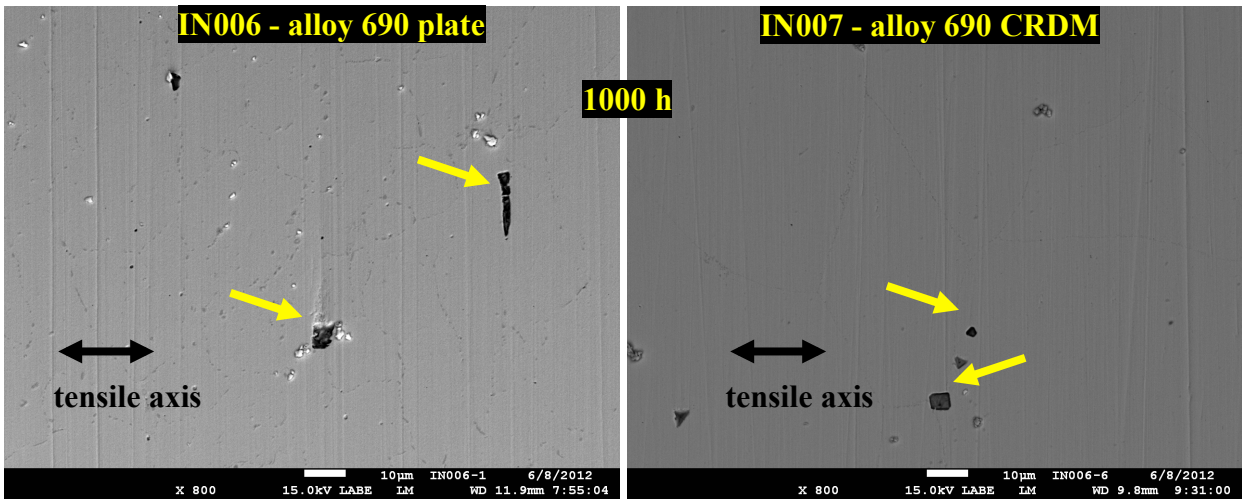

Figure 76. SEM-BSE images of the 26%CR plate and 31%CR CRDM specimen gauge sections, respectively, revealing small grain boundary carbides and larger matrix TiN particles (identified by arrows) that have partially corroded.

The test was resumed at a stress of 640 MPa, or roughly 90% of the initial yield stress of the material. This stress level was maintained for 2600 hours as shown in Figure 77, at which point the specimens were again removed and examined. Analysis of the specimens revealed that most of the TiN particles intersecting the surface were extensively corroded often leaving behind cavities. A key difference between the two materials was that small cracks were found associated with several corroded TiN stringers in the IN006 ANL plate material as shown in Figure 78(a). These cracks appeared to nucleate only off the longer TiN stringers (>15 µm) and were found to be from 2-10 µm long. They were predominantly TG, but cracks on or very near a grain boundary were occasionally observed as shown in Figure 79. No such cracks were detected off the corroded block-shaped TiN in the IN007 CRDM material (Figure 78b).

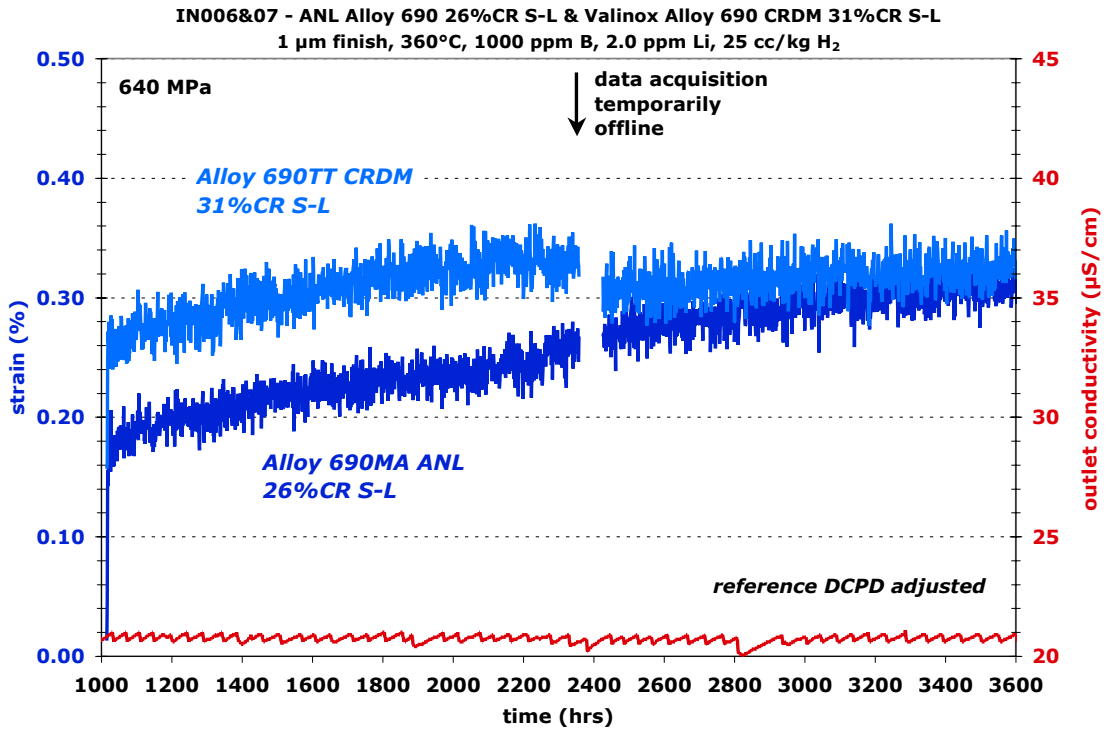

Figure 77. DCPD-based strain response for specimens IN006 and IN007 after stress increase to 640 MPa.

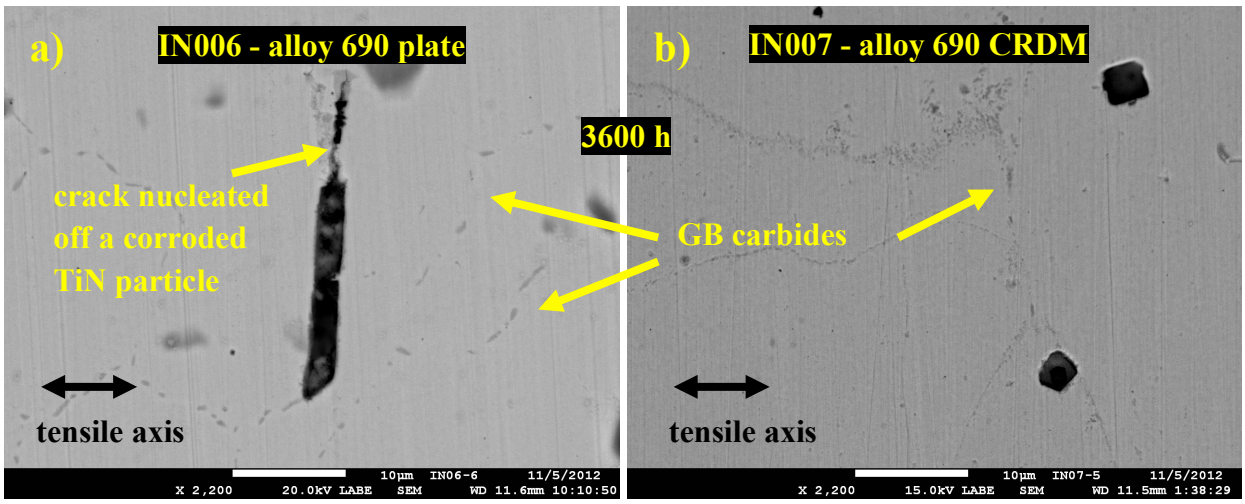

Figure 78. SEM-BSE images of the 26%CR plate and 31%CR CRDM specimens revealing grain boundary carbides and corroded TiN particles. Cracks nucleated from the ends of corroded TiN stringers were observed in the plate material while no cracking was observed in the CRDM material.

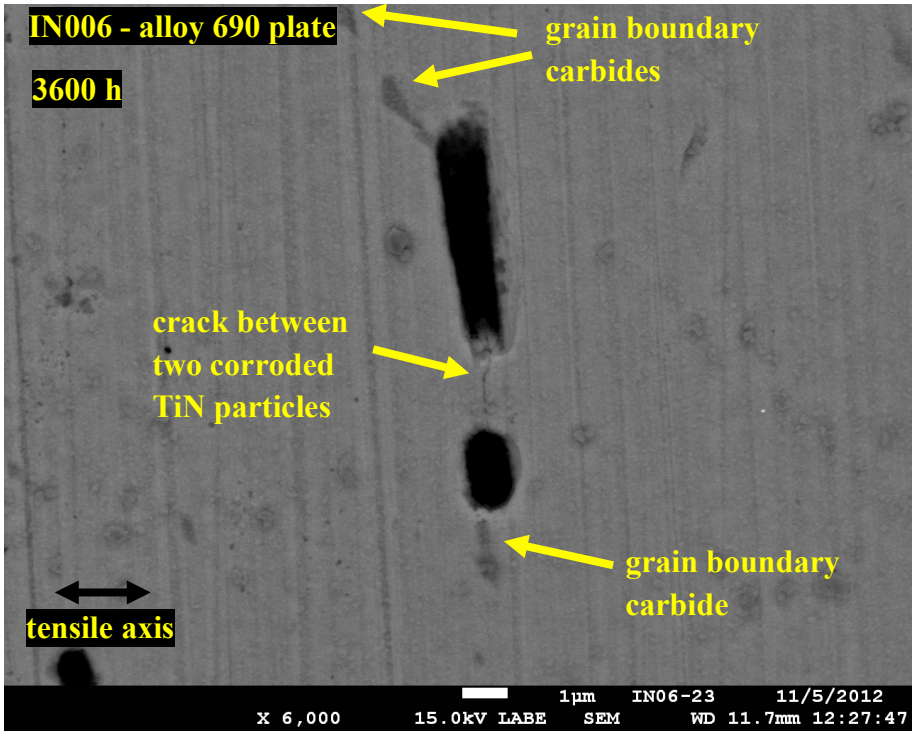

Figure 79. SEM-BSE image showing a crack between two corroded TiN particles that appears to be on a grain boundary in the 26%CR plate specimen IN006 after 3600 h.

The small cracks into the alloy 690 from the corroded TiN particles represent SCC initiation precursors, and the test was resumed with the possibility that crack nucleation and growth would be detected by DCPD for the IN006 specimen in a relatively short period of time. Upon resuming the test at 3600 h, the load was increased until a small indication of plastic yield was observed in the reloading curve resulting in applied stress of 715 MPa. As shown in Figure 80, no DCPD indication of crack initiation was observed over a subsequent period of ~1700 hours. Since this test was meant to be a first scoping experiment to assess conditions for SCC nucleation in SCC-susceptible alloy 690 materials, the decision was made to further augment the crack initiation process by increasing the applied load and inducing additional plastic strain in the specimens. As tensile straining is performed with the specimens loaded in series, both specimens are subjected to the same loads but are not constrained to strain by the same amount. The 26%CR plate specimen IN006 (which had a lower degree of cold work) yielded first, underwent ~0.6% plastic strain, and achieved a stress of ~790 MPa as shown in Figure 81. The undulations in the plastic strain curve are thought to be due to dynamic strain aging that has been observed in elevated temperature air tensile tests performed on these materials. The 31%CR CRDM specimen IN007 showed slight non-linear response, but did not undergo obvious plastic deformation despite reaching nearly the same stress level.

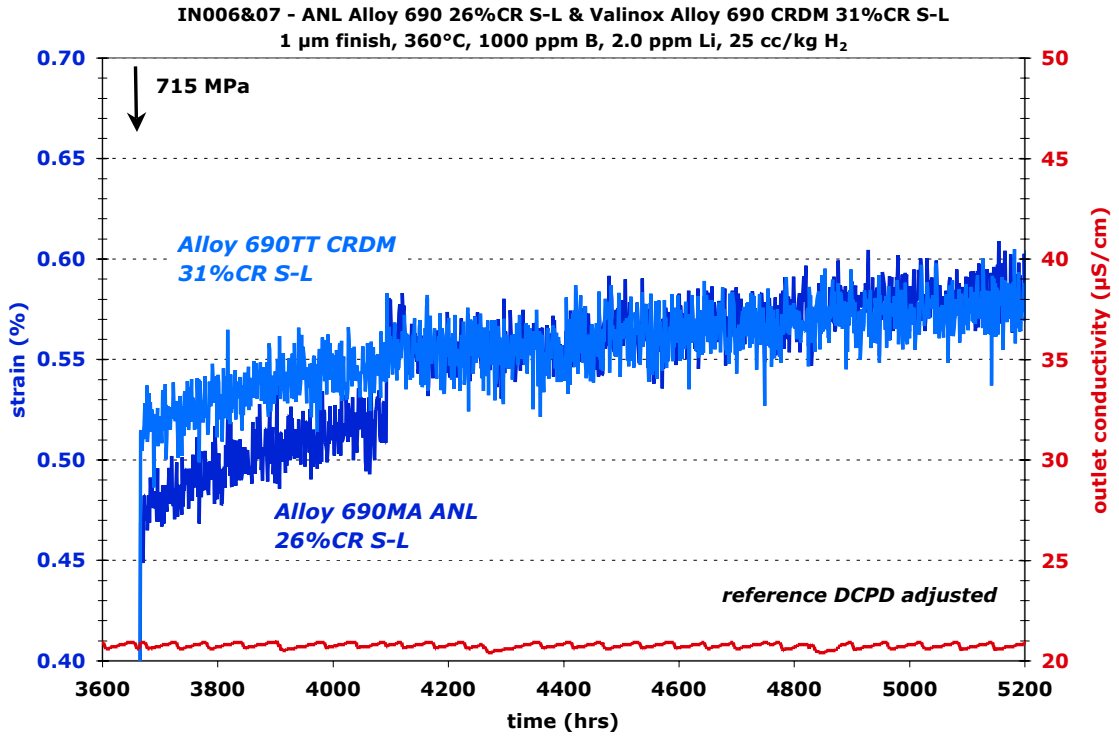

Figure 80. DCPD-based strain response of the two cold-rolled alloy 690 specimens (IN006 and IN007) from 3630 - 5200 hours after stress increase to 715 MPa.

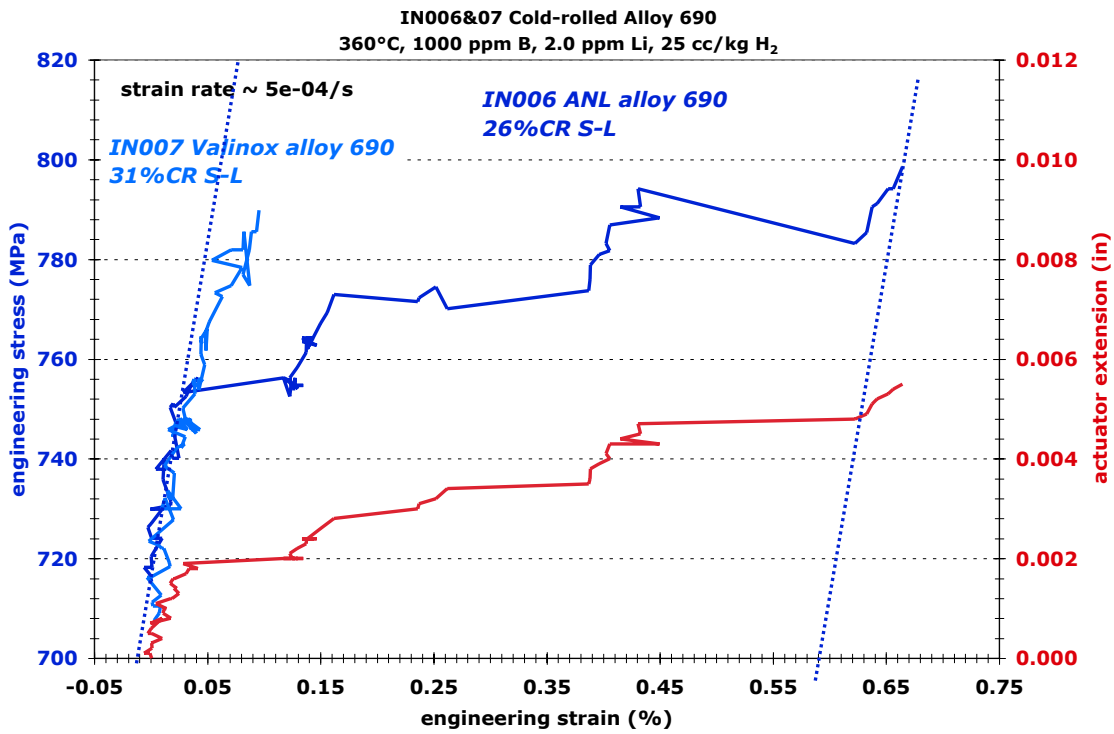

Figure 81. Tensile straining performed on the alloy 690 materials at ~5300 hours. The 26%CR plate material (IN006) underwent approximately 0.6% plastic strain while the 31%CR CRDM material (IN007) did not yield.

After application of this more significant level of plastic strain in the 26%CR plate specimen that was observed to have cracks nucleated off corroded TiN stringers in the 3600 hour observation, there was a renewed expectation that measureable SCC crack initiation would occur quickly. However, once again no indication of SCC crack initiation was detected during the following ~1000 hour exposure under constant load at the yield stress as documented in Figure 82. Tensile straining over a period of ~1 hour was again applied as shown in Figure 83. The 26%CR plate specimen IN006 underwent an additional ~1.2% plastic strain, while the 31%CR CRDM specimen IN007 did not yield. In the prior straining events, the 26%CR plate specimen underwent a slight amount of strain hardening but this time the specimen exhibited an overall flat plastic strain curve indicating that geometric instability (necking) could begin during any subsequent straining. Despite the overall flat strain hardening response, a slight increase in stress was achieved by stopping the straining process at a peak in a strain serration.

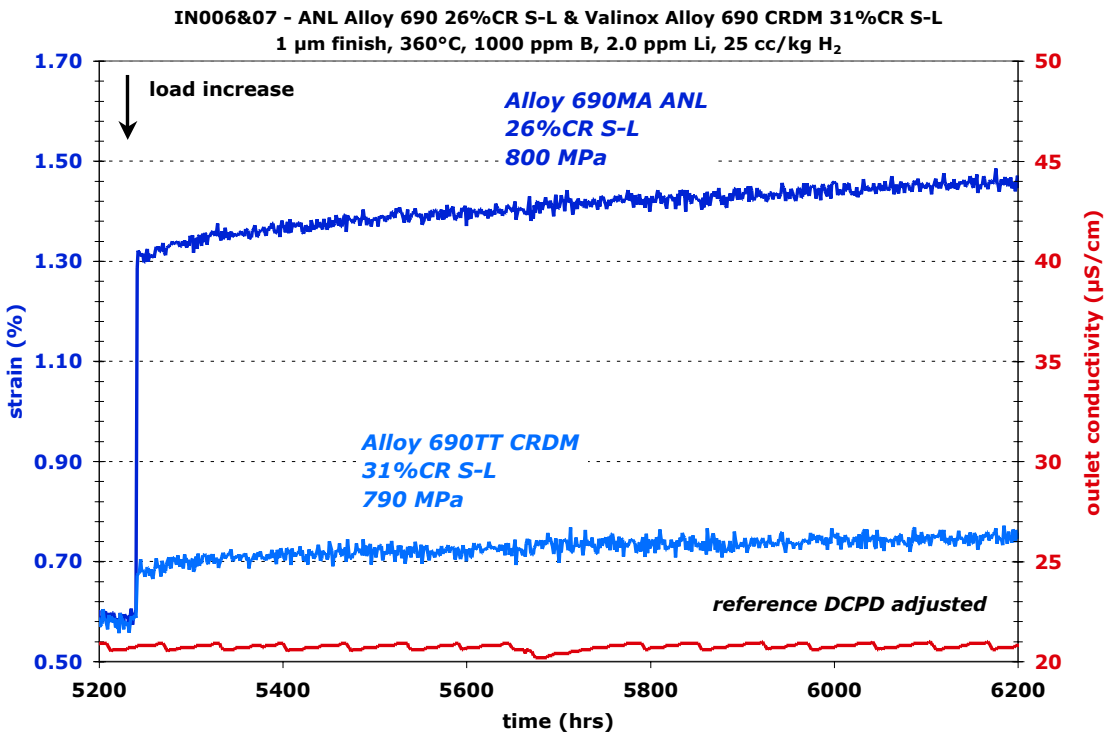

Figure 82. DCPD-based strain response for the IN006 and IN007 specimens from 5220 to 6200 hours after another load increase to 790-800 MPa.

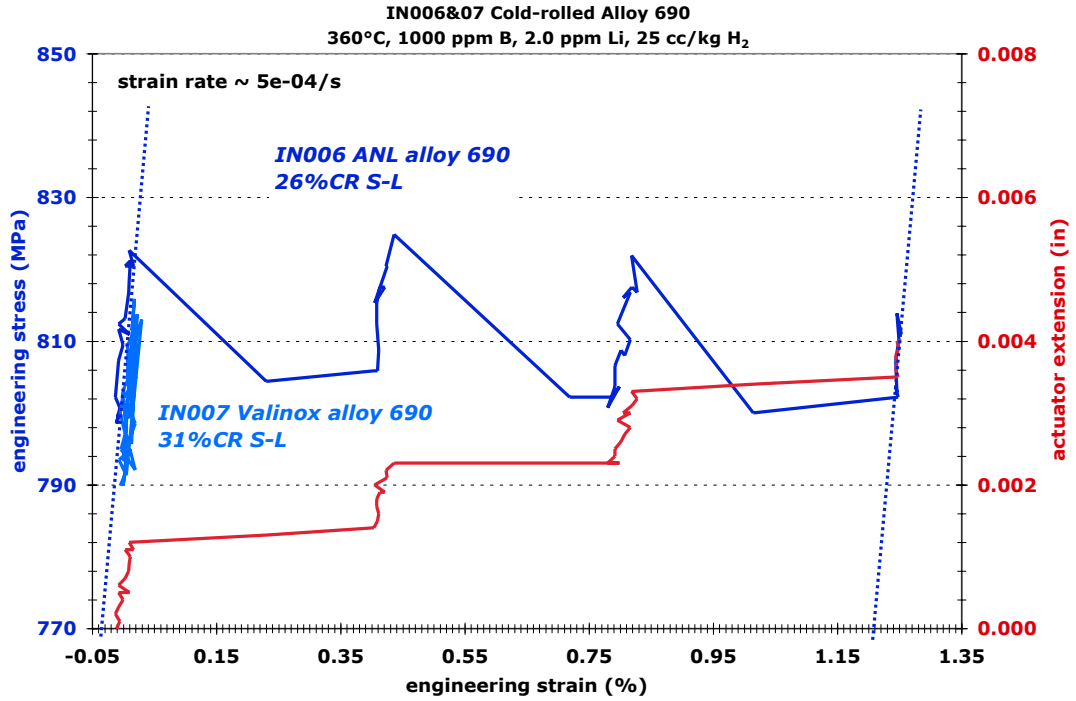

Figure 83. Tensile straining performed on the alloy 690 materials. The 26%CR plate (IN006) underwent ~1.2% plastic strain while the 31%CR CRDM (IN007) did not yield.

After ~7100 hours with no indication of SCC crack initiation (Figure 84), the decision was made to interrupt the test for another round of specimen examinations. The surface appearance of the 31%CR CRDM specimen IN007 had not noticeably changed. However, the 26%CR plate specimen IN006 exhibited a higher density of small cracks associated with the corroded TiN particles, had more cracks that appeared to be IG, and crack openings were larger as illustrated in Figures 85 and 86. Another important difference was that there were obvious surface strains in the specimen as illustrated in Figure 87. A much higher density of Ni-Fe spinels were also found on the specimen compared to the previous observation at 3600 hours. Figure 88 shows that the spinels were often decorating cracks or surface strained regions. Further surveys of the surface revealed that crack lengths were now more frequently in the 10 µm range and crack openings were often ~1 µm, even though there had been no obvious in-situ indication of crack initiation by DCPD.

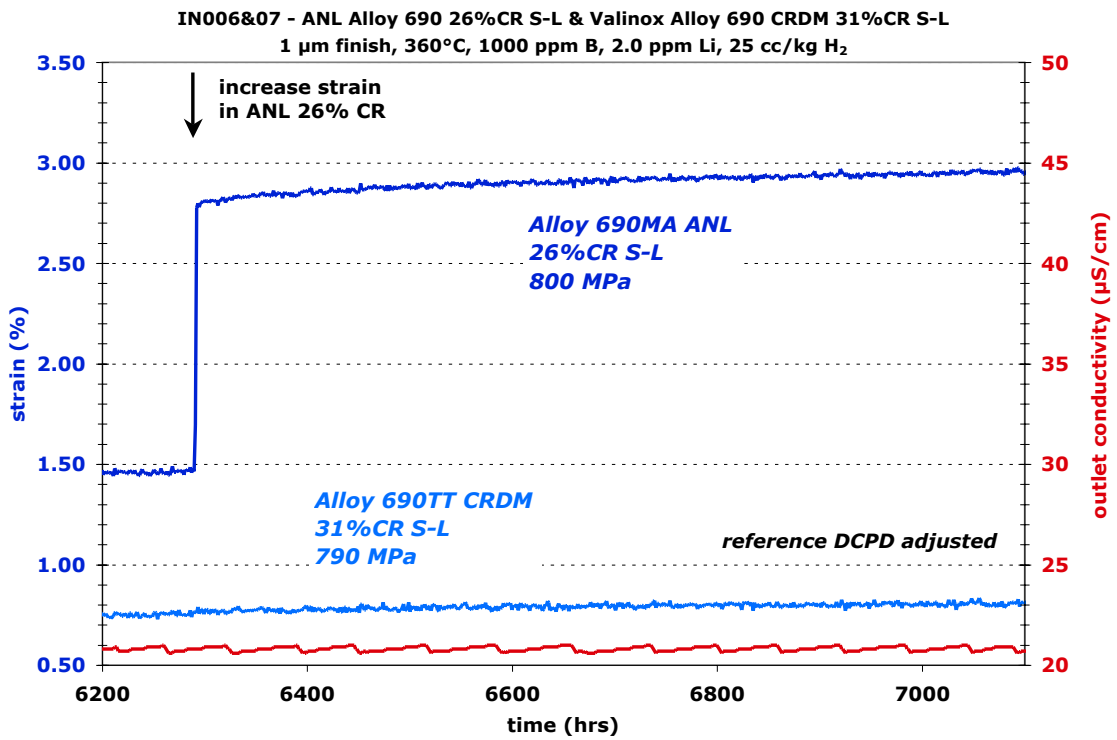

Figure 84. DCPD-based strain response of the two CR alloy 690 specimens (IN006 and IN007) from 6200 - 7100 hours after plastic deformation in plate specimen IN006.

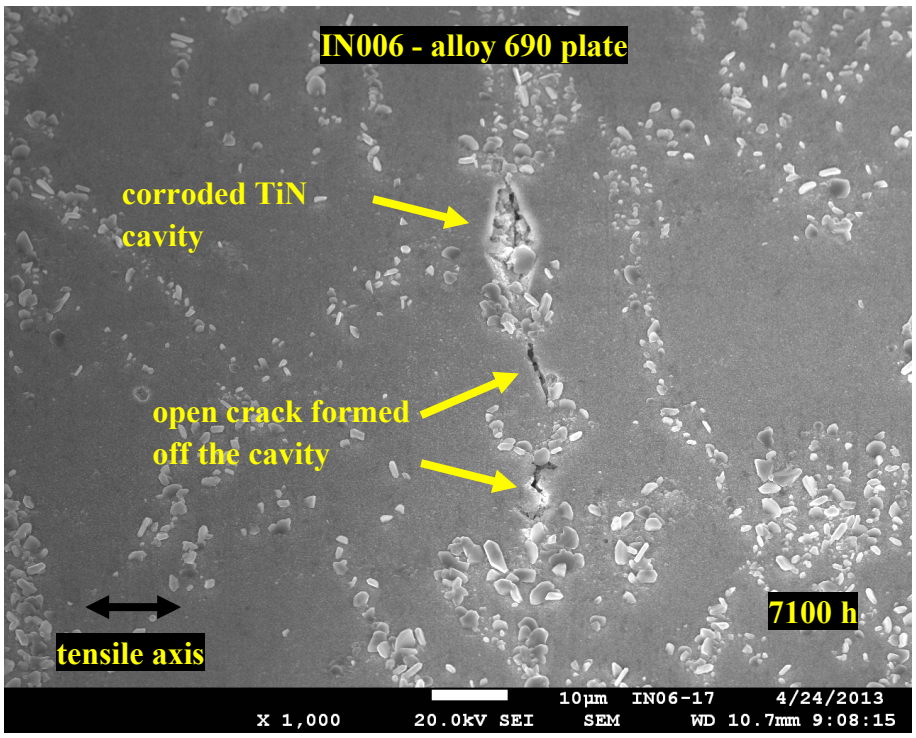

Figure 85. Example of surface crack morphology in the 26%CR plate specimen (IN006) after ~7100 hours of exposure.

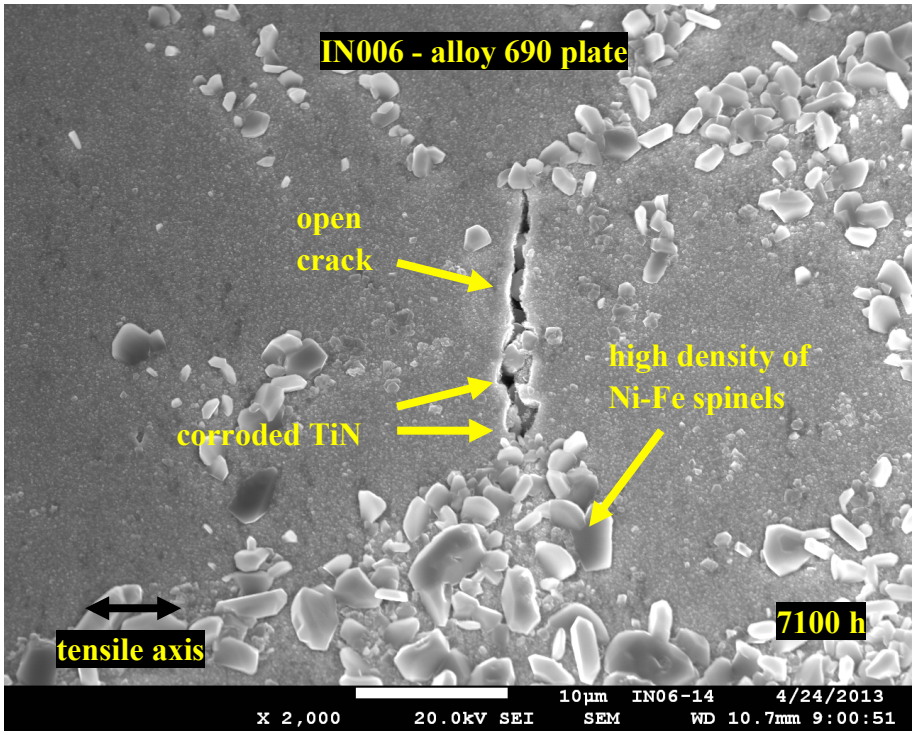

Figure 86. Example of surface crack morphology in the 26%CR plate specimen (IN006) after ~7100 hours of exposure.

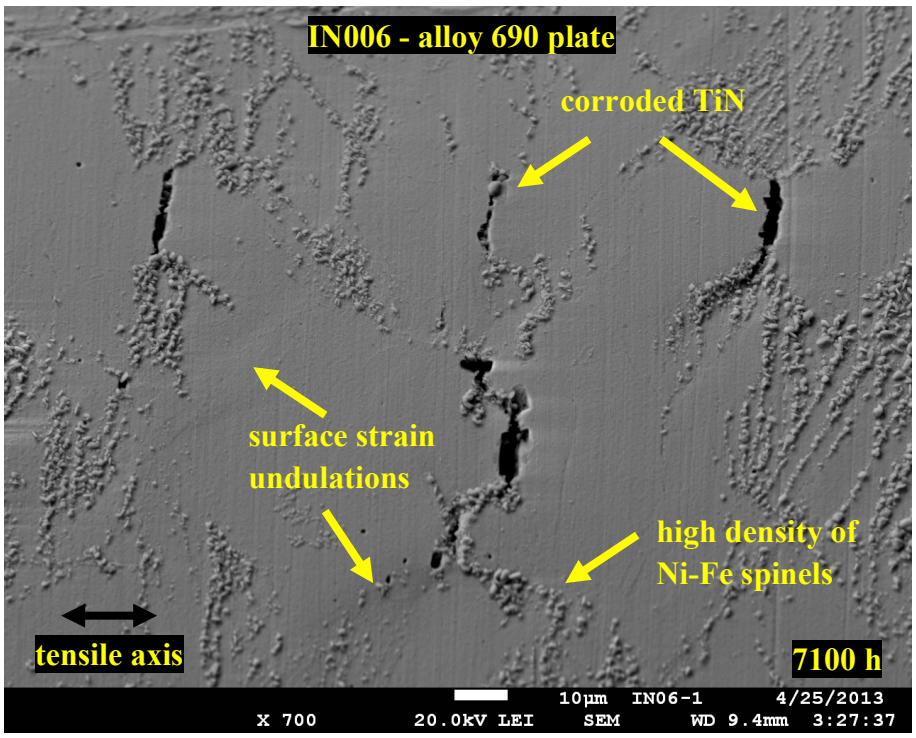

Figure 87. Observable surface strains on the 26%CR plate specimen (IN006) after ~7100 hours of exposure. Surface strains were often obscured by Ni-Fe spinels.

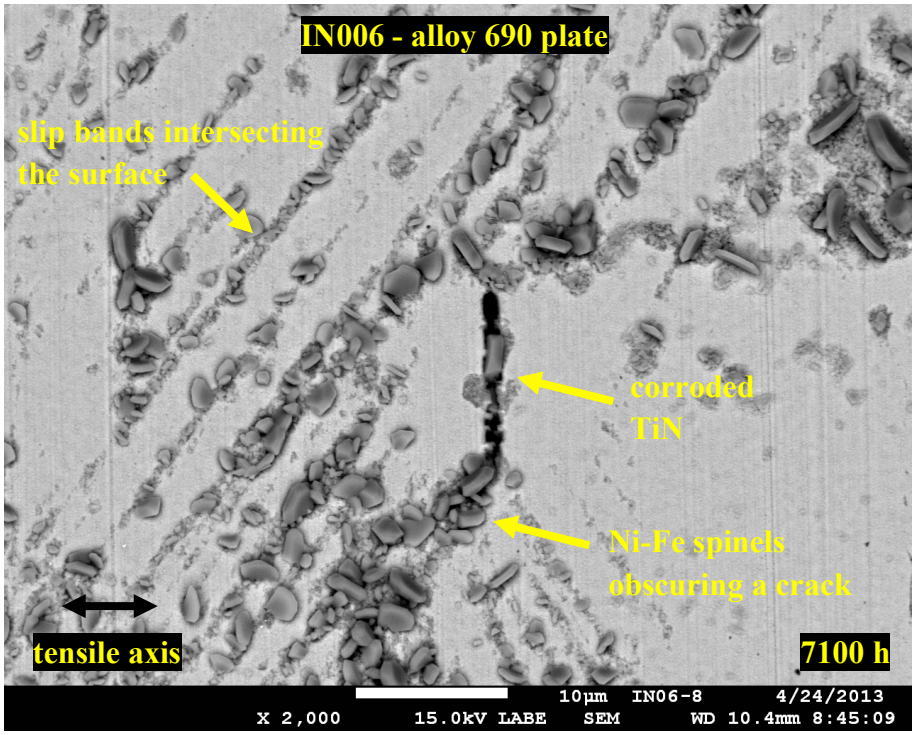

Figure 88. Ni-Fe spinels located on what appear to be twin boundaries and a crack nucleated off a corroded TiN particle on the 26%CR plate specimen (IN006) after ~7100 hours of exposure.

While cross-section examinations of unstressed alloy 690 surface exposure specimens had shown a protective Cr_2O_3 film above grain boundaries intersecting the surface, no information was available on what was occurring below the surface of exposed grain boundaries in the alloy 690 specimens under stress. In order to obtain initial information on the small IG surface cracks formed in the IN006 specimen, a FIB was used to form trenches into the specimens to expose selected subsurface cracks in cross section. Figure 89 shows a step-by-step example of the trenching process where an IG crack nucleated off a corroded TiN stringer is revealed. With a resulting size of ~5 µm in all dimensions, the trench is in the same size range as the TiN particles and is not expected to have any significant effect on the crack initiation behavior.

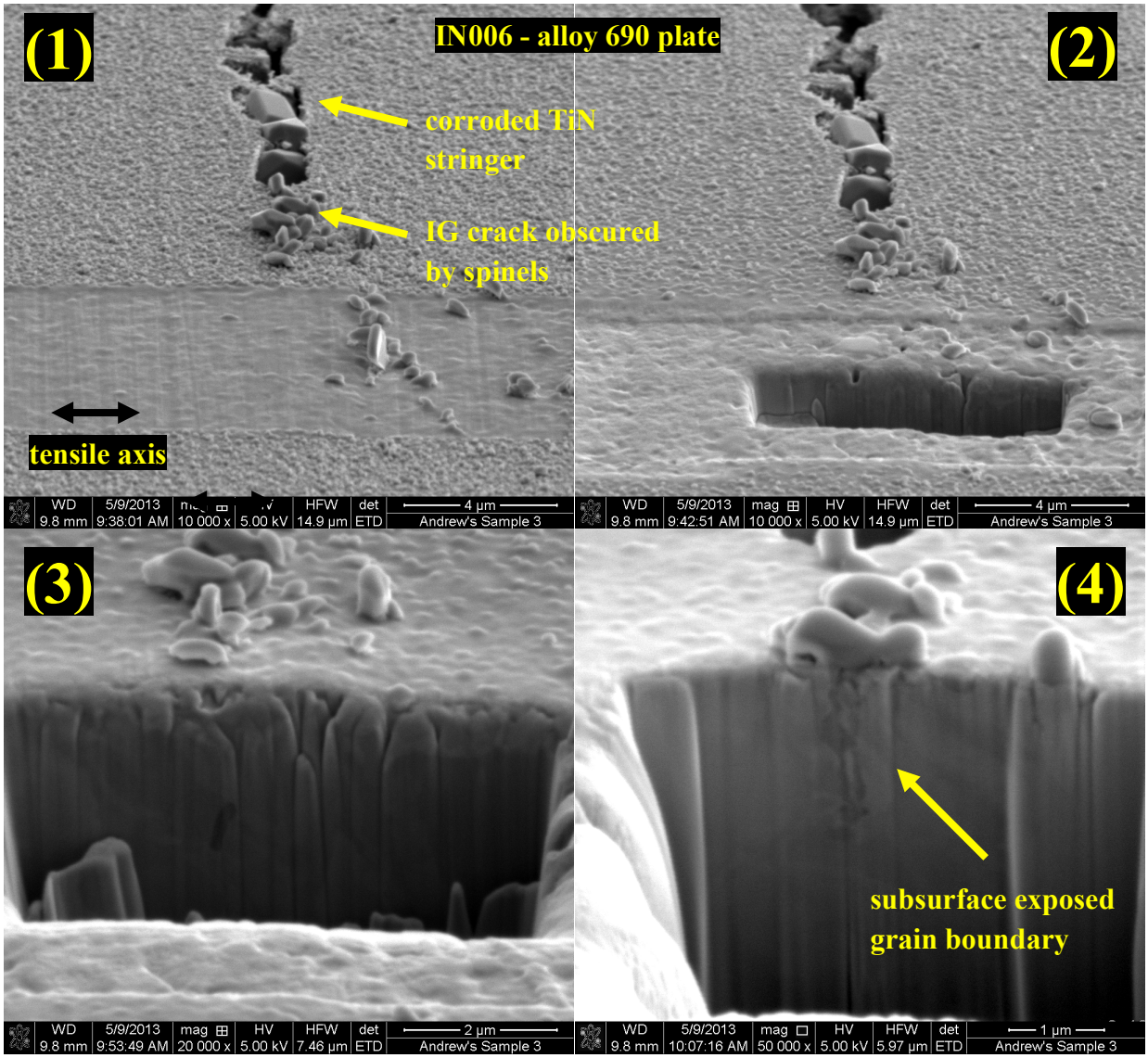

Figure 89. Step-by-step imaging of the formation of a trench into the surface of the 26%CR plate specimens (IN006) to reveal a subsurface IG crack in cross section.

As discussed previously, a small fraction of the TiN particles were coincident with grain boundaries, and in several cases, the cracks that nucleated off these corroded particles were IG. The FIB trench process was used to view these types of cracks with two examples shown in Figures 90 and 91. These cracks were verified to be IG by the presence of semi-continuous carbides that are only found on grain boundaries in this material. The cracks were limited to a rather shallow depth of 1-2 µm, and crack wall penetrative oxidation (commonly seen in alloy 690) was observed in both specimens. The uniform extent of attack off crack walls suggests that the IG crack extension may have formed during the dynamic straining event at 6300 hours and no further IGSCC growth occurred under constant load from 6300 to 7100 hours.

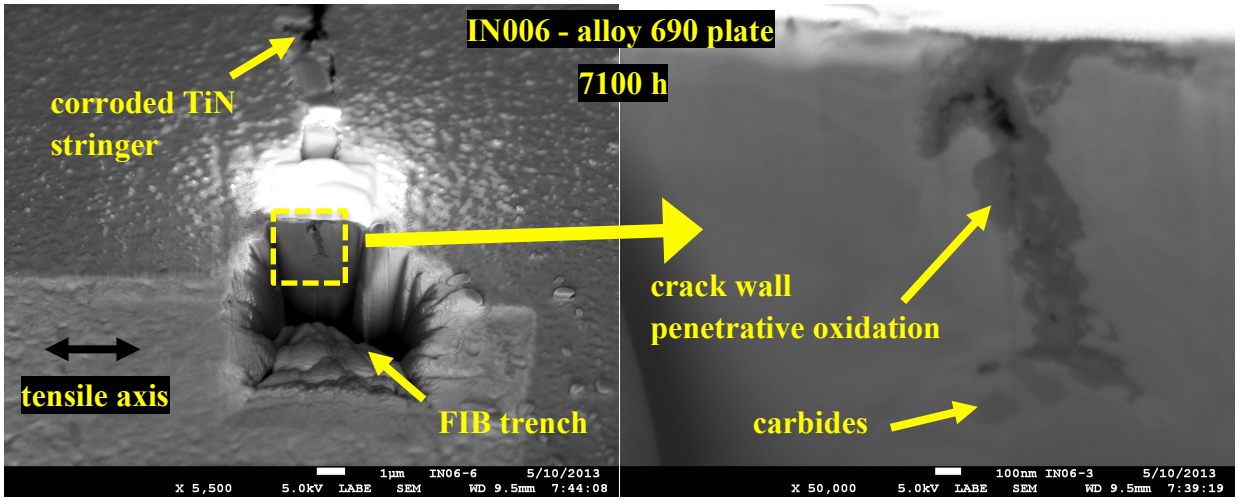

Figure 90. Strain driven IG crack in the 26%CR plate specimen as viewed in cross section using the FIB trench process. Cracking was limited to a depth of ~1 µm.

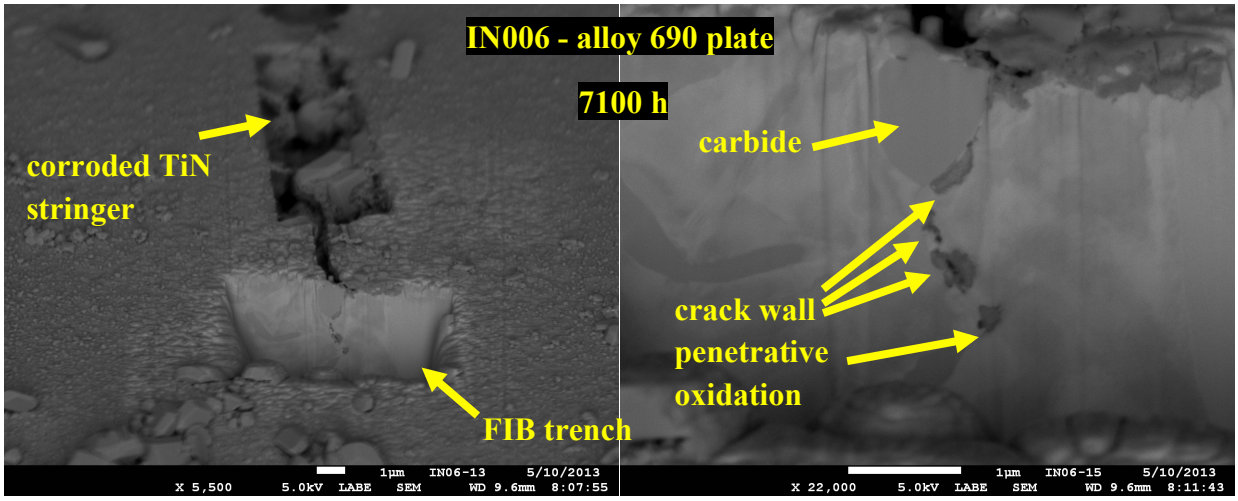

Figure 91. Second example of a strain driven IG crack in the 26%CR plate specimen as viewed in cross section using the FIB trench process. Cracking was limited to a depth of ~2 µm.

These small IG cracks represent likely precursors for IGSCC nucleation in the smooth surface specimens. However with no clear indication of a transition to IGSCC by either DCPD or SEM observations, the specimens were again reloaded into a crack initiation test system for further exposure. An additional ~0.2% plastic straining was applied to ensure that the specimens were at the maximum possible load. Surprisingly, it was possible to increase the load slightly to produce an applied stress of ~850 MPa for the specimens, a value that is beyond the ~750-780 MPa ultimate tensile strength of the 26%CR alloy 690 plate material when it was air-tensile tested at 360°C. The increased strength is due to an as-yet unidentified, aging-induced microstructural change at 360°C and may be linked to the increase in resistivity that is seen in alloy 690 at 360°C. APT examinations have been performed with a notion that Ni-Cr clustering and/or Ni_2Cr precipitation would be observed due to long-range ordering, but none was found. Efforts to identify this mechanism are continuing.

After ~500 hours (to ~7600 h total test time) at 850 MPa with no indication of crack initiation, the 26%CR plate specimen IN006 was plastically strained an additional ~0.8% (Figure 92), bringing the total plastic strain up to ~4%. The yield point again increased, this time up to ~890 MPa, but then the stress decreased slightly to ~870 MPa with a concurrent flat plastic strain response that reinforced that the specimen was beginning to neck. In order to avoid runaway straining during constant load, the stress was dropped slightly to 860 MPa. No initiation was observed from ~7650 hours to ~8100 hours as shown in Figures 93 and 94 for the 26%CR plate and 31%CR CRDM specimens, respectively. Then a final ~1.7% plastic strain was added to the 26%CR alloy 690 plate, bringing the total strain up to ~6%. The stress after straining dropped to ~810 MPa due to a more significant reduction in load carrying capacity that occurred during this straining event. While there was no obvious DCPD indication of crack initiation for the IN006 specimen, the measured strain increased slowly at the applied load as shown in Figure 95. The decision was made to stop the test after a total exposure time of 9144 hours (>1 year).

Detailed optical and SEM characterizations of the gauge surfaces were performed on both specimens. Surprisingly, the 26%CR plate specimen IN006 still did not reveal evidence for macroscopic crack nucleation. The gauge surface appearance is illustrated by the SEM images in Figure 96. The small precursor cracks identified earlier in the test associated with TiN stringers remained, but significant growth of these cracks was not observed even after the additional aggressive straining and applied loads greater than its expected ultimate strength. The decision was made to not restart this specimen, and a series of cross-sections were then prepared and systematic examinations of shallow cracks were conducted. They confirmed the relatively low density of shallow cracks and the lack of SCC initiation in the IN006 specimen (Figure 97).

SEM examinations were also performed on the 31%CR CRDM specimen IN007 documenting the surface condition after the 9144-hour exposure as illustrated in Figure 98. Quite different than the IN006 specimen, no DCPD evidence for yielding was seen for the IN007 specimen during the 7 load increases. The surface characteristics were similar to those documented after

3600 hours (Figure 78b). The large matrix TiN particles were corroded, but cracks were not detected near these particles or in other locations such as grain boundary triple points.

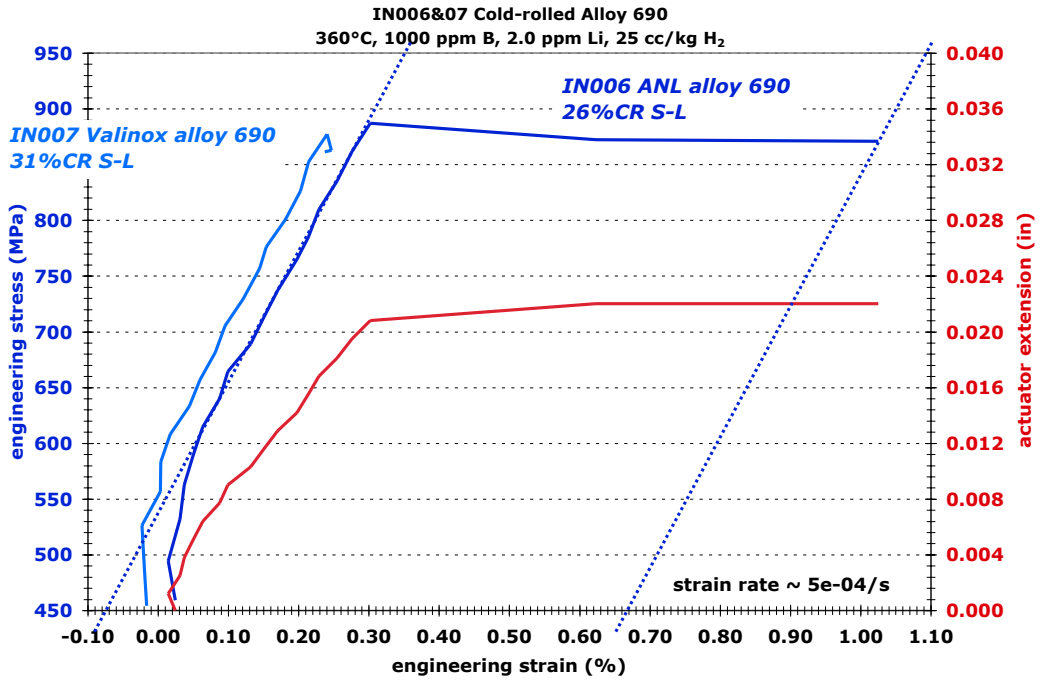

Figure 92. Plastic strain applied to the 26%CR ANL alloy 690 plate specimen IN006 at ~7600 h.

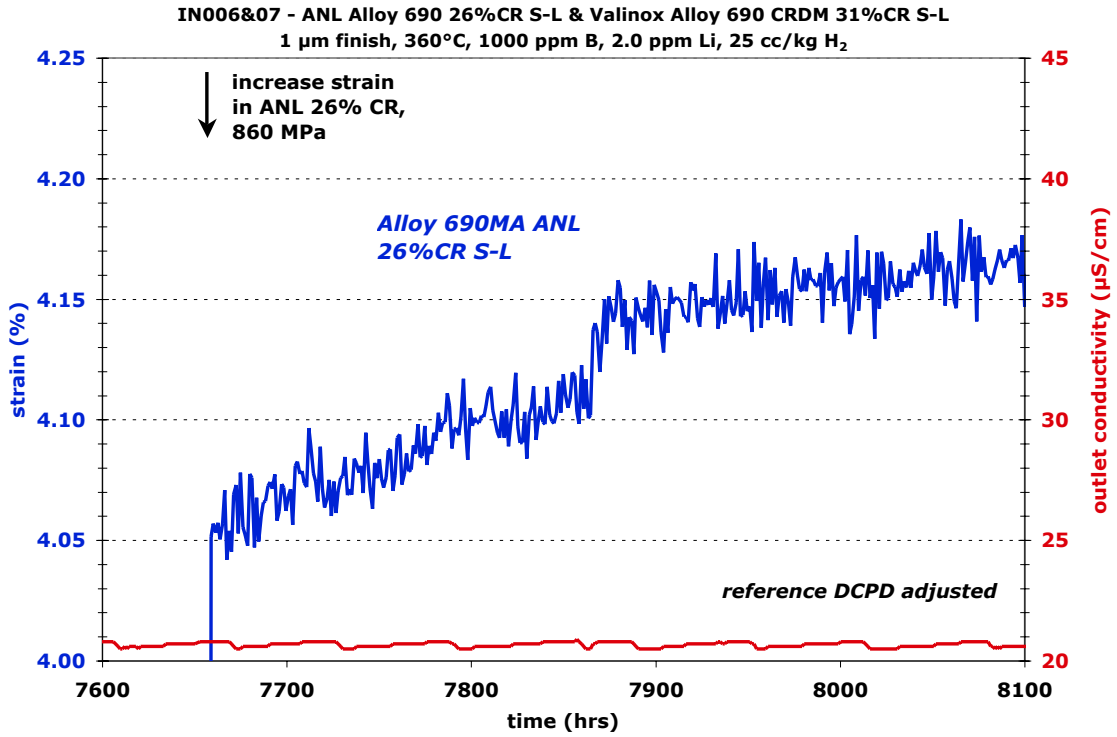

Figure 93. DCPD-based strain response of the 26%CR ANL alloy 690 plate specimen IN006 from 7650 to 8100 hours.

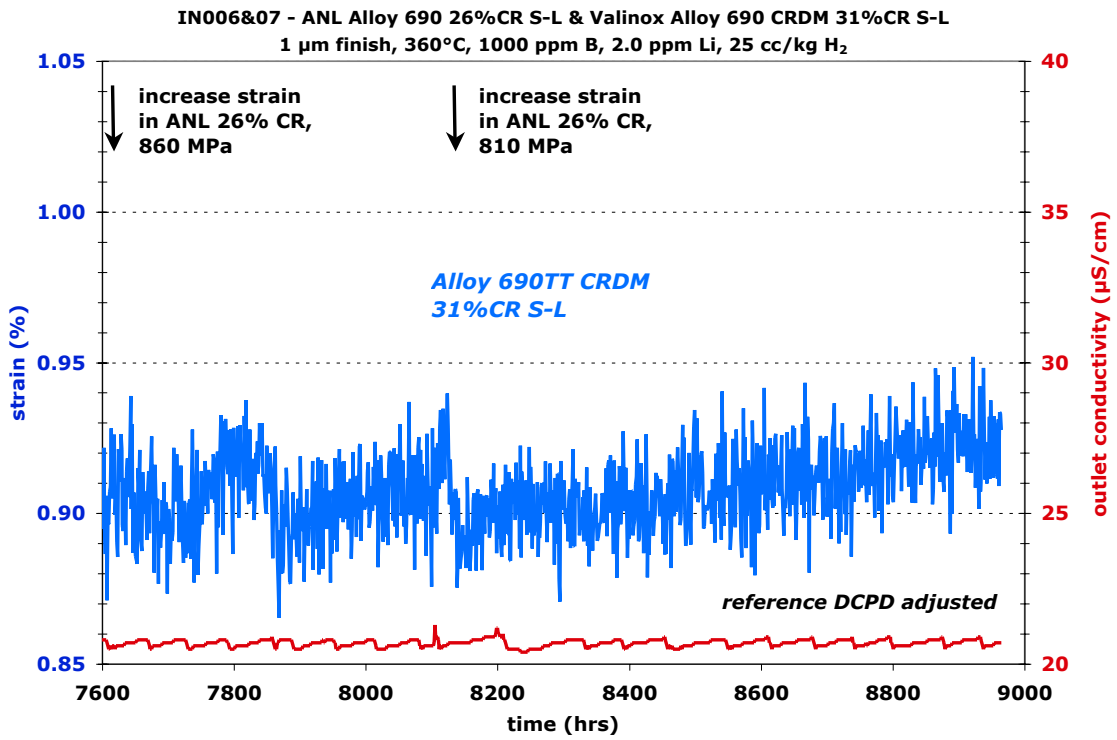

Figure 94. DCPD-based strain response of the 31%CR alloy 690 CRDM specimen IN007 from 7600 to 8950 hours.

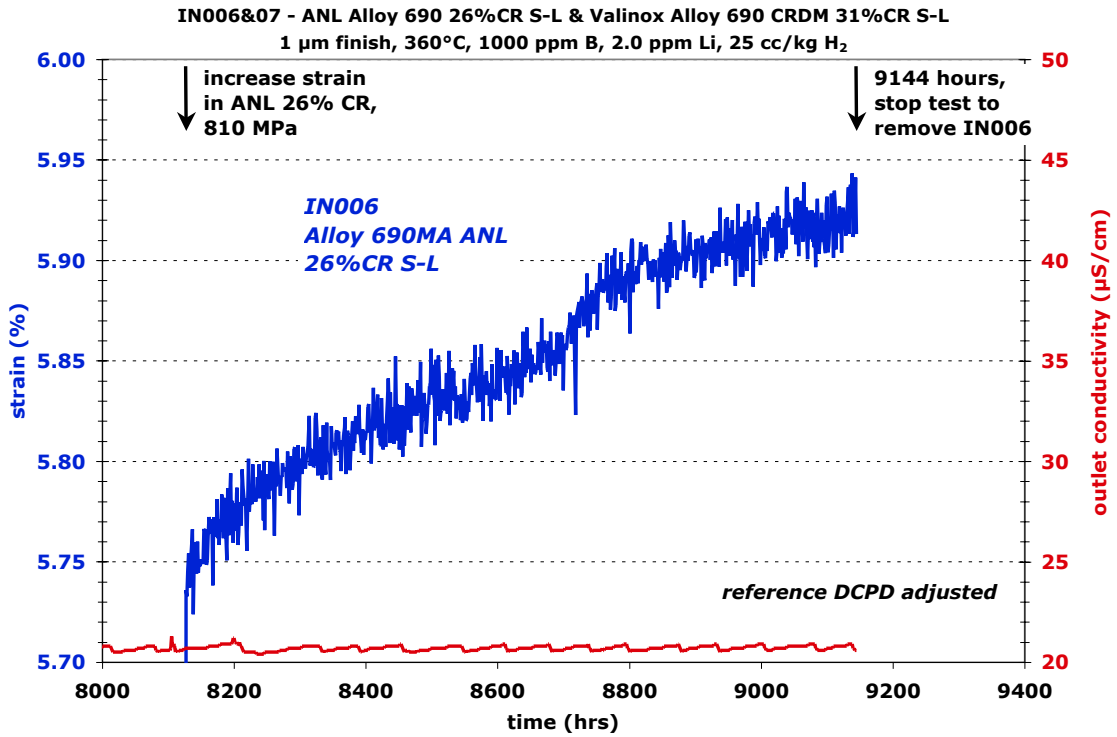

Figure 95. DCPD-based strain response of the 26%CR ANL alloy 690 plate specimen IN006 from 8150 to 9144 hours.

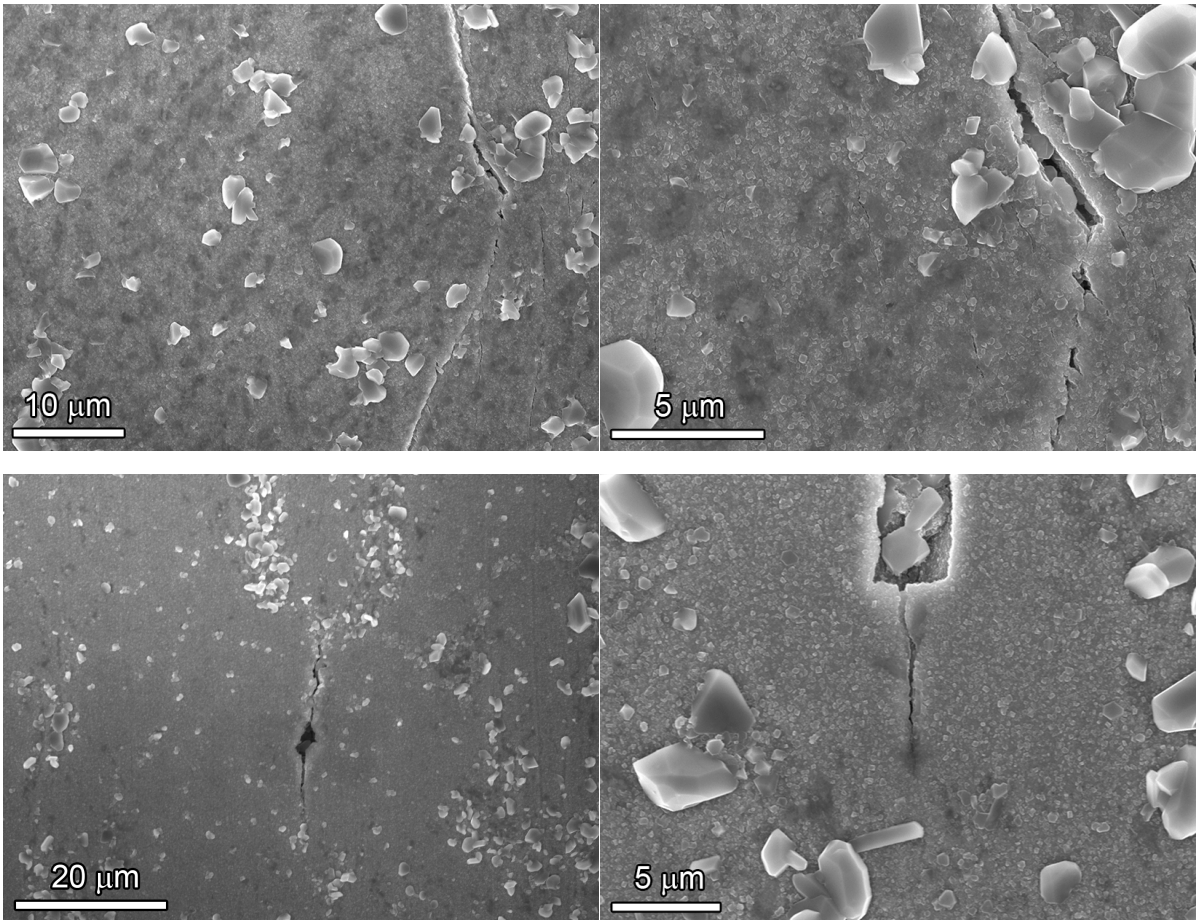

Figure 96. SEM-SE images of the gauge surface appearance for specimen IN006 after 9144 h.

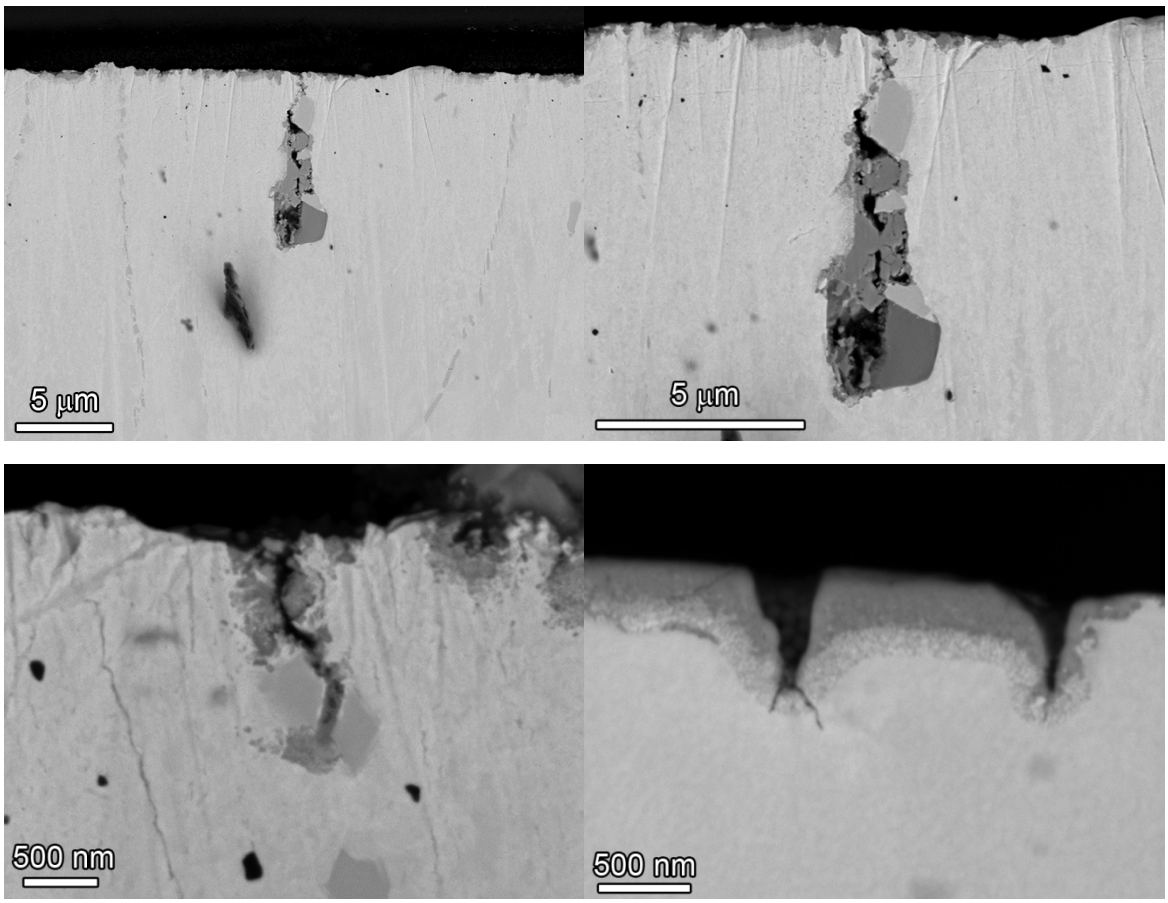

Figure 97. SEM-BSE images of IN006 cross-section after 9144 h.

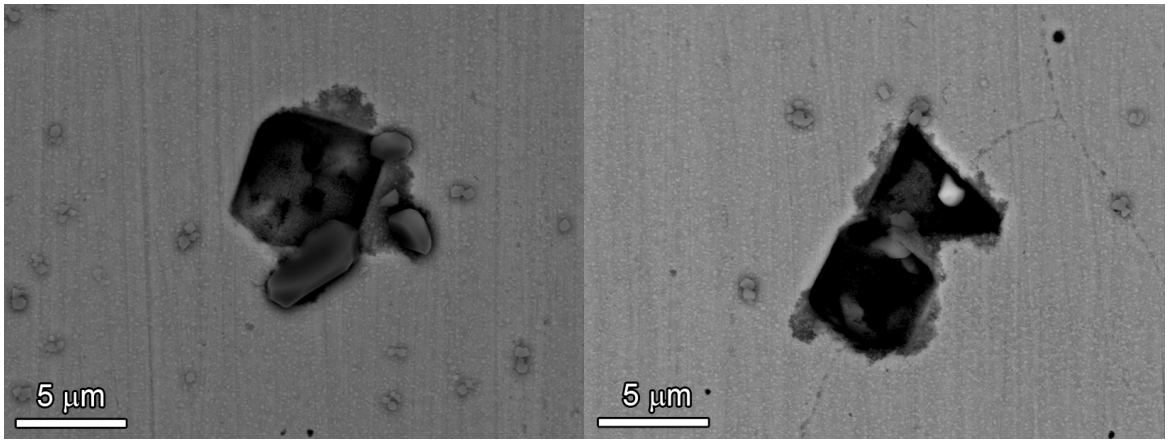

Figure 98. SEM-BSE images of IN007 surface at 9144 h showing two TiN inclusions, one TG (left) and one IG (right). Attack of the surrounding metal is observed at TiN, but no IG cracks were observed.

The lack of any observed surface cracks on the IN007 specimen and the fact that it had not seen significant plastic deformation made it worthwhile to continue the SCC initiation test. However before reloading the specimen, FIB sectioning was performed to examine several grain boundaries intersecting the surface. An example of one of these FIB trenches and the near-surface microstructure is presented in Figure 99. Similar to the alloy 690 surface corrosion results summarized in Figure 70, grain boundaries were not attacked in the highly stressed IN007 specimen even after the long-term exposure in 360°C PWR primary water.

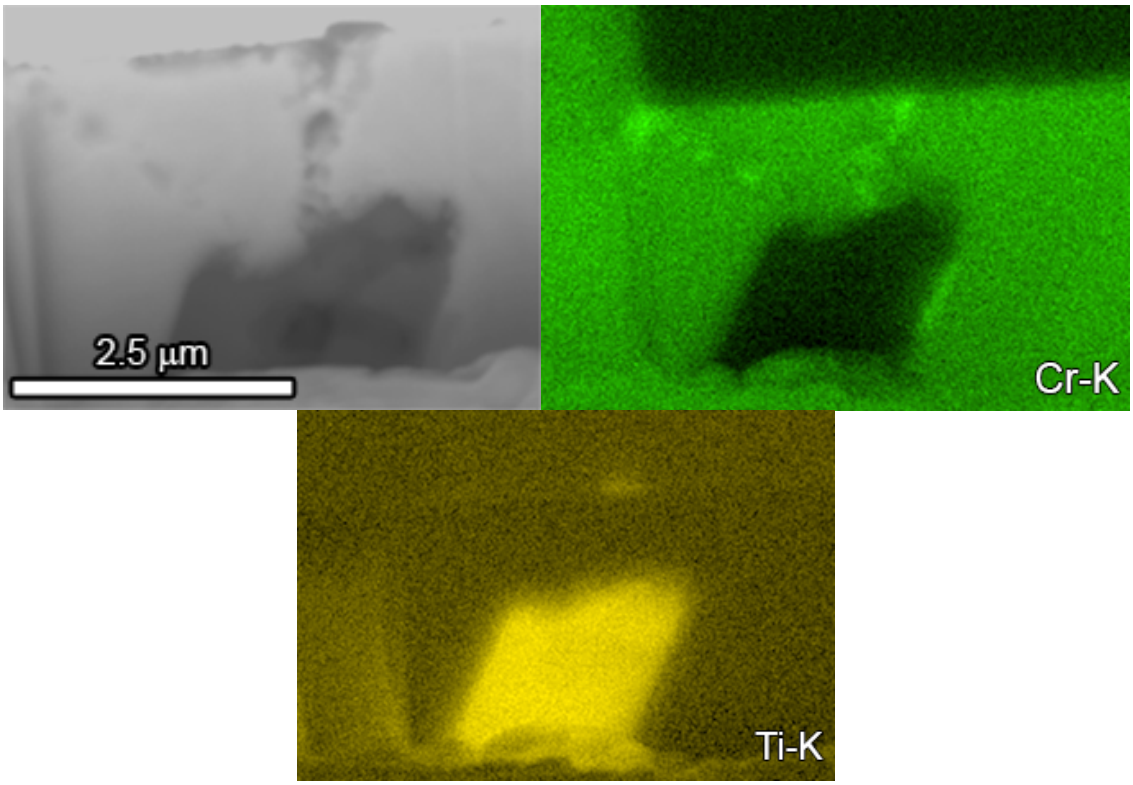

Figure 99. Near-surface grain boundary microstructure from a FIB trench in the IN007 specimen after 9144 h. Corrosion of the grain boundary is observed extending from the TiN inclusion.

The 31%CR CRDM specimen IN007 was reloaded to its current yield stress of 860 MPa without any significant plastic deformation. After ~340 hours at constant load, dynamic plastic deformation was produced by a slow loading ramp of ~$1x10^{-8}$ s^{-1} as shown in Figure 100 with the intent to reach ~0.5% plastic strain. A jump in DCPD-measured strain was detected after ~120 hours of slow straining with an indicated increase of ~0.3% strain before the loading ramp was ended. This jump suggested that crack nucleation may have occurred and constant load conditions were reestablished at 460 hours (total test time of 9744 hours). DCPD response was closely monitored and a slight increase in slope was detected over the next ~200 hours. Before the decision could be made to shut down the test, the IN007 specimen rapidly failed after a total test time of 9950 hours.

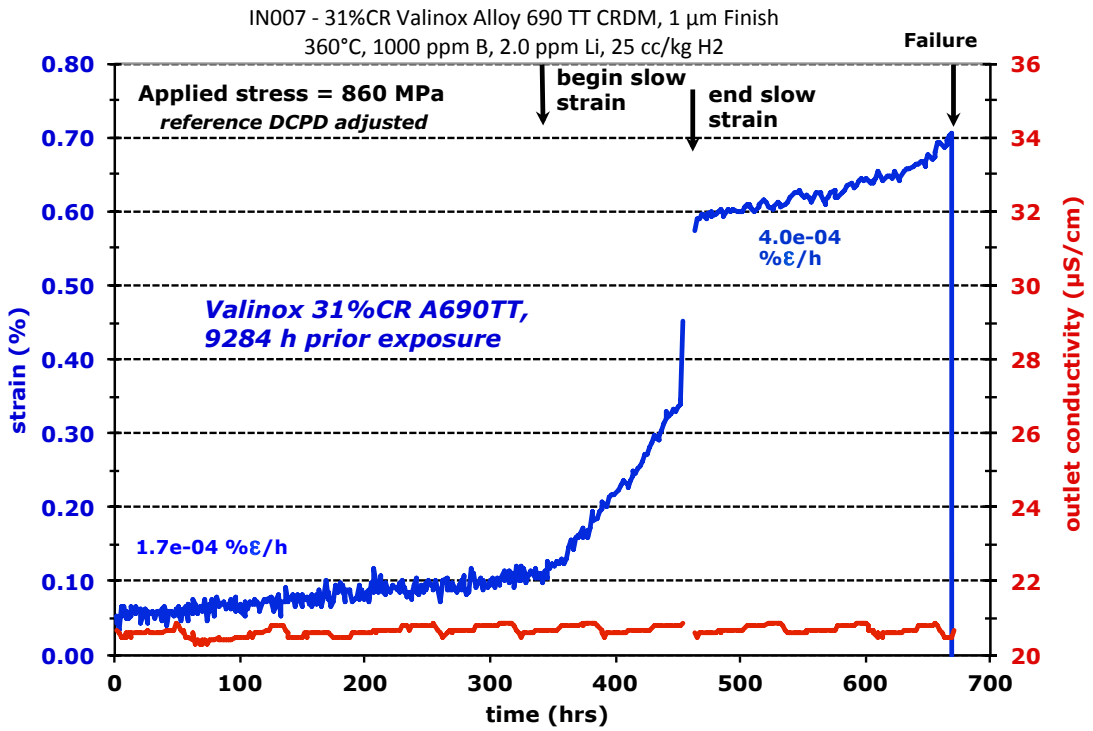

Figure 100. DCPD-based strain response of the 31%CR alloy 690 CRDM specimen IN007 after restart at the yield stress (860 MPa).

SEM characterizations were performed on the fracture surface and gauge section surfaces to document the cracking morphology and distribution. The fracture surface revealed extensive IG cracking as illustrated in Figure 101. Through the use of low kV backscatter imaging, it was possible to observe slight changes in the surface oxide thickness. Two distinct regions of oxidation were observed; one of darker contrast (highlight by the dashed yellow lines) and lighter contrast (highlighted by the dashed red lines) as compared to the bright contrast of the unoxidized metal. In all three regions, IG cracking was observed by SEM-SE imaging (Figure 102). At higher magnifications (Figure 103) the differences in the three regions becomes obvious using SEM-BSE. In the highly oxidized region (#1) the surface is darker with no apparent carbides present due to the surrounding oxide masking the signal. In the region of secondary attack (#2) the IG carbides can be discerned but the surrounding metal is only slightly oxidized and does not mask the carbide signal. Lastly, in the final fracture region (#3) the IG carbides are highly contrasted by the unoxidized bright metal. Differences in the IG surfaces were discovered by high-resolution SEM (SE and BSE) imaging with local regions exhibiting clear evidence of extended exposure in 360°C water. These regions are identified as IGSCC, but all that is known is that the cracks most likely opened up during the observed strain jump. Other IG areas had little or no evidence of surface corrosion and probably were exposed during the final rapid failure. A distribution of small IG cracks was also detected on the gauge surface as documented in Figure 104. These cracks tended to be less than 50 µm in length and may have opened up during the loading ramp at ~9740 hours.

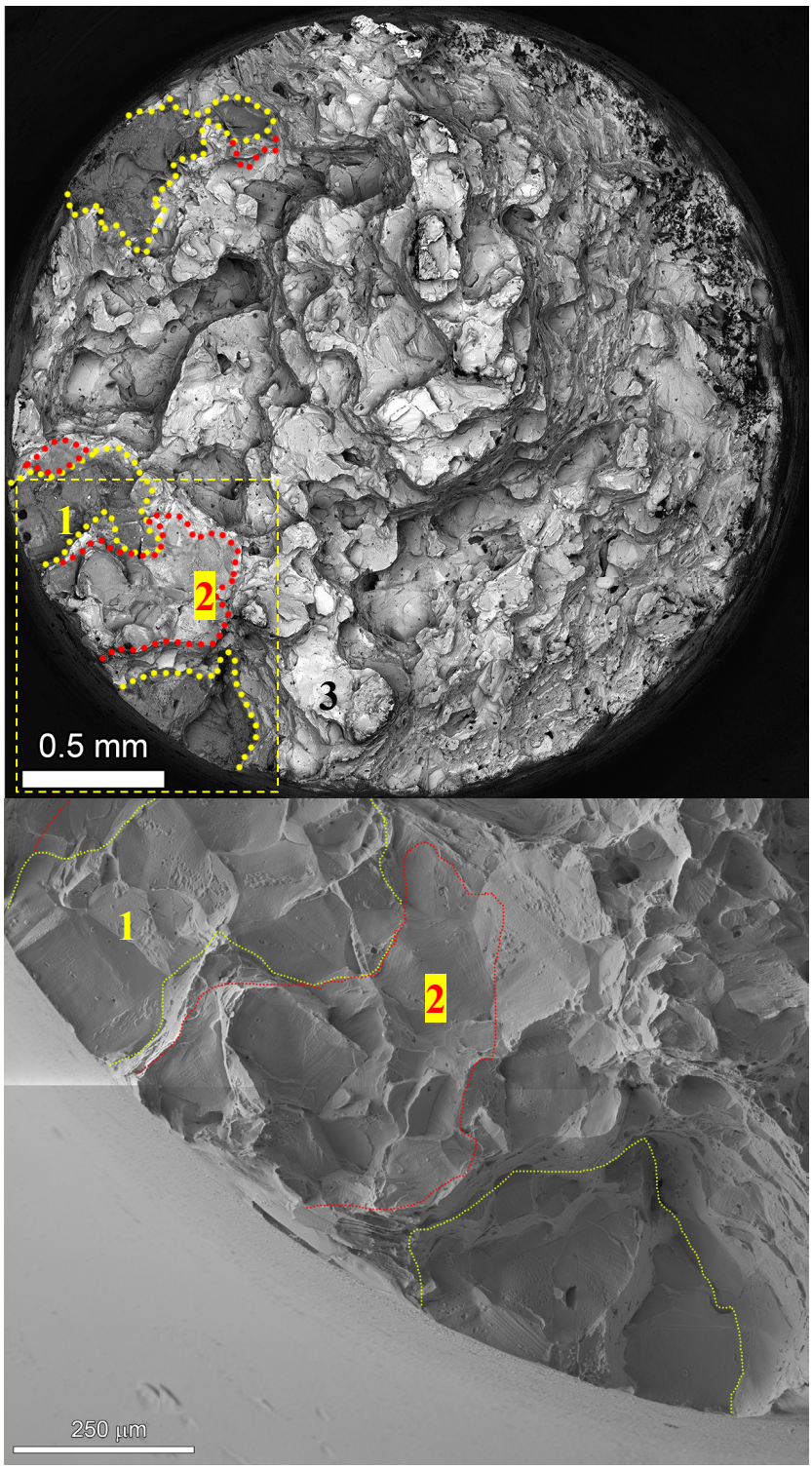

Figure 101. Low kV SEM-BSE of the fracture surface and high kV SEM-SE micrographs illustrating the fracture surface for the 31%CR CRDM specimen IN007. Several pockets of IG cracking were found where yellow is initial SCC, red is secondary SCC. Remainder of fracture surface appears to be mixture of IG and TG fracture with no apparent oxide.

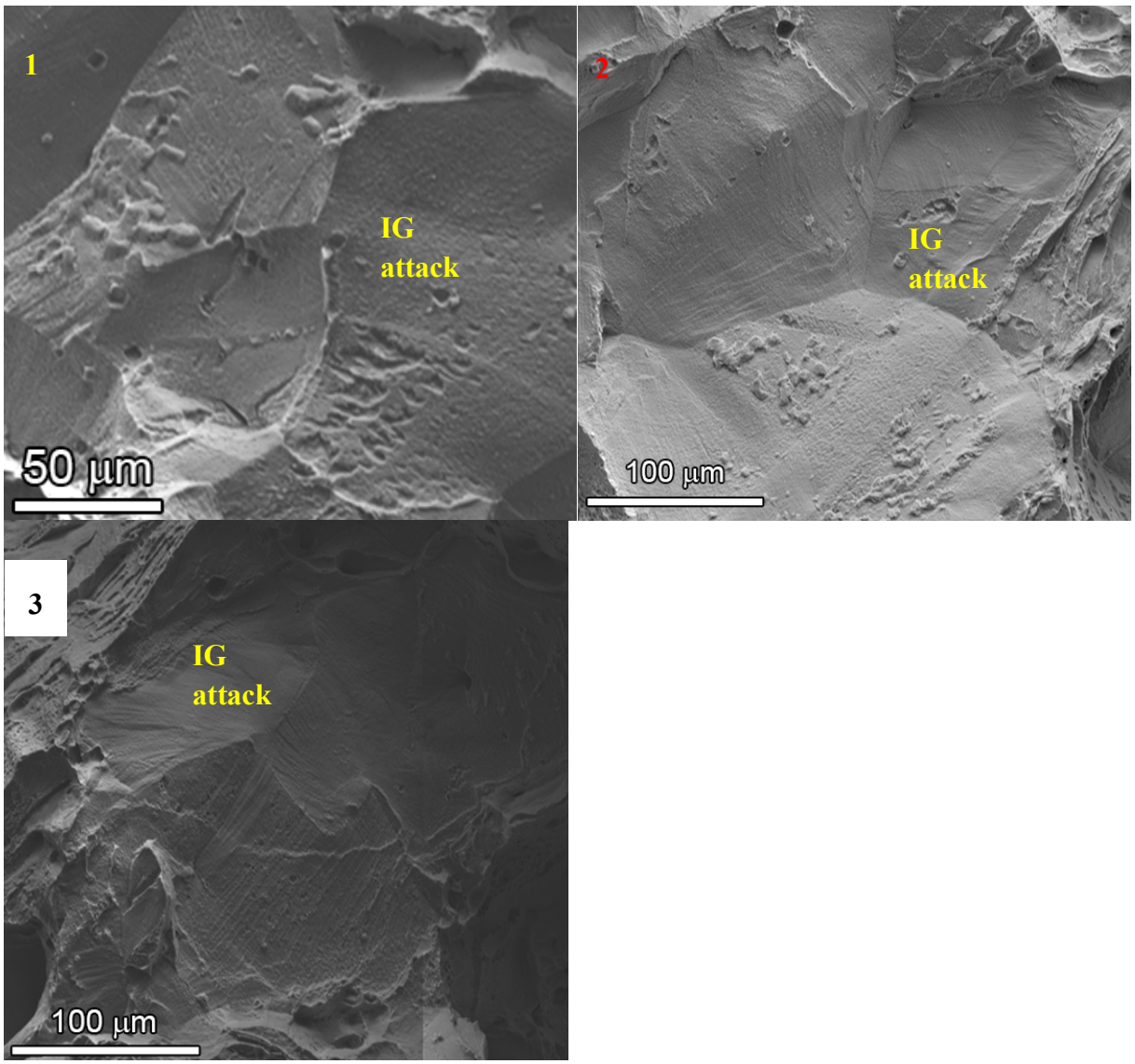

Figure 102. SEM-SE images of IG cracking of various regions denoted in Figure 101.

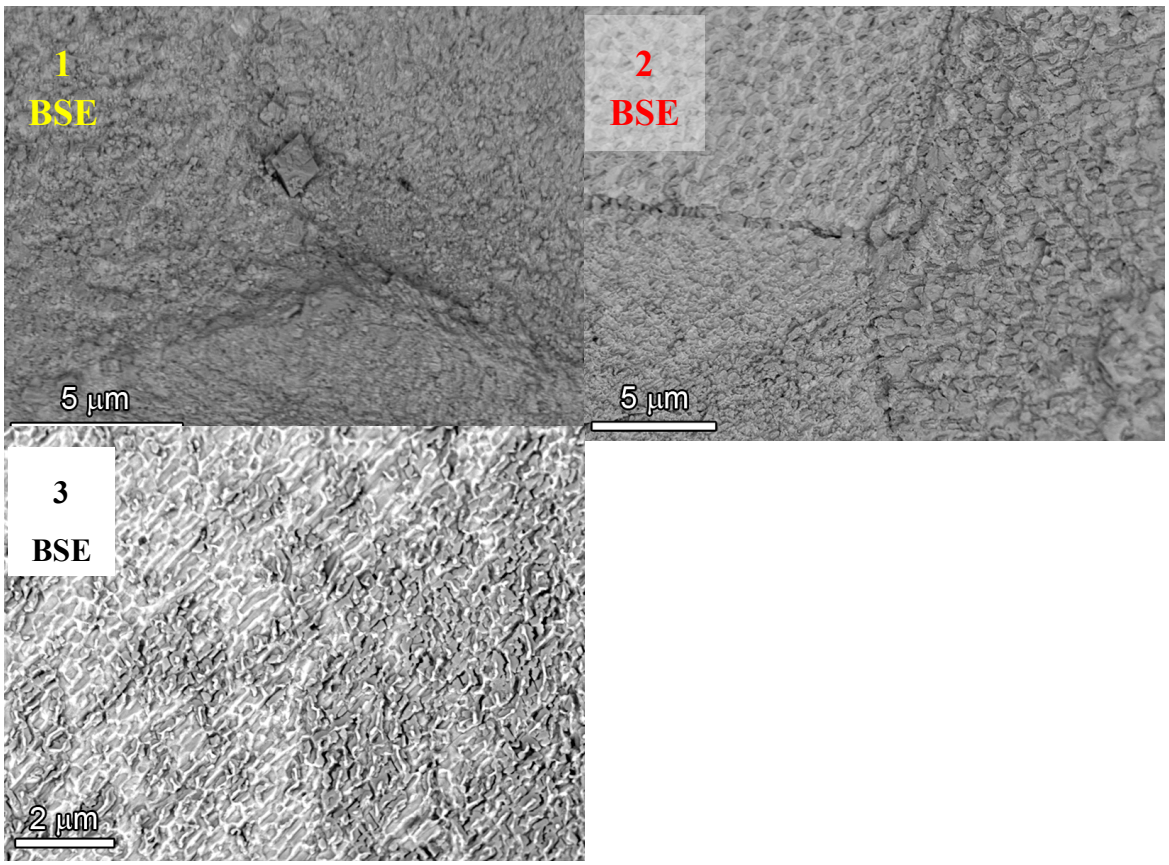

Figure 103. High magnification SEM-BSE images of IG cracking of various regions denoted in Figure 101.

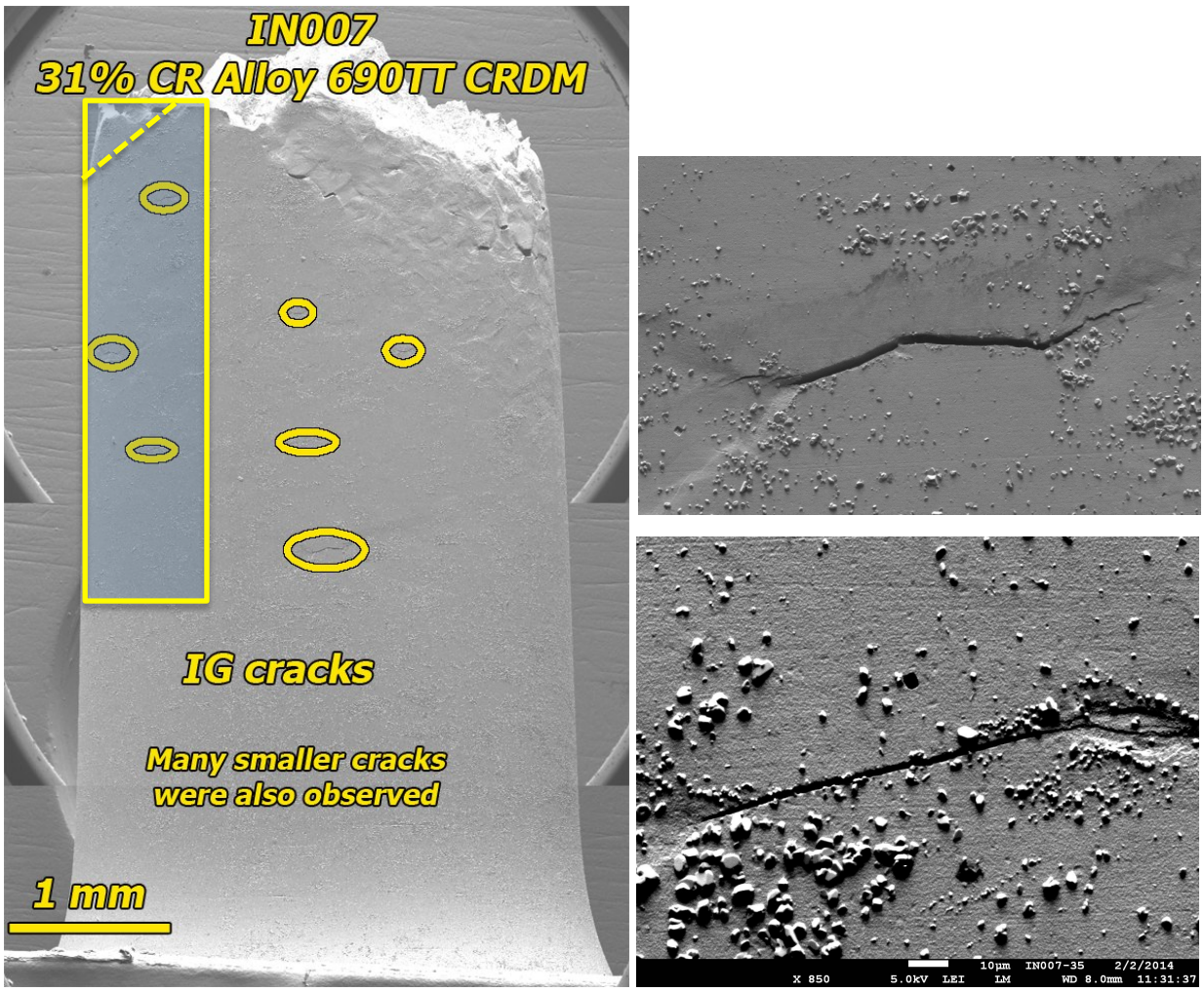

Figure 104. SEM-SE images from the gauge surface of the 31%CR CRDM specimen IN007. The yellow box indicates where a cross-section sample was prepared. The dotted line indicates a portion of the cross-section slice that was removed to due to necking damage.

Upon imaging the fracture surfaces of IN007, it was apparent that there were two distinct regions of intergranular failure that appeared oxidized in low kV backscatter images. Additionally, in the regions of rapid, catastrophic failure (i.e., where the bright contrast signified metallic surfaces that had not been oxidized) there also appeared regions of IG failure. The flat intergranular surfaces appeared to be highly decorated with carbides, suggesting that there may have been creep cracks present in the material. In order better ascertain as to whether creep cracks were present, a cross-section of the gauge region was prepared to analyze the microstructure. Figure 105 illustrates an SEM-BSE montage of a section of the IN007 surface. A small notch was cut out. In this cross section, three cracks were identified.

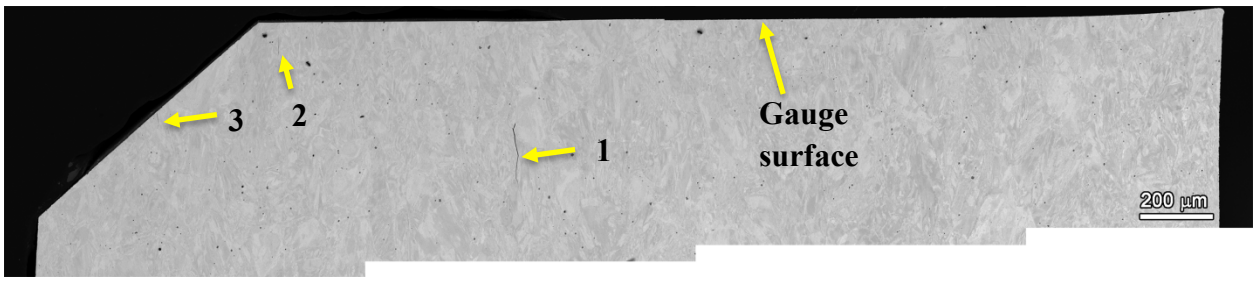

Figure 105. SEM-BSE cross-section image of the IN007 gauge section depicted in Figure 104. Cross-section is flipped and rotated 90 degrees.

The first crack (IG crack #1) was observed at ~500 µm deep from the gauge surface (Figure 105), and at moderate magnifications was determined to be IG (Figure 106). Our previous research on high Cr, Ni-based alloys has demonstrated that penetrative oxidation observed along crack walls can be used to not only indicate the age of an SCC crack, but determine if it was an active crack. Active SCC cracks typically will show very little penetrative oxidation near the leading tip and gradually become thicker along the crack walls farther from the growing crack. Two different regions of IG crack #1 were examined (Figure 106), one ~60-80 µm behind the leading tip (yellow dashed box), and the second at the leading crack tip (red dashed box). From Figure 107, which illustrates the yellow boxed region farther behind the leading crack tip, a continuous 200 nm thick penetrative oxidation layer is apparent on either side of the crack. Closer to the leading crack tip (~4-5 µm), the penetrative oxidation is shown to be ~75-100 nm thick (Figure 108). Finally, at the leading crack tip (also Figure 108) there appears to be very little to no penetrative oxidation at the crack tip. Hence, it was determined that crack #1 was an active SCC crack tip.

Crack tips #2 and #3, both of which were much closer to the surface were also observed to be intergranular (Figure 109), but had a much different appearance than did crack tip #1. At low magnifications, the most apparent difference is the rippled appearance of crack tips #2 and #3 versus the smooth crack walls of crack tip #1. This rippled appearance is indicative of creep cracking, as the metal in between the carbides has been deformed in a ductile manner. This morphology was readily observed in the final fracture surfaces of IN007 (Figure 103). At high magnification, these crack tips appear to have little to no penetrative oxide along the walls (Figure 110). Although cracks #2 and #3 were not observed to intersect the gauge surface, they were close enough to the surface that they may have connected with other creep cracks (or even SCC cracks), allowing ingress of water. In fact, a small amount of penetrative oxidation was observed in crack #3, although unlike the continuous nature of the penetrative oxidation in SCC cracks, the oxidation observed here appears to be discontinuous. If these creep cracks were eventually filled with high temperature water, it would be expected that the walls would be decorated with penetrative oxidation.

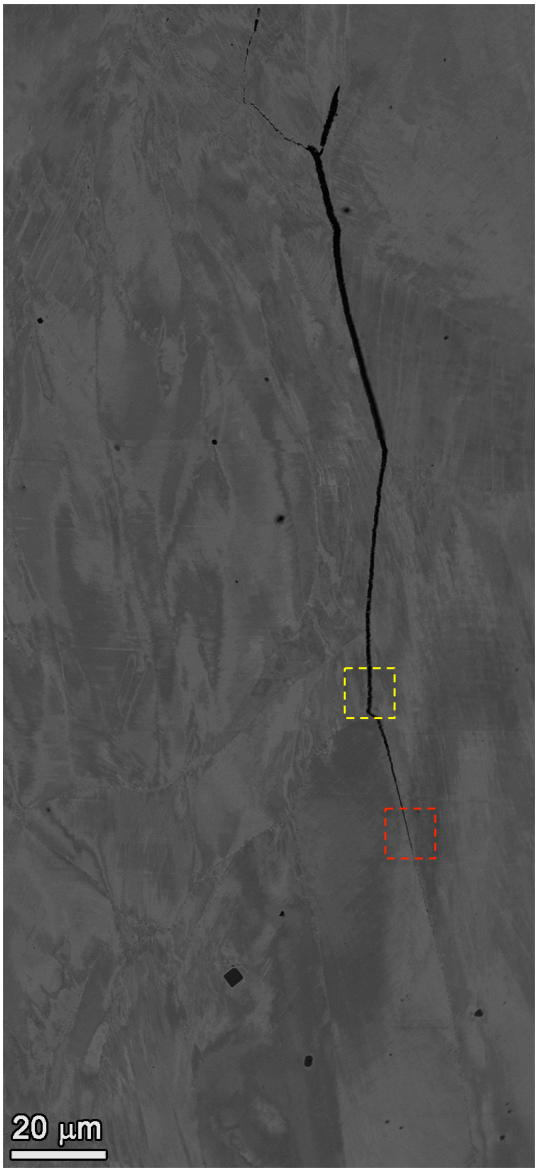

Figure 106. SEM-BSE micrograph of crack #1 in Figure 105. Note the red box near the visible crack tip and the yellow box further behind.

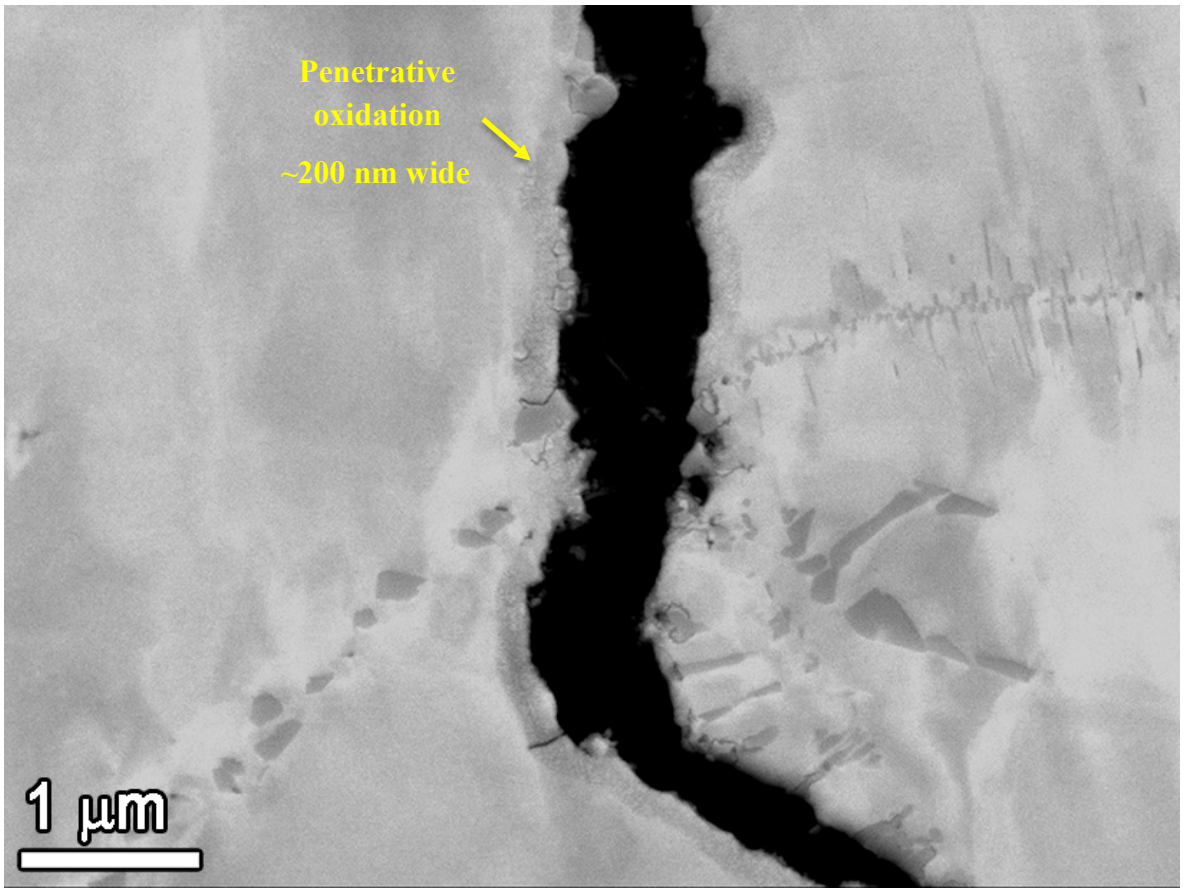

Figure 107. SEM-BSE image showing penetrative oxidation in the yellow box in Figure 106.

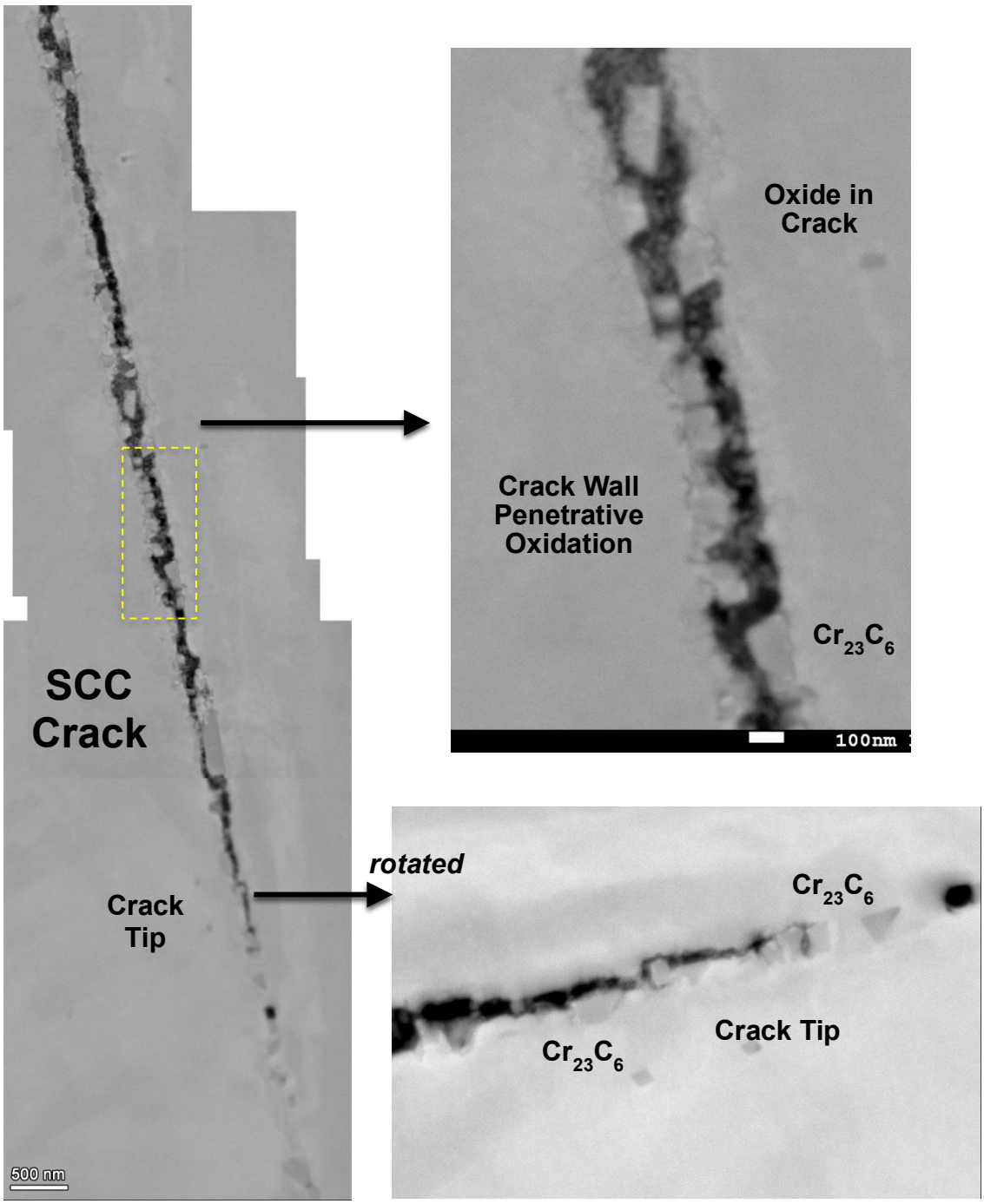

Figure 108. SEM-BSE images showing penetrative oxidation in the dashed red box in Figure 106.

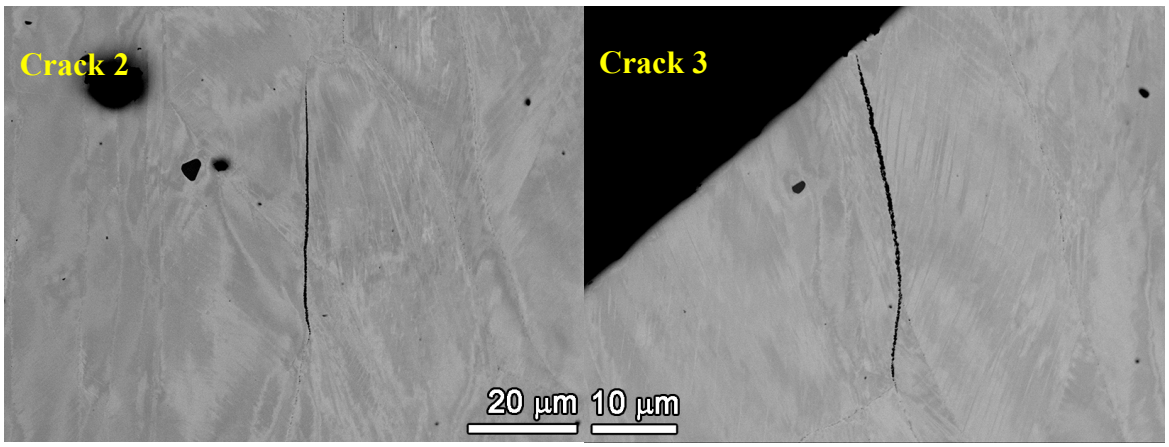

Figure 109. SEM-BSE images showing low magnification images of crack #2 and #3.

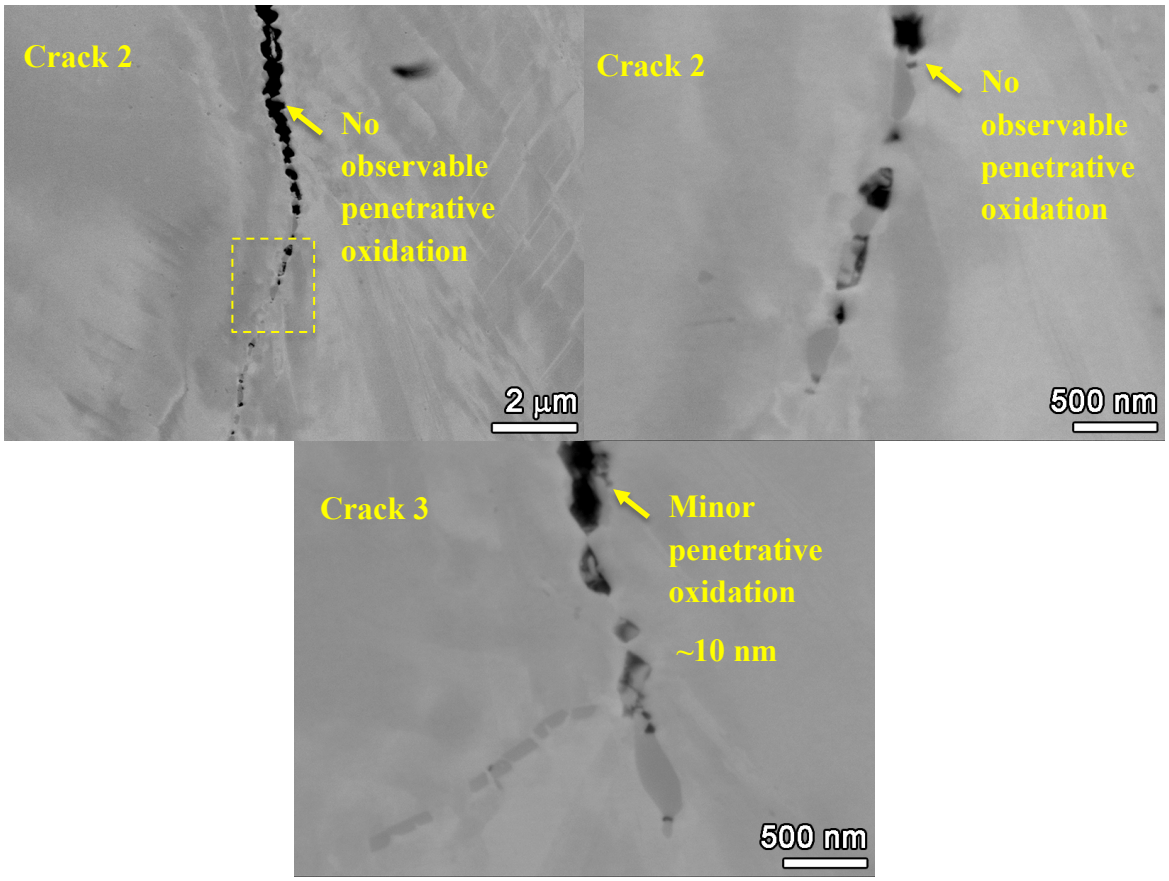

Figure 110. SEM-BSE images of crack #2 and crack #3 (see Figure 105), both of which were identified as creep cracks. No significant penetrative oxidation was observed.

TEM of Cracks in IN007

In order to better understand the differences between SCC cracks and creep cracks in IN007, site specific FIB TEM samples were produced at the leading tips of crack #1 and #3 and examined

using high resolution STEM annular DF imaging in conjunction with EDS mapping. Figures 111 and 112 show low and high magnification STEM DF/EDS elemental maps of crack tip #1, highlighting the last 5.5 µm of the SCC crack. From the annular DF image and the Cr-K map, it is apparent that the carbides are adhering to either side of the crack and that the metal is not deformed between the carbides. As was observed in the SEM-BSE images, the penetrative oxidation is observed to gradually become thicker moving away from the leading tip. Aside from the Cr depletion of the bulk grain microstructure, there was no enhanced Cr depletion ahead of the leading SCC crack tip. Ahead of the crack tip, voids were observed adjacent to the carbides, but there was no apparent oxide in the voids nor did the cracks appear to coalesce. At high magnification over the last 800 nm of the leading crack tip, the gradual decrease of the penetrative oxidation to the leading tip can be observed. The oxidation at the very leading tip can be seen moving around a Cr carbide. No Cr depletion was observed ahead of the crack tip.

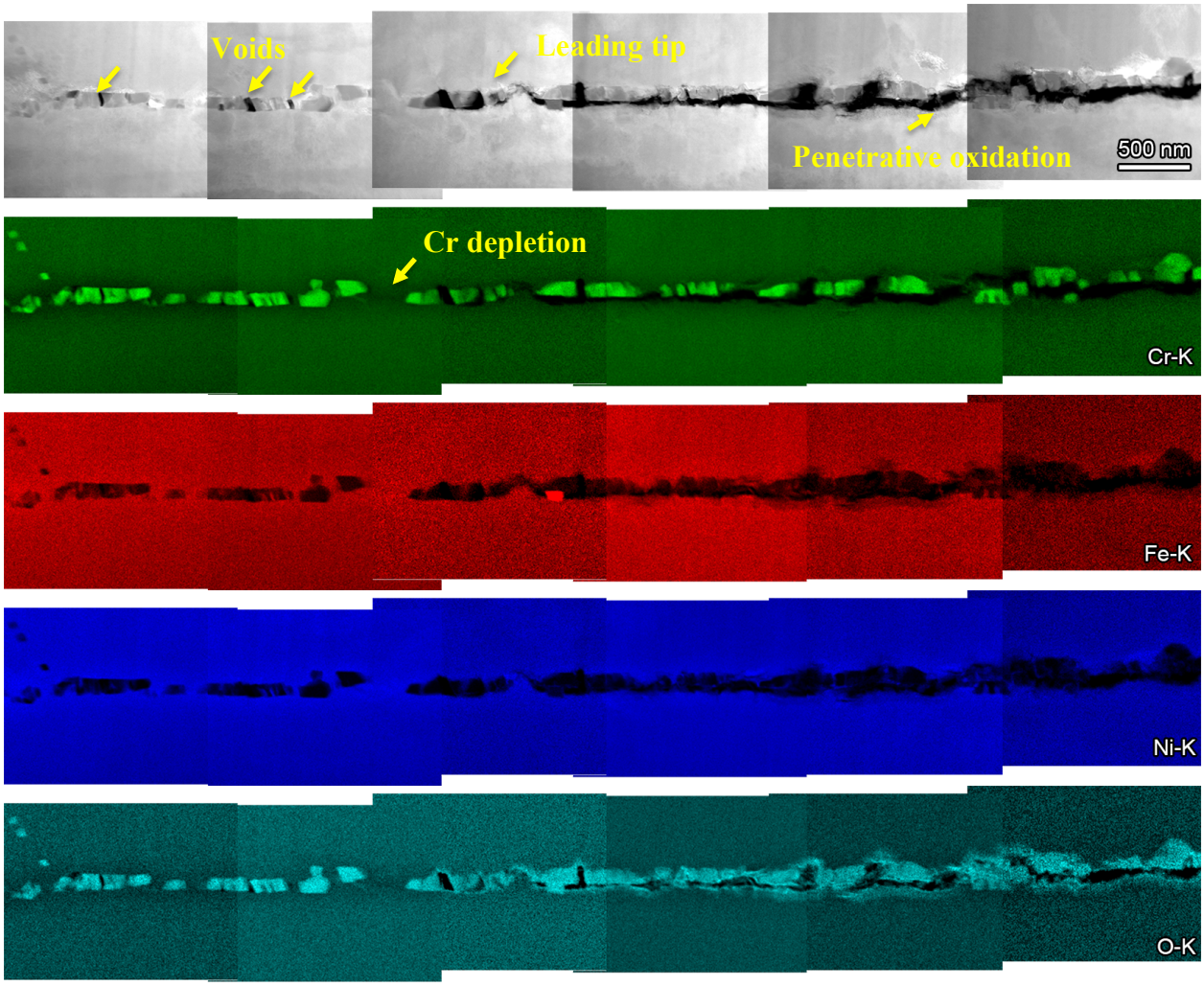

Figure 111. TEM Angular DF and EDS elemental map montages of crack #1 (see Figure 105).

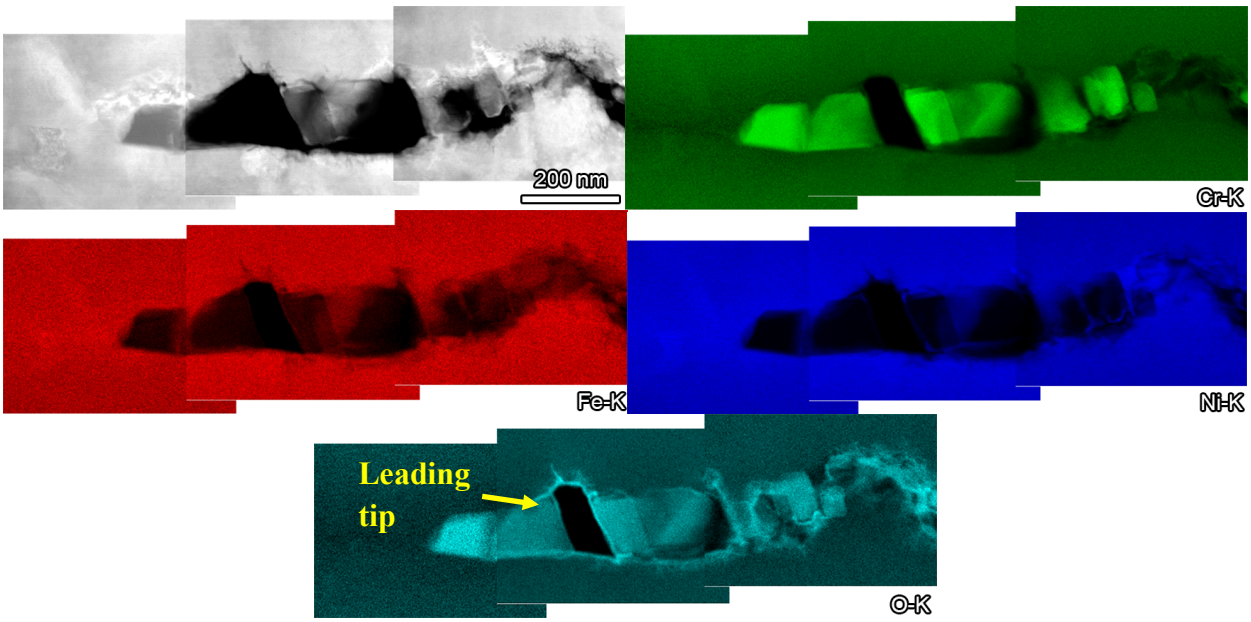

Figure 112. High magnification TEM angular DF and EDS elemental map montages crack #1 (see Figure 105).

Figures 113, 114 and 115 show low and high magnification STEM DF/EDS elemental maps of creep crack #3 (see Figure 105), highlighting the last ~5.5 µm up to the leading tip. As shown in the backscatter SEM images, the creep cracks are distinguished by the dimpled fracture appearance in the open crack region where metal on either side of the grain boundary in between carbides has failed in a ductile fashion (Figure 113). Ahead of the creep crack there appears to be a high density of voids along the boundary adjacent to carbides. EDS mapping in Figure 114 revealed that there was no apparent chemical segregation around these voids. The only chemical segregation observed was Cr depletion along the grain boundary, but this originates from the bulk microstructure already being depleted during the thermal treating process. No enhanced Cr depletion is noted near the leading crack tip. While minor, there was an O signal detected in the creep crack (Figure 115) suggesting that water had made its way into the crack to form oxides. A Fe-K signal near the leading tip and in the fibrous oxide in the crack were observed, suggesting water did make its way into the crack. The appearance of sporadic penetrative oxidation along the crack walls also denotes that the crack had opened first and then was later exposed to water. This is distinctly different from the continuous penetrative oxidation that grows gradually thicker along the crack walls from the tip in exposed SCC cracks.

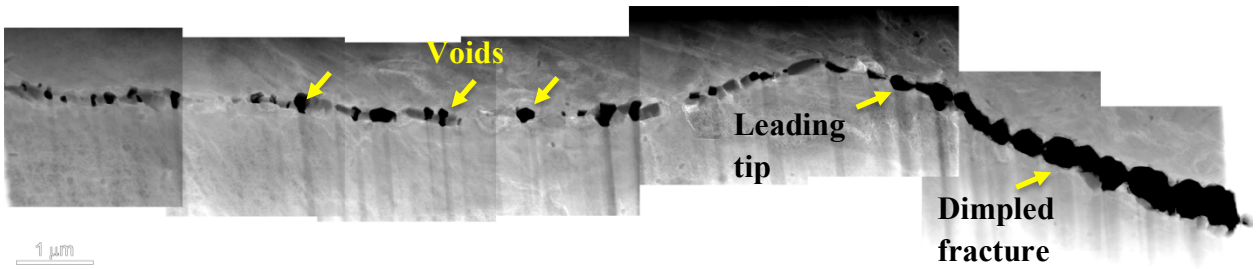

Figure 113. TEM Angular DF montage of crack #3 (see Figure 105).

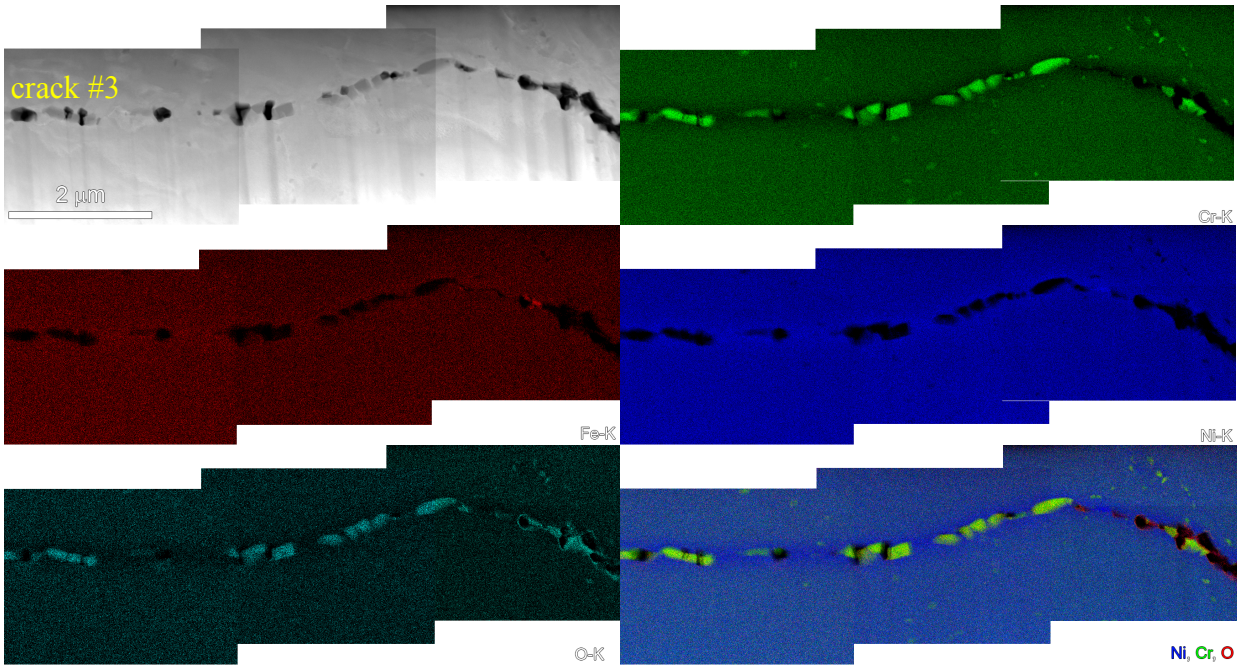

Figure 114. TEM Angular DF and EDS elemental map montages of crack #3 (see Figure 105).

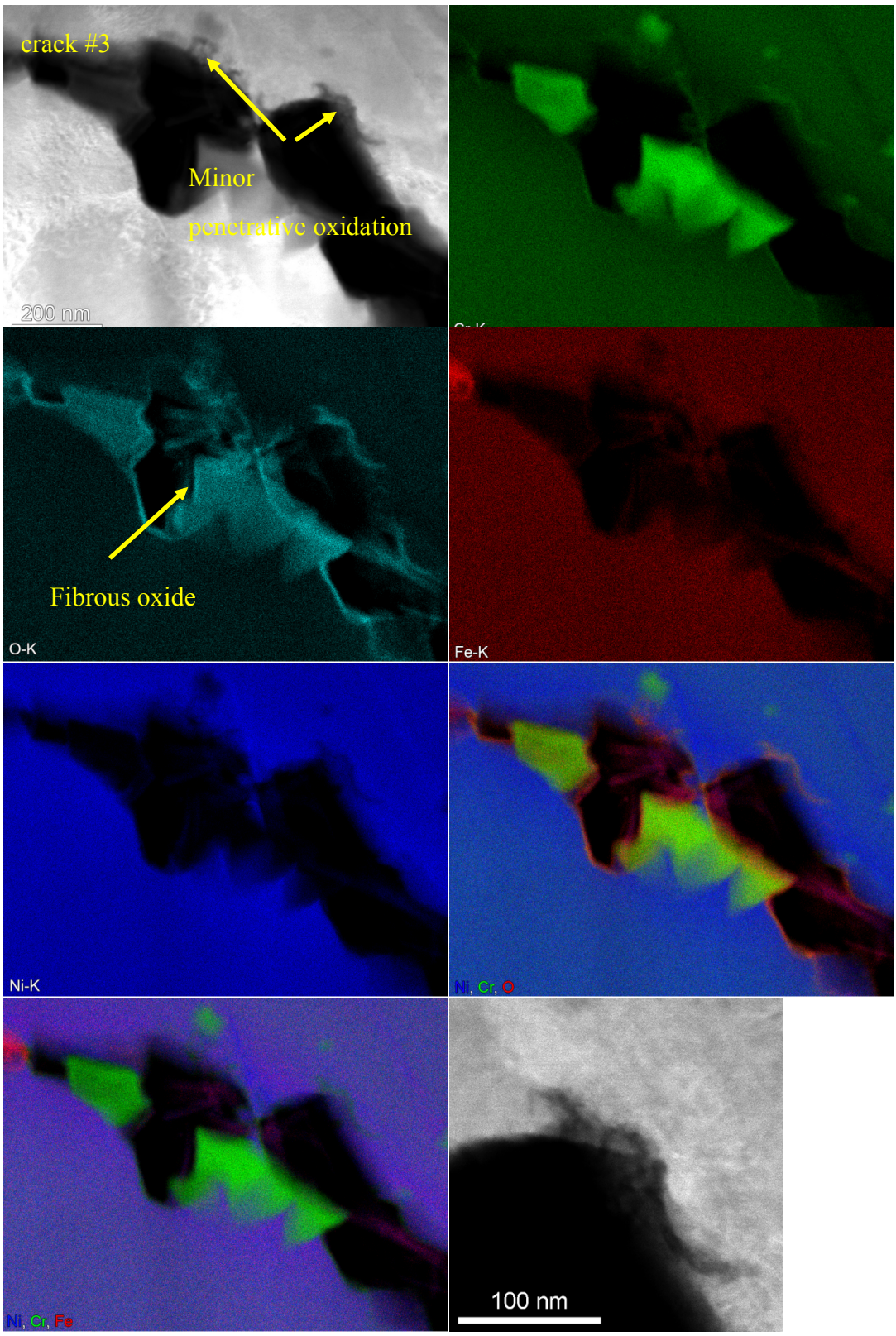

Figure 115. TEM Angular DF and EDS elemental maps of crack tip #3 (see Figure 105).

Several unexpected results were obtained from the highly cold-worked IN006 and IN007 specimens. The 26%CR plate specimen IN006 was subjected to multiple plastic deformations that produced a large number of shallow IG and TG surface cracks typically from TiN stringers. Even after 9144 hours at extremely high applied stress in 360°C PWR primary water, macroscopic SCC initiation did not occur. In comparison, the 31%CR CRDM specimen IN007 was exposed for an even longer time without any precursor cracking under constant load conditions. Initiation and rapid growth to failure was observed after slow straining was applied at a stress close to the expected ultimate strength. The mechanism of crack nucleation is uncertain, however isolated creep cavitation was detected and may play a role in the transition from micro-to-macrocrack initiation. Additional work is needed to better define the mechanical and environmental aspects necessary to promote SCC initiation in the alloy 690 materials.

SCC Initiation Test Results on Tensile Strained Alloy 690 (IN009-IN012)

Four scoping tests were performed on tensile-strained alloy 690 materials. IN009 was made from alloy 690 billet originally purchased by GE (heat B25K), while IN010 was made from the ANL alloy 690 plate (the same heat as used for the IN006 cold-rolled specimen discussed above). Both specimens were cold tensile strained to ~18% plastic strain, and then the gauge sections were polished to a 1 μm finish prior to testing at 360°C. At about 350 hours into the test, a lightning strike that caused a power spike that forced the test system to overload the specimens. The IN009 specimen made from the GE alloy 690 was strained an additional ~4%, while the IN010 ANL alloy 690 plate specimen was strained an additional ~12%. The specimens were removed from the test system for examination, and while both were still in good condition (no necking or other unusual features), this shutdown was used as an opportunity to exchange the GE specimen for a specimen made from the same 31%CR CRDM material as IN007. In addition, the decision was made to increase the tensile strain and attempt to match the measured initial yield strengths for the CR IN006 and IN007 specimens. The new CRDM specimen (IN011) was cold tensile strained to 41% plastic strain, while the alloy 690 plate specimen (IN010) was cold strained to a total tensile plastic strain up to 31%.

These two specimens, again with a 1 μm diamond polish on the gauge section, were tested at constant load at 360°C. During the initial loading, the alloy 690 CRDM specimen IN011 was allowed to undergo ~1% plastic strain in an attempt to reach the yield stress in the ANL alloy 690 plate specimen IN010. However, the stress versus strain plot for the CRDM specimen showed a slightly negative slope during plastic straining indicating that necking may have already begun. Load was adjusted to prevent the specimen from undergoing in-situ straining failure, and after ~1400 hours of exposure as shown in Figure 116, the test was stopped to examine the specimens. SEM-based examinations in unstrained regions of the surface revealed that TiN particles were corroded as observed in IN006 and IN007, but no cracks into the alloy 690 were found. In the necked region of the 41% tensile strained alloy 690 CRDM, significant

strains were observed on the surface as shown in Figure 117. Small TG cracks were observed to have nucleated from some of the corroded TiN particles as illustrated in Figure 117d and in Figure 118.

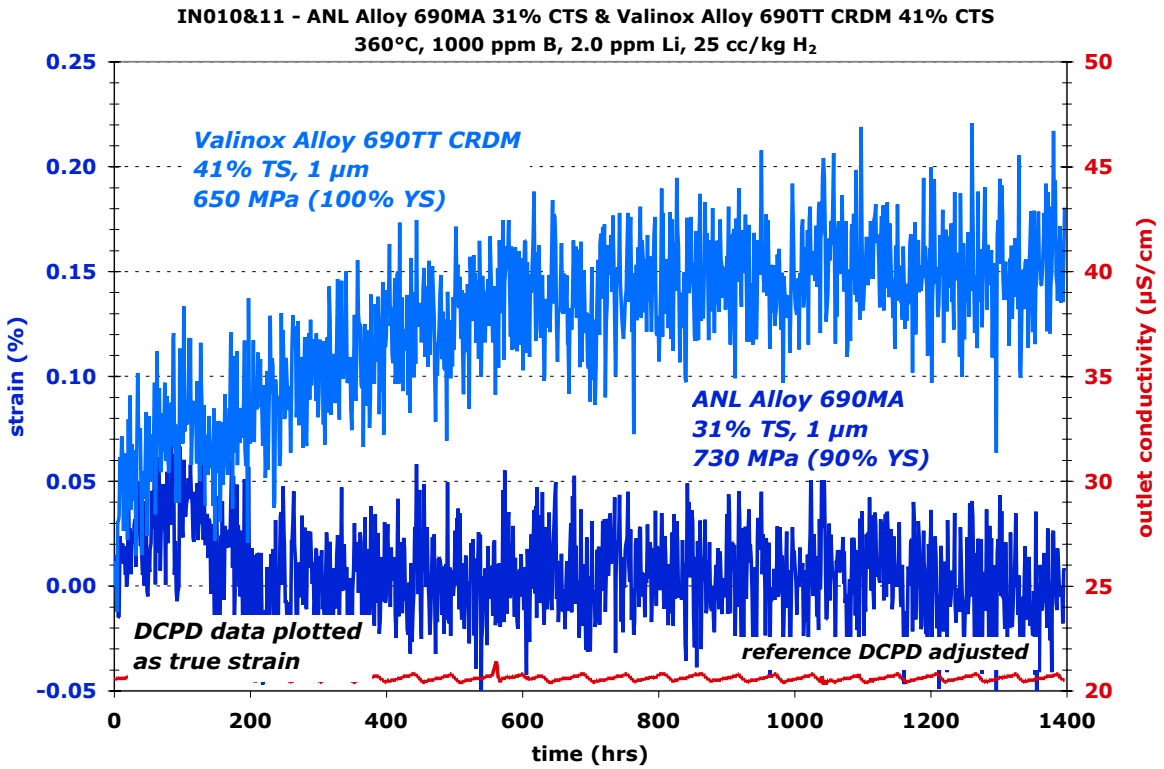

Figure 116. 31% tensile strained ANL alloy 690 plate (IN010) and 41% tensile strained alloy 690 CRDM (IN011) response during exposure in 360°C simulated PWR primary water at constant load near the yield stress.

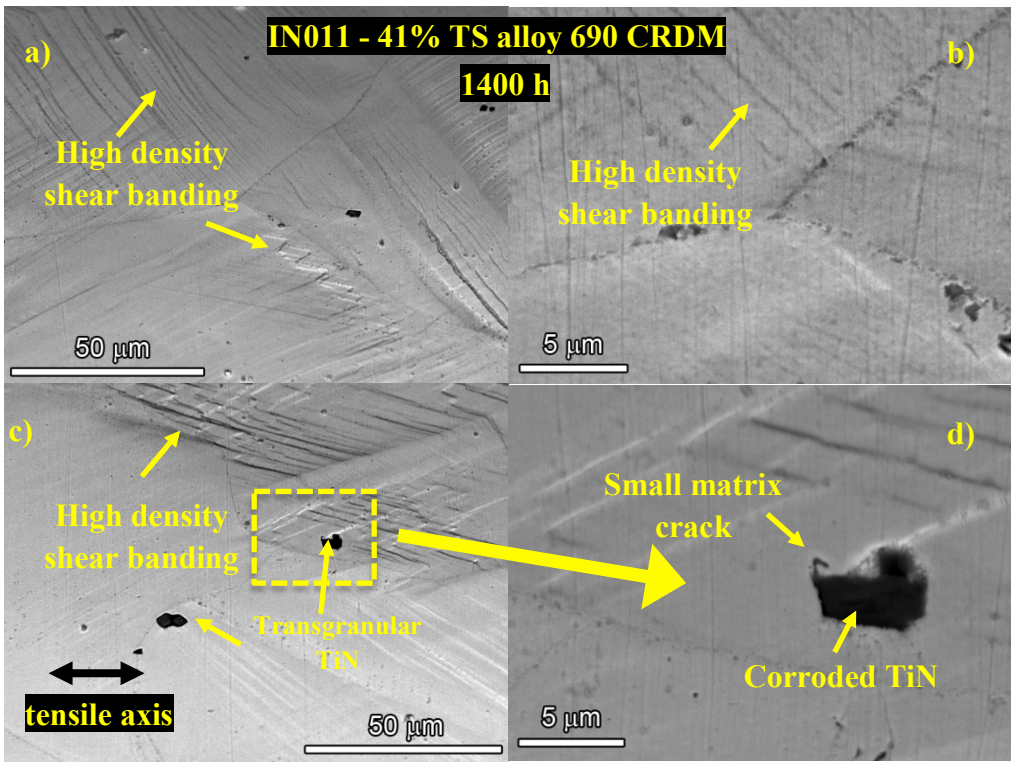

Figure 117. SEM-BSE images of the surface of 41% tensile strained alloy 690 CRDM specimen IN011 showing high levels of shear banding. No apparent IG crack initiation was observed. Representative grain structures are shown in a) and b). Corrosion and cracking of TG TiN particles was observed (c-d).

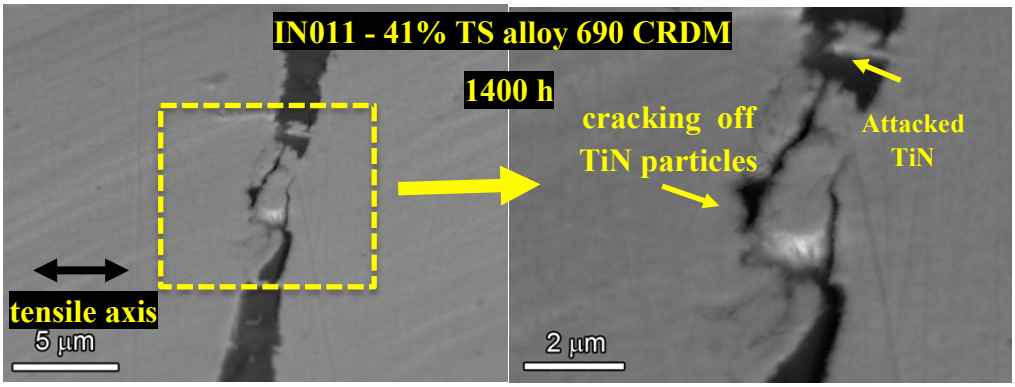

Figure 118. SEM-BSE images of the surface of 41% tensile strained alloy 690 CRDM specimen IN011. Corrosion and cracking of TG TiN particles was observed.

The decision was made to discontinue the test on the 41% tensile strained specimen, and it was metallographically prepared in cross-section to allow characterizations of damage microstructures. The in-situ plastic strain introduced into the specimen did result in surface damage near grain boundaries as illustrated in Figure 119 where a small V-shaped crack is observed to have formed. No evidence for grain boundary corrosion near or at the surface was observed, and instead a thin Cr_2O_3 film was found above grain boundaries intersecting the surface as shown in Figure 120, consistent with observations of unstressed specimens discussed earlier in this report. Void formation observed throughout material adjacent to carbides was due to the initial 41% cold-tensile straining and there was no indication that the void density or size increased during the initiation test at 360°C.

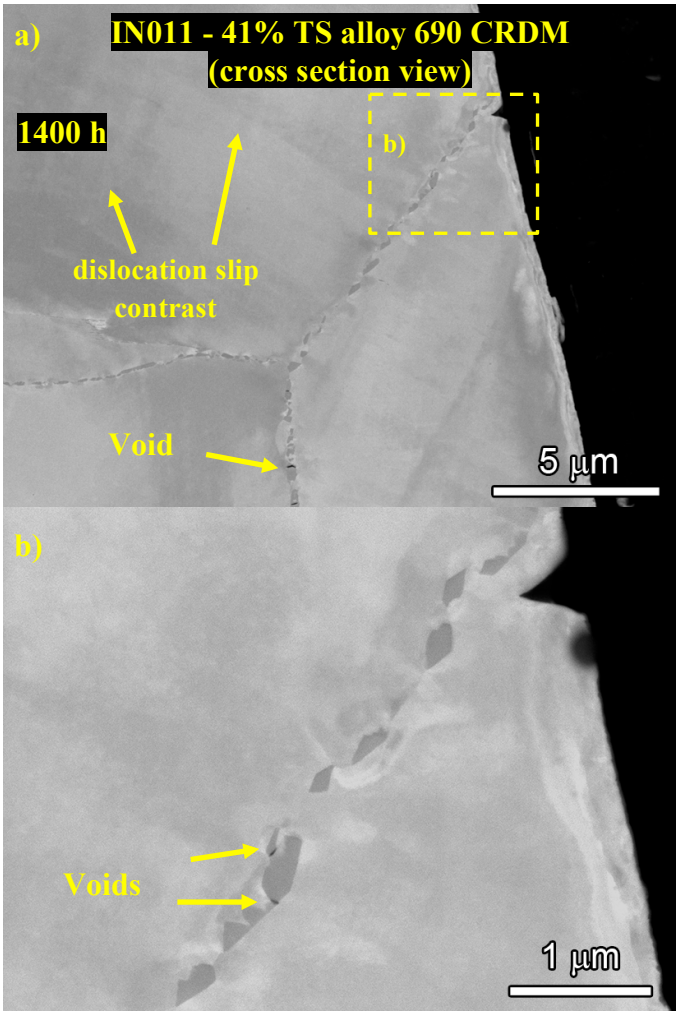

Figure 119. These cross section images illustrate deformation seen close to a grain boundary intersecting the surface of the specimen. The V-shaped feature is likely a result of a slip band. Void formation adjacent to carbides as shown here was seen throughout the necked region, including in the bulk away from the surface. No evidence for localized grain boundary corrosion or oxidation is seen.

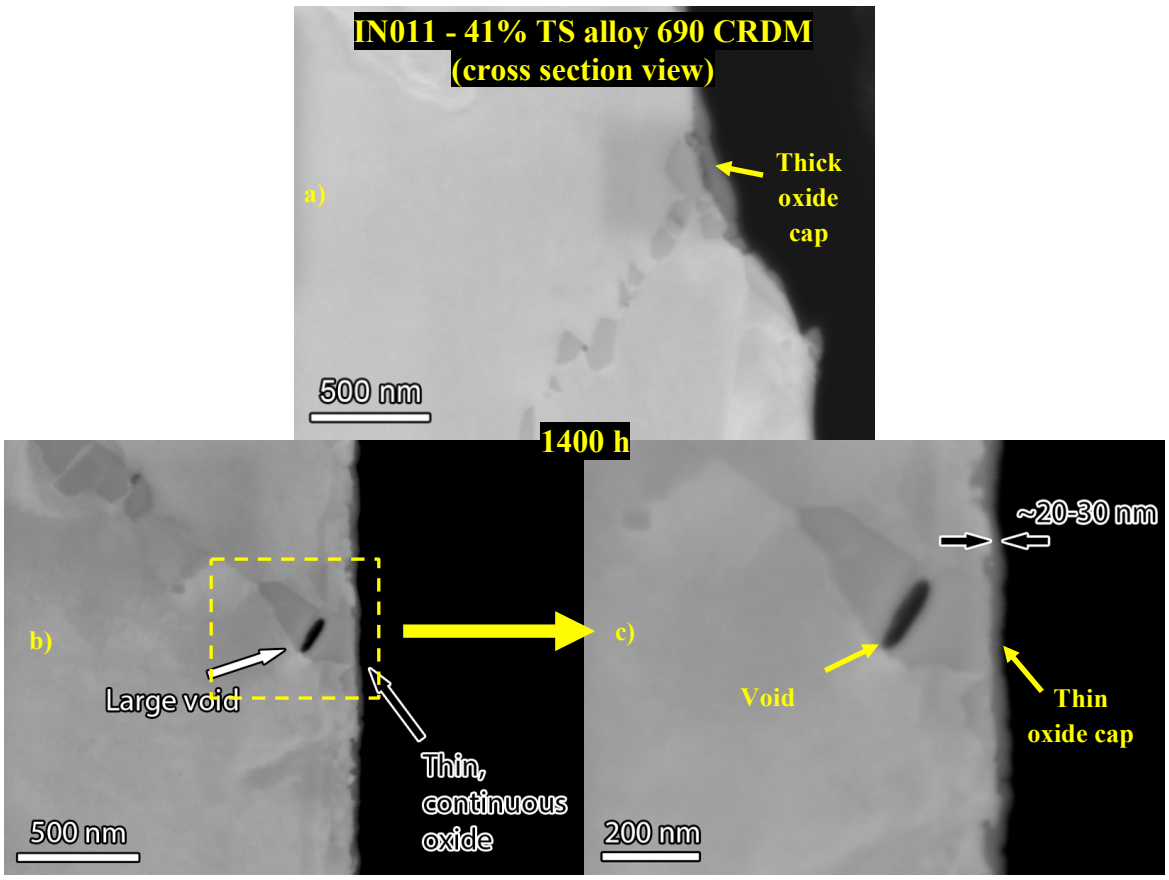

Figure 120. SEM-BSE images of the 41% tensile strained alloy 690 CRDM illustrating a thin, 20-30 nm, continuous oxide at the surface and voids between IG carbides.

A third exposure on tensile strained material followed and consisted of pairing the 31% tensile strained, ANL alloy 690 plate specimen (IN010) having 1400 hour of prior exposure with a new alloy 690 CRDM specimen (IN012) of the same heat, this time with the specimen plastically strained to 24%. Knowing that IN012 was going to have a lower strength than IN010 due to a lower degree of cold work, the gauge diameter of IN010 was made slightly larger so that the yield load would be similar. An overview of the entire test is shown in Figure 121. As with the test on the CR specimens (IN006/IN007), periodic load and strain increases were applied as indicated in the plot, however two additional loading schemes were also employed. From ~1200 to ~1700 hours, a 0.001 Hz cycle with R = 0.5 was applied every 10 hours. This produced no observable change in the specimen response, and at ~1700 hours, the load cycle was removed and followed by slowly increasing the load (stress) that induced a small amount of plastic strain. In this instance, the alloy 690 CRDM specimen IN012 underwent ~1.5% plastic strain while the ANL alloy 690 plate specimen IN010 underwent ~0.2% plastic strain. After another 1000 hours with no indication of crack initiation, the load was again increased to induce additional plastic strain. This time it was the ANL alloy 690 plate specimen that underwent significant plastic strain while the alloy 690 CRDM specimen IN012 did not plastically strain at all.

As this test was reaching ~3000 hours of exposure, the test on the CR specimens (IN006/IN007) reached ~6300 hours of exposure with no indication of crack initiation. With a strong likelihood that the application of periodic plastic strain would not sufficiently accelerate the crack initiation process for the IN010/IN012 specimens, the decision was made to apply continuous slow straining. At ~3200 h, loading was converted to constant extension rate at 2.6×10^{-8} in/sec at the actuator. Neglecting load-train stretch (it is small under these conditions of low strain hardening) and assuming that the extension is evenly distributed between the two specimens, this produces a gauge strain rate of $\sim 1 \times 10^{-7}$ s^{-1}, which is well within the typical range often used for slow-strain-rate SCC experiments.

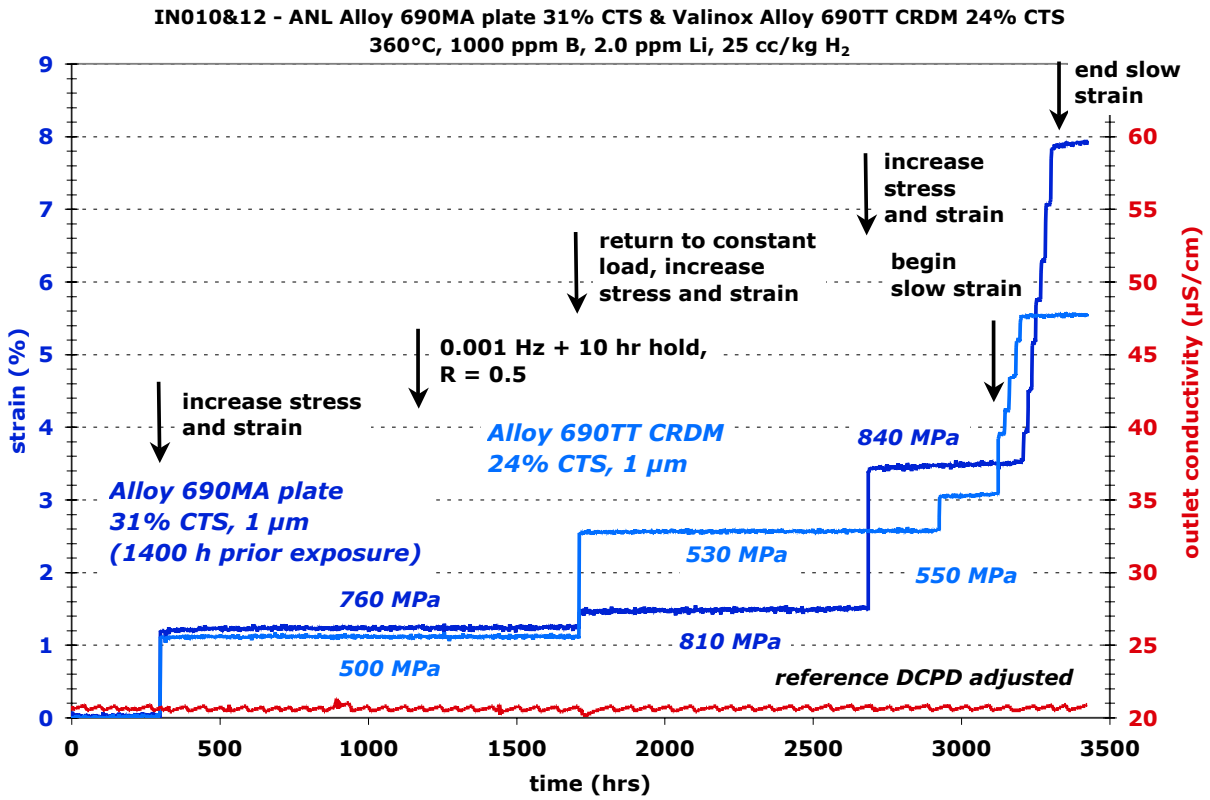

Figure 121. Overview of the entire test on the 31% tensile strained alloy 690 plate (IN010) combined with a 24% cold tensile strained alloy 690 CRDM specimen (IN012). Note that IN010 has 1400 hours of prior exposure.

Figure 122 shows this portion of the test in greater detail and includes the load change data. The steps in the strain plots are due to a combination of load train elasticity, friction between the pullrod and the pullrod environmental seal, and probably dynamic strain aging. As can be seen, the 24%TS alloy 690 CRDM specimen IN012 underwent ~2.5% plastic strain before it sufficiently strain hardened to drive the 31% cold tensile strained alloy 690 plate to start plastically straining. At this point, all additional extension was absorbed only by the plate specimen, and upon reaching ~4.5% plastic strain after a period of ~200 hours, the test was converted back to constant load. The test was then ended ~100 hours later to perform specimen examinations.

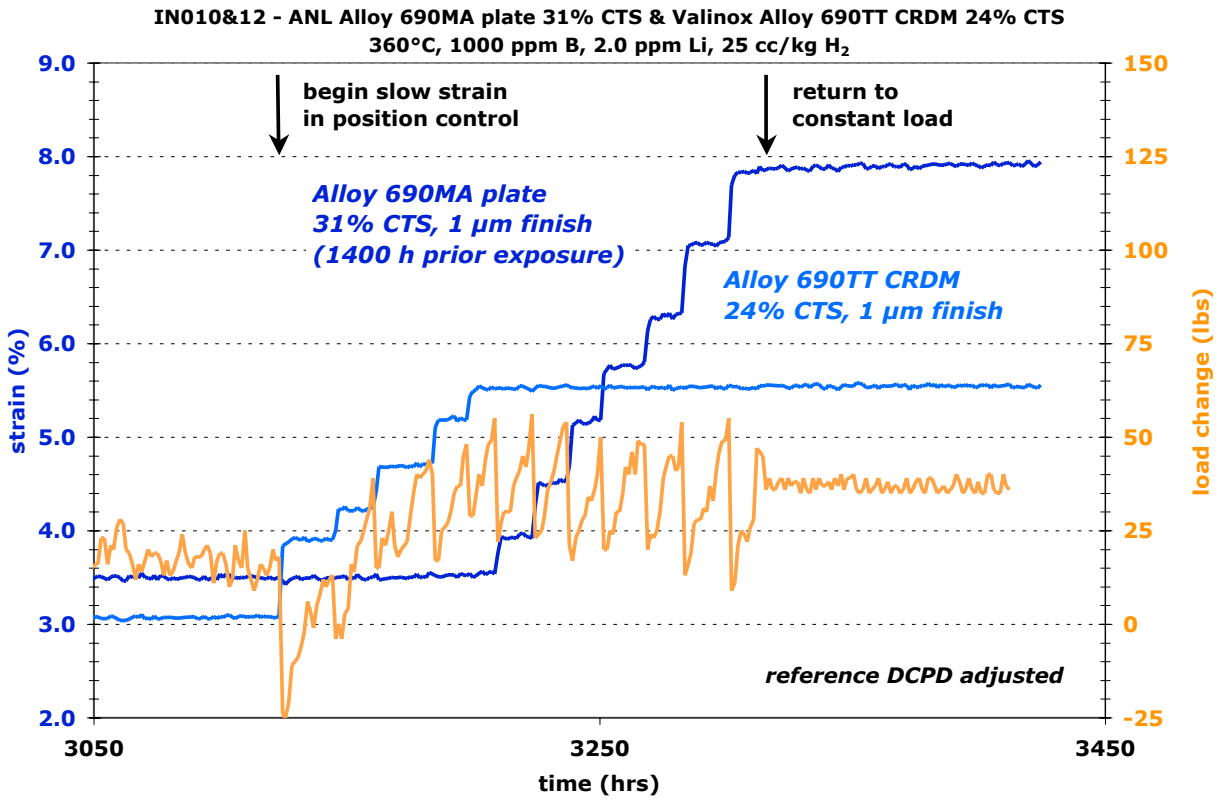

Figure 122. Slow straining response of the 31%TS alloy 690 plate (IN010) combined with a 24%TS alloy 690 CRDM specimen (IN012). Note that IN010 has 1400 hours of prior exposure.

Examinations have only been performed on the 31% tensile strained ANL alloy 690 plate specimen IN010 with Figures 123 and 124 showing a high density of slip bands intersecting the surface as well as cracks having nucleated from corroded TiN particles. Small TG cracks can be seen associated with many of the slip lines.

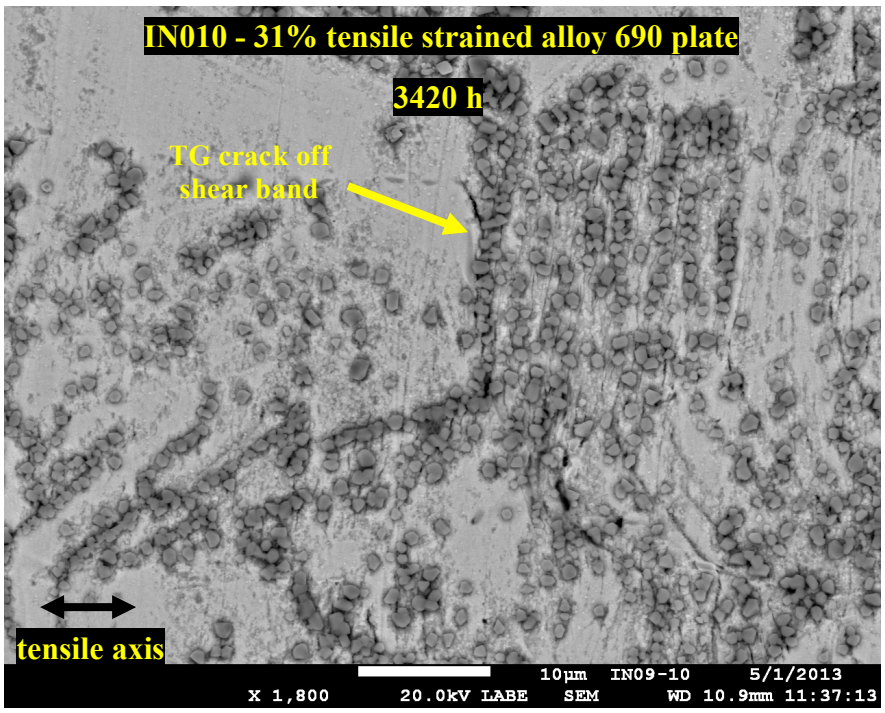

Figure 123. SEM-BSE image of the surface the 31%TS ANL alloy 690 plate specimen (IN010) showing shear bands intersecting the surface. Cracks appear to have formed at many shear bands. Large Ni-Fe spinels on the surface obscure the view.

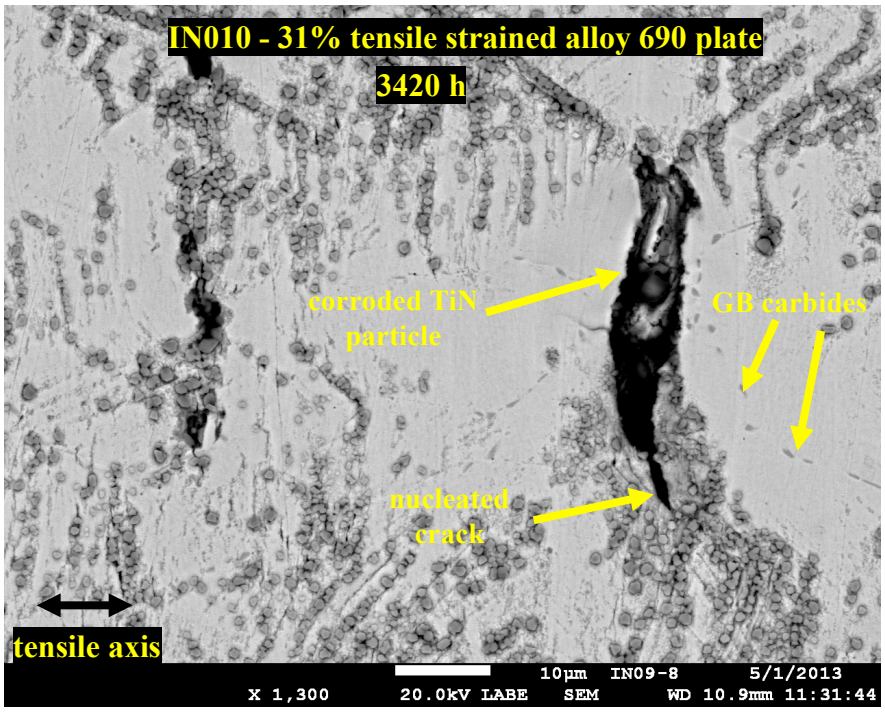

Figure 124. SEM-SE image of the surface the 31%TS ANL alloy 690 plate specimen (IN010) showing shear bands intersecting the surface and cracks nucleated off of corroded TiN particles.

Blunt Notch SCC Initiation Tests on Cold-Worked CRDM Specimens

Mechanisms controlling crack initiation in cold-worked alloy 690 are also been evaluated at General Electric Corporate Research under a PNNL subcontract using blunt-notch CT specimens. Standard 0.5T CT specimens are being used, but the notch tip was "wet ground" to a ~0.6 mm radius using a diamond wheel and given a final polish at PNNL to a 1 µm diamond finish. This created a well-controlled surface from which crack initiation and advance can be monitored using DCPD techniques and matches the surface condition for the tensile specimens. Two 31%CF alloy 690 CRDM specimens, c672 (Valinox heat RE243) and c673 (Sumitomo heat E67074C), were provided by PNNL and tested in series. Specimens were equilibrated for about a week in 360°C PWR primary water, loaded to 27.5 MPa√m and held for ~500 hours, then increased to 44 MPa√m over ~200 hours and again held for ~500 hours. The test response is presented in Figures 125 and 126 showing DCPD-measured crack length versus test time. If there was no evidence of sustained crack advance during the hold time at 44 MPa√m, the load cycle was repeated as shown. The 31%CF Valinox specimen c672 shows a change in crack-growth rate during the 3rd hold at ~2050 hours (Figure 125). Crack initiation clearly occurred and the growth rate evolved from ~$6x10^{-9}$ to $2.5x10^{-8}$ mm/s as the crack developed. Similar behavior was observed for the 31%CF Sumitomo specimen c673 that also shows a change in crack-growth rate during the 3rd hold at ~2200 hours. The growth rate evolved from ~$3x10^{-9}$ to $1.8x10^{-8}$ mm/s as the crack developed. Unfortunately, the test was not stopped at this point to investigate the blunt notch surface for evidence of cracks, and a 4th cycle was applied. This produced a significant increase in the DCPD-measured crack-growth rates likely due to sharp increase in the distribution and depth of cracks. The test was ended after 2560 hours and specimens were sent to PNNL for optical and SEM examinations.

Preliminary examinations focused on the notch surfaces for the c672 and c673 specimens. Because the notch was polished before testing, cracks were readily identified by SEM-BSE imaging. Crack distributions from a singe area on both specimens were documented as indicated in Figures 127 and 128 with individual cracks further highlighted in red. In order to better illustrate the morphology and size of the surface cracks, higher magnification images are presented in Figures 129 and 130 for specimen c672 and in Figures 131 and 132 for specimen c673. The cracks are clearly IG and surface features suggest significant deformation had occurred during crack nucleation. EDM sectioning was then performed to obtain 5 slices (~2 mm thick), equally spaced across the thickness of the specimen so that subsurface cracks could be mapped in cross-section. SEM-BSE and optical images for the 5 cross-sections are shown in Figures 133 and 134 for c672 and c673, respectively. Much more extensive cracking can be seen for specimen c673 (Figure 134) particularly with slices 1-4 showing major cracks that had propagated to a depth >0.3 mm. This is in comparison to specimen c672 (Figure 133) where only slide 3 revealed deep IG cracks during these low magnification characterizations.

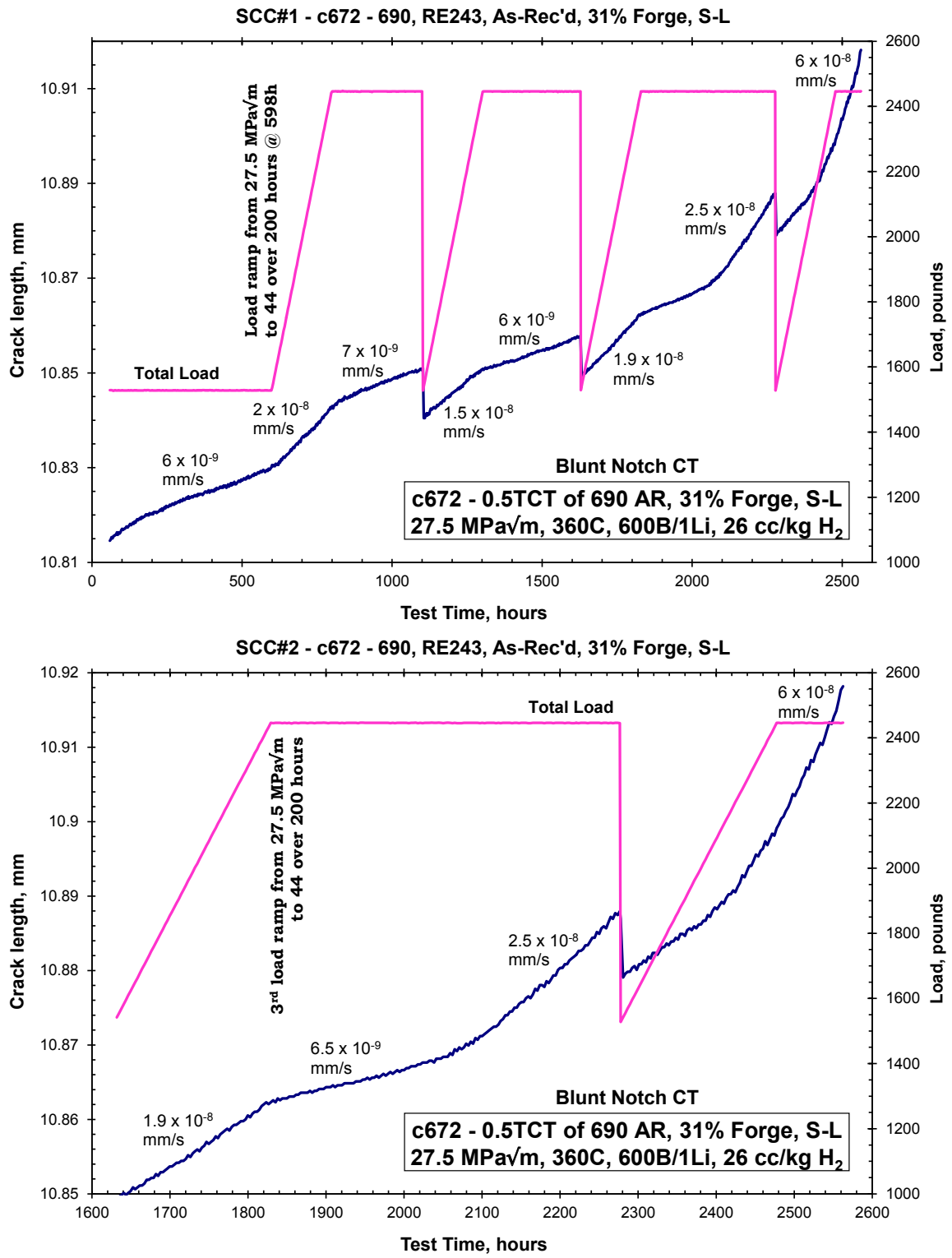

Figure 125. Crack length versus time response for the 31%CF Valinox CRDM specimen c672 blunt notch specimen.

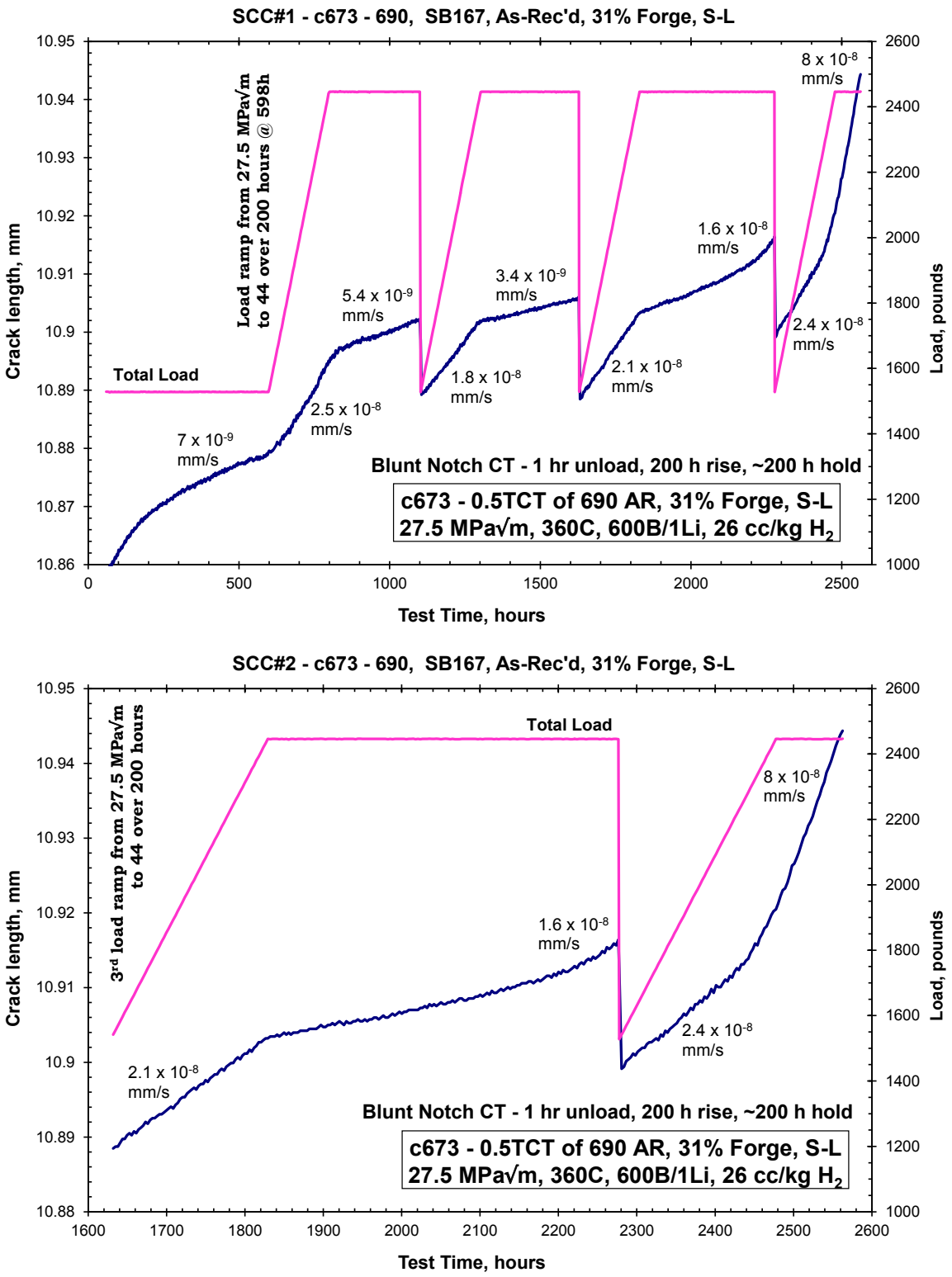

Figure 126. Crack length versus time response for the 31%CF Sumitomo CRDM specimen c673 blunt notch specimen.

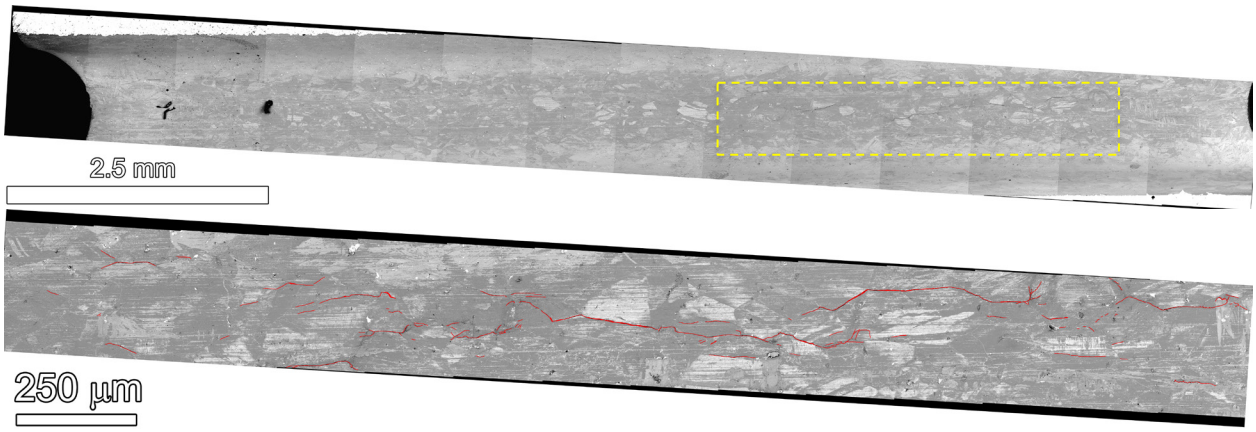

Figure 127. SEM-BSE montage of a) the entire notch of C672 (31%CF Valinox CRDM) and b) a selected higher magnification montage of the dashed yellow box in a) showing cracks.

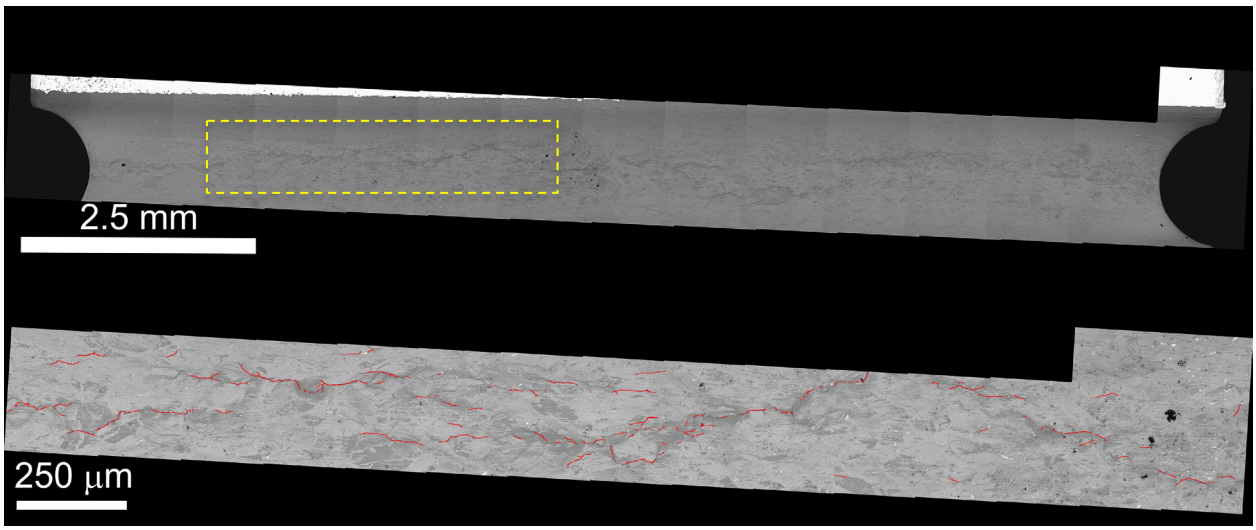

Figure 128. SEM-BSE montage of a) the entire notch of C673 (31%CF Sumitomo CRDM) and b) a selected higher magnification montage of the dashed yellow box in a) showing cracks.

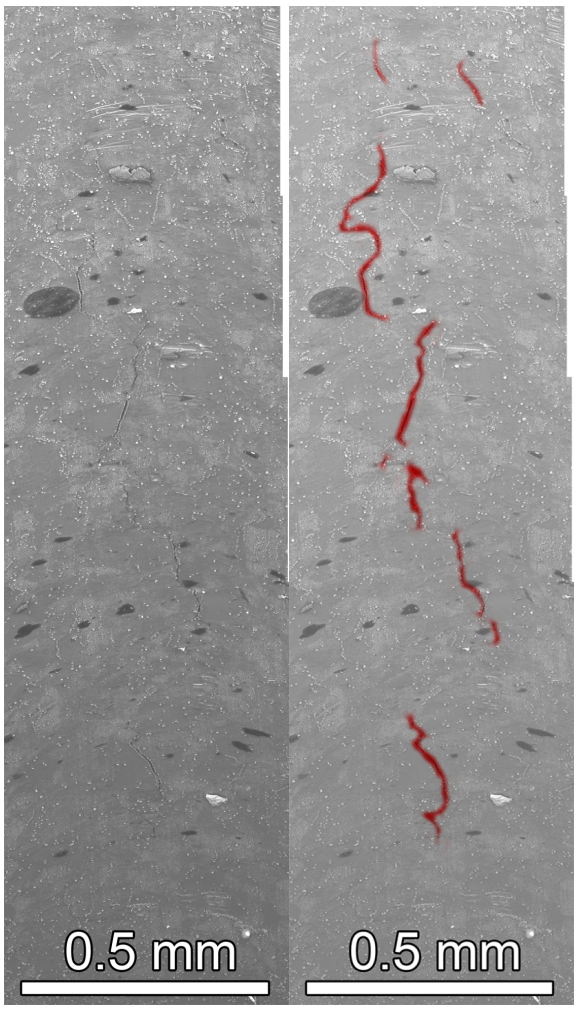

Figure 129. SEM-SE image of a portion of the 31%CF Valinox CRDM specimen c672 notch showing several nucleated cracks (highlighted by red marker in right image). Note that the image was taken at an oblique angle.

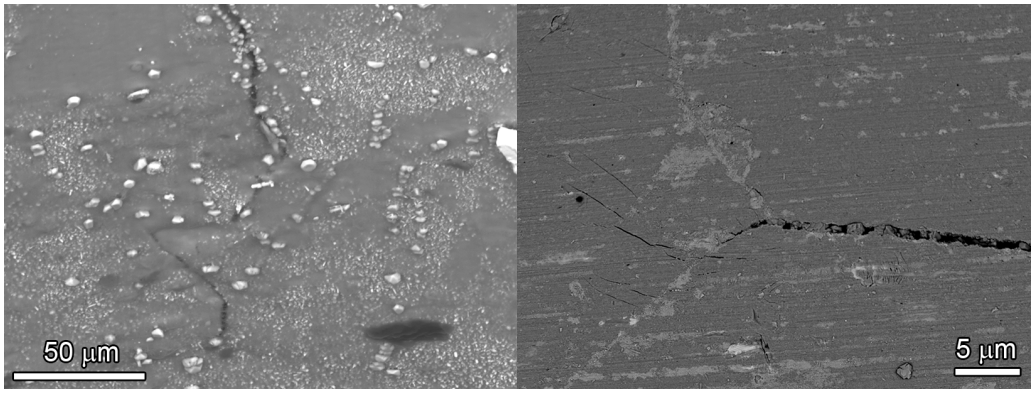

Figure 130. Higher magnification SEM-SE images showing cracks on the notch surface of the 31%CF Valinox CRDM specimen c672.

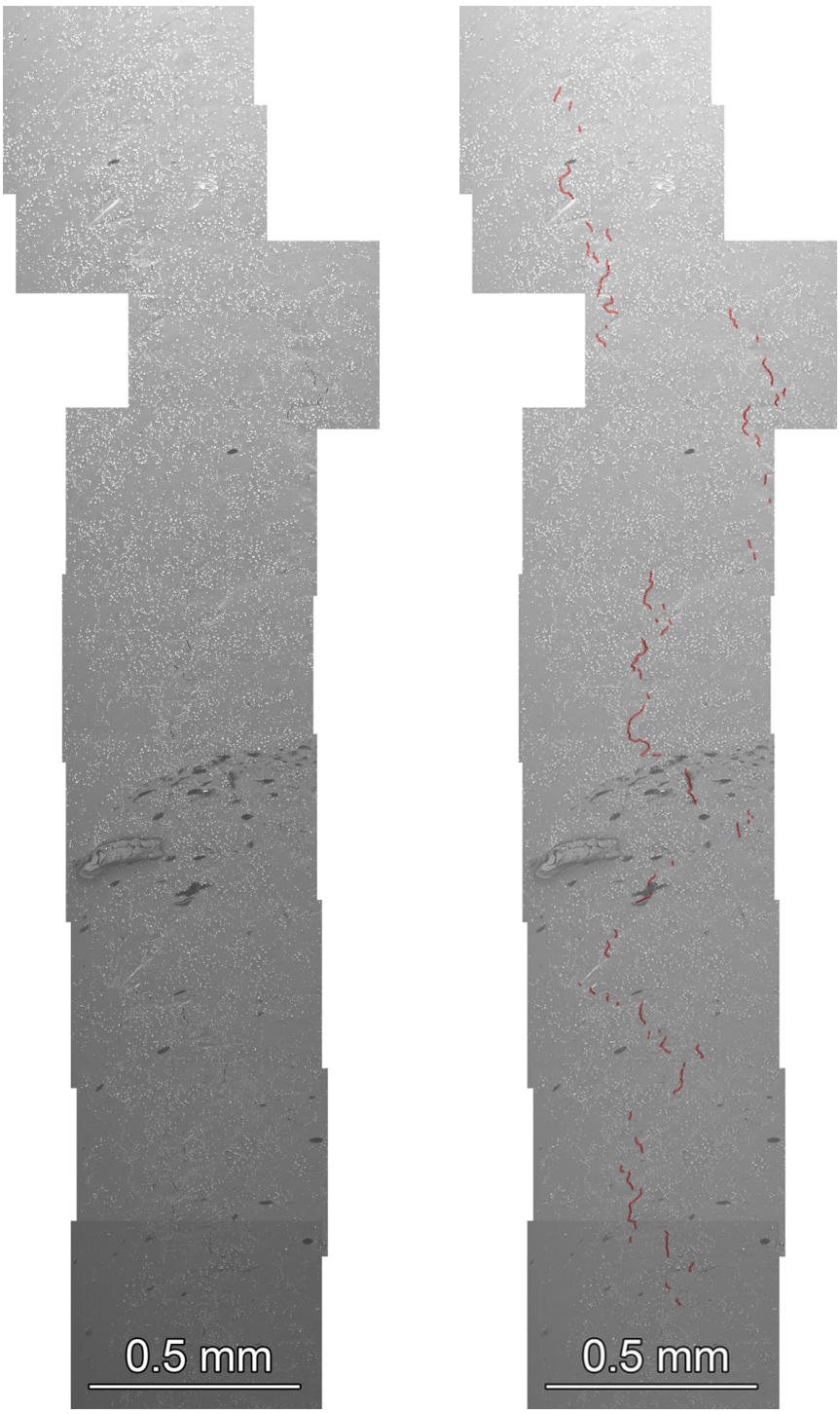

Figure 131. SEM-SE image of a portion of the 31%CF Sumitomo CRDM specimen c673 notch showing several nucleated cracks (highlighted by red marker in right image).

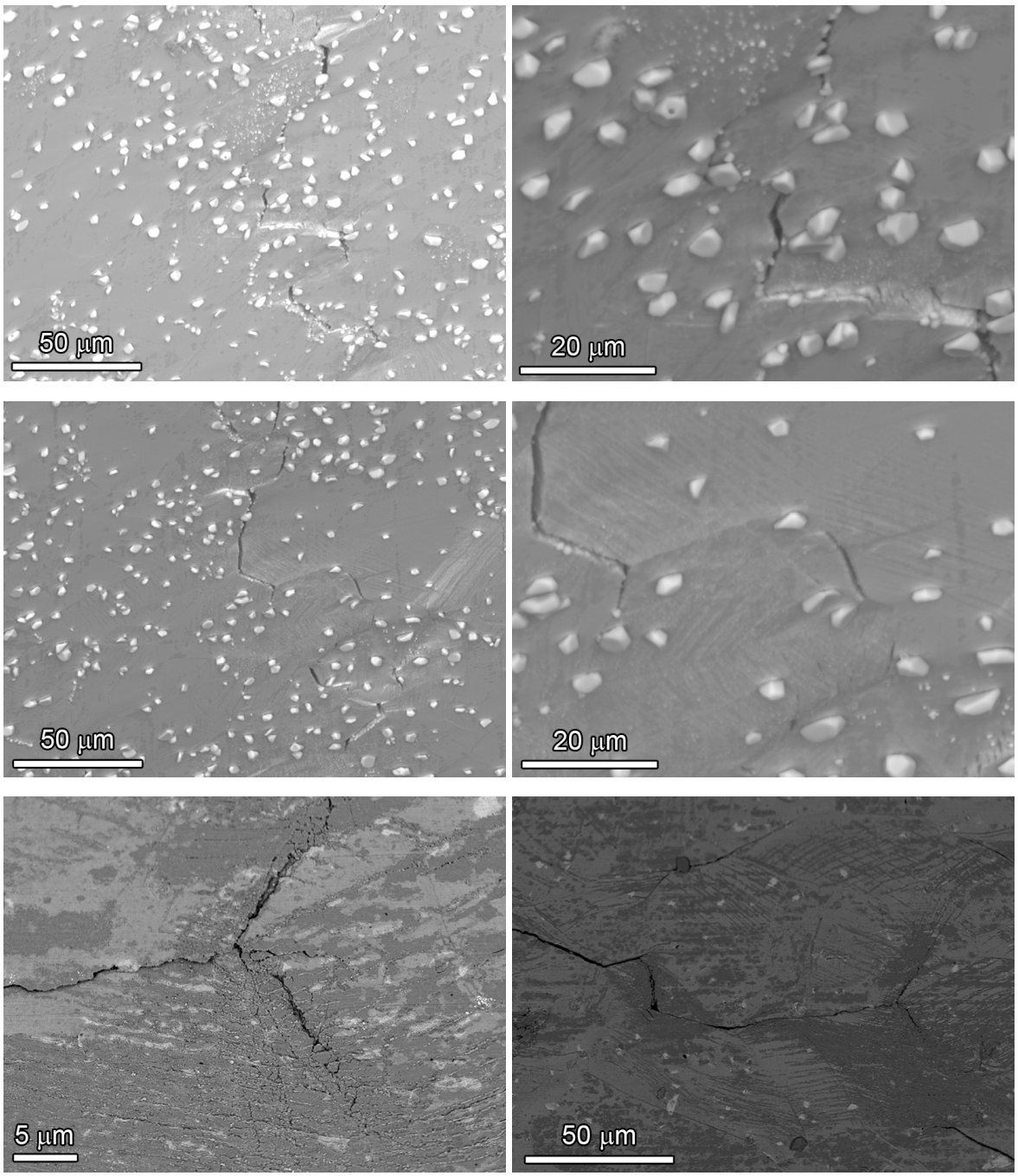

Figure 132. Higher magnification SEM images showing cracks on the notch of 31%CF Sumitomo CRDM specimen c673.

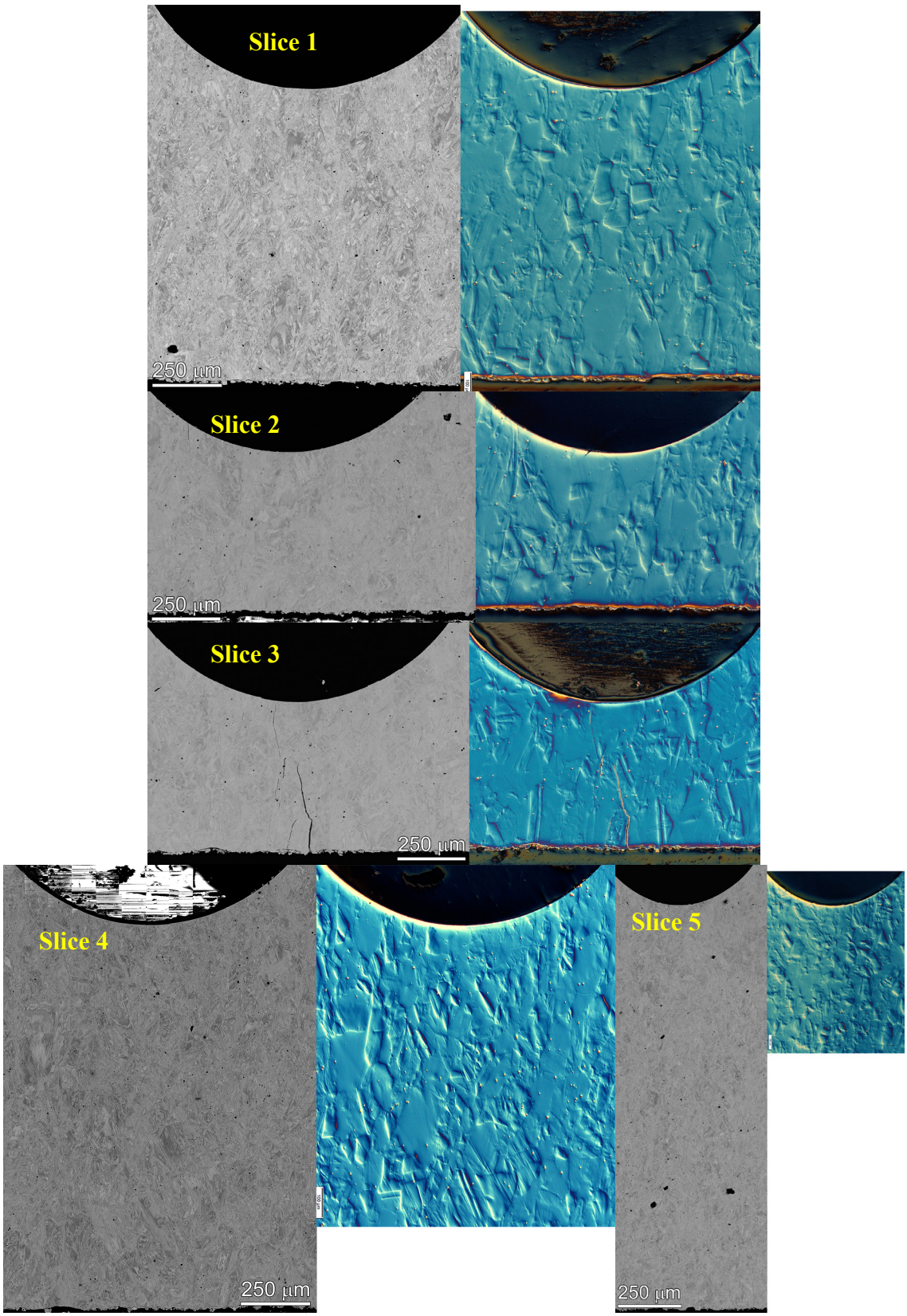

Figure 133. SEM (BSE) and optical micrographs of five slices in C672.

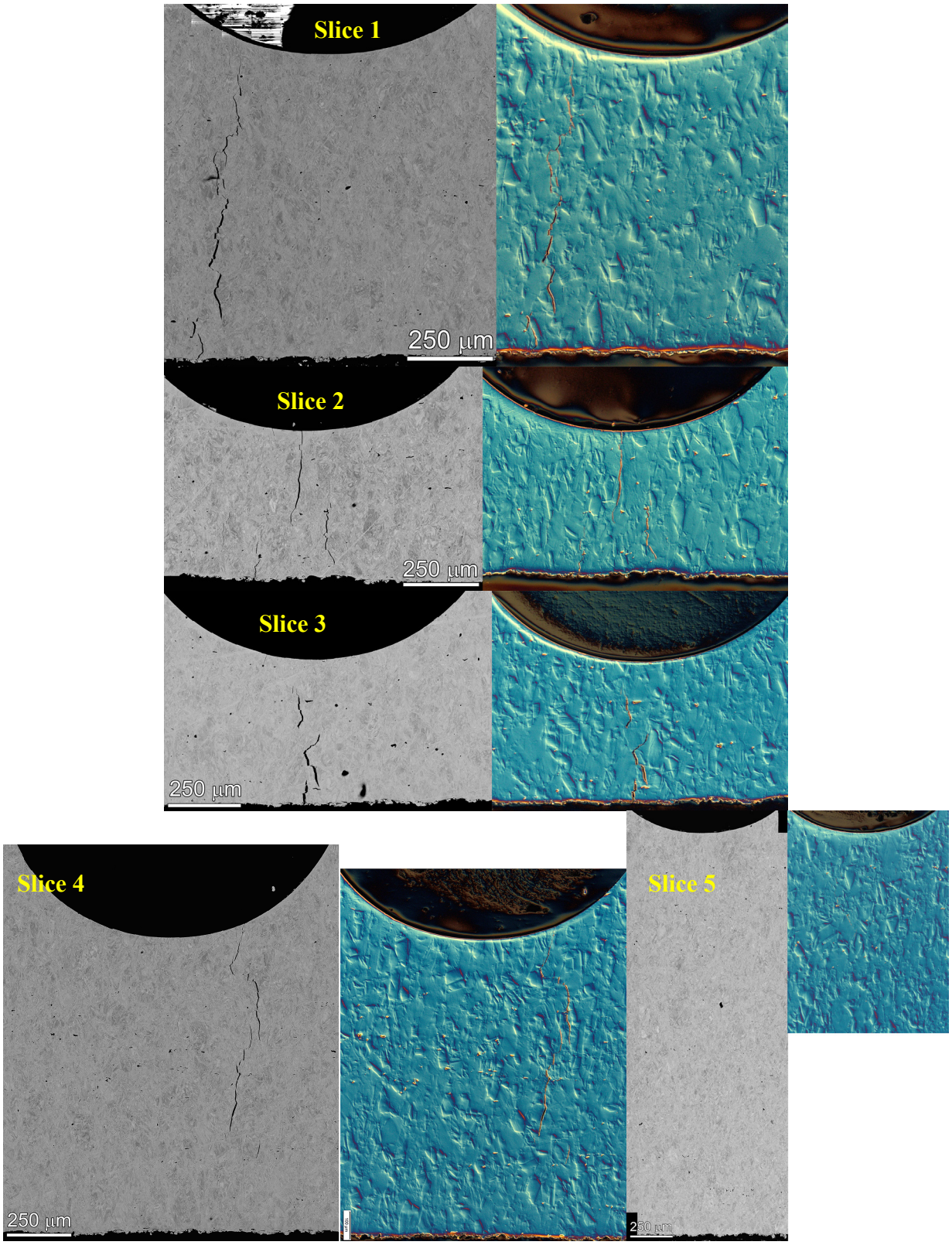

Figure 134. SEM-BSE and optical micrographs of five cross-section slices in C673.

Closer examinations of crack characteristics were made at higher magnifications and identified two fundamentally different types of cracks. Typical examples of these cracks are shown in Figure 135 from the c672 cross-section slice #1. Larger and more open cracks were found to have obvious crack wall oxidation and crack-tip structures consistent with that expected for SCC cracks. Crack-wall penetrative oxidation nanostructures and sharp IG crack tips are illustrated in Figure 136. These characteristics are entirely consistent with our previous measurements [29,30] on IGSCC tips from crack-growth test specimens. The second type of crack present was quite different as documented in Figure 137. These cracks were found at distances >~100 µm from the notch surface and were reasonably tight with evidence for grain boundary cavity formation. Most important is that there was no evidence for corrosion/oxidation along the crack walls indicating that these cracks had not been exposed to high-temperature water or the exposure time was very short. Because of these features, they have been identified as "creep" cracks and were found in most cross-sections. Two other examples are shown in Figures 138 and 139. Cavities can be seen at the crack tip region that formed at the grain boundary - carbide interfaces, and the evidence for the cavities is present along the main crack in the form of a dimpled appearance. Clearly, creep cavitation and cracking occurred during the blunt notch loading ramps as no such cavities were observed during any constant load initiation testing (or in any previous SCC CGR testing).

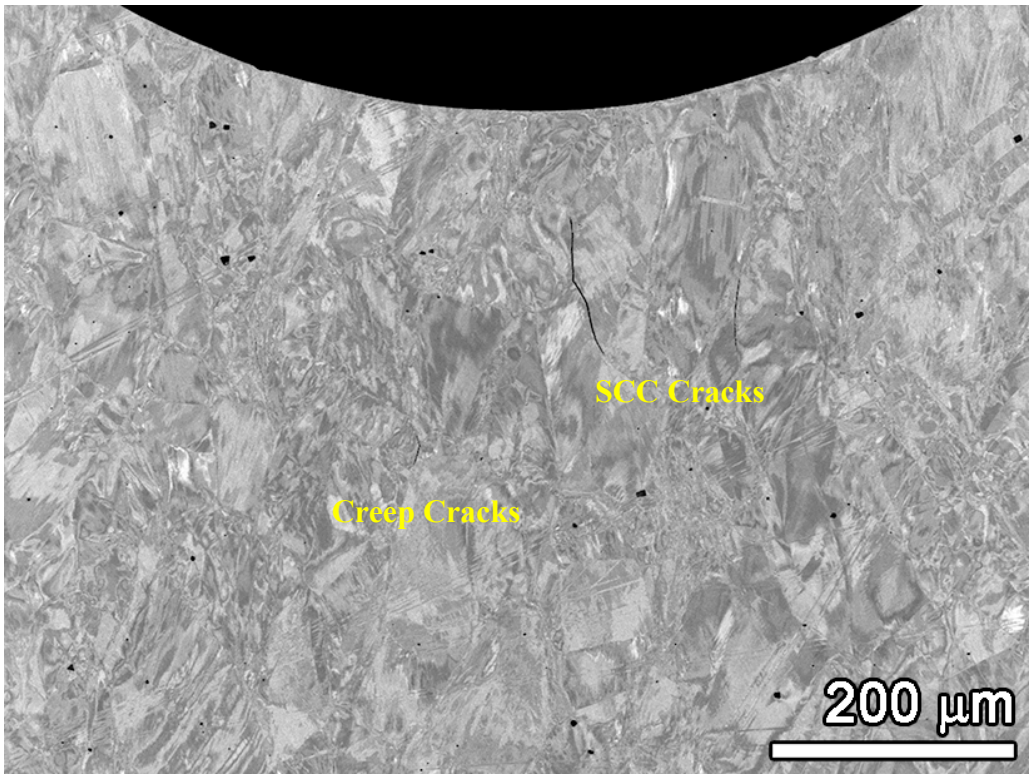

Figure 135. Blunt notch c672 cross-section slice #1 showing what are identified as SCC and creep cracks.

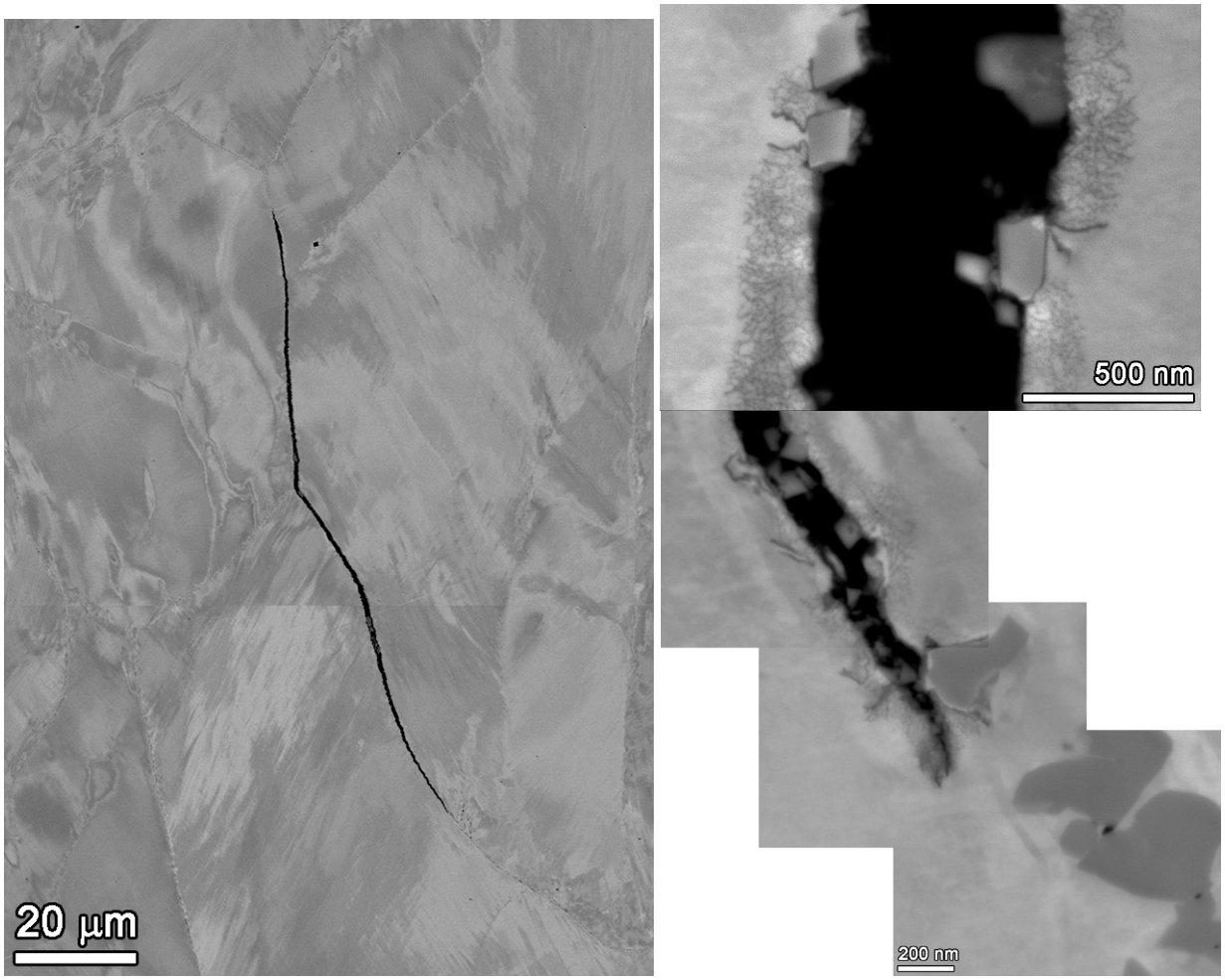

Figure 136. IGSCC crack in blunt notch specimen c672 cross-section slice #1 that clearly shows crack wall and crack tip corrosion.

Figure 137. Apparent creep cracks in blunt notch specimen c672 cross-section slice #1 showing no evidence for corrosion or oxidation along the crack walls.

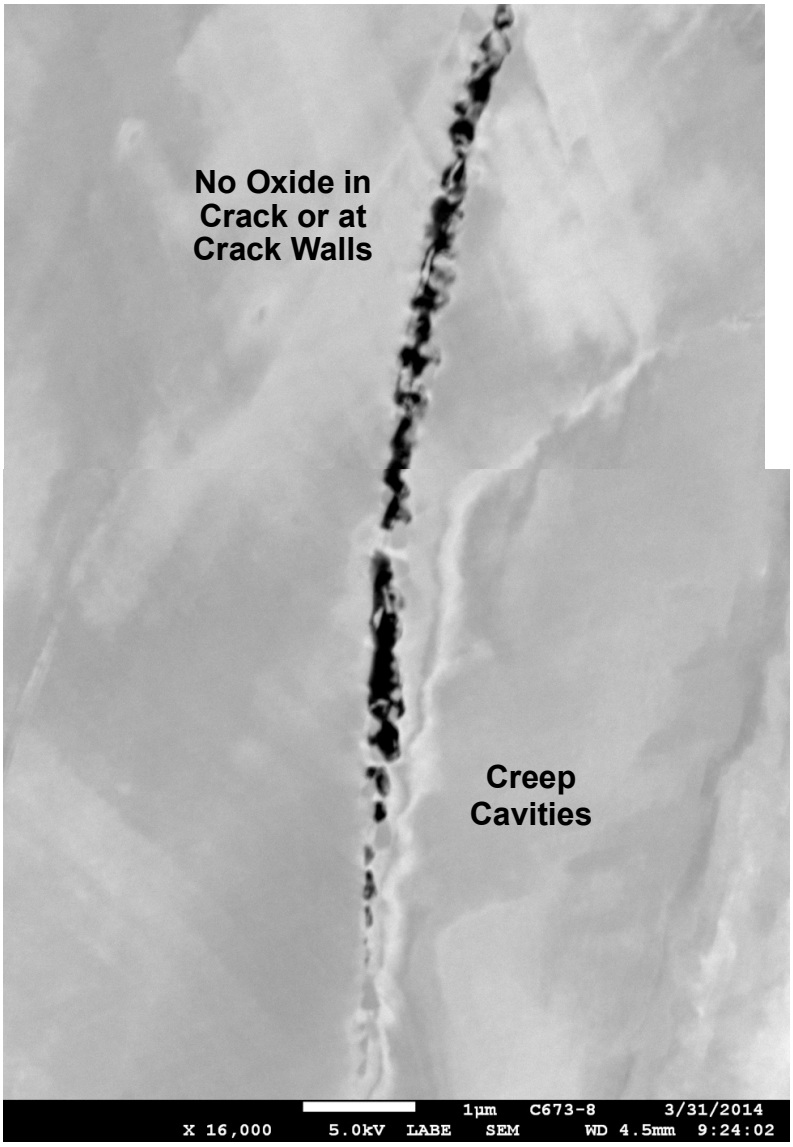

Figure 138. Example of IG creep crack and cavities in cross-section slice #2 from blunt notch specimen c672.

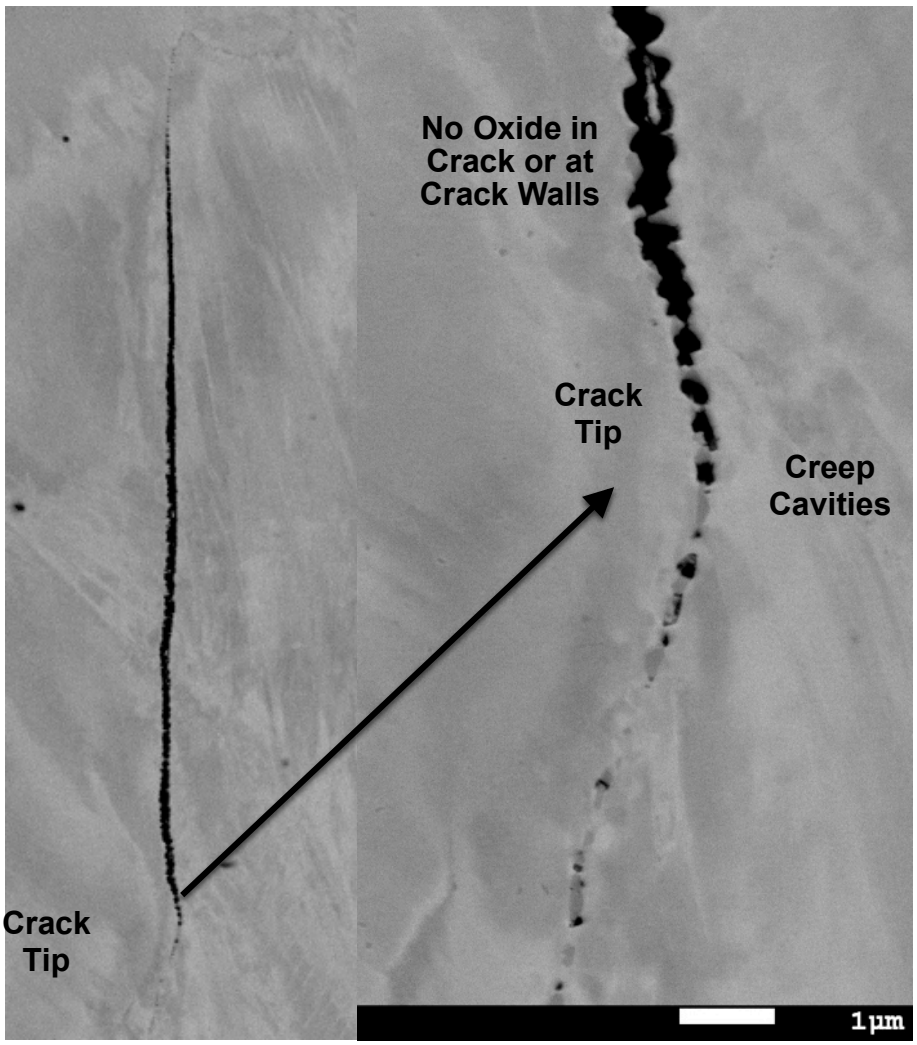

Figure 139. SEM-BSE cross-section image of c673 slice #4 showing creep crack tips. This slice had many large SCC cracks.

The main question that remains unanswered is whether creep cracking is responsible for the crack nucleation and growth observed in the blunt notch tests. To get a better assessment of the creep crack distributions, their locations were mapped on several cross-sections as presented in Figures 140 and 141 for c672 and c673, respectively. Small creep cracks are identified across the notch with a few close to the surface and most at a distance >100 µm below the surface. With the experiments that have been run, it has not been possible to conclude whether the creep cracks are responsible for nucleation on the surface. It seems very likely that the distribution of subsurface creep cracks promotes rapid growth of short cracks from the surface and leads to conditions for SCC growth at constant stress intensity. Much more work is needed to understand how the loading ramps employed in these blunt notch tests can produce such extensive creep cavitation and cracking. It is important to note that the same slow-strain-rate deformation was used for the IN007 tensile specimen and once again creep cracking was identified.

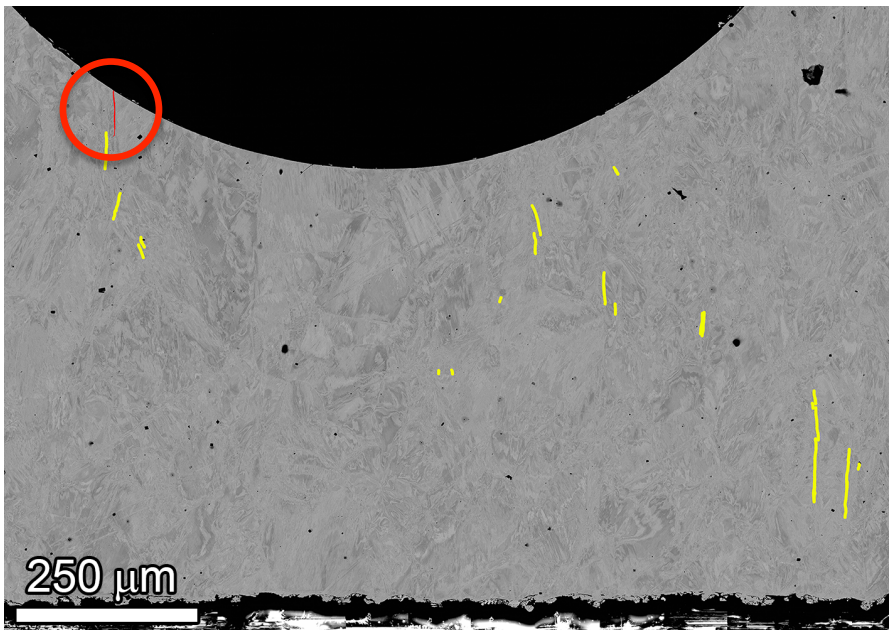

Figure 140. SEM-BSE image of C672 cross-section slice #2 showing cracks identified as SCC (red) and creep (yellow).

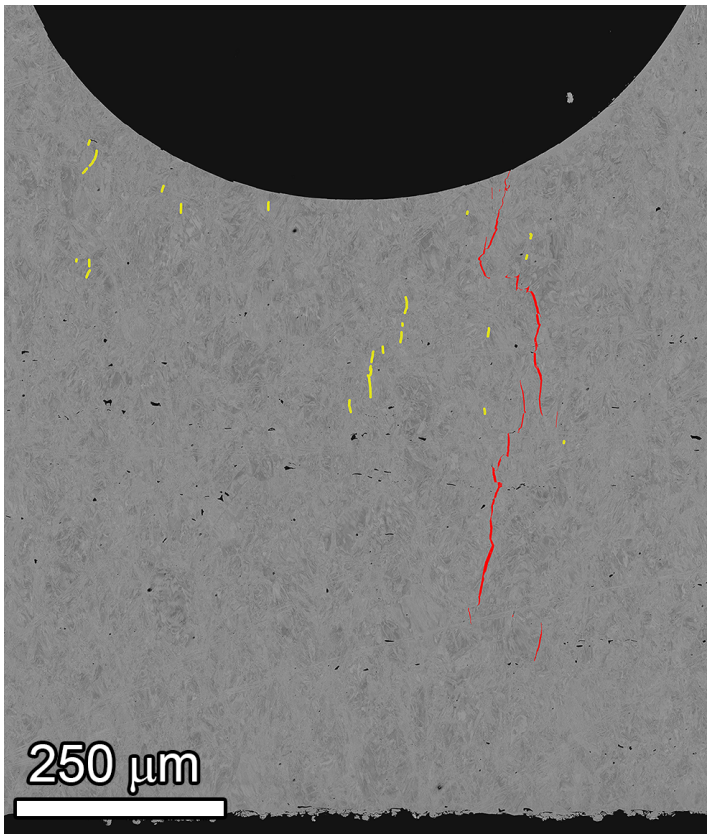

Figure 141. SEM-BSE image of C673 cross-section slice #4 showing cracks identified as SCC (red) and creep (yellow).

Critical Stress Intensity for SCC Growth on Cold Worked Alloy 690

To better understand the SCC susceptibility of highly cold-worked alloy 690 and implications for SCC initiation and short-crack growth, efforts were made to measure SCC propagation rates at low K levels on alloy 690. Low stress intensities and the possibility of a threshold stress intensity for SCC crack growth are of great interest for helping to understand SCC initiation and short crack growth response of these materials. K effects are also of interest to the NRC, and for this reason, this test was jointly funded between the NRC and DOE. Following standard SCC testing practice at PNNL, two specimens were tested in-series. CT098 was made from alloy 690 CRDM heat E67074C produced by Sumitomo, while CT099 was made from alloy 690 CRDM heat RE243 produced by Valinox. Material was cold forged to 31% reduction prior to fabricating specimens. SCC testing was performed using systems that provide active loading and in-situ DCPD crack length measurement enabling the stress intensity to be accurately controlled and systematically altered during a test. A practical aspect of pairing two specimens in series is that stress intensity can only be controlled to one specimen. For this test, stress intensity was controlled to the Sumitomo specimen, CT098. An overview plot for each of the specimens is provided in Figures 142 and 143.

Testing began at ~30 MPa√m to provide a baseline response and produce a fully engaged IGSCC crack front. Adjusted constant K CGRs for both materials were found to be ~$1x10^{-7}$ mm/s, consistent with the response of this same material or other alloy 690 materials tested at this cold work level. After assessing the SCC response twice at ~30 MPa√m, K was decreased to ~20 MPa√m by -dK/da over ~100 µm. This was followed by another ~150 µm of transitioning before evaluating SCC CGR behavior. This transitioning distance was estimate to be 1.5x the size of the plastic zone at 30 MPa√m.

Constant K CGRs at the corrected K of ~18 MPa√m were found to be ~$2\text{-}4x10^{-9}$ mm/s. After obtaining ~12 µm of crack extension over ~900 hours at his K level, observations at progressively higher K levels were performed over the next 5000 hours, eventually returning to a DCPD-indicated K value of ~28 MPa√m; identical to the start of the test. The adjusted CGR was found to be ~$7\text{-}8x10^{-8}$ mm/s, slightly lower than what was observed at the start of the test, and a second observation at a slightly higher K level produced a similar result. It was thought that the slightly reduced SCC CGR upon returning to ~30 MPa√m was due to ligament or contact formation over the course of the test, so aggressive 0.1 Hz (R=0.5) cycling was applied for ~0.5 mm of crack extension and was followed by retransitioning. The subsequent constant K response was unchanged, and since the DCPD-indicated crack length was at the limit of available crack extension for a 0.5T CT specimen, the decision was made to end the test and conduct post-test examinations on the specimens. Crack surface examinations such as those shown in Figure 144 for the Sumitomo CRDM CT099 revealed that SCC was entirely IG.

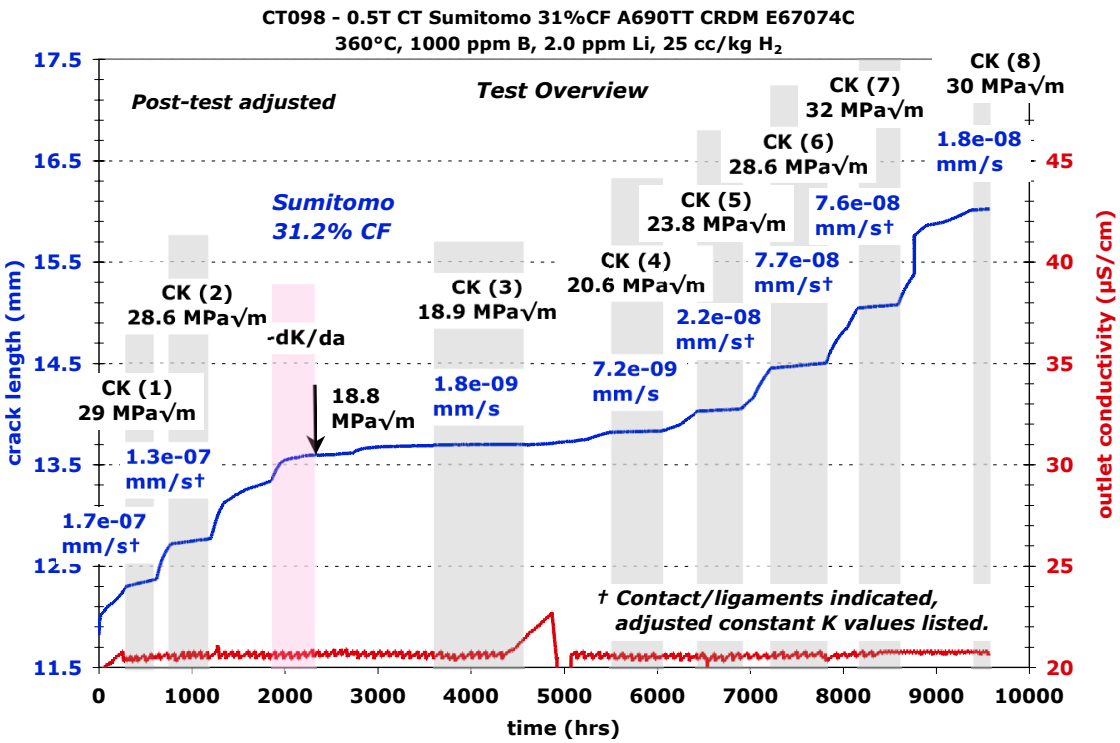

Figure 142. Overview of the entire SCC test on the 31%CF Sumitomo E67074C specimen CT098 showing crack growth rate at the different stress intensity levels.

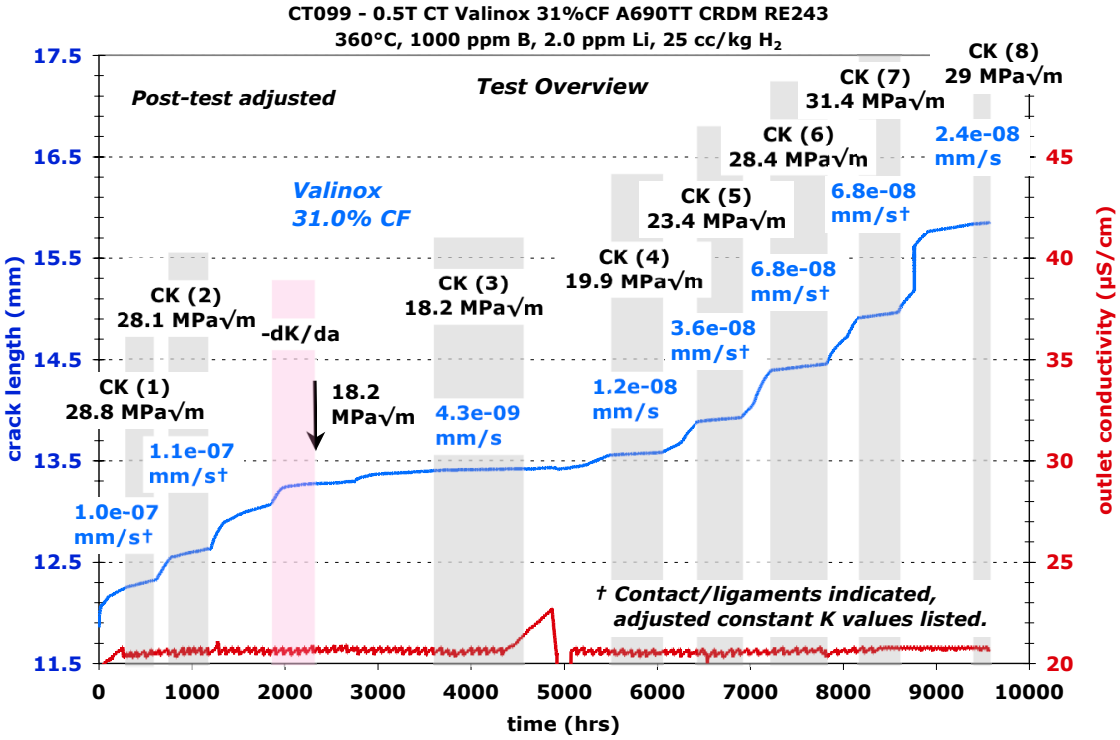

Figure 143. Overview of the entire SCC test on the 31%CF S-L/S-T Valinox CRDM RE243 specimen CT099 showing crack growth rate at each of the different stress intensity levels.

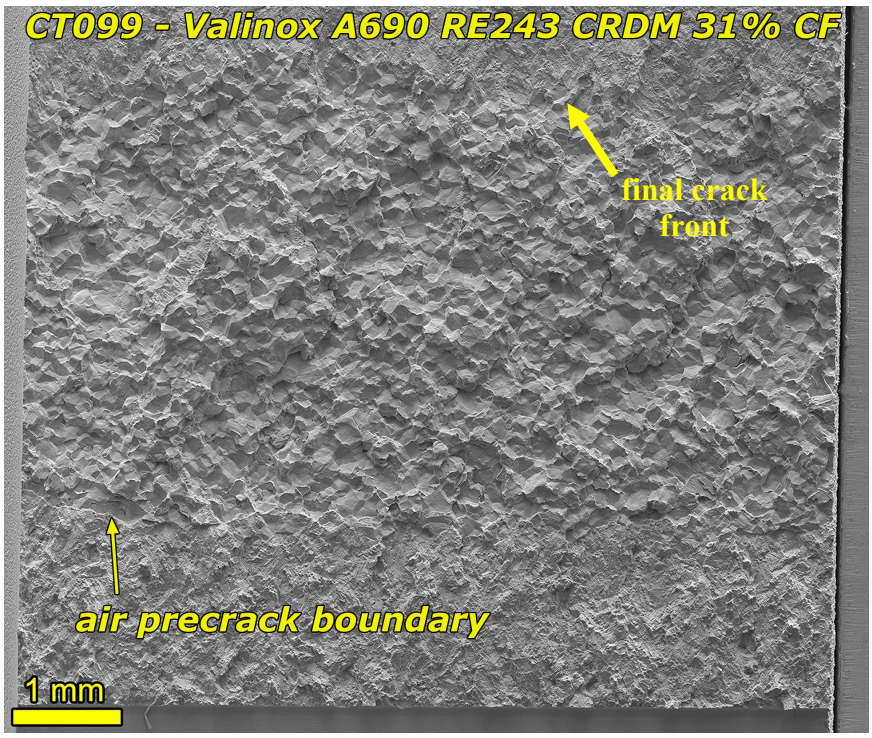

Figure 144. SEM-SE image of the entire crack growth surface of CT099 (Sumitomo CRDM).

This test revealed a strong effect of K on SCC CGRs measured at constant K as shown in Figure 145. Propagation rates were found to decrease by a factor of 30-40x between ~30 MPa√m and ~20 MPa√m. An SCC CGR of $2x10^{-9}$ mm/s represents a crack growth rate of 63 µm/year (or 0.0025"/year) suggesting that while this highly CW material is quite susceptible at moderate K levels of ~30 MPa√m and readily undergoes intergranular cracking, dropping down to 20 MPa√m and below dramatically increases the resistance to SCC crack propagation. This increase in SCC resistance is quite likely due to the protective Cr_2O_3 film that forms on grain boundaries intersecting the surface and at IG crack tips in the material. The results suggest that the protective nature of this Cr_2O_3 film is dependent on the local stress at the crack tip. Slip-oxidation is a likely mechanism with higher stress intensities causing more rapid rupture of the film. As will be discussed later, the ramifications of this K dependence for SCC initiation of alloy 690 are significant, as not only is the film highly effective at preventing precursor formation under constant load conditions, but it also appears that a significantly deep flaw will be needed to produce a sufficiently high crack tip stress (and stress intensity) to allow transitioning to an actively growing crack.

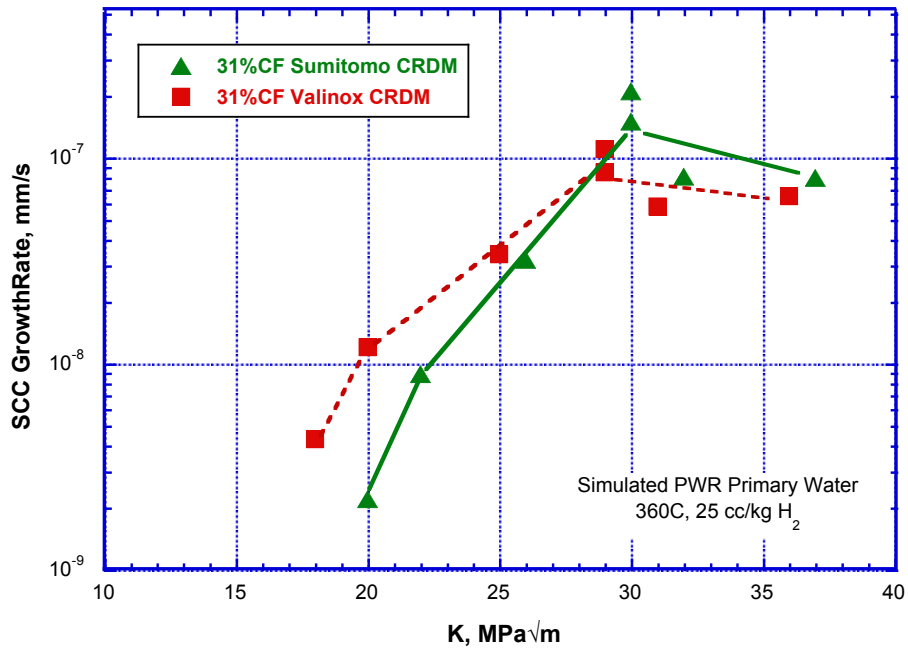

Figure 145. Crack growth rate as a function of K for the 31%CF alloy 690 CRDM materials in 360°C PWR primary water.

Constant Load Tensile Tests on 31% Cold Forged Alloy 690 (IN024 – IN032) and 21% Cold Forged Alloy 690 (IN033 - IN044)

While alloy 690 exhibits excellent resistance to intergranular attack (with or without stress) because of the highly protective Cr_2O_3 film that forms over grain boundaries intersecting the surface, the long term viability of this protective film and initiation resistance of alloy 690 should still be assessed. The protective film has been shown to be stable out to ~9000 hours (1 year) on two specimens (IN006/07) that were tested under aggressive conditions that included plastic straining. However, there are still unknown aspects of the long term microstructural evolution of alloy 690, one example being the unknown microstructural evolution that is causing the resistivity of this material to increase over time when exposed at 360°C. Long term deformation, i.e., creep, may also affect the film stability or may enable creep crack precursor formation not related to comprising the protective surface film. To enable the task of performing long term observations, a 36-specimen actively loaded and actively monitored test system was built. This test system also has the potential to benefit the NRC and industry in assessing the SCC initiation resistance of alloy 690 relative to alloy 600. A number of shakedown activities and small modifications were needed to achieve desired performance, but testing in this system is now underway.

For the first ~2100 hours of operation of the first long term test, 21 alloy 690 specimens have been exposed. These include four heats in a 31%CF condition and three heats in a 21% CF condition. Three heats - Sumitomo E67074C, Valinox RE243, and TK-VDM (Doosan) 133454

are CRDM materials, and one heat - TK-VDM 114092 is in the form of plate material. There are three specimens for each combination of heat and cold forge condition, and within each set of three, one has been polished to a 1 µm surface condition, and the other two have a "C" finish on the gauge section. All specimens are being exposed at their yield stress. Due to limited space in the autoclave, only one specimen from each combination of heat and cold forge level could be instrumented for DCPD crack initiation detection. The non-referenced strain response for each of these instrumented specimens is summarized in Figures 146 and 147. All are exhibiting typical resistivity evolution that is producing asymptotically increasing non-referenced strains that are not representative of actual creep response. The resistivity effect is expected to diminish substantially after ~1 year. This test was recently stopped to remove 9 alloy 600 specimens, and insert 15 new alloy 690 specimens. These new alloy 690 specimens include the ANL (Special Metals) plate heat NX3297HK-12 of alloy 690 in a 26%CR condition, the GE (Allvac) plate heat B25K in an 18% CF condition, the TK-VDM 114092 plate in a 21% CF condition, the Valinox CRDM heat RE243 in a 12% CF condition, and the GE plate heat again in a 12% CF condition. This test has been restarted with specimens reloaded to their yield stress. Both the ANL and GE plate heats were previously observed to be very susceptible to SCC crack growth at the cold work levels used here. The current plan is to stop the test once every six months to selectively remove, examine, and reinstall specimens.

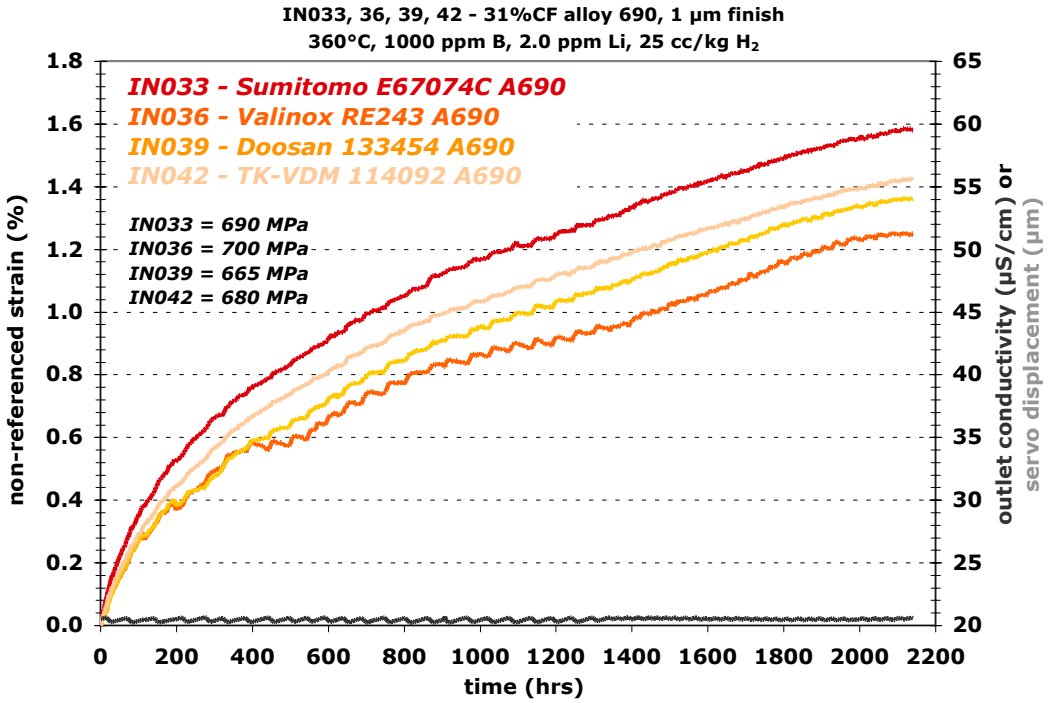

Figure 146. Non-referenced strain response for four heats of 31% CF alloy 690 undergoing long term constant load exposure at 360°C in the PNNL 36-specimen initiation test system. For each heat of material at this CW level, there are 3 specimens in the test rig.

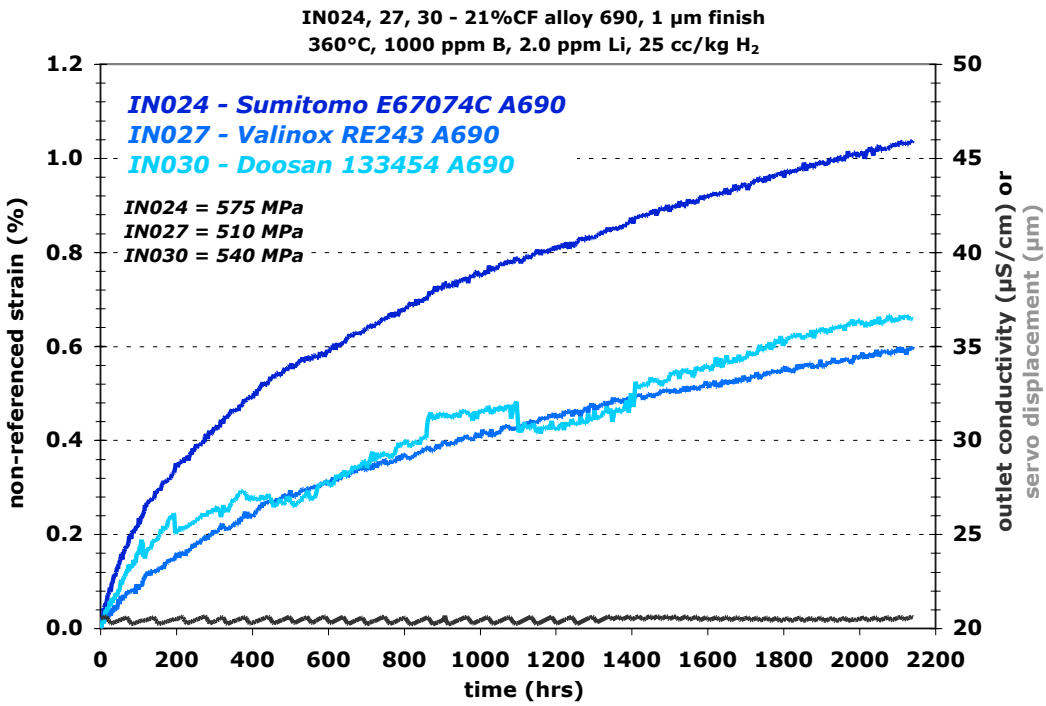

Figure 147. Non-referenced strain response for three heats of 31% CF alloy 690 undergoing long term constant load exposure at 360°C in the PNNL 36 specimen initiation test system. For each heat of material at this CW level, there are 3 specimens in the test rig.

Discussion of Alloy 690 SCC Initiation Results

The approach for SCC initiation testing was established by our experiments on cold-worked alloy 600 (described earlier in this report) where crack nucleation was successfully detected within ~2500 hours. Even though it is clear that the mechanisms controlling corrosion and SCC are different for alloy 600 and alloy 690 in PWR primary water, cold-worked alloy 690 has been shown by many investigators to be highly susceptible to SCC crack growth. Moreover, SCC propagation rates comparable to those for mill-annealed alloy 600 have been measured for highly cold-worked alloy 690 materials. This similarity in SCC propagation rates led to an expectation that highly cold-worked alloy 690 would also be susceptible to SCC initiation in constant load tests.

The first phase of the SCC initiation test plan for alloy 690 was built around this hypothesis and utilized materials that exhibit high primary water SCC propagation rates (~$1x10^{-7}$ mm/s) when in a CW condition. SCC susceptible 26-31%CR materials (IN006/IN007) were selected to critically evaluate this assumption and begin investigations of key factors influencing SCC initiation in alloy 690. The lack of SCC initiation in these specimens after long exposures in 360°C simulated PWR primary water at high stresses modified expectations. While the total test time for the CR alloy 690 specimens is only 2-3x higher than the measured SCC initiation times for cold-worked alloy 600, surface characterizations on both stressed and unstressed alloy 690 revealed important differences in oxidation microstructures. A continuous chromia film forms

above alloy 690 grain boundaries and effectively blocks IG corrosion/oxidation that acts as a precursor to SCC initiation in alloy 600. Results for the first constant load tests on SCC-susceptible alloy 690 specimens indicate that this protective chromia film is not broken down even after long exposures at the yield stress. Therefore, modifications to the testing approach were made to determine whether precursor cracks could be generated by other means. The most obvious method, which is the one being used for this work, is dynamic straining.

Several different straining methods were explored in these early SCC initiation experiments. For the highly CR materials known to be susceptible to SCC growth, it was decided to periodically induce small amounts of in-situ tensile deformation at a moderate strain rate of ~$5x10^{-4}$ s^{-1}. The intent was to create surface damage and compromise the protective film leading to formation of SCC precursors. Most of this evaluation focused on the 26%CR ANL plate specimen IN006 when micrometer-length cracks were observed to nucleate off corroded TiN stringers that intersected the surface. Increasing plastic strain was found to increase the density and size of IG and TG cracks. However despite several applications of plastic strain and almost 4000 hours of additional exposure at very high stress, these cracks did not exceed ~10 µm in depth showing that alloy 690 is remarkably resistant to additional growth under this straining condition.

For another series of specimens that were cold tensile strained prior to SCC initiation testing, the effect of cyclic loading and slow strain rate extension were both assessed. While it was understood that cyclic loading up to yield stress would produce only elastic strains, it was hoped that the strains would be sufficiently large to disrupt the surface oxide film. Although testing conditions were limited, no change in specimen response was observed during cyclic loading. The same specimens were then subjected to slow strain rate testing to ~3.5% plastic strain over a period of eight days (strain rate of ~$1x10^{-7}$ s^{-1}). This produced a high density of slip bands intersecting the surface with many having the appearance of cracks with lengths up to ~10 µm. These results are consistent with the slow strain rate testing of alloy 690 in 360°C PWR primary water by Moss [17]. Surface cracks of a similar length (average ~3 µm) were reported indicating that continuous dynamic strain can clearly lead to crack formation in alloy 690.

This assessment of slow strain effects was continued on initiation specimens and blunt notch specimens. When IN007 (31%CF Valinox RE243) was subjected to an order of magnitude slower strain rate (~$1x10^{-8}$ s^{-1}) than previous slow strain rate observations, SCC initiation was observed to take place. Post-test examination revealed not only IGSCC cracking but also a substantial amount of creep cracking. Concurrent blunt notch tests on highly CW alloy 690 where slow loading ramps were applied to produce strain surface strain rates of ~$1x10^{-8}$ s^{-1} also resulted in SCC initiation and creep crack formation. In both cases, creep cracks were found that had been exposed to water demonstrating that these creep cracks can play a role in the SCC initiation process. While these tests established a means to produce SCC initiation, the details by which it occurred could not be determined from these tests. Specifically, the question is whether creep cracks grow to intersect the surface, or whether both SCC cracks and creep cracks nucleate simultaneously and through percolation processes, eventually link up to result in a crack that is

sufficiently long to produce a stress intensity needed for initiated SCC response. A new series of tests are being planned to clarify which process is dominant.

These results clearly demonstrate that alloy 690 materials can exhibit quite different susceptibility to SCC initiation versus SCC growth. Highly cold-worked alloy 690 that shows very high SCC propagation rates in tests on compact tension specimens are remarkably resistant to SCC initiation in constant load tests on polished specimens. The parallel assessment of alloy 690 surface corrosion microstructures has shown that this material is resistant to IG corrosion/oxidation due to the formation of a protective chromia film above the grain boundaries that intersect the surface. As a result, SCC initiation from a smooth surface appears to be extremely difficult without aggressive straining to thin or break this protective oxide layer. It is interesting to note that strong Cr depletion is observed along grain boundaries to micrometer depths below the surface. Therefore if the protective layer is breached, IG corrosion and SCC of the Cr-depleted grain boundary might be expected. Microstructural examinations question this possibility since shallow IG cracks have been created after dynamic straining in the 26%CR ANL specimen IN006, yet there is no indication of intergranular attack or IGSCC propagation.

An important conclusion from these early experiments is that more aggressive plastic deformation appears to be required to nucleate cracks in alloy 690. Low K SCC testing has also revealed that while CW alloy 690 is highly susceptible to IGSCC at moderate stress intensities, at lower stress intensities, it appears that the crack growth rate falls off dramatically, possibly reaching insignificant crack growth rates at a still moderate K level of 20 MPa√m. Thus, for SCC initiation to occur, it appears that dynamic straining at very high stresses may be needed to produce precursor cracks that will be under sufficiently high stress to undergo SCC initiation. Of course an issue for this scenario is whether it represents a possible loading condition for service components.

From the alloy 600 initiation tests, it appears that SCC imitation can be distilled down to the notion that precursor flaws of sufficient size to produce a SCC-relevant stress intensity are needed for initiated response. This is readily achieved in alloy 600 by stress-assisted intergranular attack during constant load exposure. In alloy 690, an equivalent constant load microstructurally-based degradation process does not appear to exist. However, since alloy 690 can be highly susceptible to SCC crack growth at plant-relevant stress intensities, it is worth considering whether other processes can achieve the necessary precursor flaw. The next phase of the experimentation at PNNL focuses on an improved understanding possible precursor morphologies. The effect of dynamic straining on IGSCC precursor and creep crack formation will continue to be studied. A key goal is to understand how stress, stress intensity and strain affect crack nucleation. Initiation specimens and blunt notch tests will be utilized. Another aspect that will be considered is whether local defects can produce sufficiently high stress intensities to cause SCC initiation in alloy 690. CT specimens with notch geometries ranging from a sharp fatigue precrack up to a notch root radius used for the blunt notch initiation tests

will be explored. Small defects will also be created on tensile initiation specimens. These will likely be dimple type defects.

Summary and Conclusions

Observations of alloy 600 initiation suggest that the mechanism to SCC initiation distills down to producing a flaw that has an SCC-relevant stress intensity to drive SCC growth. This is readily achieved in alloy 600 by stress-assisted intergranular attack during constant load exposure. SCC experimentation has revealed that cold worked alloy 690 is extremely resistant to SCC initiation even though it is highly susceptible to SCC growth. The first attempts to produce SCC initiation in constant load tests at high stress, a method observed to be very effective in alloy 600, did not produce SCC despite the formation of small TG and IG cracks into the matrix from corroded TiN intersecting the surface. Detailed microstructural investigations of alloy 690 exposed to PWR primary water revealed that a protective chromia layer forms above grain boundaries, and this film appears to remain protective during constant load testing at high stresses. However, significant grain boundary chromium depletion was detected for several hundred micrometers below the surface that may allow IG oxidation and SCC if the chromia film can be breached. Efforts to accelerate the crack initiation process by application of tensile loading type plastic strain rates produced more significant surface cracking, but no evidence of SCC. The small surface precursor cracks remained in the micrometer size range and showed no evidence of growth. However, in the case of very low strain rates, SCC initiation was achieved in both tensile specimens and blunt notch specimens. Somewhat unexpectedly, extensive IG creep cracking was observed in the initiated specimens suggesting that they played a major role in producing the necessary precursor flaw. The experiments that were performed were unable to provide sufficient information to confirm this though. The observation of successful initiation does show that as with alloy 600, alloy 690 simply needs a flaw of sufficient depth for crack initiation to occur. A new series of tests are underway to explore whether there are any potentially plant relevant scenarios that could lead to SCC initiation in alloy 690.

Acknowledgments

The authors would like to recognize the collaborative funding from the Office of Basic Energy Sciences for APT characterizations, the Nuclear Regulatory Commission for SCC crack growth tests on alloy 690 materials and Rolls Royce & Associates for detailed examinations on cold-worked microstructures. These collaborations have been essential to the success of the SCC research. Critical technical assistance is also recognized from Rob Seffens, Anthony Guzman and Clyde Chamberlin.

References

1. M. B. Toloczko, M. J. Olszta, D. K. Schreiber and S. M. Bruemmer, *Stress Corrosion Crack Initiation of Alloy 600 in PWR Primary Water Environments*, Technical Milestone Report M3LW-13OR0403032, Light Water Reactor Sustainability Program, DOE Office of Nuclear Energy, March 2013.

2. M. B. Toloczko, M. J. Olszta, D. K. Schreiber and S. M. Bruemmer, *Corrosion and Stress Corrosion Crack Initiation of Cold-Worked Alloy 690 in PWR Primary Water Environments*, Technical Milestone Report M2LW-13OR0402035, Light Water Reactor Sustainability Program, DOE Office of Nuclear Energy, September 2013.

3. D. S. Morton, et. al., "SCC Initiation Testing of Nickel-Base Alloys in High Temperature Water," *Proc. 14th International Conference on Environmental Degradation of Materials in Nuclear Power Systems-Water Reactors*, American Nuclear Society, 2009.

4. S. M. Bruemmer and M. B. Toloczko, *Pacific Northwest National Laboratory Investigation of Stress Corrosion Cracking in Nickel-Base Alloys,* NUREG/CR-7103, Volume 1, Nuclear Regulatory Commission, Office of Nuclear Regulatory Research, May 2011.

5. S. M. Bruemmer and M. B. Toloczko, *Pacific Northwest National Laboratory Investigation of Stress Corrosion Cracking in Nickel-Base Alloys,* NUREG/CR-7103, Volume 2, Nuclear Regulatory Commission, Office of Nuclear Regulatory Research, November 2011.

6. I.S. Raju and J.C. Newman, Jr., *Stress-Intensity Factors for Circumferential Surface Cracks in Pipes and Rods under Tension and Bending Loads*, NASA Technical Memorandum 87594, August, 1985.

7. L.A. James and W.J. Mills, "Review and Synthesis of Stress Intensity Factors Solution Applicable to Cracks in Bolts," *Engineering Fracture Mechanics,* Vol. 30, No. 5, pg. 641, 1988.

8. A. Carpinteri, "Stress Intensity Factors for Straight-Fronted Edge Cracks in Round Bars," *Engineering Fracture Mechanics,* Vol. 42, No. 6, pg. 1035, 1992.

9. C.S. Shin and C.Q. Cai, "Experimental and Finite Element Analyses on Stress Intensity Factors of an Elliptical Surface Crack in a Circular Shaft Under Tension and Bending," *International Journal of Fracture,* Vol. 129, pg. 239, 2004.

10. J. Toribio, N. Àlvarez, B. Gonzàlez, J.C. Matos, "A Critical Review of Stress Intensity Factor Solutions for Surface Cracks in Round Bars Subjected to Tension Loading," *Engineering Failure Analysis,* Vol. 16, 2009, pg. 794.

11. *Materials Reliability Program (MRP) Crack Growth Rates for Evaluating Primary Water Stress Corrosion Cracking (PWSCC) of Thick-Wall Alloy 600 Materials*, MRP-55, Revision 1, Project Managers: J. Hickling, A. McIlree, R. Pathania, EPRI, 2002.

12. S. LeHong, C. Amzallag, A. Gelpi, "Modeling of Stress Corrosion Crack Initiation on Alloy 600 in Primary Water of PWRs," *Proc. 9th International Symposium on Environmental Degradation of Materials in Nuclear Power Systems - Water Reactors,* The Minerals, Metals, and Materials Society, 1999, pg. 115.

13. S. M. Bruemmer, M. J. Olszta, D. K. Schreiber, N. R. Overman and M. B. Toloczko, *Characterizations and Stress Corrosion Cracking Evaluations of Alloy 600 CRDM Nozzle Heats from the Davis Besse Nuclear Power Plant,* NRC Report, August 2013.

14. D. S. Dunn, J. Collins, D. Alley, B. Alexandreanu, M. B. Toloczko and S. M. Bruemmer, "Primary Water Stress Corrosion Cracking Tests and Metallurgical Analysis of Davis Besse Control Rod Drive Mechanism Nozzle #4," *Proc. 16th Int. Conf. Environmental Degradation of Materials in Nuclear Power Systems – Water Reactors,* NACE International, 2014.

15. D. K. Schreiber, M. J. Olszta, L. E. Thomas and S. M. Bruemmer, "Grain Boundary Characterization of Alloy 600 Prior To and After Corrosion by Atom Probe Tomography and Transmission Electron Microscopy," *ibid 14*.

16. D. K. Schreiber, M. J. Olszta, D. W. Saxey K. Krusha, K. L. Moore, S. Lozano-Perez and S. M. Bruemmer, "Examinations of Oxidation and Sulfidation in Alloy 600 Grain Boundaries Exposed to Simulated PWR Primary Water," *J. Microscopy and Microanalysis,* 19-03, 2013, 676.

17. R. A. Morris, N. Lewis and D. S. Morton, "3D Analysis of Surface Treatment Effect on the Oxidation of Grain Boundaries in Alloy 600," *ibid 14*.

18. M. J. Olszta, D. K. Schreiber, L. E. Thomas and S. M. Bruemmer, "Penetrative Internal Oxidation from Alloy 690 Surfaces and Stress Corrosion Crack Walls during Exposure to PWR Primary Water," *Proc. 15th International Conference on Environmental Degradation of Materials in Nuclear Power Systems-Water Reactors,* The Minerals, Metals and Materials Society, 2012.

19. M. J. Olszta, D. K. Schreiber, M. B. Toloczko and S. M. Bruemmer, "Alloy 690 Surface Nanostructures During Exposure to PWR Primary Water and Potential Influence on Stress Corrosion Crack Initiation," *ibid 14.*

20. S. M. Bruemmer, M. J. Olszta, M. B. Toloczko and L. E. Thomas, "High-Resolution Characterizations of Grain Boundary Damage and Stress Corrosion Cracks in Cold-Rolled Alloy 690," *ibid 18.*